

# **Ion and Defect Migration Control and its Effect in Organo Lead Halide Perovskites**

*Dissertation*

zur Erlangung des akademischen Grades  
eines Doktors der Naturwissenschaften (Dr. rer. nat.)  
im Promotionsprogramm  
Polymer Science  
der Bayreuther Graduiertenschule für Mathematik und Naturwissenschaften

vorgelegt von

**Yu Zhong**

geboren in Chongqing, China

Bayreuth, 2020



This doctoral thesis was prepared at the department of Organic and Hybrid Electronics (Macromolecular Chemistry I) at the University of Bayreuth from August 2016 to March 2019 supervised by Prof. Dr. Sven Hüttner and then at the department of Optoelectronics of Soft Matter (Experimental physics II) at the University of Bayreuth from April 2019 until May 2020 supervised by Prof. Dr. Anna Köhler.

Date of submission: 08.06.2020

Date of defence: 15.09.2020

Acting director: Prof. Dr. Markus Lippitz

Doctoral committee:

Prof. Dr. Anna Köhler	(reviewer)
-----------------------	------------

Prof. Dr. Mukundan Thelakkat	(reviewer)
------------------------------	------------

Junior Prof. Dr. Anna Schenk	(chairman)
------------------------------	------------

Prof. Dr. Ralf Moos	
---------------------	--





# Contents

<b>1 Abstract .....</b>	<b>1</b>
1.1 English Abstract .....	1
1.2 Deutsche Kurzzusammenfassung .....	3
<b>2 Introduction .....</b>	<b>5</b>
2.1 Motivation .....	5
2.2 Organo Metal Halide Perovskite Material .....	6
2.3 Optical Properties .....	10
2.4 Defects.....	12
2.5 Perovskite Solar Cell Operation .....	22
2.6 References .....	29
<b>3 Overview.....</b>	<b>41</b>
3.1 Overall Synopsis and Conclusion .....	41
3.2 Contents of the Individual Chapter.....	43
3.3 Author's Contributions.....	50
<b>4 Emission Enhancement and Intermittency in Polycrystalline Organolead Halide Perovskite Films.....</b>	<b>53</b>
<b>5 In situ Investigation of Light Soaking in Organolead Halide Perovskite Films .....</b>	<b>69</b>
<b>6 Role of PCBM in the Suppression of Hysteresis in Perovskite Solar Cells .....</b>	<b>85</b>
<b>7 Investigating Two-Step MAPbI<sub>3</sub> Thin Film Formation during Spin Coating by Simultaneous in situ Absorption and Photoluminescence Spectroscopy .....</b>	<b>105</b>
<b>8 Crystallization Kinetics of Controlled Solvent Vapor Assisted Annealing of Organo Lead Perovskite Film .....</b>	<b>131</b>
<b>9 Appendix.....</b>	<b>153</b>
9.1 List of Publications .....	153
9.2 Abbreviations .....	155
9.3 Acknowledgements.....	157
9.4 Eidesstattliche Versicherung und Erklärungen.....	159



# 1 Abstract

## 1.1 English Abstract

Organo lead halide perovskites have emerged as the pioneer of new photovoltaic materials in the last decade, because their extraordinary optoelectronic properties lead to corresponding highly efficient photovoltaic devices. Although a lot of researchers worked on these materials in very recent time, many fundamental questions still remain unanswered to date. One of them is the material instability which can be induced by illumination and external electric field. As these two factors unavoidably play a role under operational conditions of perovskite solar cells (PSCs), it is significant to find out their influence factors and to minimize their impacts. Two peculiarities related to the photo- and electric-induced instability, which impede the stable output of PSCs, are studied in this thesis. One is that the power conversion efficiency (PCE) of PSCs declines quickly under continuous illumination. The second one is that the current density-voltage ( $J$ - $V$ ) curve of PSCs shows hysteresis, depending on the respective measurement conditions.

In order to clarify the first problem, a wide-field photoluminescence (PL) microscope was employed to study the local changes of perovskite films under illumination. The investigation in Chapter 4 presents that perovskite individual grains/nanocrystals exhibit PL intermittency, indicating the spacially confined transitions between bimolecular recombination and Auger non-radiative recombination. This reflects that a large number of ions/defects exists in polycrystalline perovskite films and those in most cases can result in poor emission properties. Chapter 5 discusses the observed decrease of local PL, while at the macroscale the PL enhances. The decrease in PL intensity happens at a similar timescale as the PCE decay of PSCs. Hence, we propose that this local PL quenching is related to the photo-induced PSC deterioration. Combined with the observations regarding the PL blinking in Chapter 4, this behavior is attributed to the accumulation of ions/defects by light soaking. In a working PSC, the ion redistribution under illumination leads to the decrease of external luminescence, which will directly influence the open circuit voltage ( $V_{oc}$ ) and the PCE.

The  $J$ - $V$  hysteresis problem has attracted attention in the field and studies manifest that phenyl-C61-butyric acid methyl ester (PCBM) can suppress hysteresis. Besides the positive effects of trap state elimination by PCBM, Chapter 6 demonstrates that PCBM hinders the migration of iodine related defects under working bias, which is supposed to be responsible for hysteresis. The retarded ionic migration is proven by PL microscopy investigations and by the increase of its activation energy estimated from temperature-dependent chronoamperometric measurements. Using a PCBM-grafted polymer as an interfacial layer in PSCs, hysteresis is still pronounced compared to the device with a PCBM layer. It indicates that the diffusion or incorporation of PCBM molecules in the perovskite material is crucial, as the diffusion of PCBM molecules that are grafted on polymer backbones is strongly impeded. Thus, PCBM molecules in the bulk of the perovskite suppress iodine ions or vacancies migration, moderating the built-in field shift in PSC caused by external bias.

Chapter 4 and Chapter 5 highlight that the PL intermittency and local PL intensity decay phenomena are weakened by the PCBM layer, while in Chapter 6 the passivation of mobile

ions or vacancies by PCBM is emphasized. These investigations suggest a way to eliminate the photo- and electric-induced negative effects by the use of additives or interfacial layer. Apart from this method, the preparation of high-quality perovskite films is another important way. The high-quality film typically exhibits less defect states and mobile ions in the material and can improve the PSC stability. Perovskite films with less grain boundary area, i.e. with large grain sizes, also have the similar effect. Hence, Chapter 7 and Chapter 8 focus on the control of perovskite film formation by looking into the perovskite film evolution during spin coating and annealing.

In Chapter 7, absorption and PL spectra were *in-situ* recorded when methylammonium iodide (MAI) dissolved in dimethylformamide (DMF) was spin coated on a  $\text{PbI}_2$  layer. The results reveal that the crystal formation occurs in the first 20 seconds. We firstly explicitly analyzed the optical properties on this time scale. In brief, the formation of  $\text{MAPbI}_3$  capping layer and its dissolution-recrystallization were the major changes detected during spin coating. As the dissolution-recrystallization process strongly influences the final film quality, it is important to control the speed of this process. Furthermore, developing an in-depth understanding of the measured optical spectra allows us to explore the change of the film thickness during the spin coating and the respective phases of perovskite formation.

In Chapter 8, with the assistance of a solvent vapor assisted annealing method, we could grow perovskite films with large grains and concomitantly minimize grain boundary area and defect densities. From *in-situ* grazing incidence wide-angle X-ray scattering (GIWAXS) measurements, it is found that DMF vapor treatment during annealing slows down the crystallization. By systematically increasing the vapor concentration, it is possible to enlarge the crystal size. However, too high DMF vapor concentrations lead to the formation of pinholes, as DMF can liquefy and partially dissolve perovskite crystals. This work indicates that the precise control of solvent vapor assisted annealing is necessary to obtain high-quality perovskite films.

## 1.2 Deutsche Kurzzusammenfassung

Organo-Blei-Halogenid-Perowskite haben sich im letzten Jahrzehnt als ein vielversprechendes neues Photovoltaik-Material mit interessanten optoelektronischen Eigenschaften herausgestellt, die bereits zur Demonstration hocheffizienter Solarzellen geführt haben. Trotz den intensiven Forschungen an diesen Materialien, bleiben viele grundlegende Fragen bis heute unbeantwortet. Eine von diesen ist die Materialinstabilität, welche durch Beleuchtung oder externe elektrische Felder beeinträchtigt werden kann. Da diese beiden Faktoren unter Betriebsbedingungen von Perowskit-Solarzellen (PSCs) unvermeidlich eine Rolle spielen, ist es wichtig, ihre Einflussfaktoren herauszufinden und deren Auswirkungen zu minimieren. In dieser Arbeit werden zwei Besonderheiten im Zusammenhang mit der photo- und elektrisch-erzeugten Instabilität erforscht, die die stabile Leistung von Perowskit-Solarzellen beeinträchtigen. Der eine ist, dass der Wirkungsgrad (PCE) von Perowskit-Solarzellen bei andauernder Beleuchtung abnimmt. Der andere Aspekt ist, dass die Stromdichte-Spannungs-Kennlinie ( $J$ - $V$ -Kennlinie) von Perowskit-Solarzellen abhängig von den entsprechenden Messbedingungen eine Hysterese zeigt.

Um das erste Problem zu klären, wurde mittels Weitfeld-Photolumineszenzmikroskopie die lokalen Veränderungen von Perowskitfilme unter Beleuchtung untersucht. Die Ergebnisse in Kapitel 4 zeigen, dass einzelne Perowskit-Kristallkörner/Nanokristalle Unstetigkeiten in ihrer Photolumineszenz (PL) aufweisen, was auf räumlich begrenzten Wechsel zwischen bimolekularer Rekombination und nicht strahlender Auger-Rekombination hinweist. Dies spiegelt die große Anzahl an Ionen/Defekten in polykristallinen Perowskitfilmen wider, und diese können in den meisten Fällen zu schlechten Emissionseigenschaften führen. In Kapitel 5 wird die beobachtete Abnahme der mikroskopisch lokalen PL Intensität diskutiert, während auf makroskopischer Ebene eine Zunahme der PL beobachtet wird. Die Abnahme der PL Intensität findet auf einer ähnlichen Zeitspanne wie die Abnahme des Wirkungsgrades der Perowskit-Solarzelle statt, was einen gegenseitigen Zusammenhang nahelegt. Kombiniert mit den Beobachtungen bezüglich des PL-Blinkens in Kapitel 4, wird dieses Verhalten auf die Akkumulation von Ionen/Defekten durch Lichtabsorption zurückgeführt. Bei einer PSC führt die Ionenunverteilung unter Beleuchtung zur Abnahme der externen Lumineszenz, was sich direkt auf die Leerlaufspannung ( $V_{oc}$ ) und den Wirkungsgrad auswirkt.

Das Problem der  $J$ - $V$ -Hysterese hat unter Forschern große Aufmerksamkeit auf sich gelenkt und Studien zeigen, dass Phenyl-C61-Buttersäuremethylester (PCBM) die Hysterese unterbinden kann. Neben den positiven Effekten der PCBM basierten Eliminierung von Fallenzustände, zeigt Kapitel 6, dass PCBM die Migration von mit Jod assoziierten Defekten verhindert, was für einem erheblichen Teil der Hysterese verantwortlich gemacht wird. Die verminderte Ionenmigration wird durch PL-Mikroskopieuntersuchungen nachgewiesen. Ebenso wird eine Erhöhung der Aktivierungsenergie von Ionenmigration gemessen, welche aus temperaturabhängigen chronoamperometrischen Messungen abgeschätzt wurde. Zum Vergleich dient eine Grenzflächenschicht aus polymerisiertem PCBM in den Perowskit-Solarzellen, wo die Hysterese im Vergleich zu dem Bauteil mit einer reinen PCBM-Schicht immer noch ausgeprägt ist. Dies deutet darauf hin, dass die Diffusion oder die Inkorporation von PCBM-Molekülen im Perowskit-Film von entscheidender Bedeutung ist, da die Diffusion von PCBM-Molekülen, die auf die Polymerhauptketten aufgepfropft sind, stark behindert wird.

Weise unterdrücken PCBM-Moleküle im Perowskitfilm die Migration von Jodionen oder Leerstellen und moderieren so die „built-in“ Feldverschiebung in der PSC.

In Kapitel 4 und Kapitel 5 wird gezeigt dass die Phänomene der PL-Intermittenz und des lokale Intensitätsabfalls der PL durch eine PCBM-Schicht geschwächt werden, während in Kapitel 6 die Passivierung mobiler Ionen oder Leerstellen durch PCBM behandelt wird. Diese Untersuchungen schlagen einen Weg vor, die photo- und elektrisch-erzeugten negativen Effekte durch die Verwendung von Additiven oder Grenzflächenschichten zu eliminieren. Neben dieser Methode ist die Herstellung hochwertiger Perowskitfilme ein weiterer wichtiger Faktor. Hochwertige Filme weisen typischerweise weniger Defektzustände und mobile Ionen im Material auf und können die PSC-Stabilität verbessern. Ähnliche Verbesserungen zeigen auch Perowskitfilme mit weniger Korngrenzenfläche, d.h. mit großen Korngrößen. Daher konzentrieren sich Kapitel 7 und Kapitel 8 auf die Kontrolle der Perowskitfilmbildung, indem die Entwicklung des Perowskitfilms während des Spin-coatings und des Ausheizens bzw. Kristallisationsprozesses untersucht wird.

In Kapitel 7 wurden Absorptions- und PL-Spektren *in-situ* während des Prozessierens im „Spin-Coating“ Verfahren aufgenommen, als in Dimethylformamid (DMF) gelöstes Methylammoniumiodid (MAI) auf eine  $\text{PbI}_2$ -Schicht geschleudert wurde. Die Ergebnisse zeigen, dass die Kristallbildung in den ersten 20 Sekunden erfolgt. Wir analysieren zunächst die optischen Eigenschaften auf dieser Zeitskala. Die Bildung einer  $\text{MAPbI}_3$ -Deckschicht und ihre Auflösungs-Rekristallisation während des „Spin-Coating“ Prozesses wurden festgestellt. Der Auflösungs-Rekristallisationsprozess beeinflusst die endgültige Filmqualität sehr stark, und deshalb ist es wichtig, die Geschwindigkeit dieses Prozesses zu kontrollieren. Darüber hinaus können wir durch die Entwicklung eines tieferen Verständnisses der gemessenen optischen Spektren die Änderung der Schichtdicke während der Rotationsbeschichtung und die jeweiligen Phasen der Perowskitbildung untersuchen.

In Kapitel 8 konnten wir mit Hilfe einer lösungsmitteldampfunterstützten Ausheizmethode Perowskitfilme mit großen Körnern wachsen und gleichzeitig Korngrenzen und Defektdichten minimieren. Aus *in-situ* Messungen der Weitwinkel-Röntgenstreuung unter streifendem Einfall (GIWAXS) wird festgestellt, dass die DMF-Dampfbehandlung während des Ausheizens die Kristallisation verlangsamt. Durch systematische Erhöhung der Lösungsmitteldampfkonzentration ist es möglich, die Kristallgröße zu vergrößern. Jedoch führen zu hohe DMF-Dampfkonzentration zur Bildung von Löchern (Pinholes), da DMF-Dampf verflüssigen kann und das Lösemittel Perowskitkristalle teilweise auflösen kann. Diese Arbeit zeigt die Möglichkeiten und Grenzen des lösungsmitteldampfunterstützten Ausheizens und dass eine präzise Prozesskontrolle notwendig ist, um qualitative hochwertige Perowskitfilme zu erhalten.

## 2 Introduction

### 2.1 Motivation

To retard global warming and air pollution problems, it is a current endeavor to replace traditional fossil fuels. Among the renewable energies, solar energy is one option. From 2014 to 2018, the annual growth rate of solar photovoltaics installation was more than 10%.<sup>1,2</sup> At the end of 2019, the installed global solar capacity has reached 627 GW.<sup>2</sup> About 95% of the current module production is silicon-based, which, however, is relatively energy intense in its fabrication.<sup>3</sup> Its energy pay-back time in Europe is more than 2 years.<sup>4</sup> Therefore, the urge for new technologies is driving researchers to explore and develop new materials for cheaper, less energy-intensive in production and more efficient solar cells in future.

In this context, one of the most promising materials is organo metal halide perovskite (OMHP), typically methylammonium lead halide, which has drawn extensive attention over the last 8 years. Since OMHP was firstly used in dye-sensitized solar cells as sensitizer in 2009,<sup>5</sup> the study on this type of material has advanced greatly, especially after 2012.<sup>6,7</sup> Until now, the power conversion efficiency (PCE) of perovskite solar cells (PSCs) has reached 25.2%, which is comparable to silicon solar cells.<sup>8</sup> In addition to its application in solar cells, OMHPs show impressive performance in light emitting diodes,<sup>9,10</sup> photodetectors,<sup>11,12</sup> and other optoelectronic devices.<sup>13,14</sup> Due to its low-cost and convenient fabrication technique, OMHP serves as a good candidate for up-scaling and large-area applications. PSCs have been successfully processed on flexible substrates with the highest PCE of 19.11%<sup>15</sup> and also compatible with roll-to-roll processing techniques.<sup>16,17</sup>

Despite the rapid development, there are still many questions remaining. The instability of PSCs is the currently main issue. Besides the irreversible degradation when PSC is exposed to H<sub>2</sub>O, O<sub>2</sub>, heat and UV-light,<sup>18</sup> the stabilized PCE is another concern, as PCE of a PSC strongly depends on the pretreatment, the measurement scanning direction and speed, as well as illumination conditions.<sup>19</sup> A long-standing operational performance is hard to achieve and it becomes difficult to compare the reported PCEs from various scanning conditions.<sup>20,21</sup> Thus, a fundamental understanding of this phenomenon and finding possible solutions are necessary. Directly observing perovskite film changes by photoluminescence (PL) microscopy under illumination and electric field is one focus of this thesis. By correlating the changes to the corresponding PSC performances, it is realized that the defect states and their migration are the essential factors. On this account, there is a demand to fabricate perovskite films with low defect density or with passivated defects.

To obtain perovskite films with high quality, precise control on the film formation is the key factor, including stoichiometry, thermal treatment, solvent engineering and so on.<sup>22</sup> Thus it is important to trace structure and morphology changes during film formation. For example, Hu et al. successfully identify perovskite crystal intermediates and find a critical annealing temperature to obtain smooth films by employing *in-situ* scattering and microscopy methods.<sup>23</sup> However, most of the reported characterizations concentrate on the steady state of already-prepared perovskite films, while the study on the dynamics of perovskite crystallization is rather limited. Hence, in this thesis, home-made setups are developed to detect the structural evolution

of perovskites during spin coating and during annealing. Especially, *in-situ* optical spectroscopy is easy to access and to analyze, thus yielding a great potential for widespread use. Moreover, tracking the perovskite crystallization process can further bring in insights for optimization of processing parameters.

## 2.2 Organo Metal Halide Perovskite Material

### 2.2.1 History

The mineral  $\text{CaTiO}_3$  was firstly discovered by the Russian scientist Gustav Rose in 1839 and it was the mineralogist Lev Perovski who carried out further research on this material.<sup>24</sup> After that, “perovskite” became the name for crystals with an  $\text{ABX}_3$  structure. The perovskite lattice arrangement can be generally described as a large cation A in the center of a cube which is formed by cation B and anion X,<sup>25</sup> as shown in Figure 2.1(a). The symmetry of an ideal cubic perovskite will reduce when  $\text{BX}_6$  octahedral tilts or distorts.<sup>26</sup>

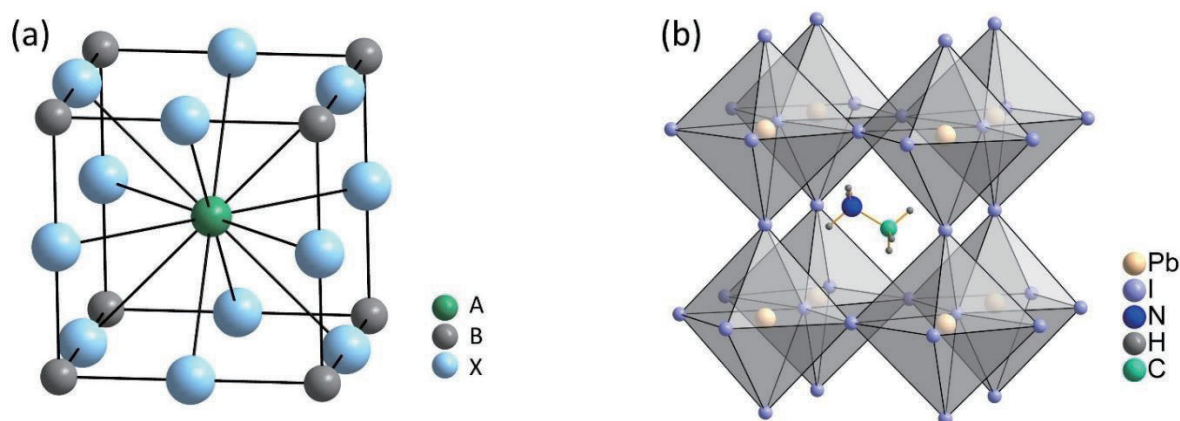


Figure 2.1: (a)  $\text{ABX}_3$  perovskite structure. (b) Crystal structure of  $\text{CH}_3\text{NH}_3\text{PbI}_3$ , where  $\text{A} = \text{MA}^+$ ,  $\text{B} = \text{Pb}^{2+}$ ,  $\text{X} = \text{I}^-$

In early studies, the perovskite methylammonium (MA) lead halide ( $\text{CH}_3\text{NH}_3\text{PbX}_3$ ,  $\text{X} = \text{Cl}, \text{Br}, \text{I}$ ), whose structure is displayed in Figure 2.1(b), functioned as a light absorption layer.<sup>6,7</sup> As the A-cation size is responsible for the distortion of the octahedra, replacing the A-cation contributes to properties such as bandgap and phase stability. Furthermore, the introduction of formamidinium (FA) ion as A-cation yields a promising development for OMHP bandgap tuning.<sup>27</sup> Instead of organic cations,  $\text{Cs}^+$  is another favorable A-cation. Many research groups have fabricated high-efficiency solar cells using triple cations in OMHP:  $\text{MA}^+$ ,  $\text{FA}^+$ ,  $\text{Cs}^+$ .<sup>28,29,30</sup> In such a OMHP, the three cations occupy the A lattice with a probability according to the stoichiometric proportions. The study of 2D layered perovskite has attracted attention owing to its high moisture stability by substituting  $\text{MA}^+$  or  $\text{FA}^+$  cation with a long hydrophobic organic cation, such as phenethylammonium ( $\text{C}_6\text{H}_5(\text{CH}_2)_2\text{NH}_3^+$ ), *n*-butylammonium ( $\text{CH}_3(\text{CH}_2)_3\text{NH}_3^+$ ).<sup>31,32</sup> On the account of toxicity of Pb element, studies on Pb-free OMHP materials are emerging. Replacing the B site,  $\text{Sn}^{2+}$  shows great potential,<sup>33,34</sup> while  $\text{Bi}^{3+}$  and  $\text{Sb}^{3+}$  are counted as promising candidates as well.<sup>35,36</sup>



As could be seen in the description above, it is known that the material organo metal halide perovskite does not contain any organometallic complex, but refers to the individual cations and anions within the perovskite. The community is sometimes not very precise on the naming and hence very frequently and especially in the beginning the expression “organometal halide perovskite” was and is used. A further more precise way is the expression “organo metalhalide perovskite”, referring to the cation and anions but also implying the existence of the metal halide cage of the perovskite. Within this thesis these expressions are used equivalently and often reflect expression which was most commonly used at that time. The expression “organolead halide” is used in Chapter 4, 5 & 6 which are the earlier publications. A further peculiarity is that it became quite common within the research community of OMHPs to simply use the word “perovskite” which actually names a crystal structure, as a simple expression to name organo metal halide perovskites.

## 2.2.2 Advantages of Organo Metal Halide Perovskite as Light Harvesters

One reason for scientists to put great effort into OMHPs is their outstanding optoelectronic properties. The band gap of MAPbI<sub>3</sub> is ~1.57 eV with a sharp absorption edge, indicating a small number of optically detected deep defect states, as demonstrated in Figure 2.2(a).<sup>37</sup> The combination of different cations and anions makes it possible to tune the band gap of OMHPs. Figure 2.2(b) shows an example when altering MA<sup>+</sup>/FA<sup>+</sup> and I<sup>-</sup>/Br<sup>-</sup> ratio in OMHP. The Snaith's group has synthesized FA<sub>0.83</sub>CS<sub>0.17</sub>Pb(I<sub>0.6</sub>Br<sub>0.4</sub>)<sub>3</sub> with an optical band gap of ~1.74 eV and the corresponding solar cell reaches a high open circuit voltage ( $V_{oc}$ ) of 1.2 V.<sup>38</sup> It needs to be mentioned that the tuned OMHPs exhibit a good incident photon-to-electron conversion efficiency (IPCE).<sup>39</sup> As illustrated in Figure 2.2(c), IPCEs of three tuned OMHPs reach a level of over 80% in a broad range from 400 nm to 800 nm. Apart from its high absorption coefficient displayed in Figure 2.2(a), another reason for the high IPCE is the effective carrier transport in OMHPs. The long carrier diffusion length in OMHPs has been highlighted in several publications, reaching >100 nm in MAPbI<sub>3</sub> and up to 1  $\mu$ m in CH<sub>3</sub>NH<sub>3</sub>PbI<sub>3-x</sub>Cl<sub>x</sub>.<sup>40,41,42</sup> This is extraordinary for semiconductors fabricated at low temperature with solution method.

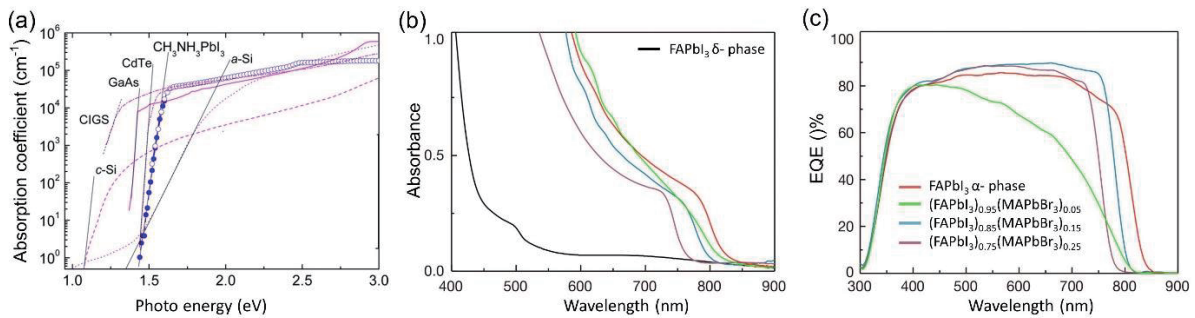


Figure 2.2: (a) Effective absorption coefficient of an MAPbI<sub>3</sub> perovskite thin film compared with other typical photovoltaic materials. All are measured at room temperature. (b) Ultraviolet-visible absorption spectra of (FAPbI<sub>3</sub>)<sub>1-x</sub>(MAPbBr<sub>3</sub>)<sub>x</sub> films with  $x = 0, 0.05, 0.15, 0.25$ . (c) External quantum efficiency (EQE) spectra of PSCs using (FAPbI<sub>3</sub>)<sub>1-x</sub>(MAPbBr<sub>3</sub>)<sub>x</sub> materials. (a) is reproduced from Ref<sup>37</sup>. (b) and (c) are reproduced from Ref<sup>39</sup>.

### 2.2.3 Versatile Fabrication Methods

Besides the good optoelectronic properties of OMHP, another major reason why OMHP attracts intensive attention is its low-cost. The raw materials, e.g. MAI and  $\text{PbI}_2$ , are simple to obtain and for its fabrication no critical processing conditions are required.<sup>43</sup> There are two major ways to fabricate perovskite films: vapor deposition and solution processing. The vapor deposition method was firstly reported by Liu et al. and perovskite was prepared by evaporating two separate sources,  $\text{PbCl}_2$  and MAI, simultaneously.<sup>44</sup> After that, Fan et al. has prepared  $\text{MAPbI}_3$  film by single source vapor deposition, i.e. using well-prepared  $\text{MAPbI}_3$  powder for evaporation.<sup>45</sup> The perovskite film from vapor deposition yields dense and uniform surfaces, with the highest solar cell efficiency above 20%.<sup>46</sup> Thus, this method is relevant for wide applications. However, until today, the most prominent approaches for the fabrication of halide perovskite thin films are based on solution processing methods. They also serve as a fundamental tool for developing new materials and optimization of devices. The most common solution processing methods are illustrated in Figure 2.3.

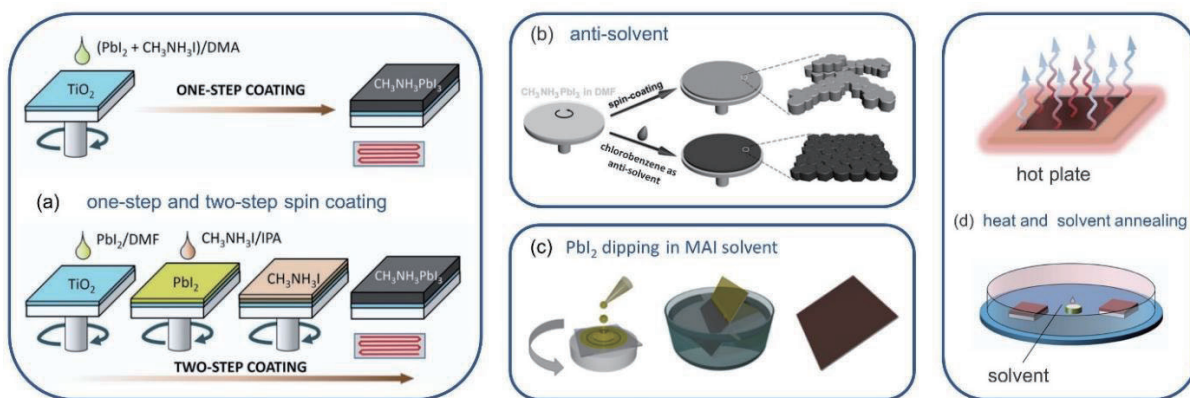


Figure 2.3: Overview of perovskite film processing from solutions. (a) One-step and two-step deposition by spin coating. (b) Anti-solvent is applied during spin coating on one-step method. (c)  $\text{PbI}_2$  layer is dipped in MAI solvent to form perovskite film. (d) Annealing of prepared film with heat or with assist of solvent vapor. (a) is reproduced from Ref<sup>47</sup>. (b) is reproduced from Ref<sup>48</sup>. (c) is reproduced from Ref<sup>49</sup>. (d) is reproduced from Ref<sup>50</sup>.

The solution processing includes two major steps: solution deposition and film annealing. There are several techniques to perform solution deposition, e.g. spin coating, blade coating, slot die coating, inkjet printing and gravure printing, through which the solution is able to form a film on a substrate.<sup>51</sup> Among them, spin coating is a versatile one used in laboratories and in Chapter 7 the evolution during spin coating is analyzed in detail. By taking use of one of these techniques, the deposition is usually conducted in one step or two steps. It means that metal halide and organo-halide species are mixed before coating or are sequentially deposited on the substrate, as displayed in Figure 2.3(a). For the one-step method, the depositing solution contains all the components of an OMHP, while two separate solutions were needed in the two-step method. To proceed with compositional engineering of the perovskite, the one-step method is typically preferable. Perovskite precursors with a single solvent lead to rough surfaces, even with pinholes.<sup>52,53</sup> This can be improved when using a mixture of solvents in precursor, e.g. dimethylformamide/dimethyl sulfoxide (DMF/DMSO),<sup>54</sup> DMSO/ $\gamma$ -butyrolactone (GBL)<sup>55</sup> and DMF/GBL.<sup>52</sup> Additionally, anti-solvents can be utilized during spin coating.<sup>55</sup> Quickly after

deposition of perovskite precursor, the anti-solvent is added, for example during the spin coating process, to induce fast crystallization over the whole film.<sup>56</sup> Figure 2.3(b) compares the morphology of films with and without anti-solvent. In case of a two-step method, metal halide and organo-halide species are spin coated sequentially on a substrate,<sup>57</sup> or a prepared metal halide film such as  $\text{PbI}_2$  is immersed in organo-halide solvent,<sup>58</sup> which is demonstrated in Figure 2.3(c). Even though the two-step method is more complex than the one-step method, it is often favored due to its high degree of controlling morphology and crystallinity.<sup>59</sup>

After solution deposition, heat annealing is necessary to initiate precursor-to-perovskite transition in most cases, as the transition activation energy needs to be reached.<sup>60</sup> The annealing temperature needs attention, as too low temperatures hinder perovskite transformation and too high temperatures result in degradation.<sup>61</sup> The annealing can be achieved by putting the films on a hot plate, where it is also possible to employ an additional solvent atmosphere to gain more control on the perovskite formation process, as illustrated in Figure 2.3(d). It has been reported that perovskite films that were annealed with some solvent vapor, e.g. DMF,<sup>50</sup> isopropanol (IPA)<sup>62</sup> and DMSO,<sup>63</sup> showed very smooth surface and higher crystallinity. However, studies with the precise control of the solvent vapor concentration are scarce and it is in focus of Chapter 8.

## 2.2.4 Challenges

One serious problem for upscaling and commercialization of PSC is its instability, with regard to humidity,<sup>64</sup> heat,<sup>65</sup> UV radiation<sup>66</sup> and oxygen.<sup>67</sup> When PSCs are exposed to light and air, under operational condition, they rapidly degrade on timescale of hours.<sup>68</sup> The redistribution of mobile ions under bias or illumination gives rise to this unstable output.<sup>69,70</sup> Apart from its intrinsic stability, another source of instability is the chemically active charge transport within the material and interfacial degradation.<sup>71,72</sup>

Another concern is the toxicity of OMHP materials because of Pb. Researchers have suggested a possible way of OMHP into the environment, where the degradation product containing Pb is partially solubilized in water,<sup>73</sup> so that plants absorb lead from the OMHP contaminated soil.<sup>74</sup> Up to now, efficient and at the same time economically attractive recycling strategies for perovskite based optoelectronic devices have not been demonstrated.<sup>75,76</sup> Furthermore, the PCEs of lead-free OMHPs, with a current record efficiency of 10.18%,<sup>77</sup> are still significantly less efficient compared to their lead containing counterparts. Thus it can be summarized that even though there have been expanding research activities concentrating on OMHPs towards its commercialization of photovoltaic in the last 8 years, its stability and recycling are still key issues that need to be solved. Nonetheless, the very recent emergence of OMHP as a new class of photovoltaic material shows the importance of continuing research and further material development.

## 2.3 Optical Properties

### 2.3.1 Absorption

To understand the optical properties of OMHPs, it is necessary to first consider their electronic structure and band gap. For MAPbI<sub>3</sub>, the top of the valence band is primarily composed of the antibonding state between Pb(6s) and I(5p) orbitals and the bottom of the conduction band is formed by the antibonding state of Pb(6p) and I(5p) orbitals.<sup>78,79</sup> Thus the inorganic [PbI<sub>6</sub>]<sup>4-</sup> octahedral mainly contributes to the band gap. Hence, the main role of MA<sup>+</sup> is to influence the titling of Pb-I-Pb bonding within the octahedron through the hydrogen bonding, rather than directly impacting the perovskite band structure.<sup>80,81</sup>

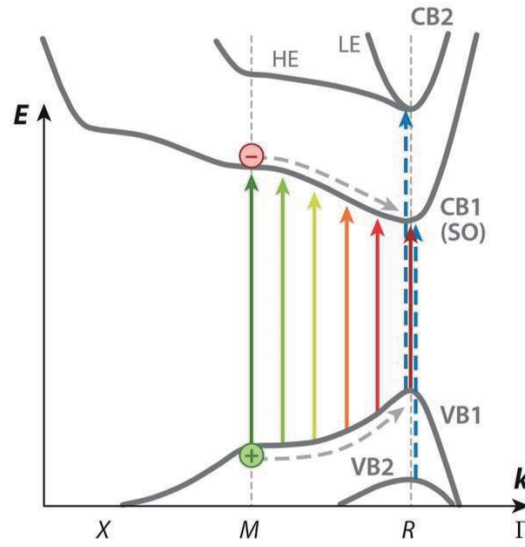


Figure 2.4: Electronic band structure of Pm3m cubic MAPbI<sub>3</sub> obtained by DFT calculations from Ref<sup>82</sup>. X, M and R donate points of high symmetry within the reciprocal lattice. The solid lines with up-arrow represent the allowed optical transitions. The blue dashed lines with arrow represent dipole-allowed transition. The grey dashed lines with arrow indicate the flow of photogenerated carriers towards R point. This figure is reproduced from Ref<sup>83</sup>.

Several DFT calculations on the electronic structure have been reported<sup>84,85,82</sup> and one of them is exhibited in Figure 2.4. The direct bandgap transition at R contributes to the band-edge absorption. The secondary transition at M is also optically allowed. In reciprocal space, the photogeneration of electron-hole pairs between M and R points is possible and the generated carriers flow easily towards R and recombine.<sup>82,83</sup> Hence, the absorption continuum above band-edge is observed, as shown in Figure 2.2 (a).

### 2.3.2 Radiative and Non-radiative Recombination

In general, the dynamics of carrier recombination in classical inorganic semiconductors is expressed as:<sup>83</sup>

$$\frac{dn}{dt} = G - k_1 n - k_2 n^2 - k_3 n^3 \quad (1)$$

$G$  is the charge carrier generation rate,  $k_1$  is the monomolecular recombination rate constant,  $k_2$  is the bimolecular charge recombination rate constant and  $k_3$  is the Auger recombination rate constant.<sup>86</sup> The monomolecular recombination is associated to trap-assisted recombination, which happens when an individual carrier is captured in a trap state. Time-resolved PL, time-resolved microwave conductance and transient spectroscopy have been conducted to derive  $k_1$  in MAPbI<sub>3</sub> and most of the results are in the range of  $10^{-5} \sim 10^{-6} \text{ s}^{-1}$ .<sup>42,87,88</sup> This decay rate  $k_1$  is related to the energetic depth of the traps, their density and distribution.<sup>86</sup> Bimolecular recombination is the recombination between a hole and electron accompanied with emission. It is an intrinsic material property and hardly can be tuned by process engineering. The measured  $k_2$  in OMHPs ranges from  $\sim 10^{-9}$  to  $\sim 10^{-11} \text{ cm}^3 \cdot \text{s}^{-1}$ .<sup>88,89,90</sup> Auger recombination is the recombination process of a hole and an electron along with energy and momentum transition to a third particle.<sup>91</sup> Theoretical investigations and experimental results suggest that it rarely happens under standard sunlight illumination.<sup>88,92</sup> Both monomolecular and Auger recombination are nonradiative. As presented in Figure 2.5(a), the monomolecular and bimolecular recombination are the dominant mechanisms for carrier densities up to  $10^{18} \text{ cm}^{-3}$ , where the monomolecular is the most important at low carrier density.<sup>42,90</sup> Stranks et al. propose the monomolecular mechanism at low carrier density originates from the high concentration of defects in OMHPs. The explicit mechanism is illustrated in Figure 2.5(b). Under a low fluence, the photogenerated electrons are trapped by the subgap states, leaving a large number of “photodoped” holes with the concentration  $n_T$ . Since at a low fluence the free electron concentration  $N$  is much lower than the total free hole concentration  $N+n_T$ , the recombination shows monomolecular behavior. In the condition with a high fluence, i.e.  $N \gg n_T$ , the “photodoped” hole concentration  $n_T$  is negligible. Thus, hole-electron bimolecular recombination dominates.<sup>93</sup>

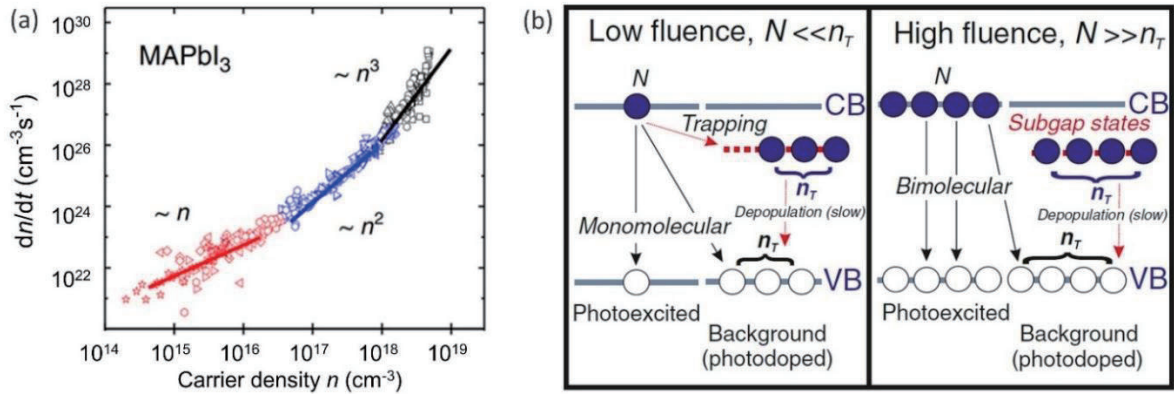


Figure 2.5: (a) Recombination rate  $dn/dt$  over charge density  $n$  of MAPbI<sub>3</sub>. The values were extracted from transient absorption measurements at  $\sim 10$  different fluences and each point represents one measurement. The solid line is for guidance. (b) Illustration of recombination mechanism under low- and high- fluence illumination. (a) is reproduced from Ref<sup>94</sup>. (b) is reproduced from Ref<sup>93</sup>.

In a solar cell, the ratio between radiative and non-radiative recombination is essential for the device performance, because the achievable open-circuit voltage  $V_{oc}$  in a solar cell is predicted by:

$$V_{oc} = V_{oc,ideal} - \frac{k_B T}{q} |\ln \eta_{ext}| \quad (2)$$



Where,  $V_{oc,ideal}$  is the ideal (maximum) limit of open circuit voltage.

$\eta_{ext}$  is the external luminescence efficiency and defined by

$$\eta_{ext} = \frac{R_{ext}}{R_{ext} + R_{nr}} \quad (3)$$

Here,  $R_{ext}$  is the external radiative rate and  $R_{nr}$  is the internal photon and carrier non-radiative loss rate.<sup>95</sup>  $\eta_{ext}$  describes the fraction of net recombination processes which result in the emission of a photon out from the cell. The higher  $\eta_{ext}$  is, the higher  $V_{oc}$  is. Thus, to minimize the non-radiative recombination helps to increase  $V_{oc}$ . The perovskite film and perovskite/charge-extraction layer interface are the two main sources of non-radiative recombination centers.<sup>96,97</sup> To characterize the radiative and non-radiative recombination in perovskites, PL resulting from bimolecular recombination is an applicable parameter. For example, the spatial PL mapping can visualize the non-radiative losses.<sup>98,99</sup> PL decay at lower fluence can be employed to evaluate defect densities, because the monomolecular recombination is dominant, reflecting the possibility of carriers being trapped by defects.<sup>100</sup>

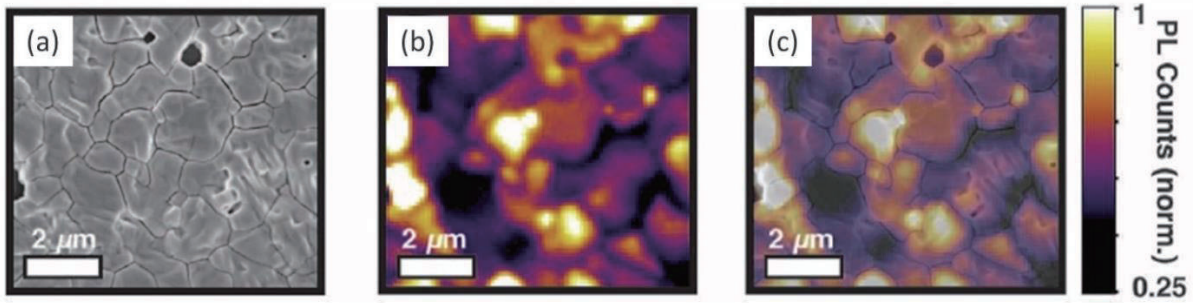


Figure 2.6: (a) Correlated SEM image of MAPbI<sub>3-x</sub>Cl<sub>x</sub> film; (b) PL image; (c) Composite SEM and PL image. They are taken at one spot. Reproduced from Ref<sup>99</sup>.

As exhibited in Figure 2.6, the PL image of a polycrystalline perovskite film was found to yield good correlation to the scanning electron microscope (SEM) image, where grain boundaries exhibit lower PL intensities due to the higher defect density there. In addition, PL lifetimes of different grains in Figure 2.6 showed that the brighter grain has a longer lifetime.<sup>99</sup> Jacobsson et al. demonstrated that the intensity distribution of PL across the film also correlated with the heterogeneity of the trap density in the film.<sup>101</sup> In this thesis, PL microscopy is one main method to study local changes in the optical properties of polycrystalline perovskite films.

## 2.4 Defects

### 2.4.1 Point Defects in Crystals

The simplest structural imperfections of crystals are those involving single lattice points, so called point defects. In semiconductors, point defects are centers of perturbation, changing material's optical, electrical and magnetic properties locally.<sup>102</sup> A point defect appears when an atom is removed from its regular lattice site (vacancy), when an atom is prevalent in addition to the regular lattice sites (interstitial), when atoms of two types exchange positions (antisite) or when an impurity occupies a substitutional site (substitutional).<sup>103</sup> Both vacancies and

interstitials exist in all real crystals.<sup>104</sup> Schottky defects and Frenkel defects are typical point defect pairs. Their formation principle is displayed in Figure 2.7. A Schottky defect occurs when oppositely charged atoms leave their corresponding lattice sites and move out of the crystal, creating a pair of oppositely charged vacancy defects. If an atom leaves its original lattice site and occupies an interstitial position within the crystal, the pair of vacancy and interstitial defect will be called Frenkel defect.<sup>104</sup>

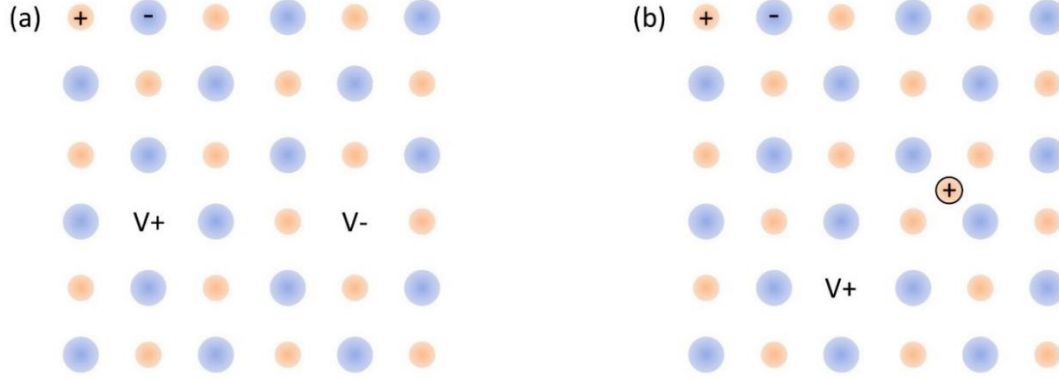


Figure 2.7: Representation of point defects in a two-dimensional structure (a) Schottky defect and (b) Frenkel defect.

The free energy change  $\Delta G$  for a crystal having  $n$  defects at a constant pressure is<sup>105</sup>

$$\Delta G = n(\Delta H_F - T\Delta S_{\text{vib}}) - T \cdot \Delta S_{\text{conf}} \quad (4)$$

where,

$T$  is the absolute temperature;

$\Delta S_{\text{conf}}$  is the entropy change due to the configurational disorder;

$\Delta H_F$  is the formation enthalpy for one defect;

$\Delta S_{\text{vib}}$  is the entropy change induced by the lattice vibrations.

The formation free energy of one defect is  $\Delta G_F = \Delta H_F - T\Delta S_{\text{vib}}$ .

$\Delta S_{\text{conf}}$  is expressed in terms of the thermodynamic probability  $W$  by:

$$\Delta S_{\text{conf}} = k \ln W = k \ln \frac{N!}{(N-n)!n!} \approx kT[N \ln N - (N-n) \ln(N-n) + n \ln n] \quad (5)$$

In which,  $k$  is the Boltzmann's constant.  $N$  is the number of lattice sites within the crystal including the defects.

At equilibrium,  $\Delta G$  reaches its minimum, i.e.  $\left. \frac{d\Delta G}{dn} \right|_T = 0$ . Applying Equation (5) into Equation (4) leads to:

$$\left. \frac{d\Delta G_F}{dn} \right|_T = \Delta H_F - T\Delta S_{\text{vib}} - kT \ln \frac{N-n}{n} = 0 \quad (6)$$

when  $n \ll N$ , the defect concentration is obtained by rearrangement of Equation (6),<sup>105</sup>

$$\frac{n}{N} = \exp\left(\frac{\Delta S_{\text{vib}}}{k}\right) \exp\left(\frac{-\Delta H_F}{kT}\right) = \exp\left(-\frac{\Delta G_F}{kT}\right) \quad (7)$$

Thus, when knowing the formation energy of the defect, it is possible to estimate the thermal equilibrium concentration of defects in a crystal. For the formation of Schottky or Frenkel pair defects,  $\Delta S_{\text{conf}}$  will increase because of the increased number of possible ways that the defects can be arranged on  $N$  lattice points.

Experimentally, due to the locally changed properties induced by defects, defect concentration estimations can be accomplished by measuring lattice parameters, electrical resistivity, electron spin resonance and electron nuclear double resonance, optical spectroscopy etc.<sup>104</sup> Several techniques are used to increase the concentration of defects above the thermal equilibrium concentration, for example by quenching from high temperatures and irradiation with energetic particles.<sup>104</sup>

### 2.4.2 Defect Migration

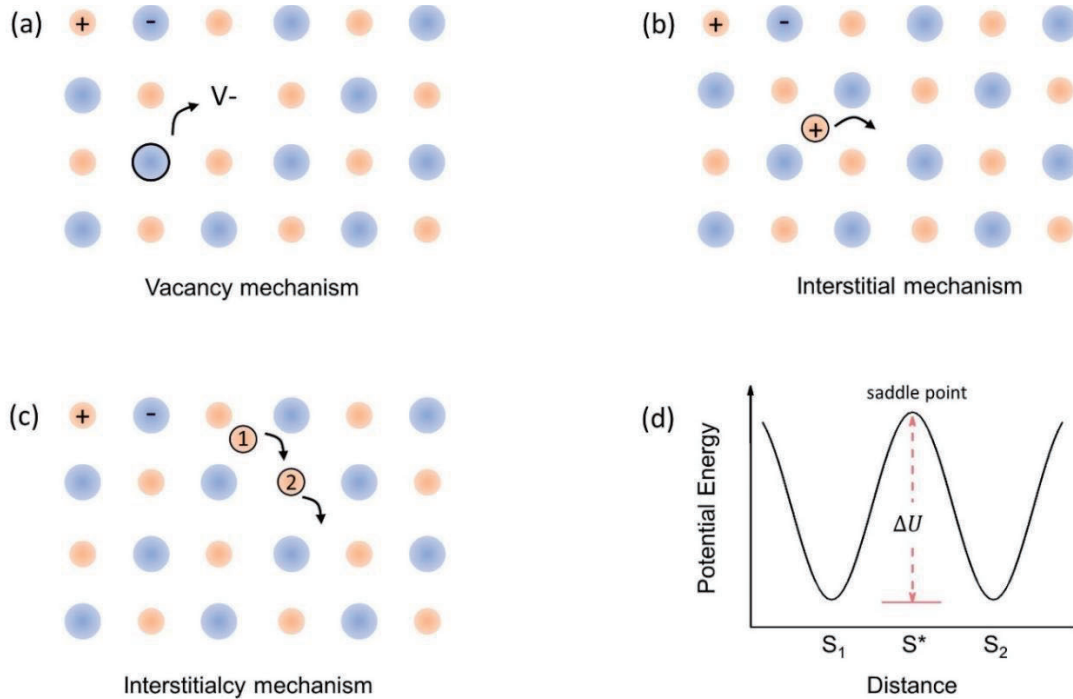


Figure 2.8: Schematic representation of three diffusion mechanisms (a) vacancy, (b) interstitial and (c) interstitialcy. (d) Potential-energy diagram of a defect as it migrates from lattice sites  $S_1$  to  $S_2$ , which are equivalent.

Defect migration within the crystal causes an atom redistribution and thus changes of the microstructure of the material. Hence, the understanding of the migration is important for the material manufacturing and application. The migration mechanisms that allow a defect to move through a lattice are illustrated in Figure 2.8 (a)-(c). For vacancy defects, it is a vacancy mechanism – an atom leaves its lattice site to occupy a nearby vacancy, creating a new vacancy at its original lattice site. For interstitial defects, there are two mechanisms: (i) interstitial mechanism and (ii) interstitialcy mechanism. In case of an interstitial mechanism, an interstitial defect jumps from its original interstitial site to a neighboring equivalent one. The interstitialcy



mechanism corresponds to a process where one interstitial atom occupies one lattice site, while the atom at the original lattice site moves to a new interstitial site. Comparing this process to the interstitial mechanism, the interstitialcy mechanism is less energetically favorable.<sup>103</sup>

For migration, the defect needs to jump over an energy barrier from one equivalent site to another. The sketch of the potential barrier along the migration path is displayed in Figure 2.8 (d) where  $\Delta U$  is the energy barrier. The jump frequency  $w$  is the probability of an atom successfully making a diffusive jump, which is also called jump probability. For the interstitial mechanism, it is<sup>106</sup>

$$w = h \cdot \exp\left(-\frac{\Delta U}{kT}\right) \quad (8)$$

Here,  $h$  is the frequency of interstitial vibration.

The diffusion coefficient  $D$  is related to  $w$  through the equation:<sup>107</sup>

$$D = fw\lambda^2 \quad (9)$$

Where,  $\lambda$  is the distance travelled in a single jump, and  $f$  represents the probability of the atom jumping in one direction relative to any other equivalent direction. If  $\lambda$  is equal to the lattice parameter  $a$ , then

$$D = fa^2h \cdot \exp\left(-\frac{\Delta U}{kT}\right) \quad (10)$$

For the vacancy mechanism, the vacancy concentration also makes a difference, as the migrating atom requires a vacancy on the neighboring sites. Thus, to estimate  $w$  and  $D$  a factor of  $\exp\left(-\frac{\Delta G_F}{kT}\right)$  needs to be multiplied. Hence, it is obvious that defect diffusion is a temperature-dependent behavior following an Arrhenius-type equation.  $D$  in solid state materials is in the range of  $10^{-6} - 10^{-25} \text{ cm}^2/\text{s}$ .<sup>108</sup> Different crystal structures and chemical bondings have an impact on  $D$  through  $f$ ,  $a$  and  $\Delta U$ . Moreover, within one crystal a change in the local structure affects  $D$ , so that for example the energy barrier  $\Delta U$  in crystal grain boundaries is typically lower than that in the crystal bulk, because of the absent surrounding atoms and the high defect concentrations in the grain boundaries.<sup>109,110,111</sup> The lowest energy barrier for diffusion is at the surface, since there is less constraint on the diffusing atoms.<sup>111</sup> More specifically,  $D$  along the grain boundary increases with the increasing misorientation angle of the adjacent boundaries, reaching a maximum when the angle becomes  $45^\circ$ .<sup>111</sup>

The migration barrier is influenced by the charge state of the defect as well, because the interaction of the ionized defect with the surrounding atoms may induce repulsive and/or attractive electronic forces.<sup>112,113</sup> Among several proposed mechanisms for charged defect migration, a normal ionization enhanced migration mechanism describes that if one defect species possesses two charge states by trapping or detrapping carriers, the change of two charge states will lead to a change of the migration barrier. As a result, a part of the defects migrate with a lower barrier, consequently facilitating migration of this defect.<sup>114</sup>

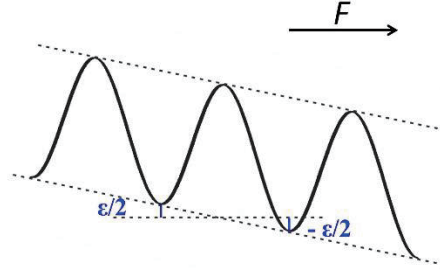


Figure 2.9: The potential barrier for defect migration, which is modified by the presence of an applied force  $F$ . It is adapted from Ref <sup>115</sup>.

When an external field, e.g. electric or stress, is applied that interacts with a defect, the diffusion will run in a preferential direction. Figure 2.9 illustrates the potential energy of a defect traveling through the lattice with an external driving force  $F$ . The barrier  $\Delta U$  is lowered by  $\varepsilon/2$  for jumping from left to right, while it is raised by  $\varepsilon/2$  for jumping from right to left.  $\varepsilon$  is the work done by the driving force over the distance  $\lambda$ :  $\varepsilon = F\lambda$ . Here, we assume that an electric field  $E$  is applied to the lattice and the defect has a charge  $q$ . In this case, the driving force is expressed by:  $F = Eq$ . The jump frequency from the left to the right  $w_1$  is:<sup>115</sup>

$$w_1 = h \cdot \exp\left(-\frac{\Delta U - \varepsilon/2}{kT}\right) = w \cdot \exp\left(\frac{\varepsilon/2}{kT}\right) = w \cdot \exp\left(\frac{F\lambda}{2kT}\right) \quad (11)$$

Similar, for the jump frequency from the right to the left  $w_2$ , it is:

$$w_2 = w \cdot \exp\left(-\frac{F\lambda}{2kT}\right) \quad (12)$$

The difference of the jump frequencies is:

$$w_1 - w_2 = w \cdot \left[ \exp\left(\frac{F\lambda}{2kT}\right) - \exp\left(-\frac{F\lambda}{2kT}\right) \right] = 2w \cdot \sinh\left(\frac{F\lambda}{2kT}\right) \quad (13)$$

This difference results in a defect migration from the left to the right on a macroscopic scale. The velocity  $v$  of the defect migration is:

$$v = (w_1 - w_2)\lambda = 2\lambda w \cdot \sinh\left(\frac{F\lambda}{2kT}\right) \quad (14)$$

When there is a specific external force,  $f$  in equation (9) becomes unity. Then, substituting  $w = D/(f\lambda^2)$  into equation (14) results in,

$$v = \left(\frac{2D}{\lambda}\right) \cdot \sinh\left(\frac{F\lambda}{2kT}\right) \quad (15)$$

By expanding the hyperbolic sine, it is

$$v = \left(\frac{DF}{kT}\right) \left[ 1 + \frac{1}{24\left(\frac{F\lambda}{kT}\right)^2} + \dots \right] \quad (16)$$

When  $F\lambda \ll kT$ , the velocity is reduced to

$$v = \frac{DF}{kT} \quad (17)$$

The mobility  $\mu$  of a charged particle is defined as

$$\mu = \frac{v}{E} \quad (18)$$

Combining equation (17) and (18) yields,

$$\mu = \frac{Dq}{kT} \quad (19)$$

Equation (19) corresponds to the Einstein equation. It describes the relationship between mobility and the diffusion coefficient. Thus, the mobility follows an Arrhenius behavior, if  $F\lambda \ll kT$ . It is important to note that if an external field is applied for an extensive time, the migrated defects can aggregate and interact. Its possible consequences are the screening of the external field, distortions of the local lattice etc., making it a much more complicated process.<sup>116</sup>

To measure the diffusion coefficient of defects in semiconductors, there are several common ways. The most widely applied one is to employ radioactive isotopes. It involves the determination of labelled atom concentration by measuring electrical, optical or paramagnetic parameters.<sup>103,107</sup> Another way is to take use of the capacitance-voltage profiling technique. Upon the time-dependent capacitance of a Schottky barrier, the profile of electrically active defects is available as well as the diffusion coefficient.<sup>117</sup> Backscattering techniques are also applied to study migration process of substitutional defects. Based on the principle that the energy loss of a particle from a backscattering process depends on the mass of the target atom, it is possible to obtain the depth distribution of the atoms.<sup>118</sup>

### 2.4.3 Point Defects in Organo Metal Halide Perovskite

As mentioned above, perovskite films fabricated at low-temperatures have a relatively low deep trap density compared with other polycrystalline inorganic solar cells materials. In polycrystalline perovskite films, the bulk trap density is in the range of  $10^{15}$ - $10^{17}$  cm<sup>-3</sup>.<sup>119</sup> The 12 native point defects in MAPbI<sub>3</sub> are: the interstitials I<sub>i</sub>, MA<sub>i</sub> and Pb<sub>i</sub> and the antisites MA<sub>Pb</sub>, MA<sub>I</sub>, Pb<sub>MA</sub>, Pb<sub>I</sub>, I<sub>MA</sub> and I<sub>Pb</sub>; the vacancies V<sub>MA</sub>, V<sub>Pb</sub>, and V<sub>I</sub>.<sup>120</sup>

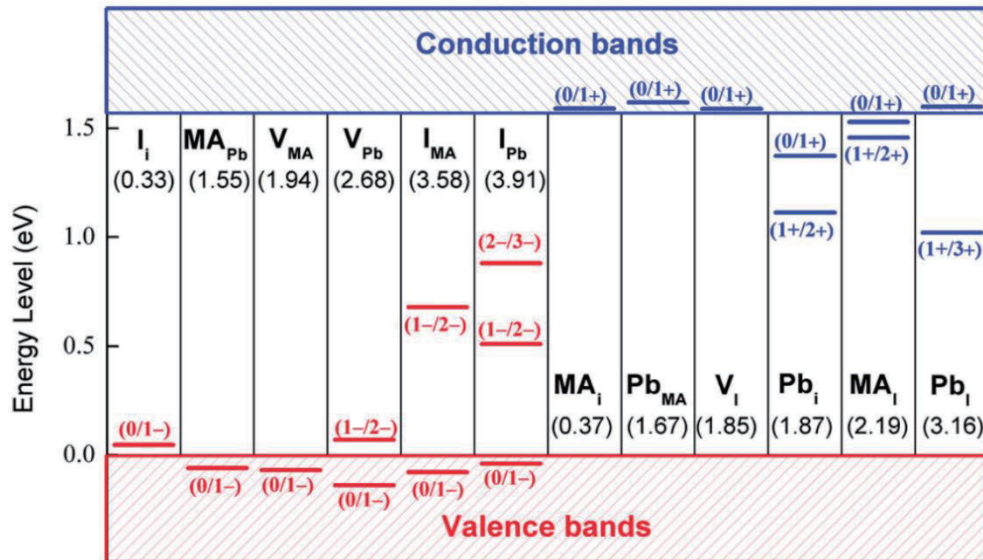


Figure 2.10: Calculated transition energy levels of point defects in MAPbI<sub>3</sub>, including I interstitial (I<sub>i</sub>) MA interstitial (MA<sub>i</sub>), Pb interstitial (Pb<sub>i</sub>), MA molecule on Pb site (MA<sub>Pb</sub>), I atom on MA site (I<sub>MA</sub>), I atom on Pb site (I<sub>Pb</sub>), Pb atom on MA site (Pb<sub>MA</sub>), MA molecule on I site (MA<sub>I</sub>), Pb atom on I site (Pb<sub>I</sub>), MA vacancy (V<sub>MA</sub>), Pb vacancy (V<sub>Pb</sub>) and I vacancy (V<sub>I</sub>). The formation energies of neutral defects are in parentheses. Reproduced from Ref<sup>121</sup>.

Density function theory (DFT) calculations have been employed to study these point defects. One common conclusion obtained is that point defects in MAPbI<sub>3</sub> with deep levels in the bandgap have high defect formation energies.<sup>122,123,124</sup> But the deep-level defects predicted by several calculations vary, including I<sub>Pb</sub>, I<sub>MA</sub>, Pb<sub>i</sub>, Pb<sub>I</sub>, V<sub>I</sub>, Pb<sub>MA</sub> and I<sub>i</sub>.<sup>122,125,126,127</sup> Deep-level defects can trap electrons or holes, working as non-radiative recombination centers.<sup>128</sup> Due to their high formation energy, they are not the dominant intrinsic defect species in MAPbI<sub>3</sub>. Instead, shallow defects are dominant. This explains the typically long carrier diffusion lengths observed in MAPbI<sub>3</sub>.<sup>122,129</sup> One calculation for the transition levels of all possible point defects in MAPbI<sub>3</sub> is listed in Figure 2.10. It shows that defects with lower formation energies such as I<sub>i</sub>, MA<sub>Pb</sub>, V<sub>MA</sub>, MA<sub>i</sub>, Pb<sub>MA</sub> and V<sub>I</sub>, locate within 0.05 eV above or below the valence band maximum or conduction band minimum.<sup>121</sup> These shallow point defects can lead to intrinsic doping of MAPbI<sub>3</sub>.<sup>122</sup> As indicated in Figure 2.10, the defects serving as acceptors are marked in red, while donors are marked in blue. It gives a hint that it is possible to control the *n*-type/*p*-type doping of MAPbI<sub>3</sub> by varying different shallow defects concentrations, which can be achieved by compositional engineering or crystal growth conditions.

#### 2.4.4 Defect Migration in Organo Metal Halide Perovskite

Several studies indicate that OMHPs are not only semiconductor but also ionic conductor, i.e. the applied bias can induce both charge carrier flow and ion flow.<sup>130,131</sup> The ion migration effect is found to be responsible for PSC current density-voltage (*J-V*) hysteresis,<sup>132,133</sup> which is a main topic in this thesis. Taking into account the different types of point defects in OMHPs, possible mobile ions are V<sub>I</sub><sup>+</sup>, I<sub>i</sub><sup>-</sup>, V<sub>MA</sub><sup>-</sup> and MA<sub>i</sub><sup>+</sup>. The exclusion of lead related defects is due to its high activation energy, as displayed in Table 2.1. To make it easier to read, V<sub>I</sub><sup>+</sup>, I<sub>i</sub><sup>-</sup>, V<sub>MA</sub><sup>-</sup> and MA<sub>i</sub><sup>+</sup> will be named with I<sup>-</sup> vacancy, I<sup>-</sup> ion, MA<sup>+</sup> vacancy and MA<sup>+</sup> ion, respectively.

Theoretical calculations and experimental measurements have been carried out to access the activation energy for the ion migration process. Some of them are summarized in Table 2.1. It becomes clear that the reported activation energies for one type of ion cover a wide range. Up to now, a consensus on the migrating species and its concrete energy barrier is still missing.

Among these studies, most works suggest that iodine related defects, i.e. I<sup>-</sup> vacancy or I<sup>-</sup> ion, are more active to migrate. The pathway of I<sup>-</sup> vacancies suggested by Eames et al. is along the I-I edge of the PbI<sub>6</sub> octahedron with an activation energy of 0.58 eV, while MA<sup>+</sup> vacancies migrate through the unit cell face comprised of four I<sup>-</sup> ions, yielding a higher activation energy of 0.84 eV.<sup>131</sup> Delugas et al. modeled the ion migration through I<sup>-</sup> vacancy and I<sup>-</sup> ion mechanisms. The results imply that at room temperature the I<sup>-</sup> vacancy is more mobile than the I<sup>-</sup> ion.<sup>134</sup> Experimental results from Cheng et al. demonstrate that under an electric field the I/Pb ratio is higher at the anode, which also supports the I<sup>-</sup> vacancy/I<sup>-</sup> ion-dominant migration.<sup>133</sup>

Table 2.1. Summary of ion migration activation energy with different methods

Ref	Calculation				Experiment			
	I <sup>-</sup> vacancy	I <sup>-</sup> ion	MA <sup>+</sup> vacancy	Pb <sup>2+</sup> vacancy	method	I <sup>-</sup> vacancy	I <sup>-</sup> ion	MA <sup>+</sup> ion
<sup>135</sup>	0.33-0.45		0.55-0.89					
<sup>136</sup>	0.08	0.08	0.46	0.8				
<sup>134</sup>	0.1	0.24						
<sup>131</sup>	0.58		0.84	2.31	T-dependent current	0.6-0.68		
<sup>137</sup>	0.28-0.45		0.70-1.12	1.39-1.78	T-dependent <i>J-V</i>	0.33		
<sup>133</sup>					T-dependent current		0.23	
<sup>138</sup>					T-dependent impedance		0.43	
<sup>139</sup>					T-dependent <i>J-V</i>			0.36
<sup>140</sup>					T-dependent impedance			0.58

\* The activation energy is obtained at room temperature of MAPbI<sub>3</sub> film. T-dependent means temperature-dependent.

Another possible mobile ion is the MA related defect. An MA<sup>+</sup> ion accumulation under an electric field detected with photothermal induced resonance (PTIR) is reported by Yuan et al.<sup>139</sup> It is not contrary to the observation of I<sup>-</sup> ion redistribution, because an applied electric field is able to drive the two ions at the same time. The elemental profile from Yamilova et al. supports this point of view.<sup>141</sup> The calculation from Azpiroz et al. shows that activation energy of MA<sup>+</sup> vacancy is 0.46 eV and that of I<sup>-</sup> vacancy and I<sup>-</sup> ion are both 0.08 eV. He proposed that the electric-field-driven migration of MA<sup>+</sup> vacancy should be in the timescale from milliseconds to minutes, while that of iodine related defects was less than 1  $\mu$ s.<sup>136</sup>

When it comes to determining the activation energy from experimental methods, it is difficult to distinguish from which ion (interstitial or vacancy) it exactly originates. Most of activation energies are obtained by measuring temperature-dependent currents, conductivities and dielectric constants accompanied with compositional detections.<sup>133,138,139</sup> Take I<sup>-</sup> vacancy and I<sup>-</sup> ion as examples: Under an electric field, I<sup>-</sup> vacancies migrate towards the cathode area, resulting in less iodine content there. In contrast, I<sup>-</sup> ions migrate towards the anode area, leaving less iodine at the cathode side. In this way, the migration of I<sup>-</sup> vacancies or I<sup>-</sup> ions leads to similar phenomenon, making a concrete assignment to a single type of defect difficult. This is the reason why the terms “iodine related defects” and “MA related defects” were used in the previous section.



### 2.4.5 Analysis of Ion Migration in Organo Metal Halide Perovskites

The charged point defect migration in OMHPs can be understood as an ion migration process based on the previous discussion. For a working OMHP solar cell, this ion migration process happens on the timescale of seconds to minutes.<sup>142,143</sup> To model this operational condition, an electric field was applied on a OMHP film through the laterally deposited electrodes, as illustrated in Figure 2.11(a). Mobile ions can be driven under an electric field and accumulate. The excess of defect ions gives rise to local physical or chemical changes, which is used to explicitly analyze the ion migration process. After applying the electric field, the elemental profile has been characterized by time of flight secondary ion mass spectrometry (ToF-SIMS),<sup>141</sup> X-ray photoelectron spectroscopy (XPS) profile<sup>133</sup> and PTIR.<sup>139</sup> All the measurements suggest an ion redistribution within the perovskite film.

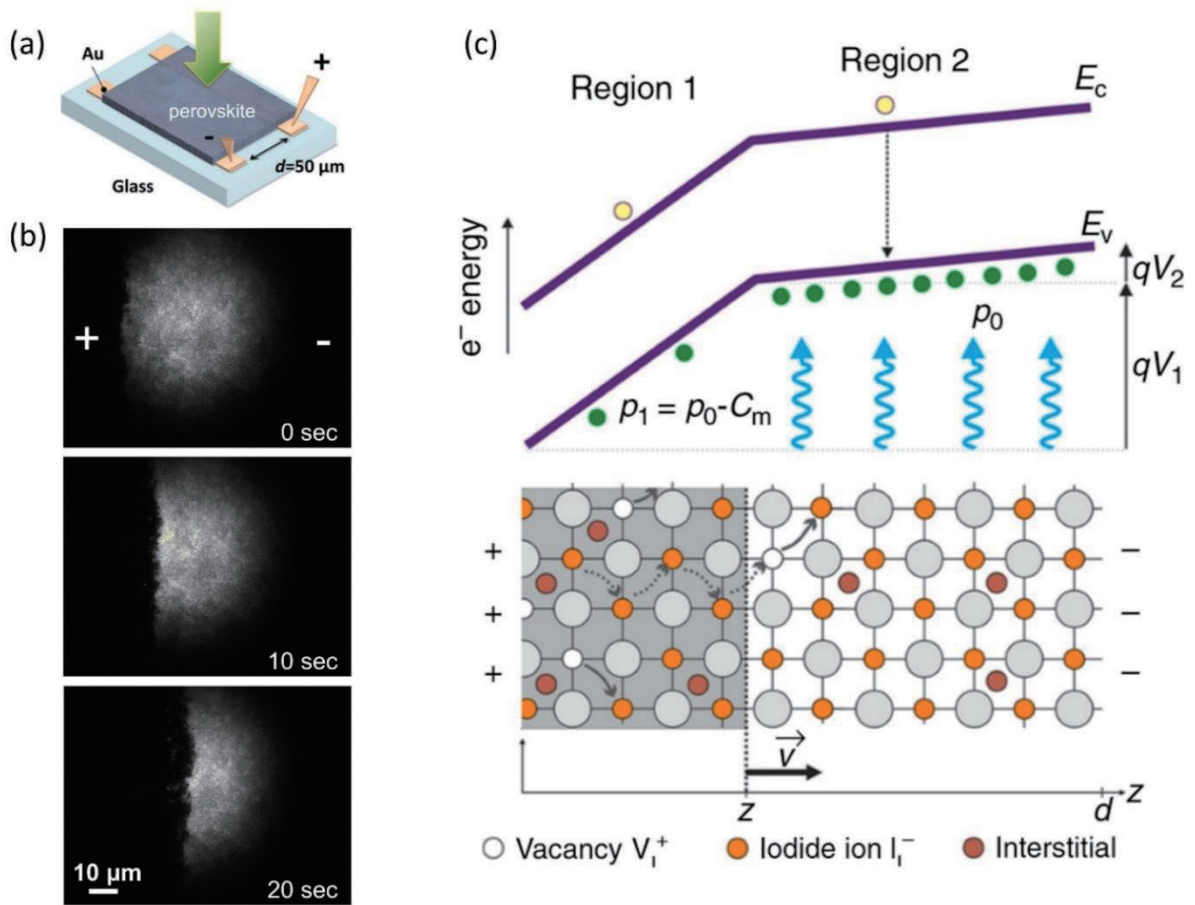


Figure 2.11: (a) Configuration of lateral perovskite device. (b) Time dependent PL images of  $\text{MAPbI}_{3-x}\text{Cl}_x$  film under an external electric field. The “+” and “-” signs indicate the polarity of the electrodes. The electric field is  $\sim 10 \text{ V}\cdot\text{m}^{-1}$  and the excitation intensity is  $\sim 40 \text{ mW}\cdot\text{cm}^{-2}$ . The perovskite film is protected by polymethylmethacrylate (PMMA) layer above. (c) Scheme of a physical model: Optoelectronic effects of  $\text{I}^-$  vacancies drifting in a perovskite film under the electric field. (a) is reproduced from Ref<sup>139</sup>. (b) is reproduced from Ref<sup>144</sup>. (c) is reproduced from Ref<sup>145</sup>.

PL microscopy is also a powerful tool to study the ion migration process *in-situ*, as PL is a good indicator for the material defect density. As discussed in Chapter 2.3, with higher defect density, PL quantum efficiency is lower and exhibits faster non-radiative decay.<sup>99</sup> The aggregation of

defects can enhance non-radiative recombination.<sup>146,147</sup> Li et al. recorded PL images when an electric field was applied laterally across a film as shown in Figure 2.11(a).<sup>144</sup> This PL evolution in Figure 2.11(b) demonstrates that a dark PL front spreads from the positive electrode to the negative. It is also reported in other publications that this phenomenon originates from ion migration in OMHPs.<sup>146,148</sup> The moving speed of the PL dark front corresponds to the drift velocity of migrating ions. With equation (18)  $\mu = v/E$ , it is possible to derive the ion mobility from the measured velocity and the applied electric field. The ion mobility obtained with this method ranges from  $10^{-8}$  to  $10^{-10} \text{ cm}^2 \cdot \text{V}^{-1} \cdot \text{s}^{-1}$ .<sup>146,144</sup> Hentz et al. have considered not only the drift of the ions under electric field, but also the diffusion effect due to a defect concentration gradient. They carried out Monte Carlo simulations to investigate the ion redistribution. Comparing the theoretical result with their observations from PL microscopy, an ion mobility of  $2.5 \cdot 10^{-11} \text{ cm}^2 \cdot \text{V}^{-1} \cdot \text{s}^{-1}$  is obtained.<sup>149</sup>

A physical model was developed by Juan Bisquert to explain the phenomenon displayed in Figure 2.11(b) observed by Li et al..<sup>145</sup> The schematic of the model is exhibited in Figure 2.11(c). The doping of a *p*-type perovskite changes through an  $\text{I}^-$  vacancy drift under bias. The doping level of the left side in Figure 2.11(c) is reduced from  $p_0$  to  $p_1$ , because  $\text{I}^-$  vacancies compensate a part of the  $\text{I}^-$  interstitials there. As  $\text{I}^-$  interstitials are the main source of intrinsic doping in perovskites, this compensation will reduce the carrier density on the left side, leading to less radiative recombination. As  $\text{I}^-$  vacancies migrate towards the right, the width of the shaded region grows with a velocity  $v$  and concomitantly the electric current changes because of the differences in carrier density after biasing. By studying the time-dependent current, it is possible to determine the ion mobility.<sup>145</sup> In this thesis, this model is used to quantify the ion migration in halide perovskite films and the detailed derivations are described in Chapter 6.

Another method to study the ion migration is Kelvin probe microscopy (KPM), which can identify the local surface potential or work function with a spatial resolution of tens of nm.<sup>150,151</sup> In OMHPs, the change of work function induced by local doping can be detected by KPM. For example, after poling for 100 s with  $1.2 \text{ V} \cdot \mu\text{m}^{-1}$ , an  $\text{MAPbI}_3$  film yielded a potential difference of 0.35 V at the two poling sides within  $30 \mu\text{m}$ .<sup>139</sup> It is attributed to the accumulation of positive ions at the negative side, lowering the surface potential. And it is analogous for the positive side. In a PSC, a similar ion accumulation within the perovskite layer after biasing has also been observed by KPM.<sup>152</sup>

Determining the mobility is also possible based on the time-resolved potential after biasing. Birkhold et al. found a lateral perovskite device yielded a slow decay of the potential and the charge density after biasing,<sup>153</sup> which is displayed in Figure 2.12 (a) – (d). After biasing, the accumulated charged ions at the two sides migrate reversely due to the concentration gradient and the charge induced electric field. Thus, the current density  $J$  of migrating ions after bias can be expressed as

$$J(x, t) = q \cdot D \cdot \nabla n_{\text{ion}}(x, t) + q \cdot \mu \cdot E(x, t) \cdot n_{\text{ion}}(x, t) \quad (17)$$

where,  $n_{\text{ion}}(x, t)$  is the evolution of ionic charge density and  $E(x, t)$  is the electric field induced by the displacement of positive and negative ions. Then, based on this equation, the experimental KPM results are simulated by a one-dimensional drift-diffusion model. The mobilities of the positive and the negative ions are obtained as  $8.3 \cdot 10^{-10} \text{ cm}^2 \cdot \text{V}^{-1} \cdot \text{s}^{-1}$  and  $9.5 \cdot 10^{-10} \text{ cm}^2 \cdot \text{V}^{-1} \cdot \text{s}^{-1}$

respectively. Measuring the time-resolved potential after biasing provides an elegant way to compare the mobility of cations and anions in OMHPs.

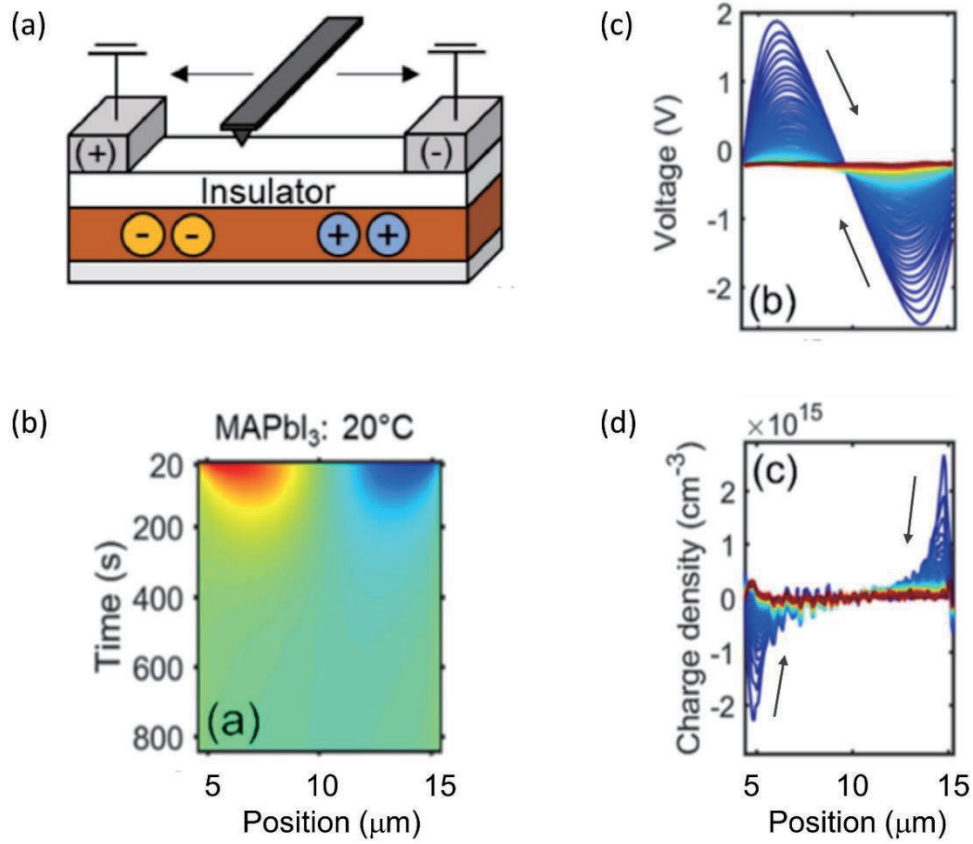


Figure 2.12: (a) Sketch of KPM measurements across the lateral electrode of the glass/MAPbI<sub>3</sub>/PMMA/SiO<sub>2</sub>/Au device after biasing with an electric field of  $0.8 \text{ V} \cdot \mu\text{m}^{-1}$ . (b) Time-resolved scanning KPM measurements after bias at  $20^\circ\text{C}$ . (c) The potential decay and (d) the charge density decay after bias. Each line represents a line scan across the electrode gap with a time resolution of 6.6 seconds. The arrows in (c) and (d) represent the evolutions along with time. Reproduced from Ref <sup>153</sup>.

## 2.5 Perovskite Solar Cell Operation

### 2.5.1 Solar Cell Architecture

In a PSC, the OMHP is working as the light harvesting material, which absorbs photons to produce electron-hole pairs that are able to split into separated free charge carriers at room temperature.<sup>154</sup> After that, carriers are transported via the electron transport layer (ETL) or the hole transport layer (HTL) and finally extracted through the corresponding electrodes, as illustrated in Figure 2.13.



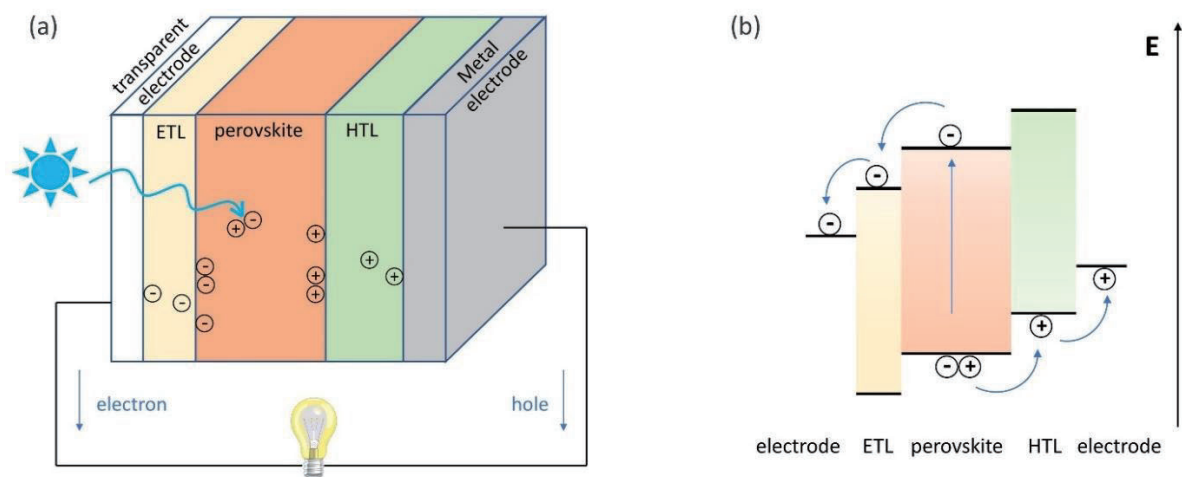


Figure 2.13: (a) Structure of a planar PSC in regular configuration. (b) Band diagram and operation principle of perovskite solar cell.

Figure 2.13(a) shows the schematic of a planar PSC, in which each layer is planar. In contrast to this, a mesoscopic structure can be implemented into the perovskite layer to help electron injection. The use of this structure was motivated by the structure of typical dye-sensitized solar cells.<sup>6</sup> Comparing to the planar PSC, the mesoscopic device is a preferred choice for perovskites with relatively short carrier diffusion lengths and yields less severe  $J$ - $V$  hysteresis which will be addressed in following session.<sup>155</sup> However, due to the complex manufacturing procedure of mesoscopic device and the improvement of intrinsic perovskite layer, the simple planar structure is more frequently adopted now.

The PSC configuration can be divided into regular ( $n$ - $i$ - $p$ ) and inverted ( $p$ - $i$ - $n$ ) type. The regular structure has its ETL on the side where the incident light first illuminates, as displayed in Figure 2.13(a), while the inverted type has its HTL on that side. The inverted configuration has the layer sequence: transparent electrode/HTL/perovskite/ETL/metal electrode.<sup>156</sup> Table 2.2 lists the most common planar material combination used in PSCs. For the transparent electrode, indium tin oxide (ITO) or fluorine-doped tin oxide (FTO) coated on glass are usually utilized. For ETL, there are two categories: metal oxides, e.g.  $\text{SnO}_2$ ,<sup>157,158</sup>  $\text{TiO}_2$ ,<sup>159,160</sup>  $\text{ZnO}$ ,<sup>161,162</sup> and fullerene derivatives such as,  $\text{C}_{60}$ ,<sup>163,164</sup> phenyl-C61-butyric acid methyl ester (PCBM)<sup>52,165</sup> and indene-C60 bisadduct (ICBA).<sup>166,167</sup> Organic and polymer materials are commonly used as HTL. In regular PSCs, spiro-OMeTAD serves as a favorable HTL.<sup>168,160,169</sup> The polymeric HTL poly(triaryl amine) (PTAA) is competitive in both structures and corresponding devices reach PCEs of 20.7%.<sup>170,171,172</sup> There are also some reports on inorganic HTLs, e.g.  $\text{NiO}_x$ <sup>157,173</sup> or  $\text{CuSCN}$ ,<sup>174</sup> which show good stability. As shown in Table 2.2, bathocuproine (BCP) works as a buffer layer between PCBM and Ag cathode. The insertion of BCP avoids the charge accumulation at the interface by forming an ohmic contact.<sup>175</sup> In general, the choice of ETL, HTL and electrodes is based on their energy band levels, so that the charge carrier transport is the most effective. Figure 2.13(b) gives us the guidance for a proper band matching. For example, the bottom of the conduction band of  $\text{TiO}_2$  and  $\text{MAPbI}_3$  is -4.2 eV and -3.9 eV, respectively. This energy offset contributes to an efficient electron extraction. The top of the valence band of Spiro-OMeTAD and  $\text{MAPbI}_3$  is -5.2 eV and -5.4 eV, separately. With this difference, holes can be readily injected into the electrode material.

Table 2.2: Summary of typical PSC structures

<i>n-i-p</i> type	Reference
FTO/TiO <sub>2</sub> /perovskite/Spiro-OMeTAD/Au	168,160
FTO/SnO <sub>2</sub> /perovskite/Spiro-OMeTAD/Au	158,169
FTO/TiO <sub>2</sub> /perovskite/PTAA/Au	171,172
<i>p-i-n</i> type	
ITO/PEDOT:PSS/perovskite/PCBM/Al	52,165
FTO/NiO <sub>x</sub> /perovskite/PCBM/BCP/Ag	173,176

## 2.5.2 Solar Cell Operation

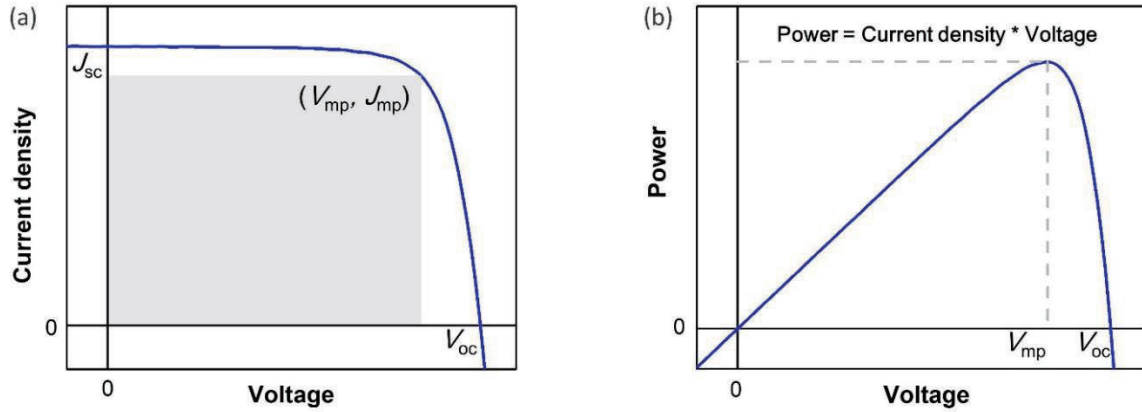


Figure 2.14: (a)  $J$ - $V$  curve of a working solar cell, showing  $V_{oc}$ ,  $J_{sc}$  and the maximum power point. (b) Solar cell output power as a function of voltage.

The most important figure of a working solar cell is its  $J$ - $V$  curve under illumination, which depicts its key characteristics. Figure 2.14(a) shows a typical  $J$ - $V$  curve. The standard illumination is solar irradiance at 1.5 airmass (1.5 AM) with the intensity of 100 mW/cm<sup>2</sup>. The open-circuit voltage  $V_{oc}$  is the maximum voltage available from a solar cell and it occurs at zero current. The short-circuit current density  $J_{sc}$  is the maximum current density and occurs when the voltage across the device is zero. The power of the solar cell is calculated by multiplying current density with voltage and it is plotted in Figure 2.14(b). The point with the highest output power in Figure 2.14(b) is defined as the maximum power point and its corresponding voltage and current density are referred to as  $V_{mp}$  and  $J_{mp}$ . The maximum power point is indicated by the grey rectangle in Figure 2.14(a). The fill factor ( $FF$ ) is a parameter that is related to the maximum power point and describes the “squareness” of a  $J$ - $V$  curve. It is defined as the ratio between the maximum power of the solar cell and the product of  $V_{oc}$  and  $J_{sc}$ :

$$FF = \frac{V_{mp} \times J_{mp}}{V_{oc} \times J_{sc}}$$

The parameter used to compare the performance of a solar cell to another one is the PCE. It describes the fraction of the incident power which is converted to electrical power:

$$\text{PCE} = \frac{V_{\text{oc}} \times J_{\text{sc}} \times FF}{\text{Input power}}$$

Based on the Shockley-Queisser limit, the maximum PCE of a perovskite solar cell is about 31%.<sup>177</sup> As the reported highest PCE of PSCs is already 25.2%,<sup>8</sup> a further enhancement of the PCE doesn't show much prospect, while a high priority in the field is to improve the stability of PSCs. Therefore, the instability of PSCs is one of the main topics studied in this thesis.

### 2.5.3 J-V Hysteresis

#### 2.5.3.1 Phenomenon

*J-V* hysteresis is a phenomena observed in *J-V* curve measurements, where the photocurrent response exhibits a discrepancy between two sweeping directions, as displayed in Figure 2.15. The direction from short circuit to open circuit is defined as forward scan and the direction from open circuit toward short circuit is referred to as reverse scan. As displayed in Figure 2.15(a), the performance in reverse scan is better than that in forward scan, thus this variation makes the determination of solar cell's PCE difficult.

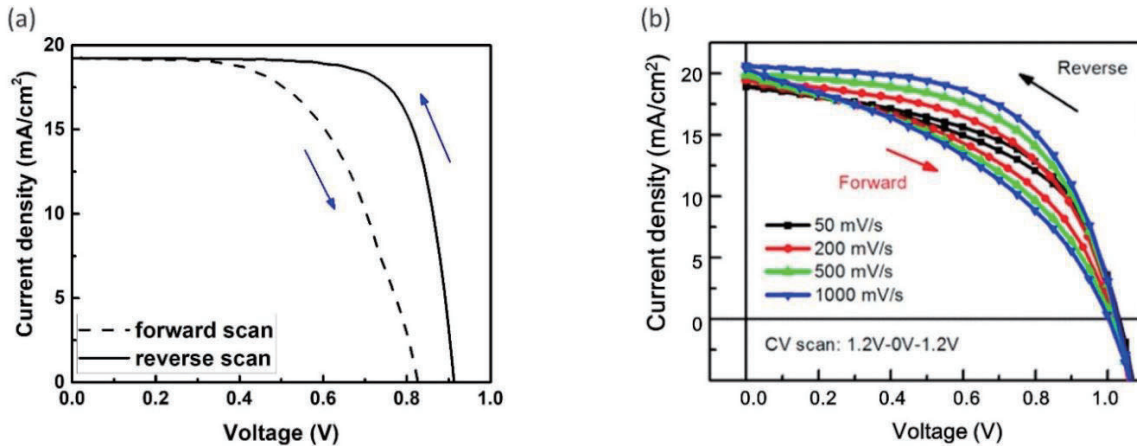


Figure 2.15: (a) A typical *J-V* curve hysteresis behavior in a PSC. The arrow represents the scan direction. (b) *J-V* response of PSCs with different scan rate. “CV scan” suggests the scan cycle. (b) is reproduced from Ref<sup>143</sup>.

Several features of hysteresis behavior have been summarized. At first, the behavior is associated with the intrinsic perovskite material and its interfaces with ETL and HTL,<sup>132</sup> as several studies have reported hysteresis-free perovskite devices achieved by defect passivation or interface engineering.<sup>178,179</sup> Also, the PSCs with TiO<sub>2</sub> mesoporous structures yield less severe hysteresis than planar TiO<sub>2</sub> layer.<sup>180</sup> Secondly, the timescale of hysteresis was found to range from ~10 seconds to ~100 seconds.<sup>132,181</sup> Thirdly, hysteresis strongly depends on the scan condition, *e.g.* scan speed and scan range. As shown in Figure 2.15(b), it is more pronounced at higher scan speeds and drops off at very slow speeds.<sup>182,183</sup> On the basis of these different experimentally observed features, the origin of the hysteresis phenomena in perovskite solar cells will be elaborated in the following.

### 2.5.3.2 Origin

**Ferroelectricity:** Ferroelectricity is the property that spontaneous polarization in the material can be modulated by an external electric field and this is one possible reason for hysteresis. Based on a theoretical study, the degree of polarization due to the interaction between the orientational  $\text{MA}^+$  dipoles and the inorganic lattice is suggested to be in the range of  $5 \mu\text{C}/\text{cm}^2$  -  $38 \mu\text{C}/\text{cm}^2$ .<sup>184,185</sup> The existence of permanent dipole in OMHPs was proven by electronabsorption spectroscopy or Stark spectroscopy.<sup>133,186</sup> Therefore, due to its ferroelectric property, the applied electric field causes the realignment of dipoles. These dipoles form an electric field -  $V_p$ . Depending on the direction of the external electric field, the net built-in potential will increase or decrease by  $V_p$ . As a result, it can facilitate or inhibit charge extraction and in a working solar cell it can lead to hysteresis.<sup>187,188</sup> However, several questions about this mechanism could not be explained. One is the timescale, as the polarization switching happens under a millisecond, estimated by DFT calculations.<sup>137,189</sup> The second is the overall small degree of ferroelectricity effect under the operational condition of a solar cell.<sup>190,191</sup> This suggests that ferroelectric polarization is not the dominant factor for the hysteresis behavior.

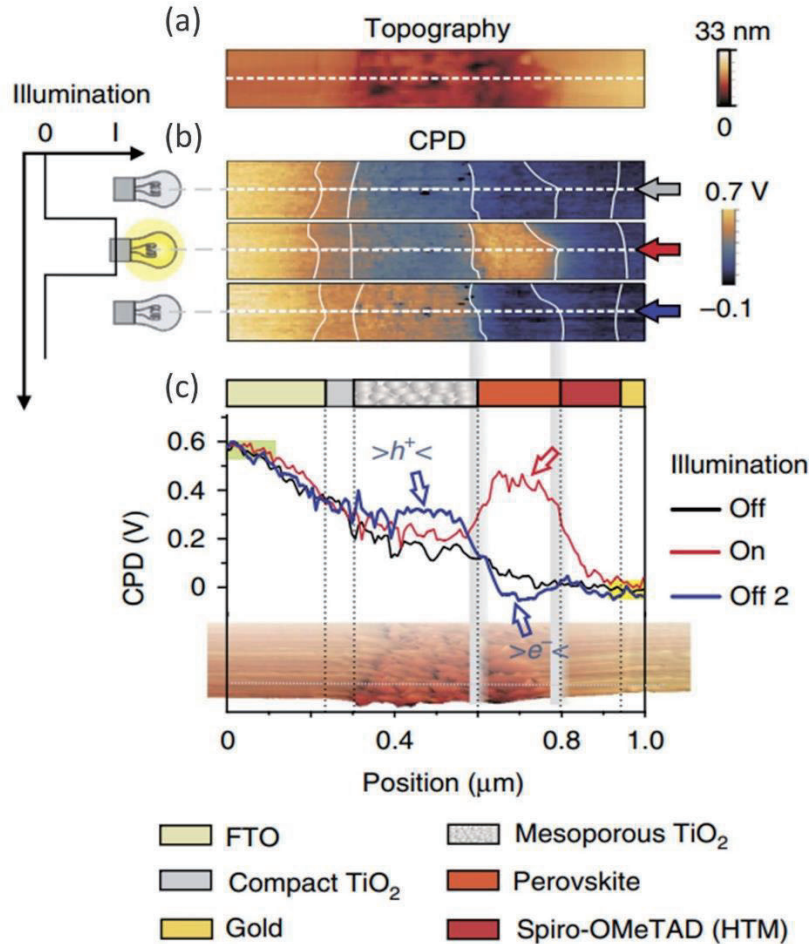


Figure 2.16: KPM characterization of the PSC at short-circuit condition. (a) Topography image of the PSC cross section. (b) Contact potential difference map and (c) line profile before illumination, under illumination and after illumination. Reproduced from Ref <sup>192</sup>.

**Charge trapping/detrapping:** Photogenerated electrons and holes can be trapped by defects under forward bias and subsequently released under short-circuit conditions. This charge

trapping and detrapping process is partially responsible for the hysteresis behavior. This mechanism is supported by the existence of defects with low formation energies, as discussed in Chapter 2.4. Also, several studies indicate most of the defects are located at the grain boundaries and at interfaces.<sup>193,194</sup> A direct evidence for this mechanism is provided by KPM characterisation by measuring the chemical potential difference (CPD) of PSCs, which is displayed in Figure 2.16. Comparing to the initial value, after illumination the CPD in the mesoporous TiO<sub>2</sub> increases, while it decreases in the perovskite layer. This effect lasts within the observation time of  $\sim 10$  min. It suggests that the excess holes in mesoporous TiO<sub>2</sub> and excess electrons in the perovskite layer are carriers that are trapped by defects.<sup>192</sup> A similar finding of charge carrier accumulation and unbalanced charge carrier transport in PSCs was accomplished with the help of electron beam-induced current measurements.<sup>195</sup> It is proposed that trap states at the interface will adjust the band structure and hinder an effective charge carrier extraction. Defect passivation has proven to significantly decrease hysteresis.<sup>196,197</sup>

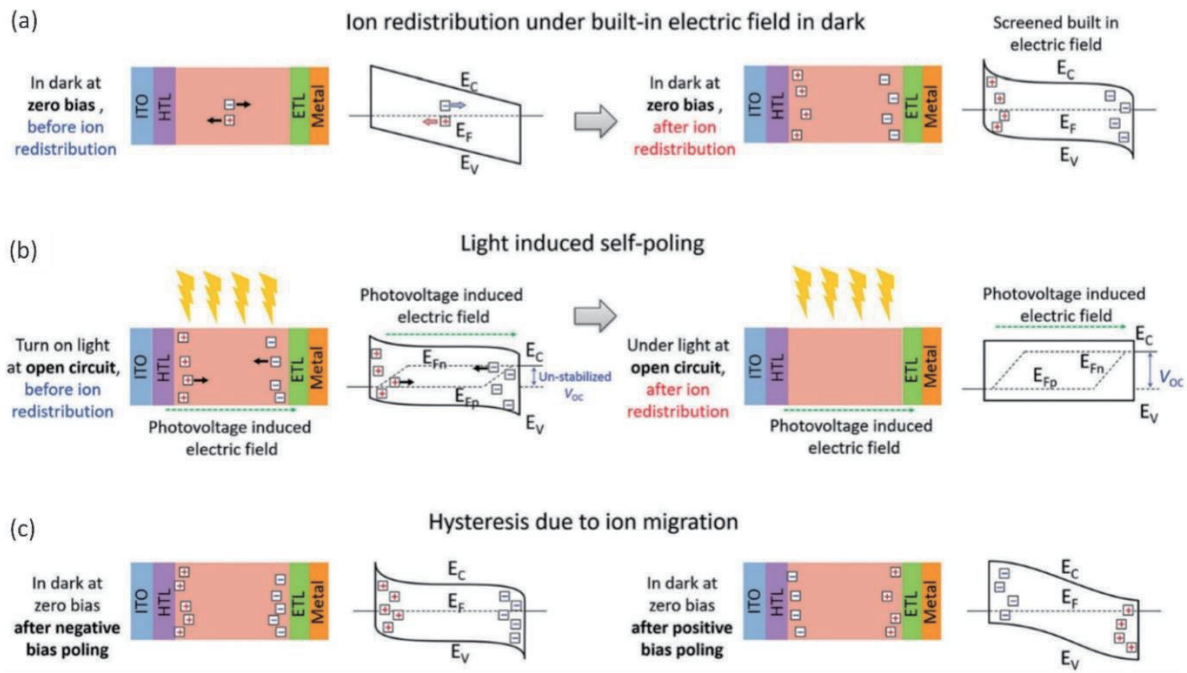


Figure 2.17: Schematic diagram of band structure considering ion migration in PSCs. (a) Band configuration of a PSC in dark at zero bias. (b) Band configuration of a PSC under illumination at open circuit condition. (c) Band configuration of a PSC in dark at zero bias after negative or positive bias poling. Reproduced from Ref<sup>198</sup>.

**Ion migration:** Under an electric field, the accumulation of mobile ions at the ETL/perovskite and the HTL/perovskite interface and the corresponding band bending are proposed to be the main contributors to hysteresis. Chapter 2.4 provides the experimental observation of ion accumulation at the perovskite/electrode interface and the corresponding discussion about the possible mobile ions in OMHPs, that are iodine and MA related defects. Detailed band diagrams under different working conditions are summarized in Figure 2.17. In dark, the built-in electric field drives negative ions towards the perovskite/ETL interface and positive ions towards the perovskite/HTL interface, as shown in Figure 2.17(a). The ion accumulation at the interfaces create an electric field to compensate the built-in electric field, hindering the collection of charge carriers.<sup>130,131,136</sup> In Figure 2.17(b), when the device is at open circuit condition under illumination, the initially accumulated ions are driven back by the photovoltage induced field.



Figure 2.17(c) shows the respective band bending after negative and positive bias poling. It indicates that after positive biasing the internal electric field enhances and can enable facile charge carrier extraction. Thus, when the PSC is scanned under different conditions, the status of ion accumulation at the interface varies, which in turn impacts the  $J$ - $V$  measurement differently. This mechanism is supported by the simulations from Tress et al.. Their simulations of  $J$ - $V$  curves considering the net built-in electric field change nicely fit to their experimental  $J$ - $V$  curves.<sup>182</sup> Besides, Li et al. found a shift of the built-in potential during the device scanning. The shift is equivalent to the change of  $V_{oc}$  between two scanning directions.<sup>133</sup> Thus, ion migration plays an important role to explain and understand the hysteresis behavior.

However, there are still open questions regarding the timescales for trapping/detrapping and the ion migration process itself. Studies underline that the time scale for charge trapping/detrapping is within microsecond,<sup>199,200</sup> while the ion redistribution requires several minutes.<sup>143</sup> This suggests that there are several effects causing the  $J$ - $V$  hysteresis. Up to now, more and more studies suggest that the hysteresis is a complex behavior, resulting from different influence factors.<sup>201,202,203</sup> Nevertheless, the synergetic effects of charge trapping/detrapping and ion migration are most likely playing the major roles in the hysteresis behavior.<sup>180,198,204</sup>

## 2.6 References

- (1) Masson, G.; Kaizuka, I. *Trends in Photovoltaic Applications 2019*; International Energy Agency, 2019.
- (2) Alice Detollenaere; Wetter, J. Van; Masson, G. *2020 Snapshot of Global PV Markets*; International Energy Agency, 2020.
- (3) Jäger-Waldau, A. *PV Status Report 2019*; Publications Office of the European Union: Luxembourg, 2019.
- (4) Philipps, S.; Warmuth, W. *Fraunhofer ISE: Photovoltaics Report*; 2019.
- (5) Kojima, A.; Teshima, K.; Shirai, Y.; Miyasaka, T. Organometal Halide Perovskites as Visible-Light Sensitizers for Photovoltaic Cells. *J. Am. Chem. Soc.* **2009**, *131* (17), 6050–6051.
- (6) Kim, H.-S.; Lee, C.-R.; Im, J.-H.; Lee, K.-B.; Moehl, T.; Marchioro, A.; Moon, S.-J.; Humphry-Baker, R.; Yum, J.-H.; Moser, J. E.; et al. Lead Iodide Perovskite Sensitized All-Solid-State Submicron Thin Film Mesoscopic Solar Cell with Efficiency Exceeding 9%. *Sci. Rep.* **2012**, *2*, 591.
- (7) Lee, M. M.; Teuscher, J.; Miyasaka, T.; Murakami, T. N.; Snaith, H. J. Efficient Hybrid Solar Cells Based on Meso-Superstructured Organometal Halide Perovskites. *Science*. **2012**, *338* (6107), 643–647.
- (8) <https://www.nrel.gov/pv/assets/pdfs/best-research-cell-efficiencies.20190923.pdf>.
- (9) Tan, Z. K.; Moghaddam, R. S.; Lai, M. L.; Docampo, P.; Higler, R.; Deschler, F.; Price, M.; Sadhanala, A.; Pazos, L. M.; Credgington, D.; et al. Bright Light-Emitting Diodes Based on Organometal Halide Perovskite. *Nat. Nanotechnol.* **2014**, *9* (9), 687–692.
- (10) Wang, N.; Cheng, L.; Ge, R.; Zhang, S.; Miao, Y.; Zou, W.; Yi, C.; Sun, Y.; Cao, Y.; Yang, R.; et al. Perovskite Light-Emitting Diodes Based on Solution-Processed Self-Organized Multiple Quantum Wells. *Nat. Photonics* **2016**, *10* (11), 699–704.
- (11) Dou, L.; Yang, Y. (Micheal); You, J.; Hong, Z.; Chang, W.-H.; Li, G.; Yang, Y. Solution-Processed Hybrid Perovskite Photodetectors with High Detectivity. *Nat. Commun.* **2014**, *5*, 5404.
- (12) Fang, Y.; Dong, Q.; Shao, Y.; Yuan, Y.; Huang, J. Highly Narrowband Perovskite Single-Crystal Photodetectors Enabled by Surface-Charge Recombination. *Nat. Photonics* **2015**, *9* (10), 679–686.
- (13) Wei, W.; Zhang, Y.; Xu, Q.; Wei, H.; Fang, Y.; Wang, Q.; Deng, Y.; Li, T.; Gruverman, A.; Cao, L.; et al. Monolithic Integration of Hybrid Perovskite Single Crystals with Heterogenous Substrate for Highly Sensitive X-Ray Imaging. *Nat. Photonics* **2017**, *11* (5), 315–321.
- (14) Kim, Y. C.; Kim, K. H.; Son, D.-Y.; Jeong, D.-N.; Seo, J.-Y.; Choi, Y. S.; Han, I. T.; Lee, S. Y.; Park, N.-G. Printable Organometallic Perovskite Enables Large-Area, Low-Dose X-Ray Imaging. *Nature* **2017**, *550* (7674), 87–91.
- (15) Cao, B.; Yang, L.; Jiang, S.; Lin, H.; Wang, N.; Li, X. Flexible Quintuple Cation Perovskite Solar Cells with High Efficiency. *J. Mater. Chem. A* **2019**, *7* (9), 4960–4970.
- (16) Hwang, K.; Jung, Y. S.; Heo, Y. J.; Scholes, F. H.; Watkins, S. E.; Subbiah, J.; Jones, D. J.; Kim, D. Y.; Vak, D. Toward Large Scale Roll-to-Roll Production of Fully Printed Perovskite Solar Cells. *Adv. Mater.* **2015**, *27* (7), 1241–1247.
- (17) Schmidt, T. M.; Larsen-Olsen, T. T.; Carlé, J. E.; Angmo, D.; Krebs, F. C. Upscaling of Perovskite Solar Cells: Fully Ambient Roll Processing of Flexible Perovskite Solar Cells with Printed Back Electrodes. *Adv. Energy Mater.* **2015**, *5* (15), 1500569.
- (18) Liu, W.; Wu, T.; Liu, M.; Niu, W.; Chueh, Y. Recent Challenges in Perovskite Solar Cells Toward Enhanced Stability, Less Toxicity, and Large-Area Mass Production. *Adv. Mater. Interfaces* **2019**, *6* (9), 1801758.
- (19) Saliba, M.; Stolterfoht, M.; Wolff, C. M.; Neher, D.; Abate, A. Measuring Aging Stability of Perovskite Solar Cells. *Joule* **2018**, *2* (6), 1019–1024.

- (20) Christians, J. A.; Manser, J. S.; Kamat, P. V. Best Practices in Perovskite Solar Cell Efficiency Measurements. Avoiding the Error of Making Bad Cells Look Good. *J. Phys. Chem. Lett.* **2015**, *6* (5), 852–857.
- (21) Zimmermann, E.; Wong, K. K.; Müller, M.; Hu, H.; Ehrenreich, P.; Kohlstädt, M.; Würfel, U.; Mastroianni, S.; Mathiazhagan, G.; Hinsch, A.; et al. Characterization of Perovskite Solar Cells: Towards a Reliable Measurement Protocol. *APL Mater.* **2016**, *4* (9), 091901.
- (22) Song, T.; Chen, Q.; Zhou, H.; Jiang, C.; Wang, H.; Yang, M.; Liu, Y. Perovskite Solar Cells: Film Formation and Properties. *J. Mater. Chem. A Mater. energy Sustain.* **2015**, *3*, 9032–9050.
- (23) Hu, Q.; Zhao, L.; Wu, J.; Gao, K.; Luo, D.; Jiang, Y.; Zhang, Z.; Zhu, C.; Schaible, E.; Hexemer, A.; et al. In Situ Dynamic Observations of Perovskite Crystallisation and Microstructure Evolution Intermediated from  $[\text{PbI}_6]^{4-}$  Cage Nanoparticles. *Nat. Commun.* **2017**, *8*, 15688.
- (24) Palache, C.; Berman, H.; Frondel, C.; Dann, J. D. The System of Mineralogy of James Dwight Dana and Edward Salisbury Dana, Yale University, 1837-1892 Volumen 1: Elements, Sulfides, Sulfosalts, Oxides; John Wiley & Sons, Inc.: New York, 1944; pp 730–735.
- (25) Kay, H. F.; Bailey, P. C. Structure and Properties of  $\text{CaTiO}_3$ . *Acta Crystallogr.* **1957**, *10* (3), 219–226.
- (26) Tilley, R. J. D. Perovskites: Structure-Property Relationships; Wiley, 2016; pp 30–32.
- (27) Eperon, G. E.; Stranks, S. D.; Menelaou, C.; Johnston, M. B.; Herz, L. M.; Snaith, H. J. Formamidinium Lead Trihalide: A Broadly Tunable Perovskite for Efficient Planar Heterojunction Solar Cells. *Energy Environ. Sci.* **2014**, *7* (3), 982–988.
- (28) Saliba, M.; Matsui, T.; Seo, J. Y.; Domanski, K.; Correa-Baena, J. P.; Nazeeruddin, M. K.; Zakeeruddin, S. M.; Tress, W.; Abate, A.; Hagfeldt, A.; et al. Cesium-Containing Triple Cation Perovskite Solar Cells: Improved Stability, Reproducibility and High Efficiency. *Energy Environ. Sci.* **2016**, *9* (6), 1989–1997.
- (29) Zhao, X.; Liu, S.; Zhang, H.; Chang, S. Y.; Huang, W.; Zhu, B.; Shen, Y.; Shen, C.; Wang, D.; Yang, Y.; et al. 20% Efficient Perovskite Solar Cells with 2D Electron Transporting Layer. *Adv. Funct. Mater.* **2019**, *29* (4), 1805168.
- (30) Bai, S.; Da, P.; Li, C.; Wang, Z.; Yuan, Z.; Fu, F.; Kawecki, M.; Liu, X.; Sakai, N.; Wang, J. T. W.; et al. Planar Perovskite Solar Cells with Long-Term Stability Using Ionic Liquid Additives. *Nature* **2019**, *571* (7764), 245–250.
- (31) Smith, I. C.; Hoke, E. T.; Solis-Ibarra, D.; McGehee, M. D.; Karunadasa, H. I. A Layered Hybrid Perovskite Solar-Cell Absorber with Enhanced Moisture Stability. *Angew. Chemie - Int. Ed.* **2014**, *53* (42), 11232–11235.
- (32) Cao, D. H.; Stoumpos, C. C.; Farha, O. K.; Hupp, J. T.; Kanatzidis, M. G. 2D Homologous Perovskites as Light-Absorbing Materials for Solar Cell Applications. *J. Am. Chem. Soc.* **2015**, *137* (24), 7843–7850.
- (33) Noel, N. K.; Stranks, S. D.; Abate, A.; Wehrenfennig, C.; Guarnera, S.; Haghighirad, A. A.; Sadhanala, A.; Eperon, G. E.; Pathak, S. K.; Johnston, M. B.; et al. Lead-Free Organic-Inorganic Tin Halide Perovskites for Photovoltaic Applications. *Energy Environ. Sci.* **2014**, *7* (9), 3061–3068.
- (34) Zuo, F.; Williams, S. T.; Liang, P. W.; Chueh, C. C.; Liao, C. Y.; Jen, A. K. Y. Binary-Metal Perovskites Toward High-Performance Planar-Heterojunction Hybrid Solar Cells. *Adv. Mater.* **2014**, *26* (37), 6454–6460.
- (35) Kong, M.; Hu, H.; Wan, L.; Chen, M.; Gan, Y.; Wang, J.; Chen, F.; Dong, B.; Eder, D.; Wang, S. Nontoxic  $(\text{CH}_3\text{NH}_3)_3\text{Bi}_2\text{I}_9$  Perovskite Solar Cells Free of Hole Conductors with an Alternative Architectural Design and a Solution-Processable Approach. *RSC Adv.* **2017**, *7* (56), 35549–35557.
- (36) Hebig, J. C.; Kühn, I.; Flohre, J.; Kirchartz, T. Optoelectronic Properties of  $(\text{CH}_3\text{NH}_3)_3\text{Sb}_2\text{I}_9$  Thin Films for Photovoltaic Applications. *ACS Energy Lett.* **2016**, *1* (1), 309–314.
- (37) De Wolf, S.; Holovsky, J.; Moon, S. J.; Löper, P.; Niesen, B.; Ledinsky, M.; Haug, F. J.; Yum, J. H.; Ballif, C. Organometallic Halide Perovskites: Sharp Optical Absorption Edge and Its Relation to Photovoltaic Performance. *J. Phys. Chem. Lett.* **2014**, *5* (6), 1035–1039.



- (38) McMeekin, D. P.; Sadoughi, G.; Rehman, W.; Eperon, G. E.; Saliba, M.; Hörantner, M. T.; Haghighirad, A.; Sakai, N.; Korte, L.; Rech, B.; et al. A Mixed-Cation Lead Mixed-Halide Perovskite Absorber for Tandem Solar Cells. *Science*. **2016**, *351* (6269), 151–155.
- (39) Jeon, N. J.; Noh, J. H.; Yang, W. S.; Kim, Y. C.; Ryu, S.; Seo, J.; Seok, S. Il. Compositional Engineering of Perovskite Materials for High-Performance Solar Cells. *Nature* **2015**, *517* (7535), 476–480.
- (40) Xing, G.; Mathews, N.; Sun, S.; Lim, S. S.; Lam, Y. M.; Gratzel, M.; Mhaisalkar, S.; Sum, T. C. Long-Range Balanced Electron- and Hole-Transport Lengths in Organic-Inorganic  $\text{CH}_3\text{NH}_3\text{PbI}_3$ . *Science*. **2013**, *342* (6156), 344–347.
- (41) Stranks, S. D.; Eperon, G. E.; Grancini, G.; Menelaou, C.; Alcocer, M. J. P.; Leijtens, T.; Herz, L. M.; Petrozza, A.; Snaith, H. J. Electron-Hole Diffusion Lengths Exceeding 1 Micrometer in an Organometal Trihalide Perovskite Absorber. *Science*. **2013**, *342* (6156), 341–344.
- (42) Wehrenfennig, C.; Eperon, G. E.; Johnston, M. B.; Snaith, H. J.; Herz, L. M. High Charge Carrier Mobilities and Lifetimes in Organolead Trihalide Perovskites. *Adv. Mater.* **2014**, *26* (10), 1584–1589.
- (43) Park, N. G. Perovskite Solar Cells: An Emerging Photovoltaic Technology. *Mater. Today* **2015**, *18* (2), 65–72.
- (44) Liu, M.; Johnston, M. B.; Snaith, H. J. Efficient Planar Heterojunction Perovskite Solar Cells by Vapour Deposition. *Nature* **2013**, *501* (7467), 395–398.
- (45) Fan, P.; Gu, D.; Liang, G.-X.; Luo, J.-T.; Chen, J.-L.; Zheng, Z.-H.; Zhang, D.-P. High-Performance Perovskite  $\text{CH}_3\text{NH}_3\text{PbI}_3$  Thin Films for Solar Cells Prepared by Single-Source Physical Vapour Deposition. *Sci. Rep.* **2016**, *6*, 29910.
- (46) Ávila, J.; Momblona, C.; Boix, P. P.; Sessolo, M.; Bolink, H. J. Vapor-Deposited Perovskites: The Route to High-Performance Solar Cell Production? *Joule* **2017**, *1* (3), 431–442.
- (47) Im, J. H.; Kim, H. S.; Park, N. G. Morphology-Photovoltaic Property Correlation in Perovskite Solar Cells: One-Step versus Two-Step Deposition of  $\text{CH}_3\text{NH}_3\text{PbI}_3$ . *APL Mater.* **2014**, *2* (8).
- (48) Xiao, M.; Huang, F.; Huang, W.; Dkhissi, Y.; Zhu, Y.; Etheridge, J.; Gray-Weale, A.; Bach, U.; Cheng, Y. B.; Spiccia, L. A Fast Deposition-Crystallization Procedure for Highly Efficient Lead Iodide Perovskite Thin-Film Solar Cells. *Angew. Chemie - Int. Ed.* **2014**, *53* (37), 9898–9903.
- (49) Docampo, P.; Bein, T. A Long-Term View on Perovskite Optoelectronics. *Acc. Chem. Res.* **2016**, *49* (2), 339–346.
- (50) Liu, J.; Gao, C.; He, X.; Ye, Q.; Ouyang, L.; Zhuang, D.; Liao, C.; Mei, J.; Lau, W. Improved Crystallization of Perovskite Films by Optimized Solvent Annealing for High Efficiency Solar Cell. *ACS Appl. Mater. Interfaces* **2015**, *7* (43), 24008–24015.
- (51) Howard, I. A.; Abzieher, T.; Hossain, I. M.; Eggers, H.; Schackmar, F.; Ternes, S.; Richards, B. S.; Lemmer, U.; Paetzold, U. W. Coated and Printed Perovskites for Photovoltaic Applications. *Adv. Mater.* **2019**, *31* (26), 1806702.
- (52) Kim, H. B.; Choi, H.; Jeong, J.; Kim, S.; Walker, B.; Song, S.; Kim, J. Y. Mixed Solvents for the Optimization of Morphology in Solution-Processed, Inverted-Type Perovskite/Fullerene Hybrid Solar Cells. *Nanoscale* **2014**, *6* (12), 6679–6683.
- (53) Jeon, Y.-J.; Lee, S.; Kang, R.; Kim, J.-E.; Yeo, J.-S.; Lee, S.-H.; Kim, S.-S.; Yun, J.-M.; Kim, D.-Y. Planar Heterojunction Perovskite Solar Cells with Superior Reproducibility. *Sci. Rep.* **2015**, *4*, 6953.
- (54) Tang, Z.; Tanaka, S.; Ito, S.; Ikeda, S.; Taguchi, K.; Minemoto, T. Investigating Relation of Photovoltaic Factors with Properties of Perovskite Films Based on Various Solvents. *Nano Energy* **2016**, *21*, 51–61.
- (55) Jeon, N. J.; Noh, J. H.; Kim, Y. C.; Yang, W. S.; Ryu, S.; Seok, S. Il. Solvent Engineering for High-Performance Inorganic–Organic Hybrid Perovskite Solar Cells. *Nat Mater* **2014**, *13* (9), 897–903.
- (56) Nayak, P. K.; Moore, D. T.; Wenger, B.; Nayak, S.; Haghighirad, A. A.; Fineberg, A.; Noel, N. K.; Reid, O. G.; Rumbles, G.; Kukura, P.; et al. Mechanism for Rapid Growth of Organic–Inorganic Halide Perovskite Crystals. *Nat. Commun.* **2016**, *7*, 13303.

- (57) Burschka, J.; Pellet, N.; Moon, S. J.; Humphry-Baker, R.; Gao, P.; Nazeeruddin, M. K.; Grätzel, M. Sequential Deposition as a Route to High-Performance Perovskite-Sensitized Solar Cells. *Nature* **2013**, *499* (7458), 316–319.
- (58) Xiao, Z.; Bi, C.; Shao, Y.; Dong, Q.; Wang, Q.; Yuan, Y.; Wang, C.; Gao, Y.; Huang, J. Efficient, High Yield Perovskite Photovoltaic Devices Grown by Interdiffusion of Solution-Processed Precursor Stacking Layers. *Energy Environ. Sci.* **2014**, *7* (8), 2619–2623.
- (59) Im, J. H.; Jang, I. H.; Pellet, N.; Grätzel, M.; Park, N. G. Growth of  $\text{CH}_3\text{NH}_3\text{PbI}_3$  Cuboids with Controlled Size for High-Efficiency Perovskite Solar Cells. *Nat. Nanotechnol.* **2014**, *9* (11), 927–932.
- (60) Moore, D. T.; Sai, H.; Tan, K. W.; Smilgies, D. M.; Zhang, W.; Snaith, H. J.; Wiesner, U.; Estroff, L. A. Crystallization Kinetics of Organic-Inorganic Trihalide Perovskites and the Role of the Lead Anion in Crystal Growth. *J. Am. Chem. Soc.* **2015**, *137* (6), 2350–2358.
- (61) Saliba, M.; Tan, K. W.; Sai, H.; Moore, D. T.; Scott, T.; Zhang, W.; Estroff, L. A.; Wiesner, U.; Snaith, H. J. Influence of Thermal Processing Protocol upon the Crystallization and Photovoltaic Performance of Organic-Inorganic Lead Trihalide Perovskites. *J. Phys. Chem. C* **2014**, *118* (30), 17171–17177.
- (62) Sun, X.; Zhang, C.; Chang, J.; Yang, H.; Xi, H.; Lu, G.; Chen, D.; Lin, Z.; Lu, X.; Zhang, J.; et al. Mixed-Solvent-Vapor Annealing of Perovskite for Photovoltaic Device Efficiency Enhancement. *Nano Energy* **2016**, *28*, 417–425.
- (63) Zuo, L.; Dong, S.; De Marco, N.; Hsieh, Y. T.; Bae, S. H.; Sun, P.; Yang, Y. Morphology Evolution of High Efficiency Perovskite Solar Cells via Vapor Induced Intermediate Phases. *J. Am. Chem. Soc.* **2016**, *138* (48), 15710–15716.
- (64) Yang, J.; Siempelkamp, B. D.; Liu, D.; Kelly, T. L. Investigation of  $\text{CH}_3\text{NH}_3\text{PbI}_3$  degradation Rates and Mechanisms in Controlled Humidity Environments Using in Situ Techniques. *ACS Nano* **2015**, *9* (2), 1955–1963.
- (65) Conings, B.; Drijkoningen, J.; Gauquelin, N.; Babayigit, A.; D’Haen, J.; D’Olieslaeger, L.; Ethirajan, A.; Verbeeck, J.; Manca, J.; Mosconi, E.; et al. Intrinsic Thermal Instability of Methylammonium Lead Trihalide Perovskite. *Adv. Energy Mater.* **2015**, *5* (15), 1500477.
- (66) Bryant, D.; Aristidou, N.; Pont, S.; Sanchez-Molina, I.; Chotchunangatchaval, T.; Wheeler, S.; Durrant, J. R.; Haque, S. A. Light and Oxygen Induced Degradation Limits the Operational Stability of Methylammonium Lead Triiodide Perovskite Solar Cells. *Energy Environ. Sci.* **2016**, *9* (5), 1655–1660.
- (67) Aristidou, N.; Sanchez-Molina, I.; Chotchuangchutchaval, T.; Brown, M.; Martinez, L.; Rath, T.; Haque, S. A. The Role of Oxygen in the Degradation of Methylammonium Lead Trihalide Perovskite Photoactive Layers. *Angew. Chemie - Int. Ed.* **2015**, *54* (28), 8208–8212.
- (68) Leijtens, T.; Eperon, G. E.; Noel, N. K.; Habisreutinger, S. N.; Petrozza, A.; Snaith, H. J. Stability of Metal Halide Perovskite Solar Cells. *Adv. Energy Mater.* **2015**, *5* (20), 1500963.
- (69) Leijtens, T.; Hoke, E. T.; Grancini, G.; Slotcavage, D. J.; Eperon, G. E.; Ball, J. M.; De Bastiani, M.; Bowring, A. R.; Martino, N.; Wojciechowski, K.; et al. Mapping Electric Field-Induced Switchable Poling and Structural Degradation in Hybrid Lead Halide Perovskite Thin Films. *Adv. Energy Mater.* **2015**, *5* (20), 1500962.
- (70) deQuilettes, D. W.; Zhang, W.; Burlakov, V. M.; Graham, D. J.; Leijtens, T.; Osherov, A.; Bulović, V.; Snaith, H. J.; Ginger, D. S.; Stranks, S. D. Photo-Induced Halide Redistribution in Organic-Inorganic Perovskite Films. *Nat. Commun.* **2016**, *7*, 11683.
- (71) Wei, D.; Wang, T.; Ji, J.; Li, M.; Cui, P.; Li, Y.; Li, G.; Mbengue, J. M.; Song, D. Photo-Induced Degradation of Lead Halide Perovskite Solar Cells Caused by the Hole Transport Layer/Metal Electrode Interface. *J. Mater. Chem. A* **2016**, *4* (5), 1991–1998.
- (72) Leijtens, T.; Eperon, G. E.; Pathak, S.; Abate, A.; Lee, M. M.; Snaith, H. J. Overcoming Ultraviolet Light Instability of Sensitized  $\text{TiO}_2$  with Meso-Superstructured Organometal Tri-Halide Perovskite Solar Cells. *Nat. Commun.* **2013**, *4*, 2885.

- (73) Hailegnaw, B.; Kirmayer, S.; Edri, E.; Hodes, G.; Cahen, D. Rain on Methylammonium Lead Iodide Based Perovskites: Possible Environmental Effects of Perovskite Solar Cells. *J. Phys. Chem. Lett.* **2015**, *6* (9), 1543–1547.
- (74) Li, J.; Cao, H.-L.; Jiao, W.-B.; Wang, Q.; Wei, M.; Cantone, I.; Lü, J.; Abate, A. Biological Impact of Lead from Halide Perovskites Reveals the Risk of Introducing a Safe Threshold. *Nat. Commun.* **2020**, *11*, 310.
- (75) Kadro, J. M.; Hagfeldt, A. The End-of-Life of Perovskite PV. *Joule* **2017**, *1* (1), 29–46.
- (76) Serrano-Lujan, L.; Espinosa, N.; Larsen-Olsen, T. T.; Abad, J.; Urbina, A.; Krebs, F. C. Tin- and Lead-Based Perovskite Solar Cells under Scrutiny: An Environmental Perspective. *Adv. Energy Mater.* **2015**, *5* (20).
- (77) Kamarudin, M. A.; Hirotani, D.; Wang, Z.; Hamada, K.; Nishimura, K.; Shen, Q.; Toyoda, T.; Iikubo, S.; Minemoto, T.; Yoshino, K.; et al. Suppression of Charge Carrier Recombination in Lead-Free Tin Halide Perovskite via Lewis Base Post-Treatment. *J. Phys. Chem. Lett.* **2019**, *10* (17), 5277–5283.
- (78) Umebayashi, T.; Asai, K.; Kondo, T.; Nakao, A. Electronic Structures of Lead Iodide Based Low-Dimensional Crystals. *Phys. Rev. B* **2003**, *67* (15), 155405.
- (79) Brandt, R. E.; Stevanović, V.; Ginley, D. S.; Buonassisi, T. Identifying Defect-Tolerant Semiconductors with High Minority-Carrier Lifetimes: Beyond Hybrid Lead Halide Perovskites. *MRS Commun.* **2015**, *5* (2), 265–275.
- (80) Huang, W.; Yue, S.; Liu, Y.; Zhu, L.; Jin, P.; Wu, Q.; Zhang, Y.; Chen, Y.; Liu, K.; Liang, P.; et al. Observation of Unusual Optical Band Structure of  $\text{CH}_3\text{NH}_3\text{PbI}_3$  Perovskite Single Crystal. *ACS Photonics* **2018**, *5* (4), 1583–1590.
- (81) Lee, J. H.; Bristowe, N. C.; Bristowe, P. D.; Cheetham, A. K. Role of Hydrogen-Bonding and Its Interplay with Octahedral Tilting in  $\text{CH}_3\text{NH}_3\text{PbI}_3$ . *Chem. Commun.* **2015**, *51* (29), 6434–6437.
- (82) Even, J.; Pedesseau, L.; Katan, C. Analysis of Multivalley and Multibandgap Absorption and Enhancement of Free Carriers Related to Exciton Screening in Hybrid Perovskites. *J. Phys. Chem. C* **2014**, *118* (22), 11566–11572.
- (83) Herz, L. M. Charge-Carrier Dynamics in Organic-Inorganic Metal Halide Perovskites. *Annu. Rev. Phys. Chem.* **2016**, *67* (1), 65–89.
- (84) Amat, A.; Mosconi, E.; Ronca, E.; Quarti, C.; Umari, P.; Nazeeruddin, M. K.; Grätzel, M.; De Angelis, F. Cation-Induced Band-Gap Tuning in Organohalide Perovskites: Interplay of Spin–Orbit Coupling and Octahedra Tilting. *Nano Lett.* **2014**, *14* (6), 3608–3616.
- (85) Even, J.; Pedesseau, L.; Jancu, J.-M.; Katan, C. Importance of Spin–Orbit Coupling in Hybrid Organic/Inorganic Perovskites for Photovoltaic Applications. *J. Phys. Chem. Lett.* **2013**, *4* (17), 2999–3005.
- (86) Johnston, M. B.; Herz, L. M. Hybrid Perovskites for Photovoltaics: Charge-Carrier Recombination, Diffusion, and Radiative Efficiencies. *Acc. Chem. Res.* **2016**, *49*, 146–154.
- (87) Savenije, T. J.; Ponseca, C. S.; Kunneman, L.; Abdellah, M.; Zheng, K.; Tian, Y.; Zhu, Q.; Canton, S. E.; Scheblykin, I. G.; Pullerits, T.; et al. Thermally Activated Exciton Dissociation and Recombination Control the Carrier Dynamics in Organometal Halide Perovskite. *J. Phys. Chem. Lett.* **2014**, *5* (13), 2189–2194.
- (88) Milot, R. L.; Eperon, G. E.; Snaith, H. J.; Johnston, M. B.; Herz, L. M. Temperature-Dependent Charge-Carrier Dynamics in  $\text{CH}_3\text{NH}_3\text{PbI}_3$  Perovskite Thin Films. *Adv. Funct. Mater.* **2015**, *25* (39), 6218–6227.
- (89) Yamada, Y.; Nakamura, T.; Endo, M.; Wakamiya, A.; Kanemitsu, Y. Photocarrier Recombination Dynamics in Perovskite  $\text{CH}_3\text{NH}_3\text{PbI}_3$  for Solar Cell Applications. *J. Am. Chem. Soc.* **2014**, *136* (33), 11610–11613.
- (90) Manser, J. S.; Kamat, P. V. Band Filling with Free Charge Carriers in Organometal Halide Perovskites. *Nat. Photonics* **2014**, *8* (9), 737–743.
- (91) Pincherle, L. Auger Effect in Semiconductors. *Proc. Phys. Soc. Sect. B* **1955**, *68* (5), 319–320.

- (92) Staub, F.; Rau, U.; Kirchartz, T. Statistics of the Auger Recombination of Electrons and Holes via Defect Levels in the Band Gap - Application to Lead-Halide Perovskites. *ACS Omega* **2018**, 3 (7), 8009–8016.
- (93) Stranks, S. D.; Burlakov, V. M.; Leijtens, T.; Ball, J. M.; Goriely, A.; Snaith, H. J. Recombination Kinetics in Organic-Inorganic Perovskites: Excitons, Free Charge, and Subgap States. *Phys. Rev. Appl.* **2014**, 2 (3), 034007.
- (94) Richter, J. M.; Abdi-Jalebi, M.; Sadhanala, A.; Tabachnyk, M.; Rivett, J. P. H.; Pazos-Outón, L. M.; Gödel, K. C.; Price, M.; Deschler, F.; Friend, R. H. Enhancing Photoluminescence Yields in Lead Halide Perovskites by Photon Recycling and Light Out-Coupling. *Nat. Commun.* **2016**, 7, 13941.
- (95) Miller, O. D.; Yablonovitch, E.; Kurtz, S. R. Strong Internal and External Luminescence as Solar Cells Approach the Shockley-Queisser Limit. *IEEE J. Photovoltaics* **2012**, 2 (3), 303–311.
- (96) Pazos-Outón, L. M.; Xiao, T. P.; Yablonovitch, E. Fundamental Efficiency Limit of Lead Iodide Perovskite Solar Cells. *J. Phys. Chem. Lett.* **2018**, 9 (7), 1703–1711.
- (97) Stolterfoht, M.; Wolff, C. M.; Márquez, J. A.; Zhang, S.; Hages, C. J.; Rothhardt, D.; Albrecht, S.; Burn, P. L.; Meredith, P.; Unold, T.; et al. Visualization and Suppression of Interfacial Recombination for High-Efficiency Large-Area Pin Perovskite Solar Cells. *Nat. Energy* **2018**, 3 (10), 847–854.
- (98) Draguta, S.; Thakur, S.; Morozov, Y. V.; Wang, Y.; Manser, J. S.; Kamat, P. V.; Kuno, M. Spatially Non-Uniform Trap State Densities in Solution-Processed Hybrid Perovskite Thin Films. *J. Phys. Chem. Lett.* **2016**, 7 (4), 715–721.
- (99) DeQuilettes, D. W.; Vorpahl, S. M.; Stranks, S. D.; Nagaoka, H.; Eperon, G. E.; Ziffer, M. E.; Snaith, H. J.; Ginger, D. S. Impact of Microstructure on Local Carrier Lifetime in Perovskite Solar Cells. *Science* **2015**, 348 (6235), 683–686.
- (100) deQuilettes, D. W.; Koch, S.; Burke, S.; Paranj, R. K.; Shropshire, A. J.; Ziffer, M. E.; Ginger, D. S. Photoluminescence Lifetimes Exceeding 8  $\mu$ s and Quantum Yields Exceeding 30% in Hybrid Perovskite Thin Films by Ligand Passivation. *ACS Energy Lett.* **2016**, 1 (2), 438–444.
- (101) Jacobsson, T. J.; Correa-Baena, J. P.; Halvani Anaraki, E.; Philippe, B.; Stranks, S. D.; Bouduban, M. E. F.; Tress, W.; Schenk, K.; Teuscher, J.; Moser, J. E.; et al. Unreacted PbI<sub>2</sub> as a Double-Edged Sword for Enhancing the Performance of Perovskite Solar Cells. *J. Am. Chem. Soc.* **2016**, 138 (32), 10331–10343.
- (102) Ozerov, R. R.; Vorobyev, A. A. *Physics for Chemists*; Elsevier, 2007; pp 105–250.
- (103) Lannoo, M.; Bourgoin, J. *Point Defects in Semiconductors I*; Springer Series in Solid-State Sciences; Springer Berlin Heidelberg: Berlin, Heidelberg, 1981; Vol. 22, pp 1-65,155-243.
- (104) Henderson, B. *Defects in Crystalline Solids*; Edward Arnold Ltd: London, 1972; pp 1–49.
- (105) Kröger, F. A. *The Chemistry of Imperfect Crystals*; North-Holland, 1964; Vol. 68.
- (106) Tiwari, G. P.; Mehrotra, R. S.; Iijima, Y. *Solid State Diffusion and Bulk Properties*; Springer Berlin Heidelberg: Berlin, Heidelberg, 2005; pp 69–111.
- (107) Borg, R. J.; Dienes, G. J. *An Introduction to Solid State Diffusion*; 1990; Vol. 94, pp 53-125,173-286.
- (108) Glicksman, M. E. *Diffusion in Solids: Field Theory, Solid-State Principles, and Applications*; Wiley, 1999; pp 235–279.
- (109) Farver, J.; Yund, R. Silicon Diffusion in a Natural Quartz Aggregate: Constraints on Solution-Transfer Diffusion Creep. *Tectonophysics* **2000**, 325 (3–4), 193–205.
- (110) Suzuoka, T. Lattice and Grain Boundary Diffusion in Polycrystals. *Trans. Japan Inst. Met.* **1961**, 2, 25–32.
- (111) Was, G. S. *Fundamentals of Radiation Materials Science*; Springer Berlin Heidelberg, 2007; pp 155–190.
- (112) Weiser, K. Theory of Diffusion and Equilibrium Position of Interstitial Impurities in the Diamond Lattice. *Phys. Rev.* **1962**, 126 (4), 1427–1436.



- (113) Bourgoin, J. C.; Corbett, J. W. Enhanced Diffusion Mechanisms. *Radiat. Eff.* **1978**, *36* (3–4), 157–188.
- (114) Peak, D.; Corbett, J. W.; Bourgoin, J. C. Ionization Enhanced Diffusion. *J. Chem. Phys.* **1976**, *65* (3), 1206–1210.
- (115) Philibert, J. *Atom Movements - Diffusion and Mass Transport in Solids*; EDP Sciences, 2012.
- (116) Guidoni, S. E.; Aldao, C. M. On Diffusion, Drift and the Einstein Relation. *Eur. J. Phys.* **2002**, *23* (4), 395–402.
- (117) Heiser, T.; Mesli, A. Determination of the Copper Diffusion Coefficient in Silicon from Transient Ion-Drift. *Appl. Phys. A Solids Surfaces* **1993**, *57* (4), 325–328.
- (118) Fontell, A.; Arminen, E.; Turunen, M. Application of the Backscattering Method for the Measurement of Diffusion of Zinc in Aluminium. *Phys. Status Solidi* **1973**, *15* (1), 113–119.
- (119) Huang, J.; Yuan, Y.; Shao, Y.; Yan, Y. Understanding the Physical Properties of Hybrid Perovskites for Photovoltaic Applications. *Nat. Rev. Mater.* **2017**, *2* (7), 17042.
- (120) Ball, J. M.; Petrozza, A. Defects in Perovskite-Halides and Their Effects in Solar Cells. *Nat. Energy* **2016**, *1* (11), 16149.
- (121) Yin, W. J.; Shi, T.; Yan, Y. Unique Properties of Halide Perovskites as Possible Origins of the Superior Solar Cell Performance. *Adv. Mater.* **2014**, *26* (27), 4653–4658.
- (122) Yin, W.-J.; Shi, T.; Yan, Y. Unusual Defect Physics in  $\text{CH}_3\text{NH}_3\text{PbI}_3$  Perovskite Solar Cell Absorber. *Appl. Phys. Lett.* **2014**, *104* (6), 063903.
- (123) Buin, A.; Comin, R.; Xu, J.; Ip, A. H.; Sargent, E. H. Halide-Dependent Electronic Structure of Organolead Perovskite Materials. *Chem. Mater.* **2015**, *27* (12), 4405–4412.
- (124) Meggiolaro, D.; De Angelis, F. First-Principles Modeling of Defects in Lead Halide Perovskites: Best Practices and Open Issues. *ACS Energy Lett.* **2018**, *3* (9), 2206–2222.
- (125) Buin, A.; Pietsch, P.; Xu, J.; Voznyy, O.; Ip, A. H.; Comin, R.; Sargent, E. H. Materials Processing Routes to Trap-Free Halide Perovskites. *Nano Lett.* **2014**, *14* (11), 6281–6286.
- (126) Agiorgousis, M. L.; Sun, Y. Y.; Zeng, H.; Zhang, S. Strong Covalency-Induced Recombination Centers in Perovskite Solar Cell Material  $\text{CH}_3\text{NH}_3\text{PbI}_3$ . *J. Am. Chem. Soc.* **2014**, *136* (41), 14570–14575.
- (127) Du, M. H. Efficient Carrier Transport in Halide Perovskites: Theoretical Perspectives. *J. Mater. Chem. A* **2014**, *2* (24), 9091–9098.
- (128) Yin, W. J.; Yang, J. H.; Kang, J.; Yan, Y.; Wei, S. H. Halide Perovskite Materials for Solar Cells: A Theoretical Review. *J. Mater. Chem. A* **2015**, *3* (17), 8926–8942.
- (129) Kim, J.; Lee, S. H.; Lee, J. H.; Hong, K. H. The Role of Intrinsic Defects in Methylammonium Lead Iodide Perovskite. *J. Phys. Chem. Lett.* **2014**, *5* (8), 1312–1317.
- (130) Xiao, Z.; Yuan, Y.; Shao, Y.; Wang, Q.; Dong, Q.; Bi, C.; Sharma, P.; Gruverman, A.; Huang, J. Giant Switchable Photovoltaic Effect in Organometal Trihalide Perovskite Devices. *Nat. Mater.* **2015**, *14* (2), 193–198.
- (131) Eames, C.; Frost, J. M.; Barnes, P. R. F.; O'Regan, B. C.; Walsh, A.; Islam, M. S. Ionic Transport in Hybrid Lead Iodide Perovskite Solar Cells. *Nat. Commun.* **2015**, *6*, 7497.
- (132) Snaith, H. J.; Abate, A.; Ball, J. M.; Eperon, G. E.; Leijtens, T.; Noel, N. K.; Stranks, S. D.; Wang, J. T. W.; Wojciechowski, K.; Zhang, W. Anomalous Hysteresis in Perovskite Solar Cells. *J. Phys. Chem. Lett.* **2014**, *5* (9), 1511–1515.
- (133) Li, C.; Tscheuschner, S.; Paulus, F.; Hopkinson, P. E.; Kießling, J.; Köhler, A.; Vaynzof, Y.; Huettnner, S. Iodine Migration and Its Effect on Hysteresis in Perovskite Solar Cells. *Adv. Mater.* **2016**, *28* (12), 2446–2454.
- (134) Delugas, P.; Caddeo, C.; Filippetti, A.; Mattoni, A. Thermally Activated Point Defect Diffusion in Methylammonium Lead Trihalide: Anisotropic and Ultrahigh Mobility of Iodine. *J. Phys. Chem. Lett.* **2016**, *7* (13), 2356–2361.

- (135) Haruyama, J.; Sodeyama, K.; Han, L.; Tateyama, Y. First-Principles Study of Ion Diffusion in Perovskite Solar Cell Sensitizers. *J. Am. Chem. Soc.* **2015**, *137* (32), 10048–10051.
- (136) Azpiroz, J. M.; Mosconi, E.; Bisquert, J.; De Angelis, F. Defect Migration in Methylammonium Lead Iodide and Its Role in Perovskite Solar Cell Operation. *Energy Environ. Sci.* **2015**, *8* (7), 2118–2127.
- (137) Meloni, S.; Moehl, T.; Tress, W.; Franckevičius, M.; Saliba, M.; Lee, Y. H.; Gao, P.; Nazeeruddin, M. K.; Zakeeruddin, S. M.; Rothlisberger, U.; et al. Ionic Polarization-Induced Current–Voltage Hysteresis in  $\text{CH}_3\text{NH}_3\text{PbX}_3$  Perovskite Solar Cells. *Nat. Commun.* **2016**, *7*, 10334.
- (138) Yang, T.-Y.; Gregori, G.; Pellet, N.; Grätzel, M.; Maier, J. The Significance of Ion Conduction in a Hybrid Organic-Inorganic Lead-Iodide-Based Perovskite Photosensitizer. *Angew. Chemie* **2015**, *127* (27), 8016–8021.
- (139) Yuan, Y.; Chae, J.; Shao, Y.; Wang, Q.; Xiao, Z.; Centrone, A.; Huang, J. Photovoltaic Switching Mechanism in Lateral Structure Hybrid Perovskite Solar Cells. *Adv. Energy Mater.* **2015**, *5* (15), 1500615.
- (140) Bag, M.; Renna, L. A.; Adhikari, R. Y.; Karak, S.; Liu, F.; Lahti, P. M.; Russell, T. P.; Tuominen, M. T.; Venkataraman, D. Kinetics of Ion Transport in Perovskite Active Layers and Its Implications for Active Layer Stability. *J. Am. Chem. Soc.* **2015**, *137* (40), 13130–13137.
- (141) Yamilova, O. R.; Danilov, A. V.; Mangrulkar, M.; Fedotov, Y. S.; Luchkin, S. Y.; Babenko, S. D.; Bredikhin, S. I.; Aldoshin, S. M.; Stevenson, K. J.; Troshin, P. A. Reduction of Methylammonium Cations as a Major Electrochemical Degradation Pathway in  $\text{MAPbI}_3$  Perovskite Solar Cells. *J. Phys. Chem. Lett.* **2020**, *11* (1), 221–228.
- (142) Unger, E. L.; Hoke, E. T.; Bailie, C. D.; Nguyen, W. H.; Bowering, A. R.; Heumüller, T.; Christoforo, M. G.; McGehee, M. D. Hysteresis and Transient Behavior in Current-Voltage Measurements of Hybrid-Perovskite Absorber Solar Cells. *Energy Environ. Sci.* **2014**, *7* (11), 3690–3698.
- (143) Chen, B.; Yang, M.; Zheng, X.; Wu, C.; Li, W.; Yan, Y.; Bisquert, J.; Garcia-Belmonte, G.; Zhu, K.; Priya, S. Impact of Capacitive Effect and Ion Migration on the Hysteretic Behavior of Perovskite Solar Cells. *J. Phys. Chem. Lett.* **2015**, *6* (23), 4693–4700.
- (144) Li, C.; Guerrero, A.; Zhong, Y.; Gräser, A.; Luna, C. A. M.; Köhler, J.; Bisquert, J.; Hildner, R.; Huettner, S. Real-Time Observation of Iodide Ion Migration in Methylammonium Lead Halide Perovskites. *Small* **2017**, *13* (42), 1701711.
- (145) Li, C.; Guerrero, A.; Huettner, S.; Bisquert, J. Unravelling the Role of Vacancies in Lead Halide Perovskite through Electrical Switching of Photoluminescence. *Nat. Commun.* **2018**, *9*, 5113.
- (146) Deng, X.; Wen, X.; Lau, C. F. J.; Young, T.; Yun, J.; Green, M. A.; Huang, S.; Ho-Baillie, A. W. Y. Electric Field Induced Reversible and Irreversible Photoluminescence Responses in Methylammonium Lead Iodide Perovskite. *J. Mater. Chem. C* **2016**, *4* (38), 9060–9068.
- (147) Stranks, S. D. Nonradiative Losses in Metal Halide Perovskites. *ACS Energy Lett.* **2017**, *2* (7), 1515–1525.
- (148) Fassel, P.; Ternes, S.; Lami, V.; Zakharko, Y.; Heimfarth, D.; Hopkinson, P. E.; Paulus, F.; Taylor, A. D.; Zaumseil, J.; Vaynzof, Y. Effect of Crystal Grain Orientation on the Rate of Ionic Transport in Perovskite Polycrystalline Thin Films. *ACS Appl. Mater. Interfaces* **2019**, *11* (2), 2490–2499.
- (149) Hentz, O.; Singh, A.; Zhao, Z.; Gradečak, S. Visualizing Nonradiative Mobile Defects in Organic–Inorganic Perovskite Materials. *Small Methods* **2019**, *3* (7), 1900110.
- (150) Collins, S. D.; Mikhnenko, O. V.; Nguyen, T. L.; Rengert, Z. D.; Bazan, G. C.; Woo, H. Y.; Nguyen, T.-Q. Observing Ion Motion in Conjugated Polyelectrolytes with Kelvin Probe Force Microscopy. *Adv. Electron. Mater.* **2017**, *3* (3), 1700005.
- (151) Zerweck, U.; Loppacher, C.; Otto, T.; Grafström, S.; Eng, L. M. Accuracy and Resolution Limits of Kelvin Probe Force Microscopy. *Phys. Rev. B* **2005**, *71* (12), 125424.
- (152) Weber, S. A. L.; Hermes, I. M.; Turren-Cruz, S. H.; Gort, C.; Bergmann, V. W.; Gilson, L.; Hagfeldt, A.; Graetzel, M.; Tress, W.; Berger, R. How the Formation of Interfacial Charge Causes Hysteresis in Perovskite Solar Cells. *Energy Environ. Sci.* **2018**, *11* (9), 2404–2413.



- (153) Birkhold, S. T.; Precht, J. T.; Giridharagopal, R.; Eperon, G. E.; Schmidt-Mende, L.; Ginger, D. S. Direct Observation and Quantitative Analysis of Mobile Frenkel Defects in Metal Halide Perovskites Using Scanning Kelvin Probe Microscopy. *J. Phys. Chem. C* **2018**, *122* (24), 12633–12639.
- (154) D’Innocenzo, V.; Grancini, G.; Alcocer, M. J. P.; Kandada, A. R. S.; Stranks, S. D.; Lee, M. M.; Lanzani, G.; Snaith, H. J.; Petrozza, A. Excitons versus Free Charges in Organo-Lead Tri-Halide Perovskites. *Nat. Commun.* **2014**, *5*, 3586.
- (155) Salim, T.; Sun, S.; Abe, Y.; Krishna, A.; Grimsdale, A. C.; Lam, Y. M. Perovskite-Based Solar Cells: Impact of Morphology and Device Architecture on Device Performance. *J. Mater. Chem. A* **2015**, *3* (17), 8943–8969.
- (156) Mali, S. S.; Hong, C. K. P-i-n/n-i-p Type Planar Hybrid Structure of Highly Efficient Perovskite Solar Cells towards Improved Air Stability: Synthetic Strategies and the Role of p-Type Hole Transport Layer (HTL) and n-Type Electron Transport Layer (ETL) Metal Oxides. *Nanoscale* **2016**, *8* (20), 10528–10540.
- (157) Wang, K. C.; Shen, P. S.; Li, M. H.; Chen, S.; Lin, M. W.; Chen, P.; Guo, T. F. Low-Temperature Sputtered Nickel Oxide Compact Thin Film as Effective Electron Blocking Layer for Mesoscopic NiO/CH<sub>3</sub>NH<sub>3</sub>PbI<sub>3</sub> Perovskite Heterojunction Solar Cells. *ACS Appl. Mater. Interfaces* **2014**, *6* (15), 11851–11858.
- (158) Yang, D.; Yang, R.; Wang, K.; Wu, C.; Zhu, X.; Feng, J.; Ren, X.; Fang, G.; Priya, S.; Liu, S. High Efficiency Planar-Type Perovskite Solar Cells with Negligible Hysteresis Using EDTA-Complexed SnO<sub>2</sub>. *Nat. Commun.* **2018**, *9*, 3239.
- (159) Gao, X.; Li, J.; Baker, J.; Hou, Y.; Guan, D.; Chen, J.; Yuan, C. Enhanced Photovoltaic Performance of Perovskite CH<sub>3</sub>NH<sub>3</sub>PbI<sub>3</sub> Solar Cells with Freestanding TiO<sub>2</sub> Nanotube Array Films. *Chem. Commun.* **2014**, *50* (48), 6368–6371.
- (160) Wu, Q.; Xue, C.; Li, Y.; Zhou, P.; Liu, W.; Zhu, J.; Dai, S.; Zhu, C.; Yang, S. Kesterite Cu<sub>2</sub>ZnSnS<sub>4</sub> as a Low-Cost Inorganic Hole-Transporting Material for High-Efficiency Perovskite Solar Cells. *ACS Appl. Mater. Interfaces* **2015**, *7* (51), 28466–28473.
- (161) Kumar, M. H.; Yantara, N.; Dharani, S.; Graetzel, M.; Boix, P. P.; Mathews, N. Flexible, Low-Temperature, Solution Processed ZnO-Based Perovskite Solid State Solar Cells. *Chem. Commun.* **2013**, *49* (94), 11089–11091.
- (162) Son, D. Y.; Im, J. H.; Kim, H. S.; Park, N. G. 11% Efficient Perovskite Solar Cell Based on ZnO Nanorods: An Effective Charge Collection System. *J. Phys. Chem. C* **2014**, *118* (30), 16567–16573.
- (163) Golubev, T.; Liu, D.; Lunt, R.; Duxbury, P. Understanding the Impact of C<sub>60</sub> at the Interface of Perovskite Solar Cells via Drift-Diffusion Modeling. *AIP Adv.* **2019**, *9* (3), 035026.
- (164) Lin, H.; Jeon, I.; Xiang, R.; Seo, S.; Lee, J.; Li, C.; Pal, A.; Manzhos, S.; Goorsky, M. S.; Yang, Y.; et al. Achieving High Efficiency in Solution-Processed Perovskite Solar Cells Using C<sub>60</sub>/C<sub>70</sub> Mixed Fullerenes. *ACS Appl. Mater. Interfaces* **2018**, *10* (46), 39590–39598.
- (165) Yang, Y.; You, J.; Hong, Z.; Chen, Q.; Cai, M.; Song, T. Bin; Chen, C. C.; Lu, S.; Liu, Y.; Zhou, H. Low-Temperature Solution-Processed Perovskite Solar Cells with High Efficiency and Flexibility. *ACS Nano* **2014**, *8* (2), 1674–1680.
- (166) Wang, Q.; Shao, Y.; Dong, Q.; Xiao, Z.; Yuan, Y.; Huang, J. Large Fill-Factor Bilayer Iodine Perovskite Solar Cells Fabricated by a Low-Temperature Solution-Process. *Energy Environ. Sci.* **2014**, *7* (7), 2359–2365.
- (167) Chen, J.; Lian, X.; Zhang, Y.; Yang, W.; Li, J.; Qin, M.; Lu, X.; Wu, G.; Chen, H. Interfacial Engineering Enables High Efficiency with a High Open-Circuit Voltage above 1.23 v in 2D Perovskite Solar Cells. *J. Mater. Chem. A* **2018**, *6* (37), 18010–18017.
- (168) Nam, J. K.; Chai, S. U.; Cha, W.; Choi, Y. J.; Kim, W.; Jung, M. S.; Kwon, J.; Kim, D.; Park, J. H. Potassium Incorporation for Enhanced Performance and Stability of Fully Inorganic Cesium Lead Halide Perovskite Solar Cells. *Nano Lett.* **2017**, *17* (3), 2028–2033.
- (169) Matsui, T.; Seo, J.-Y.; Saliba, M.; Zakeeruddin, S. M.; Grätzel, M. Room-Temperature Formation of Highly Crystalline Multication Perovskites for Efficient, Low-Cost Solar Cells. *Adv. Mater.* **2017**, *29* (15), 1606258.

- (170) Liu, X.; Cheng, Y.; Liu, C.; Zhang, T.; Zhang, N.; Zhang, S.; Chen, J.; Xu, Q.; Ouyang, J.; Gong, H. 20.7% Highly Reproducible Inverted Planar Perovskite Solar Cells With Enhanced Fill Factor and Eliminated Hysteresis. *Energy Environ. Sci.* **2019**, *12* (5), 1622–1633.
- (171) Yang, W. S.; Noh, J. H.; Jeon, N. J.; Kim, Y. C.; Ryu, S.; Seo, J.; Seok, S. Il. High-Performance Photovoltaic Perovskite Layers Fabricated through Intramolecular Exchange. *Science*. **2015**, *348* (6240), 1234–1237.
- (172) Jeon, N. J.; Noh, J. H.; Yang, W. S.; Kim, Y. C.; Ryu, S.; Seo, J.; Seok, S. Il. Compositional Engineering of Perovskite Materials for High-Performance Solar Cells. *Nature* **2015**, *517* (7535), 476–480.
- (173) He, Q.; Yao, K.; Wang, X.; Xia, X.; Leng, S.; Li, F. Room-Temperature and Solution-Processable Cu-Doped Nickel Oxide Nanoparticles for Efficient Hole-Transport Layers of Flexible Large-Area Perovskite Solar Cells. *ACS Appl. Mater. Interfaces* **2017**, *9* (48), 41887–41897.
- (174) Qin, P.; Tanaka, S.; Ito, S.; Tetreault, N.; Manabe, K.; Nishino, H.; Nazeeruddin, M. K.; Grätzel, M. Inorganic Hole Conductor-Based Lead Halide Perovskite Solar Cells with 12.4% Conversion Efficiency. *Nat. Commun.* **2014**, *5*, 3834.
- (175) Chen, C.; Zhang, S.; Wu, S.; Zhang, W.; Zhu, H.; Xiong, Z.; Zhang, Y.; Chen, W. Effect of BCP Buffer Layer on Eliminating Charge Accumulation for High Performance of Inverted Perovskite Solar Cells. *RSC Adv.* **2017**, *7* (57), 35819–35826.
- (176) Sun, J.; Lu, J.; Li, B.; Jiang, L.; Chesman, A. S. R.; Scully, A. D.; Gengenbach, T. R.; Cheng, Y. B.; Jasieniak, J. J. Inverted Perovskite Solar Cells with High Fill-Factors Featuring Chemical Bath Deposited Mesoporous NiO Hole Transporting Layers. *Nano Energy* **2018**, *49*, 163–171.
- (177) Sha, W. E. I.; Ren, X.; Chen, L.; Choy, W. C. H. The Efficiency Limit of  $\text{CH}_3\text{NH}_3\text{PbI}_3$  Perovskite Solar Cells. *Appl. Phys. Lett.* **2015**, *106* (22), 221104.
- (178) Akin, S. Hysteresis-Free Planar Perovskite Solar Cells with a Breakthrough Efficiency of 22% and Superior Operational Stability over 2000 h. *ACS Appl. Mater. Interfaces* **2019**, *11* (43), 39998–40005.
- (179) Son, D.-Y.; Kim, S.-G.; Seo, J.-Y.; Lee, S.-H.; Shin, H.; Lee, D.; Park, N.-G. Universal Approach toward Hysteresis-Free Perovskite Solar Cell via Defect Engineering. *J. Am. Chem. Soc.* **2018**, *140* (4), 1358–1364.
- (180) Liu, P.; Wang, W.; Liu, S.; Yang, H.; Shao, Z. Fundamental Understanding of Photocurrent Hysteresis in Perovskite Solar Cells. *Adv. Energy Mater.* **2019**, *9* (13), 1803017.
- (181) Gottesman, R.; Haltzi, E.; Gouda, L.; Tirosh, S.; Bouhadana, Y.; Zaban, A.; Mosconi, E.; De Angelis, F. Extremely Slow Photoconductivity Response of  $\text{CH}_3\text{NH}_3\text{PbI}_3$  Perovskites Suggesting Structural Changes under Working Conditions. *J. Phys. Chem. Lett.* **2014**, *5* (15), 2662–2669.
- (182) Tress, W.; Marinova, N.; Moehl, T.; Zakeeruddin, S. M.; Nazeeruddin, M. K.; Grätzel, M. Understanding the Rate-Dependent J-V Hysteresis, Slow Time Component, and Aging in  $\text{CH}_3\text{NH}_3\text{PbI}_3$  Perovskite Solar Cells: The Role of a Compensated Electric Field. *Energy Environ. Sci.* **2015**, *8* (3), 995–1004.
- (183) Tress, W.; Correa Baena, J. P.; Saliba, M.; Abate, A.; Graetzel, M. Inverted Current-Voltage Hysteresis in Mixed Perovskite Solar Cells: Polarization, Energy Barriers, and Defect Recombination. *Adv. Energy Mater.* **2016**, *6* (19), 1600396.
- (184) Zheng, F.; Takenaka, H.; Wang, F.; Koocher, N. Z.; Rappe, A. M. First-Principles Calculation of the Bulk Photovoltaic Effect in  $\text{CH}_3\text{NH}_3\text{PbI}_3$  and  $\text{CH}_3\text{NH}_3\text{PbI}_{3-x}\text{Cl}_x$ . *J. Phys. Chem. Lett.* **2015**, *6*, 31–37.
- (185) Frost, J. M.; Butler, K. T.; Brivio, F.; Hendon, C. H.; van Schilfgaarde, M.; Walsh, A. Atomistic Origins of High-Performance in Hybrid Halide Perovskite Solar Cells. *Nano Lett.* **2014**, *14* (5), 2584–2590.
- (186) Wu, X.; Yu, H.; Li, N.; Wang, F.; Xu, H.; Zhao, N. Composition-Dependent Light-Induced Dipole Moment Change in Organometal Halide Perovskites. *J. Phys. Chem. C* **2015**, *119* (2), 1253–1259.
- (187) Chen, B.; Shi, J.; Zheng, X.; Zhou, Y.; Zhu, K.; Priya, S. Ferroelectric Solar Cells Based on Inorganic-Organic Hybrid Perovskites. *J. Mater. Chem. A* **2015**, *3* (15), 7699–7705.

- (188) Chen, B.; Zheng, X.; Yang, M.; Zhou, Y.; Kundu, S.; Shi, J.; Zhu, K.; Priya, S. Interface Band Structure Engineering by Ferroelectric Polarization in Perovskite Solar Cells. *Nano Energy* **2015**, *13*, 582–591.
- (189) Leguy, A. M. A.; Frost, J. M.; McMahon, A. P.; Sakai, V. G.; Kockelmann, W.; Law, C.; Li, X.; Foglia, F.; Walsh, A.; O'Regan, B. C.; et al. The Dynamics of Methylammonium Ions in Hybrid Organic–Inorganic Perovskite Solar Cells. *Nat. Commun.* **2015**, *6*, 7124.
- (190) Kutes, Y.; Ye, L.; Zhou, Y.; Pang, S.; Huey, B. D.; Padture, N. P. Direct Observation of Ferroelectric Domains in Solution-Processed  $\text{CH}_3\text{NH}_3\text{PbI}_3$  Perovskite Thin Films. *J. Phys. Chem. Lett.* **2014**, *5* (19), 3335–3339.
- (191) Coll, M.; Gomez, A.; Mas-Marza, E.; Almora, O.; Garcia-Belmonte, G.; Campoy-Quiles, M.; Bisquert, J. Polarization Switching and Light-Enhanced Piezoelectricity in Lead Halide Perovskites. *J. Phys. Chem. Lett.* **2015**, *6* (8), 1408–1413.
- (192) Bergmann, V. W.; Weber, S. A. L.; Javier Ramos, F.; Nazeeruddin, M. K.; Grätzel, M.; Li, D.; Domanski, A. L.; Lieberwirth, I.; Ahmad, S.; Berger, R. Real-Space Observation of Unbalanced Charge Distribution inside a Perovskite-Sensitized Solar Cell. *Nat. Commun.* **2014**, *5*, 5001.
- (193) Wang, L.; McCleese, C.; Kovalsky, A.; Zhao, Y.; Burda, C. Femtosecond Time-Resolved Transient Absorption Spectroscopy Of. *J. Am. Chem. Soc.* **2014**, *136* (35), 12205–12208.
- (194) Wu, X.; Trinh, M. T.; Niesner, D.; Zhu, H.; Norman, Z.; Owen, J. S.; Yaffe, O.; Kudisch, B. J.; Zhu, X. Y. Trap States in Lead Iodide Perovskites. *J. Am. Chem. Soc.* **2015**, *137* (5), 2089–2096.
- (195) Edri, E.; Kirmayer, S.; Mukhopadhyay, S.; Gartsman, K.; Hodes, G.; Cahen, D. Elucidating the Charge Carrier Separation and Working Mechanism of  $\text{CH}_3\text{NH}_3\text{PbI}_{3-x}\text{Cl}_x$  Perovskite Solar Cells. *Nat. Commun.* **2014**, *5*, 3461.
- (196) Lee, J. W.; Kim, S. G.; Bae, S. H.; Lee, D. K.; Lin, O.; Yang, Y.; Park, N. G. The Interplay between Trap Density and Hysteresis in Planar Heterojunction Perovskite Solar Cells. *Nano Lett.* **2017**, *17* (7), 4270–4276.
- (197) Shao, Y.; Xiao, Z.; Bi, C.; Yuan, Y.; Huang, J. Origin and Elimination of Photocurrent Hysteresis by Fullerene Passivation in  $\text{CH}_3\text{NH}_3\text{PbI}_3$  Planar Heterojunction Solar Cells. *Nat. Commun.* **2014**, *5*, 5784.
- (198) Chen, B.; Rudd, P. N.; Yang, S.; Yuan, Y.; Huang, J. Imperfections and Their Passivation in Halide Perovskite Solar Cells. *Chem. Soc. Rev.* **2019**, *48* (14), 3842–3867.
- (199) Leijtens, T.; Eperon, G. E.; Barker, A. J.; Grancini, G.; Zhang, W.; Ball, J. M.; Kandada, A. R. S.; Snaith, H. J.; Petrozza, A. Carrier Trapping and Recombination: The Role of Defect Physics in Enhancing the Open Circuit Voltage of Metal Halide Perovskite Solar Cells. *Energy Environ. Sci.* **2016**, *9* (11), 3472–3481.
- (200) Van Reenen, S.; Kemerink, M.; Snaith, H. J. Modeling Anomalous Hysteresis in Perovskite Solar Cells. *J. Phys. Chem. Lett.* **2015**, *6* (19), 3808–3814.
- (201) Jacobs, D. A.; Wu, Y.; Shen, H.; Barugkin, C.; Beck, F. J.; White, T. P.; Weber, K.; Catchpole, K. R. Hysteresis Phenomena in Perovskite Solar Cells: The Many and Varied Effects of Ionic Accumulation. *Phys. Chem. Chem. Phys.* **2017**, *19* (4), 3094–3103.
- (202) Pockett, A.; Eperon, G. E.; Sakai, N.; Snaith, H. J.; Peter, L. M.; Cameron, P. J. Microseconds, Milliseconds and Seconds: Deconvoluting the Dynamic Behaviour of Planar Perovskite Solar Cells. *Phys. Chem. Chem. Phys.* **2017**, *19* (8), 5959–5970.
- (203) Miyadera, T.; Sugita, T.; Chikamatsu, M. Hysteresis Analysis of Organolead Halide Perovskite Solar Cells by Transient Current Measurement. *Electrochemistry* **2017**, *85* (5), 276–279.
- (204) Li, C.; Guerrero, A.; Zhong, Y.; Huettnner, S. Origins and Mechanisms of Hysteresis in Organometal Halide Perovskites. *J. Phys. Condens. Matter* **2017**, *29* (19).



## 3 Overview

### 3.1 Overall Synopsis and Conclusion

Although PCE of PSC has dramatically increased in the last few years, the instability related to ion migration is still a challenge for its widespread use. Frequently observed problems in PSC are, that prolonged illumination leads to a decrease of PCE and that hysteresis is prevalent in its  $J$ - $V$  curve characteristics. The studies presented within the next chapters show, that these behaviors are strongly related to ion migration in the OMHP material. Meanwhile, the optical properties, such as the PL, are found to be directly affected by migrating ions and the prevalent defects, offering a reliable tool for profound and *in-situ* investigations. Therefore, this thesis focuses on the investigation of ion migration in PSCs, its effect on performance and the potential suppression of ion migration by interfacial layer and intrinsic perovskite quality control. The application of an additional PCBM layer can reduce the ion migration and stabilize the long-time PCE. Another way is to reduce the number of mobile ions which are the intrinsic defects in perovskites. In order to understand and minimize defect densities, the film formation and crystallization process are studied with the help of two specially developed *in-situ* setups. Figure 3.1 illustrates the respective thematic connection between each chapter.

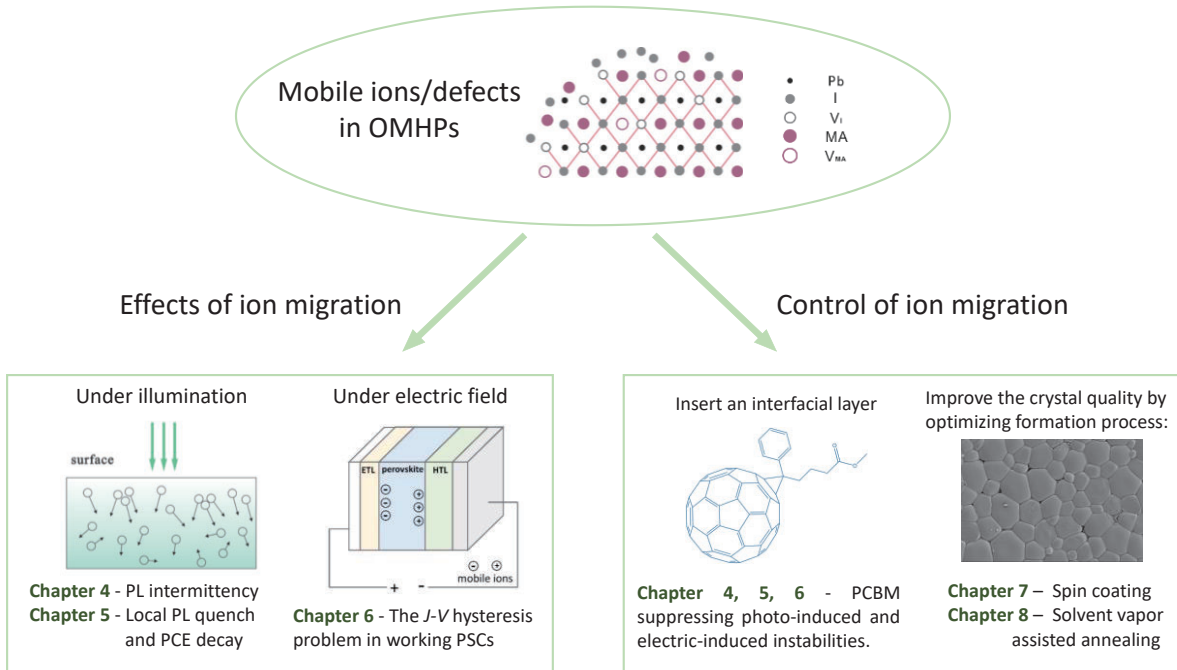


Figure 3.1: Schematic overview over the relation from Chapter 4 to Chapter 8.

Chapter 4 and Chapter 5 focus on optical properties and study the emission development in OMHP polycrystalline films under illumination using PL microscopy. Chapter 4 focuses on the PL intermittency of individual perovskite grains which are underlying a PL enhancement of the whole perovskite film under continuous illumination. In addition to this, some PL quenching areas on the scale of several-micrometers were observed, which is elucidated in Chapter 5. Based on the timescale of the PL intermittency and local PL quenching behavior, it is possible to ascribe them to prevalent mobile ions within the perovskite film. The ions migrate between grains resulting in a defect accumulation. The ionized states of the crystals enhance non-

radiative Auger recombination processes. Thus, the grains will exhibit low or high PL intensities depending on whether charges are trapped or released respectively. However, there exist some grains with higher defect density, where more ions accumulate. Consequently, PL of these grains quenches and does not recover immediately. This unstable PL behavior also has a negative impact on PSCs, as non-radiative recombination events can prevent solar cell approaching their theoretical efficiency limit. It is therefore important to immobilize or passivate the mobile ions in order to improve the photo-induced stability of OMHPs.

Chapter 6 investigates the mechanism of  $J$ - $V$  hysteresis suppression by comparing three configurations: a reference PSC, a PSC with a PCBM interfacial layer and a PSC with a PCBM grafted polymer (PPCBM) interfacial layer. I noticed that only the PSC with PCBM interfacial layer had a reduced hysteresis. With the help of PL imaging microscopy, the migration of iodide ions/vacancies under an external electric field was analyzed *in-situ*. It was found that the PPCBM layer could hardly suppress the ionic migration under bias, while the PCBM monomer layer could. The depth profile from XPS proved the incorporation of PCBM molecules in the perovskite layer. Considering the immobility of fullerenes in the case of PPCBM, it is proposed that the fullerenes at the surface of perovskite can't effectively passivate the mobile iodide ions/vacancies. Thus, hysteresis is suppressed by the PCBM molecules distributed in the bulk of the perovskite, weakening ion migration and consequently lowering the internal built-in field shift and interfacial barrier in PSCs.

In order to obtain perovskites with less mobile defects, the optimization of the perovskite film formation and crystallization process is necessary. Hence, it is important to grasp the optical and the structural changes during the film formation. Chapter 7 takes use of absorption and PL spectra recorded during the spin coating process and Chapter 8 employs X-ray scattering measured during the film annealing step. The results allow us to access the explicit evolution of the perovskite formation from the  $\text{PbI}_2$  and MAI source materials, including material conversion and crystallization dynamics. Chapter 8 furthermore introduces a setup for solvent vapor assisted annealing which can precisely control the solvent vapor pressure and temperature. By means of this method, it is possible to optimize the annealing parameters and to prepare perovskite films with large crystals.

In conclusion, my study could confirm ion/defect migration to be one major factor to cause PSCs instability. I pinpointed the underlying mechanisms in the condition of light illumination and external electric field. To suppress ion migration, the passivation of these ions by an interfacial layer and the reduction of mobile ion density which is able to be achieved by the improvement of perovskite film quality, are suggested to be constructive routes. Thus, I elaborated the kinetics of perovskite film formation and crystallization, providing a guidance on the control of perovskite film processing. Overall, the perovskite film formation kinetics, the photophysics in perovskite films and PSC deterioration mechanism learned in this thesis give insight into further development of PSCs



## 3.2 Contents of the Individual Chapter

### Emission Enhancement and Intermittency in Polycrystalline Organolead Halide Perovskite Films

Chapter 4 mainly discusses the photophysics of  $\text{MAPbI}_{3-x}\text{Cl}_x$  by correlating conventional PL characterization and high resolution wide-field PL imaging. The excitation intensity-dependent photoluminescence quantum efficiency (PLQE) measurements show that the PLQE increases with excitation intensity and reaches a saturated value of  $\sim 30\%$  when the excitation intensity is higher than  $70 \text{ mW/cm}^2$ . This can be explained by a trap-filling process, where sub-band gap traps are filled by photogenerated electrons/holes as explained in Chapter 2.3. Thus, a saturation of the PLQE value is reached when all the traps associated with non-radiative recombination have been filled as the electron/hole density increases. However, the overall PLQE is still relatively low, indicating the existence of another non-radiative recombination pathway rather than a trap-assisted recombination.

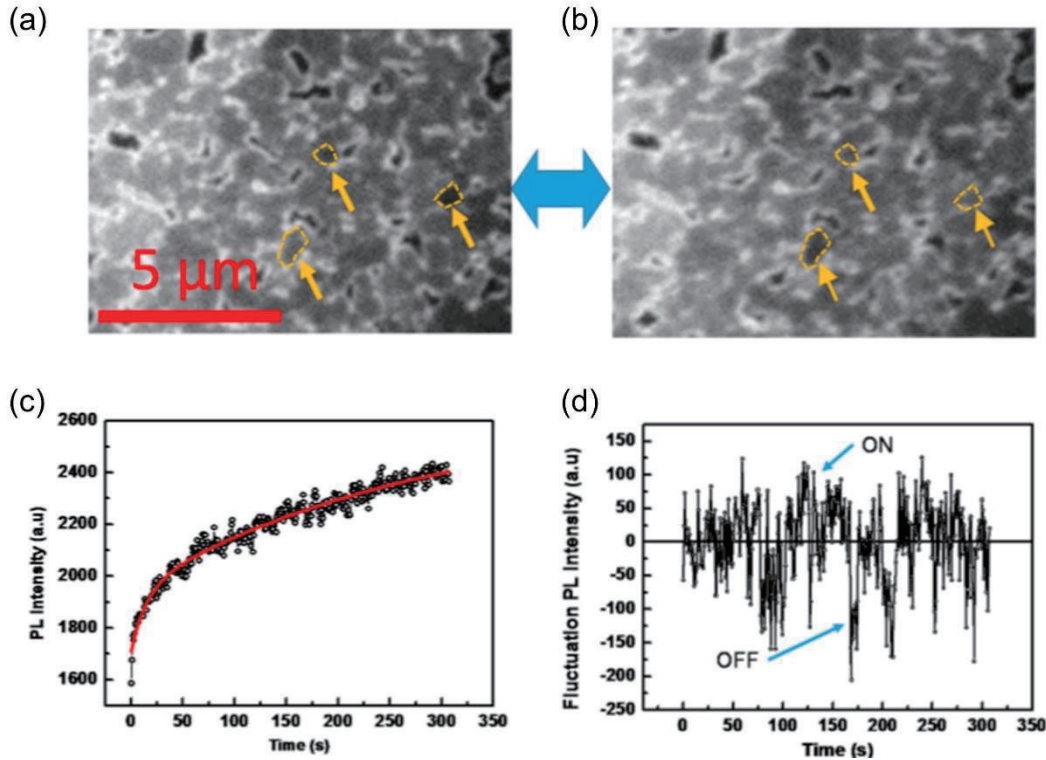


Figure 3.2: (a) PL intensity trajectory of a rectangle  $30 \mu\text{m} * 40 \mu\text{m}$ . The red-line is the fit by an exponential function. (b) PL intensity trajectory after subtraction of the exponentially increasing base line. It is extracted from a circle with  $1.5 \mu\text{m}$  diameter (c) and (d) Individual grains show PL blinking, indicated by yellow arrows.

To further understand the non-radiative recombination in the perovskite film, we used PL microscopy to study the spatial and temporal PL changes. PL images were captured every 500 ms (see Figure 3.2(a) and (b) for exemplary images). It was found that the PL intensity continuously increased within the illumination time, as shown in Figure 3.2(c). The fast PL increase in the beginning is attributed to a trap-filling process and the later slow increase is suggested to be related to defect migration and passivation. Besides the overall PL enhancement, strong fluctuations in PL intensity were observed which were beyond the experimental noise.

The fluctuations became more pronounced after an exponentially increasing baseline was subtracted, which is displayed in Figure 3.2(d). From the areas indicated by yellow circles in Figure 3.2(a) and (b), the switch between the strongly emissive state and the weakly emissive state could be observed. By comparison with the PL intermittency behavior in other materials, this appearance suggests a charge trapping process in perovskites. One of the photogenerated charge carriers (electrons or hole) can be trapped by defects, leaving the other charge carriers coupled with new electron-hole pairs. This Auger-like non-radiative recombination will be enhanced by local ionized states that are caused by ion accumulation. This effect leads to the observed weak PL. When no charges are trapped in grains, charge carriers tend to undergo bimolecular recombination, yielding a strong PL.

When the perovskite film is covered by a PCBM layer, the PL intermittency significantly decreases. One reason is that PCBM can passivate the defects in perovskite, reducing the number of charge trapping states. As Auger recombination rate is proportional to the third order of charge carrier density, another reason is that PCBM can effectively transfer the charge carriers from the perovskite, reducing the charge carrier density. This finding suggests a way to suppress the PL blinking in OMHPs.

### ***In situ* Investigation of Light Soaking in Organolead Halide Perovskite Films**

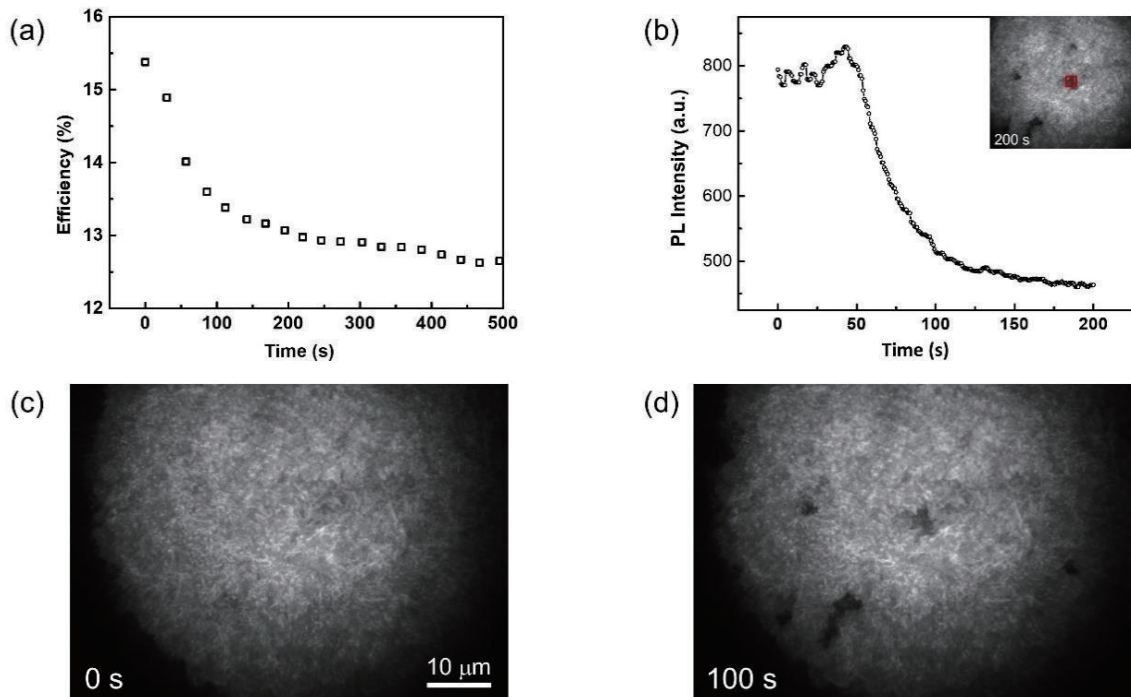


Figure 3.3: (a) The PCE decay of a PSC under continuous illumination (1.5 AM) in nitrogen atmosphere. (b) PL intensity trajectory of the region marked by red rectangle. The temporal evolution of the inserted image is shown in (c) and (d). The film is under illumination of 40 mW/cm<sup>2</sup> at 532 nm wavelength.

PSCs tend to exhibit photo-induced instabilities under continuous illumination. The PCE decay of a PSC is exemplarily shown in Figure 3.3(a). It is obvious that the PCE decreases quickly

within the first 100 seconds and after 500 seconds the PCE decreases by 18% relative to the initial PCE. The corresponding  $V_{oc}$  decreases similar to the PCE decay, while the  $J_{sc}$  remains almost constant during illumination. In PSCs typically the  $V_{oc}$  increases when the external luminescence efficiency increases. Thus the observed  $V_{oc}$  decrease is somewhat surprising at first, especially when taking into account the observation from Chapter 4, where the emission of the perovskite film increased under continuous illumination. However, the further study shows that scattered local areas display a strongly reduced PL upon long-time illumination, as exhibited in Figure 3.3(b)-(d). The relationship between this PL quenching phenomenon and the  $V_{oc}$  decay is studied in detail in Chapter 5.

Figure 3.3(b) exhibits the PL intensity change of a local area ( $\sim 2 \mu\text{m} \times 2 \mu\text{m}$ ), where the PL intensity increases in the first 45 seconds and then shows a decay. The decay time depends on the illumination intensity and it is in the range from 10 seconds to 100 seconds. This timescale corresponds to the timescale of the  $V_{oc}$  decay of the PSC. These PL inactive areas recover after being kept in dark and so does the PCE of PSC. This suggests that the enhanced non-radiative recombination in the local areas is responsible for the PSC deterioration. The proposed origin for the local PL change is the migration and localization of mobile ions, i.e. iodide ions, within the perovskite film under illumination, inducing non-radiative recombination centers. Also, the photo-induced field will facilitate ion migration in perovskite film. Thus, this study explains the negative effect of photo-induced ion migration and accumulation on the PSC performance.

## Role of PCBM in the Suppression of Hysteresis in Perovskite Solar Cells

The suppression of the  $J$ - $V$  curve hysteresis in PSCs by PCBM has been reported, but the explicit mechanism is not completely understood yet. The observation in Chapter 4 suggests that fullerenes such as PCBM do not only act as an efficient electron transport layer, but also can help to passivate the defects in perovskite films. This inspired us to study the role of a PCBM layer in PSCs in Chapter 6. In this study, PCBM serves as an interfacial layer between the ETL, i.e.  $\text{TiO}_2$ , and the perovskite. We found a significant amount of incorporation of PCBM within the grain boundaries of the perovskite film caused by dissolution during processing and diffusion while annealing. For comparison, a polymerized form of PCBM (PPCBM), i.e. fullerene molecules attached to a long polymer backbone, was used. It was discovered that the PSC with the PPCBM layer yielded more severe hysteresis than the PSC with PCBM layer, as shown in Figure 3.4.

Considering the possible origin of hysteresis, namely iodine ion/vacancy migration, we estimated the activation energy related to ion/ vacancy migration with the help of temperature-dependent chronoamperometric measurements. The results imply that the devices with PCBM exhibit a higher activation energy than the devices with PPCBM or the reference devices (FTO/ $\text{TiO}_2$ /perovskite/Spiro-OMeTAD/Au). This prompted me to look into the migration process in more detail comparing iodine ions/vacancies migration under external electric field in the three systems: single perovskite layer, perovskite/PCBM bilayer and perovskite/PPCBM bilayer. We made use of the model illustrated in Figure 2.11 and found that the ionic mobility in the perovskite/PCBM bilayer was significantly lower compared to the two other systems. These investigations suggest that the PCBM molecules are prevalent within the perovskite film

rather than only residing at the interface and this is a key factor to reduce ionic migration in the perovskite. Measuring a depth profile using XPS with sputtering corroborates the incorporation or diffusion of PCBM molecules into perovskite layer.

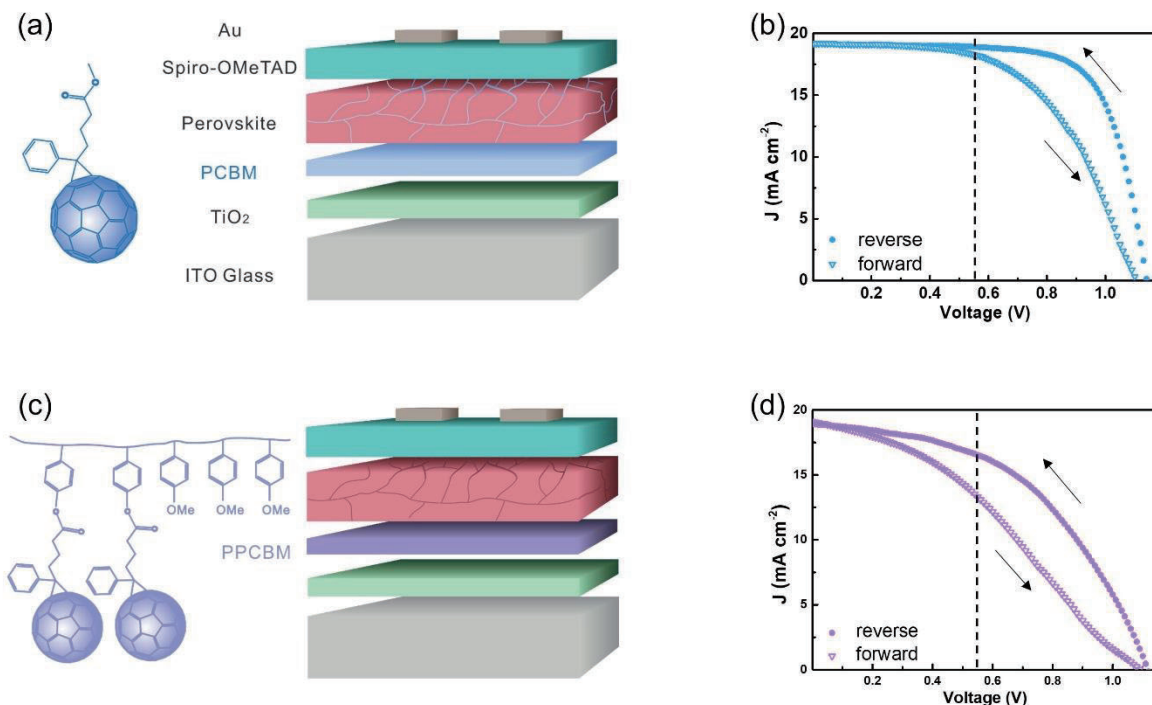


Figure 3.4: (a) PCBM structure and the PSC architecture with PCBM. (b)  $J$ - $V$  curve of the device in (a). (c) PPCBM structure and the PSC architecture with PPCBM. In PPCBM, the molar ratio of -PCBM to -C<sub>6</sub>H<sub>4</sub>OCH<sub>3</sub> is 1 to 9. (d)  $J$ - $V$  curve of the device in (c). The dashed line is to indicate the current density difference when  $V = \frac{1}{2} V_{oc}(\text{reverse})$ . The arrows represent the scan directions when measuring the  $J$ - $V$  curve.

Based on the assumption that iodine ions/vacancies migration are one of the main reasons for hysteresis, we outline the mechanism of hysteresis suppression in PSCs. PCBM molecules in the interfacial layer are able to incorporate or diffuse into the perovskite film, where they mainly locate within the grain boundaries, passivating iodine related defects. This passivation significantly hinders the ionic migration, diminishing the modulation of internal field under bias. This finding paves a way to fabricate PSCs with stable output.

## Investigating Two-Step MAPbI<sub>3</sub> Thin Film Formation during Spin Coating by Simultaneous *in situ* Absorption and Photoluminescence Spectroscopy

In order to optimize perovskite films, an *in-situ* setup was used to record the absorption and PL spectrum during the spin coating process, which is illustrated in Figure 3.5(a). Chapter 7 discusses the evolution of the optical properties when MAI solvent is spin coated on a PbI<sub>2</sub> layer.

This setup allows to record the time-dependent absorption and PL spectra with a resolution of < 0.1 second and graphically display their resolution in 2D color maps as exemplarily shown in Figure 3.5(b). Based on the spectral changes, we could identify five ranges of film formation.



In time range I, the PL spectrum shows a fast initial shift towards lower energies. In time range II, the PL shape keeps constant and the absorption showing typical MAPbI<sub>3</sub> signal is observed. In time range III, the high-energy edge of the PL shifts to lower energies and the absorption increases slightly. In time range IV, i.e. from 12.6 seconds to 14.0 seconds, the entire PL spectrum shifts from 1.63 eV to 1.60 eV, while the absorption exhibits a steep increase and then a small decrease. In time range V, no further changes are observed. By analyzing these spectral features in detail, we could explain the film formation process with the following five steps: (I) formation of a thin MAPbI<sub>3</sub> capping layer; (II) evaporation of solvent; (III) dissolution of MAPbI<sub>3</sub> capping layer; (IV) main dissolution-recrystallization process and formation of most MAPbI<sub>3</sub> crystals; (V) a temporal final stable state.

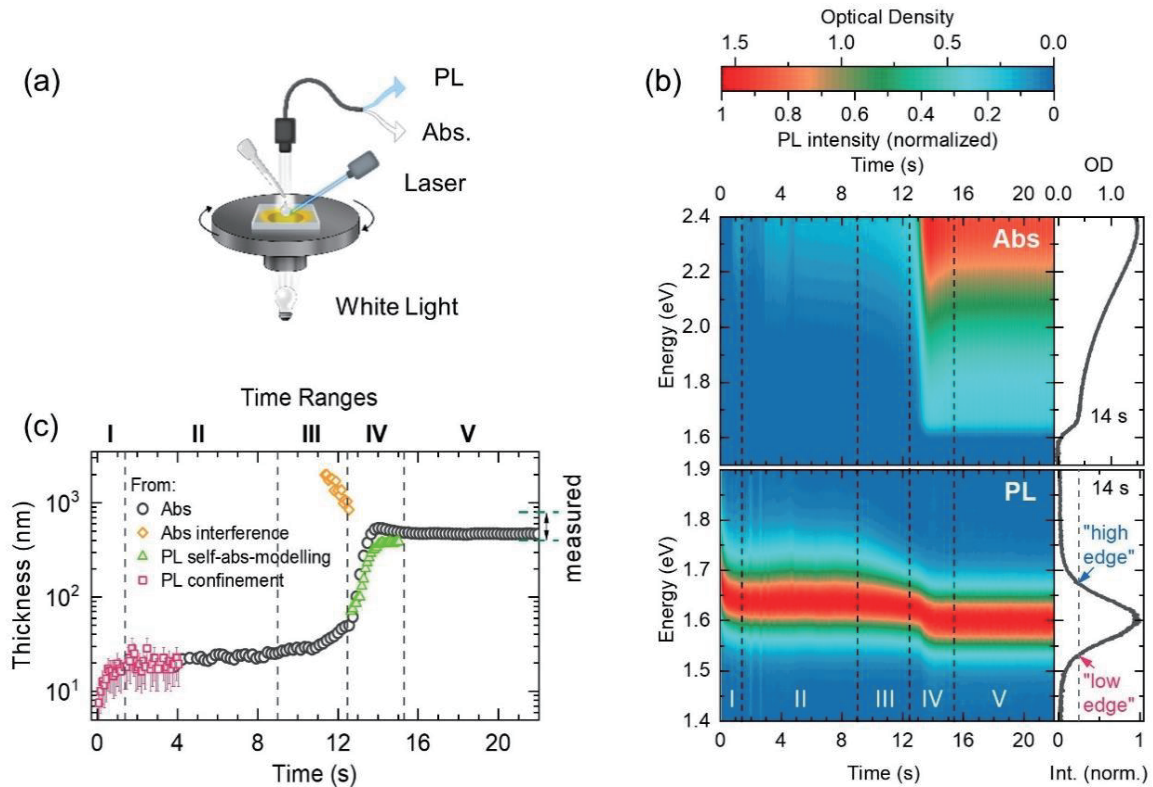


Figure 3.5: (a) Schematic of *in-situ* spectroscopy setup for spin coating method. (b) 2D absorption and PL map. Each PL spectrum is normalized to its maximum intensity. (c) The film thickness along with the spin coating time. They are derived from different spectroscopy analyses.

Furthermore, we calculated the film thickness as a function of spin-coating time based on the measured spectra shown in Figure 3.5(c). From the PL shift in time range I due to the PL confinements effect and the PL shift in time range IV originating from self-absorption, the film thickness development in these two ranges is obtained. By employing Lambert-Beer law to simulate absorption spectrum with different thicknesses and comparing them with the experimental absorption, film thickness in time range II to range V can be calculated. Also, the thickness of the entire layer is roughly estimated from the absorption interference signal observed in range III. This work provides a basis for subsequent modification of the perovskite formation process.

## Crystallization Kinetics of Controlled Solvent Vapor Assisted Annealing of Organo Lead Perovskite Film

As grain boundaries and surfaces typically possess a higher defect density compared to the bulk of the perovskite, it appears desirable to fabricate perovskite films with large grain sizes. Annealing the perovskite precursor film under some solvent vapors is a constructive way to influence the crystallization process in order to increase the grain size and crystallinity. Therefore, Chapter 8 focuses on the systematic investigation of solvent vapor assisted annealing (SVAA) of perovskite films by adjusting the vapor concentration. In this study, perovskite precursor films already prepared by a two-step spin-coating method were annealed under N<sub>2</sub> with DMF vapor for the first 30 min and then 15 min under pure N<sub>2</sub>. With a home-built setup, the DMF vapor concentration in the first 30 min could be controlled. As presented in Figure 3.6, the increase of DMF vapor concentration leads to an increase in crystal sizes, ranging from 200 nm to several micrometers.

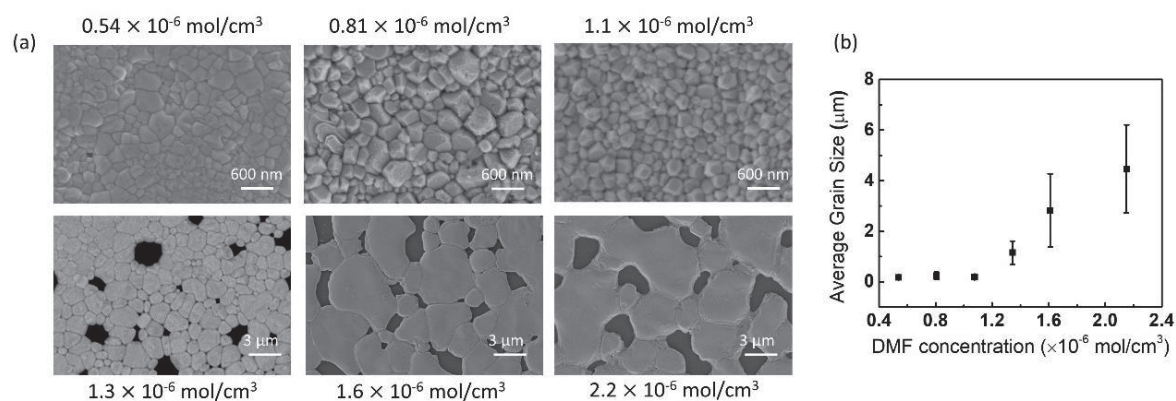


Figure 3.6: (a) SEM image of perovskite film annealed under different DMF vapor concentration. The labels represent DMF concentrations. (b) The average crystal grain sizes of perovskite film along with the DMF concentration.

To get an in-depth insight of the crystallization process, I carried out an *in-situ* grazing incidence wide-angle X-ray scattering (GIWAXS) measurement during the solvent vapor assisted annealing of an as-spun perovskite film. This measurement was with a relatively low DMF vapor concentration -  $1.0 \times 10^{-6} \text{ mol/cm}^3$ . The GIWAXS results show that an MAI-PbI<sub>2</sub>-DMF complex phase during the entire solvent assisted annealing process. This contrasts to the measurements on a precursor film that is only heat annealed (in pure N<sub>2</sub> atmosphere), which shows an MAI-PbI<sub>2</sub>-DMF complex phase only at the very beginning of annealing. During SVAA, this MAI-PbI<sub>2</sub>-DMF complex is mostly formed at the surface or grain boundary areas and it is possible to connect the nearby crystals. When DMF vapor concentration is sufficiently high, the appearance of pinholes on the final film implies that DMF vapor is able to condense on the crystal surface and dissolve small perovskite crystals. The solvent in which perovskite crystals are dissolved attaches to the undissolved large crystals and the solute grows on the crystals, which is similar to an Ostwald ripening process.

Overall, I can establish two crystallization processes during SVAA when the sample is annealed at a low concentration or a high concentration of DMF vapor. This detailed understanding will



help to precisely control the annealing process and thus the optoelectronic properties of halide perovskite films.

### 3.3 Author's Contributions

This thesis consists of five publications. Four of them have been published and one is in preparation for submission. In the following, the individual contributions of authors are specified.

#### **Chapter 4 - Emission Enhancement and Intermittency in Polycrystalline Organolead Halide Perovskite Films**

This work is published in *Molecules* (2016, 21, 8, 1081). Authors:

Cheng Li, Yu Zhong, Carlos Andres Melo Luna, Thomas Unger, Konstantin Deichsel, Anna Gräser, Jürgen Köhler, Anna Köhler, Richard Hildner and Sven Huettner

I prepared the perovskite films, performed SEM and AFM measurements and helped the manuscript organization. C. Li conducted  $J$ - $V$  curve and wide-field PL microscopy measurements, analyzed the data and wrote the manuscript. C. A. M. Luna and K. Deichsel helped the wide-field PL microscopy measurements. T. Unger carried out the PLQE and PL transient measurements. A. Gräser helped the data analysis. J. Köhler, A. Köhler and R. Hildner critically read and corrected the manuscript. S. Huettner supervised the project and corrected the manuscript.

#### **Chapter 5 - *In situ* Investigation of Light Soaking in Organolead Halide Perovskite Films**

This work is published in *APL Materials* (2019, 7, 041114). Authors:

Yu Zhong, Carlos Andres Melo Luna, Richard Hildner, Cheng Li and Sven Huettner

I fabricated perovskite solar cells, characterized their performance, conducted PL microscopy measurement, analyzed the data and wrote the manuscript. C. A. M. Luna helped the PL microscopy measurements. R. Hildner critically read and corrected the manuscript. C. Li helped the PL microscopy measurements, supervised the project and corrected the manuscript. S. Huettner supervised the project and corrected the manuscript.

#### **Chapter 6 - Role of PCBM in the Suppression of Hysteresis in Perovskite Solar Cells**

This work is published in *Advanced Functional Materials* (2020, 1908920). Authors:

Yu Zhong, Martin Hufnagel, Mukundan Thelakkat, Cheng Li and Sven Huettner

I conducted all the described experiments, data analysis and wrote the manuscript. M. Hufnagel synthesized the PCBM-grafted polymer. M. Thelakkat critically read and corrected the manuscript. C. Li and S. Huettner supervised the project and corrected the manuscript.

### **Chapter 7 - Investigating Two-Step MAPbI<sub>3</sub> Thin Film Formation during Spin Coating by Simultaneous *in situ* Absorption and Photoluminescence Spectroscopy**

This work is published in *Journal of Materials Chemistry A* (2020, 8, 5086-5094). Authors:

Mihirsinh Chauhan,<sup>‡</sup> Yu Zhong,<sup>‡</sup> Konstantin Schötz, Brijesh Tripathi, Anna Köhler, Sven Huettner and Fabian Panzer

<sup>‡</sup> Mihirsinh Chauhan and Yu Zhong contributed equally to this work.

I prepared the samples, carried out the characterizations, analyzed the absorption data in range III and helped the manuscript organization. M. Chauhan participated in *in-situ* optical measurements, conducted most part of data analysis work and helped the manuscript organization. K. Schötz analyzed the influence of self-absorption on PL. B. Tripathi, A. Köhler and S. Huettner critically read and corrected the manuscript. F. Panzer supervised the project and wrote the manuscript.

### **Chapter 8 - Crystallization Kinetics of Controlled Solvent Vapor Assisted Annealing of Organo Lead Perovskite Film**

This work is ready for submission. Authors:

Yu Zhong, Dominik Seeberger, Anna Köhler, Fabian Panzer, Cheng Li, Sven Huettner

I performed SEM, XRD and GIWAXS measurements, analyzed data and wrote the manuscript. D. Seeberger prepared perovskite films under different DMF concentrations and analyzed data. S. Huettner and I installed the solvent vapor assisted annealing setup. A. Köhler and F. Panzer critically read and corrected the manuscript. C. Li and S. Huettner helped GIWAXS measurements, supervised the project and corrected the manuscript.



# 4 Emission Enhancement and Intermittency in Polycrystalline Organolead Halide Perovskite Films

Cheng Li, Yu Zhong, Carlos Andres Melo Luna, Thomas Unger, Konstantin Deichsel, Anna Gräser, Jürgen Köhler, Anna Köhler, Richard Hildner and Sven Huettner

Published in

*Molecules*, **2016**, 21, 8, 1081

(DOI: 10.3390/molecules21081081)

## Article

# Emission Enhancement and Intermittency in Polycrystalline Organolead Halide Perovskite Films

Cheng Li <sup>1</sup>, Yu Zhong <sup>1</sup>, Carlos Andres Melo Luna <sup>2,3</sup>, Thomas Unger <sup>4</sup>, Konstantin Deichsel <sup>2</sup>, Anna Gräser <sup>1</sup>, Jürgen Köhler <sup>2</sup>, Anna Köhler <sup>4</sup>, Richard Hildner <sup>2</sup> and Sven Huettner <sup>1,\*</sup>

<sup>1</sup> Organic and Hybrid Electronics, Macromolecular Chemistry I, University of Bayreuth, Universitätsstr. 30, Bayreuth 95447, Germany; cheng.li@uni-bayreuth.de (C.L.); s2yuzhon@stmail.uni-bayreuth.de (Y.Z.); anna.graesser@uni-bayreuth.de (A.G.)

<sup>2</sup> Experimental Physics IV and Bayreuth Institute of Macromolecular Research, University of Bayreuth, Universitätsstr. 30, Bayreuth 95447, Germany; Carlos.Melo@uni-bayreuth.de (C.A.M.L.); konstantin.deichsel@gmx.de (K.D.); juergen.koehler@uni-bayreuth.de (J.K.); richard.hildner@uni-bayreuth.de (R.H.)

<sup>3</sup> Centre for Bioinformatics and Photonics—CIBioFi, Calle 13 No. 100-00, Edificio 320 No. 1069 and Departamento de Fisica, Universidad del Valle, Cali 760032, Colombia

<sup>4</sup> Experimental Physics II, University of Bayreuth, Universitätsstr. 30, Bayreuth 95447, Germany; thomas.unger@uni-bayreuth.de (T.U.); anna.koehler@uni-bayreuth.de (A.K.)

\* Correspondence: sven.huettner@uni-bayreuth.de; Tel.: +49-921-554-440

Academic Editor: Pablo Docampo

Received: 15 June 2016; Accepted: 9 August 2016; Published: 18 August 2016

**Abstract:** Inorganic-organic halide organometal perovskites have demonstrated very promising performance for opto-electronic applications, such as solar cells, light-emitting diodes, lasers, single-photon sources, etc. However, the little knowledge on the underlying photophysics, especially on a microscopic scale, hampers the further improvement of devices based on this material. In this communication, correlated conventional photoluminescence (PL) characterization and wide-field PL imaging as a function of time are employed to investigate the spatially- and temporally-resolved PL in  $\text{CH}_3\text{NH}_3\text{PbI}_{3-x}\text{Cl}_x$  perovskite films. Along with a continuous increase of the PL intensity during light soaking, we also observe PL blinking or PL intermittency behavior in individual grains of these films. Combined with significant suppression of PL blinking in perovskite films coated with a phenyl-C61-butyric acid methyl ester (PCBM) layer, it suggests that this PL intermittency is attributed to Auger recombination induced by photoionized defects/traps or mobile ions within grains. These defects/traps are detrimental for light conversion and can be effectively passivated by the PCBM layer. This finding paves the way to provide a guideline on the further improvement of perovskite opto-electronic devices.

**Keywords:** perovskite solar cells; photoluminescence; intermittency; Auger recombination; ion migration; passivation; blinking; Methylammonium Lead Halide; methylammonium lead iodide

## 1. Introduction

Together with the unprecedented development of solution-processed inorganic-organic halide organometal perovskite-based solar cells (e.g.,  $\text{CH}_3\text{NH}_3\text{PbI}_{3-x}\text{Cl}_x$  and  $\text{CH}_3\text{NH}_3\text{PbI}_3$ ), with power conversion efficiency (PCE) evolving from 3.8% [1] to 20.1% [2], the characterization of these materials has also made significant breakthroughs in the last few years [3]. A number of different methods are employed, ranging from crystallographic study [4,5], photo-physical investigation [6–8], to electrical characterization [9,10], etc. Presently, both scientific and technical interests concentrate on how to further improve PCE and decrease the energy loss during the light conversion process. However, till



now, there is still lack of a general guideline and evaluation to characterize the quality of perovskite films, especially at a microscopic scale.

Among various characterization approaches, photoluminescence (PL) measurements [6,11], in particular wide-field PL imaging [12–15], have been demonstrated to be powerful tools to reveal the underlying physics in perovskite materials, such as the distribution of defects, charge carrier lifetimes, analyzing recombination processes, etc. In general, PL characteristics of perovskite films are closely connected with its quality, in terms of the charge carrier lifetime and the recombination pathway [16]. In detail, a slow PL decay, or long carrier lifetime, is associated with less unintentional doping or defect states inside a domain, which lead to unfavorable non-radiative carrier recombination pathways [14]. Charge carrier recombination is considered as a combination of (1) trap-/defect-assisted (Shockley–Read–Hall recombination, via the sub-bandgap traps) (first order); (2) free electron-hole bimolecular (second order) and (3) Auger recombination (third order) [17,18]. Among them, radiative bimolecular recombination would be preferable as it facilitates approaching the maximum PCE, i.e., the Shockley–Queisser limit [19].

Although individual perovskite nanoparticles have been intensively studied by confocal PL microscopy [13,20,21], the knowledge on the perovskite film (i.e., ensemble of perovskite grains) [15] is still far from being fully understood. This is mainly due to the complex boundary conditions, broad distribution of particle sizes and trap sites [14]. In this communication, therefore, we apply both conventional PL characterization and the spatially-/temporally-resolved PL imaging to investigate perovskite films, revealing the possible factors hindering PCE towards the Shockley–Queisser limit.

## 2. Result and Discussion

The  $\text{CH}_3\text{NH}_3\text{PbI}_{3-x}\text{Cl}_x$  perovskite films, which are investigated in this communication, are prepared by spin-coating of a mixed halide precursor solution ( $\text{CH}_3\text{NH}_3\text{I}:\text{PbCl}_2 = (3:1)$ ) on quartz glass substrates, followed by a thermal annealing step in a nitrogen glovebox. The detailed fabrication process has been described in previous work [22]. The morphology of the film is shown in Figure 1. A uniform perovskite film is deposited on quartz substrate with only minor pinhole density due to gas release during annealing [23] (Figure 1a). We also employ atomic force microscopy (AFM) to investigate the microscopic structure of the film, shown in Figure 1b,c. It is evident that the perovskite film is comprised of densely-packed grains, which are ranging from 100 nm to 800 nm in size.

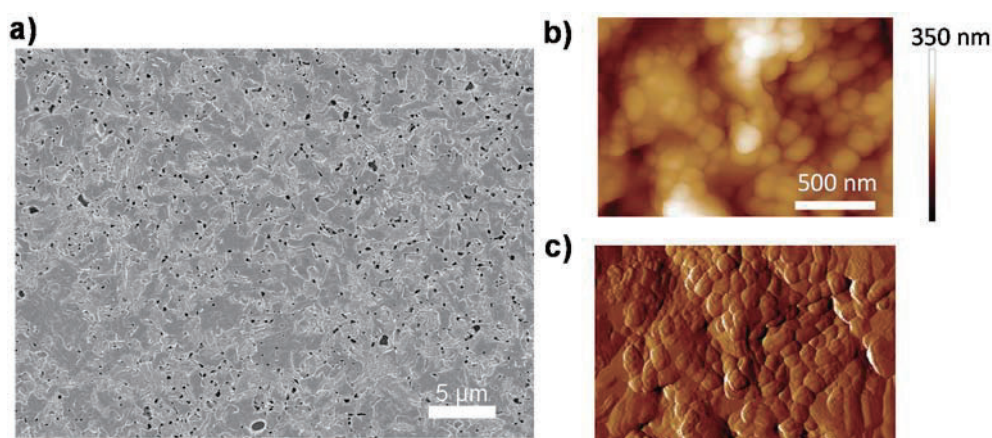


**Figure 1.** Morphology characteristics of a  $\text{CH}_3\text{NH}_3\text{PbI}_{3-x}\text{Cl}_x$  perovskite film. (a) Scanning electron microscopy (SEM) image; (b) atomic force microscopy (AFM) morphology image; and (c) AFM phase image. The color bar in (b) indicates height.

The UV-VIS optical absorption and PL spectra of  $\text{CH}_3\text{NH}_3\text{PbI}_{3-x}\text{Cl}_x$  perovskite thin film, measured with commercial spectrophotometers at room temperature are shown in the inset of Figure 2a.

The absorption edge is located at around 769 nm, which is consistent with previous other papers [24]. For the PL properties, being excited by a 532-nm laser, the emission peak is centered at around 780 nm. This small Stokes-shift (energy difference between optical absorption and emission), unlike the one in organic materials, is attributed to the small vibrational relaxation in perovskite [6]. Incorporating this perovskite film into a typical perovskite solar cell architecture (Figure S1) results in a performance as shown in Figure 2a. From the light current-voltage ( $J$ - $V$ ) curve measurement, we obtain the open circuit voltage  $V_{oc} = 1.06$  V, short circuit current  $J_{sc} = 18.9$  mA/cm<sup>2</sup> and fill factor FF = 62.3%, and, hence, the PCE is calculated as 12.5%.

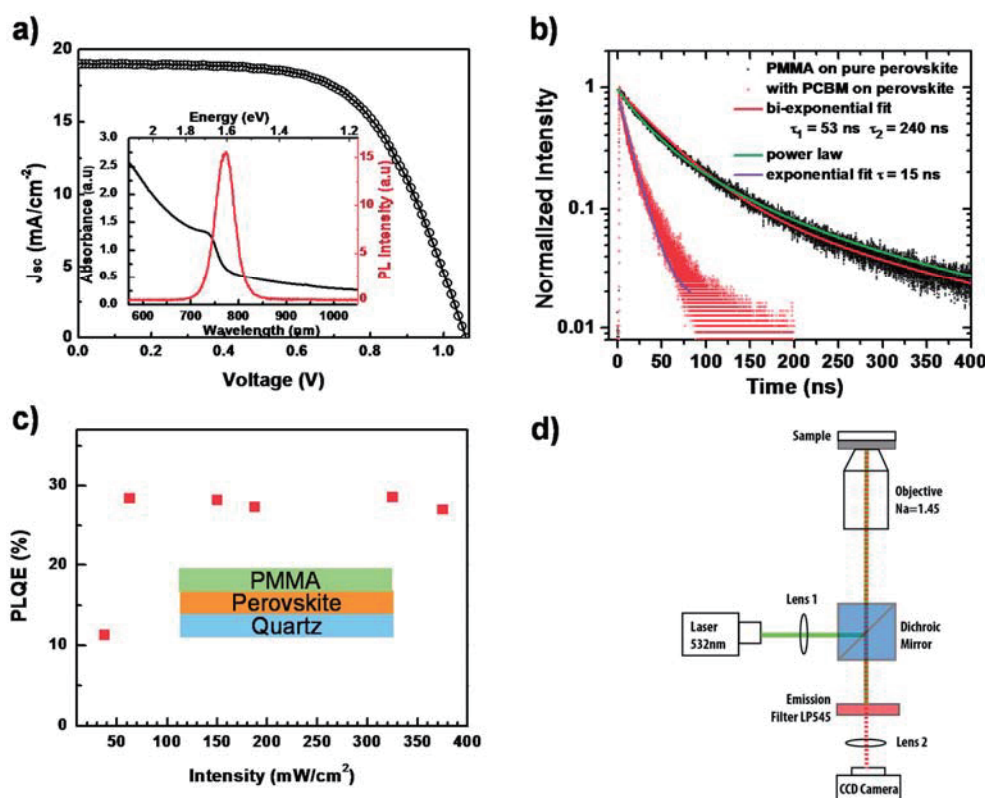


**Figure 2.** (a) Light current-voltage ( $J$ - $V$ ) curve measurement of a perovskite solar cell. The inset shows the photoluminescence (PL) and UV-VIS absorption spectra of a perovskite film; (b) Time-resolved photoluminescence measurement on a perovskite film with (red dots) and without (black dots) a PCBM quencher layer, together with fit lines; (c) Photoluminescence quantum efficiency (PLQE) of a perovskite thin film as a function of laser intensity. The inset shows the schematic of the device; (d) Schematic diagram of the PL imaging microscope.

By monitoring the PL decay after photoexcitation, we can investigate the charge carrier recombination kinetics. Figure 2b presents the normalized time-resolved PL behavior of this perovskite film under pulsed laser excitation at 485 nm, with and without a phenyl-C61-butyric acid methyl ester (PCBM) layer, respectively. The PL decay of the pure perovskite film cannot be described by a mono-exponential decay. Rather, it can be described using a power-law dependence. The best bi-exponential fit would give a dominant short decay component of about 52 ns.

Solid lines in Figure 2b represent the fits to bi-exponential decays, power-law decays and to exponential decay. For the quenched PL decay with PCBM, a diffusion model as described by Stranks et al. [6] should actually be applied. If one uses, for simplicity, an exponential fit, a decay time of 15 ns is obtained. We also carry out steady-state photoluminescence quantum efficiency (PLQE) measurements [25] on perovskite films with a PMMA layer as a function of the excitation intensity using a wavelength of 485 nm to study the recombination. As shown in Figure 2c, in the

initial low excitation intensity regime, PLQE rises with the laser intensity. We consider that this increase is associated with the possible trap-filling process, as well as the increase of exciton density as the photogenerated species [17,26]. In detail, due to the low temperature solution processing of the perovskite film, there can be various defect states within the crystallized bulk and surface, such as vacancies, interstitials, substitutions, etc. [27–29]. These defects can act as trap-assisted recombination (Shockley–Read–Hall recombination) centers, via which the free charge carriers can undergo non-radiative recombination processes [30]. These recombination centers would lead to shorter carrier life times and a lower open circuit voltage ( $V_{oc}$ ). When illuminated, these sub-bandgap traps would be filled and stabilized by photogenerated electrons/holes, reducing the non-radiative recombination probability and consequently increasing  $V_{oc}$  under light soaking [31,32]. For the higher excitation intensity, the PLQE would reach a saturated value, indicating that all traps associated with the non-radiative recombination have been filled [17,26,33]. This scenario is consistent with our experimental data. However, we note that the PLQE is still quite low, around 30%, which is supposed to approach unity according to the detailed balance model [19,34]. This implies that besides the trap-assisted recombination, there exists an additional non-radiative recombination pathway. To understand the detailed mechanism, which suppresses the further increase of PL intensity, we employ spatially- and temporally-resolved PL microscopy to investigate the perovskite film locally on the level of individual grains.

The detailed experimental setup, which is displayed in Figure 2d, has been described in a previous paper [35]. Briefly, we employed a home-built microscope, which can be operated using wide-field illumination, and a charge-coupled device (CCD) camera as detector to image the PL of large areas (diameter  $\sim 60\ \mu\text{m}$ ) of a sample. We measured typically sequences of up to 2000 PL images with exposure times as short as 50 ms per image, which allows us to follow temporal changes of the PL intensity from the perovskite film under continuous laser illumination at a wavelength of 532 nm. Here, to rule out the possible influence of environmental effects on the perovskite films, i.e., oxygen and water molecules [36,37], we spin-coated a polymethyl methacrylate (PMMA) layer with a  $\sim 200\text{-nm}$  thickness on the top of the perovskite film as the protection layer. In addition, the PMMA layer was in direct contact with the immersion oil of the microscope objective during the whole PL characterization, which further prevents oxygen from diffusing into the film.

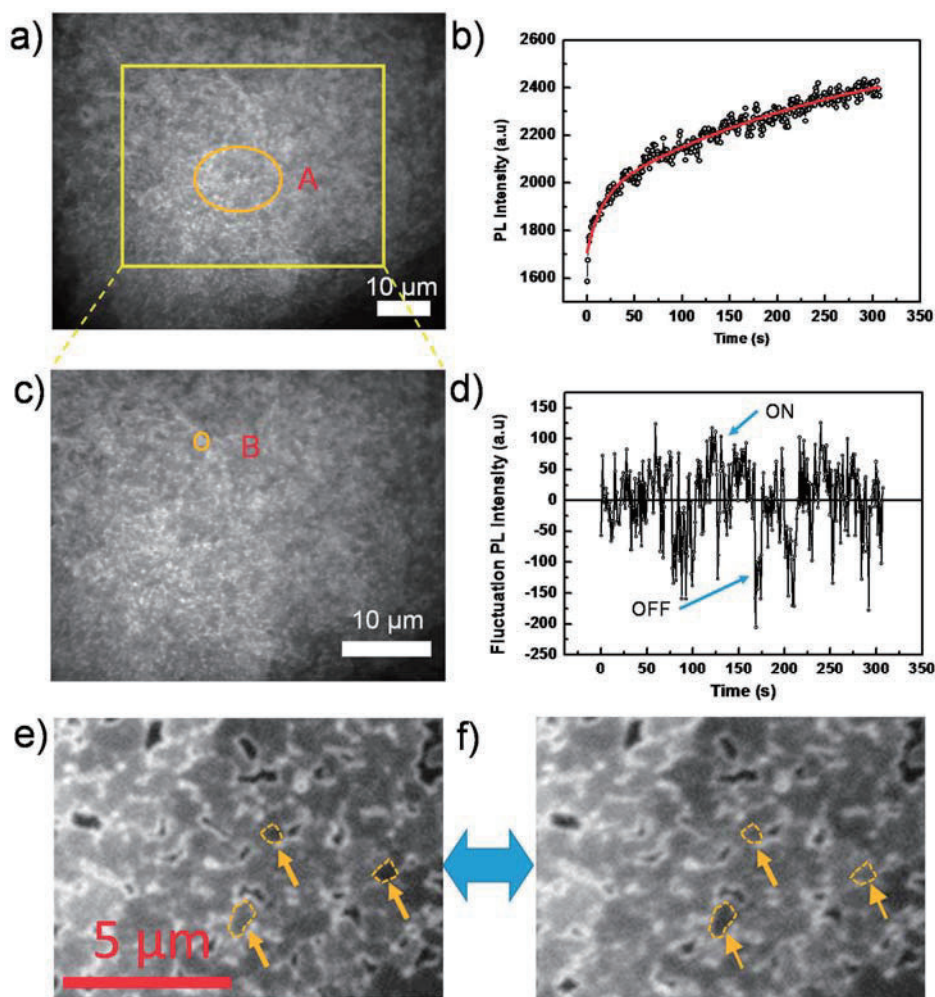
Figure 3a is an example of a wide-field PL image out of a sequence of images from a perovskite film, which agrees generally with the SEM result, showing ensembles of grains on the film and the appearance of pinholes on the surface. Note that, due to the diffraction limit, grains with a size smaller than  $\sim 300\text{ nm}$  cannot be resolved with our microscope and, thus, appear as blurred structures. However, we still observe the existence of dark crystal grain/particle boundaries. The observation of dark grain boundaries (non-radiative recombination centers) has also been observed by higher resolution confocal microscopy, as demonstrated by deQuilettes et al. [14] for example.

Figure 3b shows the PL intensity as a function of time, obtained by extracting the integrated PL of the orange circled Area A in Figure 3a from each image of the sequence. We find that the PL intensity continuously increases during the light soaking process, as shown in Figure 3b. This increase, which agrees with the previous PLQE measurement, has also been reported in other papers [17,21,38] and is attributed to trap filling processes.

Here, we note that the time dependence of the PL intensity in Area A, shown in Figure 3b, is fitted well by a bi-exponential function with time constants of  $\sim 14\text{ s}$  and  $\sim 280\text{ s}$  and prefactors of 230 and 690, respectively. Higher excitation intensities render shorter time constants, which is shown in more detail in the Supplementary Materials (Figure S2). This implies that there exist two distinct trap-filling processes, that is a quick one and a much slower one. We propose that the quick process is associated with the direct filling of defect states in the perovskite film [20]. These defects originate from the symmetry breaking of the perfect bulk crystalline structure in the vicinity of the surface or grain boundary, where well-defined facets are lacking [29]; while, for the slower one, we assume that it is ascribed to the formation and migration of defect states in the



perovskite film under light illumination. Recently, more and more studies have been carried out in this field, investigating the roles of defect formation/migration on the hysteresis and long-term (seconds to minutes) phenomena [39–41]. Hoke et al. [42] observed the presence of an iodine-rich phase in mixed halide perovskite under light irradiation. Chen et al. [43] detected the light activation and accumulation of ions by light soaking, resulting in PL quenching in the perovskite film. Yuan et al. [44] attributed the degradation of perovskite structures to the ion migration via light or external electron beam. Hentz et al. [45] also observed the formation of an iodine-rich region induced by an external electron beam.



**Figure 3.** (a) Wide-field PL image of a perovskite film taken from a sequence of 400 consecutively-recorded images with an exposure time of 50 ms, an interval time of 500 ms and an excitation intensity of 44 mW/cm<sup>2</sup>; (b) PL intensity trajectory extracted from Area A in the sequence of images in (a). The red line is the fit by an exponential function; (c) Enlarged view of the yellow square area of (a); (d) PL intensity trajectory extracted from Area B in (c) after subtraction of the exponentially increasing base line; (e,f) Individual grains in “ON” and “OFF” states, respectively, indicated by yellow arrows.

The overall continuous PL intensity enhancement, as shown in Figure 3b, is superimposed by strong PL intensity fluctuations beyond experimental noise. This behavior is reminiscent of random switching between ON (highly emissive state) and OFF (weakly emissive state) in the emission trajectory, which is known as blinking or PL intermittency [46]. The intermittency behavior is demonstrated in the Supplementary Materials (Figure S3), which shows the long-term OFF state. In addition, the video in the Supplementary Materials also clearly indicates the blinking behavior

confined within individual grains. Although the blinking behavior has been observed in perovskite nanocrystals [13,21,47], it is still not fully studied on compact films composed of the densely-packed perovskite grains [15].

To reveal the underling mechanism, we investigate individual grains, thus avoiding averaging over ensembles of grains in the film. Figure 3c displays an enlarged view of the yellow boxed area in Figure 3a, and an individual grain is highlighted by the orange circle labeled with B. As shown in Figure 3d, the PL intensity trajectory of this grain B, after subtraction of a continuous bi-exponentially-increasing baseline, shows a typical blinking behavior (see Supplementary Materials, Figure S3 for the individual grain in a shorter time scale), that is random distribution of ON/OFF states in the PL intensity trajectory. More individual grains exhibiting “ON” and “OFF” states are shown in Figure 3e,f, and the Supplementary Materials (Figure S3). Note that some ON or OFF states even last for more than 20 s, which indicates a significantly slow dynamic process.

To further investigate the detailed processes giving rise to blinking, we performed PL imaging on perovskite films coated with a PCBM layer, which acts as a PL quencher layer. Compared to the pure perovskite film, the overall PL intensity reduces significantly despite using higher excitation intensities (Figure 4a, which shows a PL image out of a sequence of images). This PCBM layer effectively separates the photogenerated charge carriers (free electron/hole or weakly bound excitons) [48], because PCBM serves as an electron acceptor and consequently quenches the radiative charge recombination (Figure S4). Figure 4b shows the integrated PL intensity of the yellow circled area in Figure 4a as a function of time, which can be well fitted by a bi-exponential function with time constants of 5.4 s and 14.6 s, respectively. This is consistent with the results displayed in Figure 2b, in which a faster (quenched) PL decay is due to the PCBM quencher layer. It is interesting to note that although the overall PL still increases as a function of time, the blinking amplitude significantly reduces below the noise level (the ratio between the fluctuation and the average emission intensity), both in the whole film and in individual grains, as shown in the inset of Figure 4b.

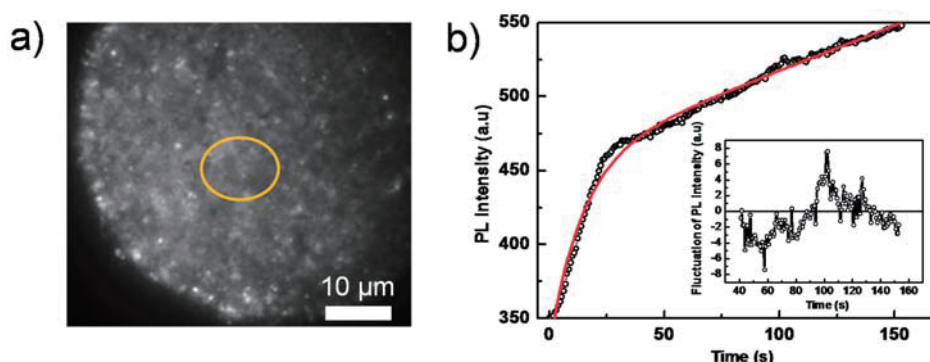


**Figure 4.** (a) Wide-field PL image of a perovskite film, covered with a PCBM quencher layer, taken from a sequence of 200 consecutively-recorded images with an exposure time of 100 ms, an interval time of 500 ms and an excitation intensity of 280 mW/cm<sup>2</sup>; (b) PL intensity trajectory extracted from the yellow circled area in the sequence of images in (a). The red line is the fitting line by a bi-exponential function. The inset shows the relative fluctuations of the PL intensity after subtraction of the bi-exponential fit function.

Based on the previous results, combining both the conventional PL characterization and wide field PL imaging, we can reveal the underlying physics in the enhancement and quenching of the PL. Though there are several models to interpret the blinking behavior [46,49,50], the presence of OFF states in perovskite film/nanoparticles is commonly attributed to additional charges due to charge trapping process [15,20,21]. When there is no charge trapped in perovskite grains, shown in Figure 5a, the dominant decay process is bi-molecular recombination (for medium carrier densities) [17], which is radiative during the recombination process, denoted as the “ON” state. In contrast, when

photogenerated charges are trapped in the grain, either by surface or bulk defect states, the ionized surrounding enhances Auger recombination [15,51]. This recombination involves a recombination of an electron and a hole, followed by a process of energy transfer to a third carrier instead of photon emission, as shown in Figure 5b. This process is non-radiative and therefore renders the grains dark in PL imaging, denoted as the “OFF” state. When these trapped charges release, the PL emission recovers to the “ON” state. This Auger recombination statistically reduces the PL intensity in the whole film, resulting in the loss in  $V_{oc}$  and PCE [52,53].

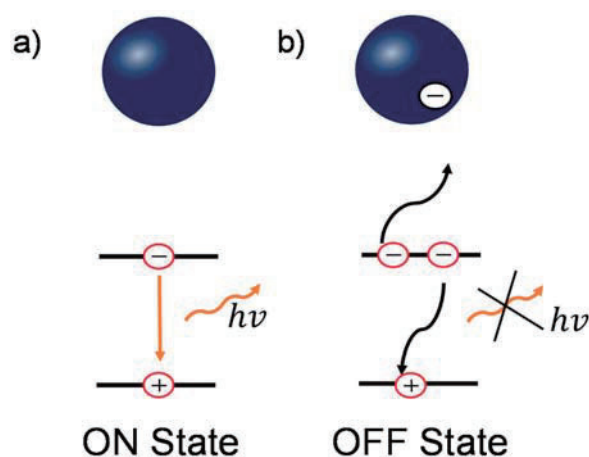


**Figure 5.** Schematic diagrams of the relationship between the charged grains and blinking behavior in perovskite. (a) In the uncharged states, the dominant recombination pathway is bi-molecular recombination; (b) In the charged states, the non-radiative three-carrier Auger recombination plays an important role. Blue ball represents an individual perovskite grain.

Note that the long durations of more than 20 s of “ON” and “OFF” states are similar to the slow response in electrical transient behavior, such as hysteresis and light-induced degradation [15,44]. This implies that it can be associated with the same mechanism, i.e., ion migration. These ions can be driven by the external electrical field and consequently accumulate, enhancing the Auger recombination locally [15]. In addition, these ions are also able to migrate between grains within the film [15,41].

When the perovskite film is covered with a PCBM quencher layer, the PL blinking is significantly suppressed (insets in Figure 4b). This is ascribed to two possible reasons: First, PCBM has been demonstrated to be a good candidate to passivate traps in perovskites, leading to a charge de-trapping process [54]. In addition, the insertion of PCBM suppresses the ionic migration among the grains of perovskite, leading to a further reduction of PL blinking [55]. Second, the Auger recombination is proportional to the third power of charge carrier density  $n^3$  [16]. Owing to the effective charge transfer process at the perovskite/PCBM interface, the negative charge carrier density ( $n_e$ ) inside the perovskite significantly decreases, giving rise to the decrease of the Auger recombination contribution.

### 3. Experimental Methods

$\text{CH}_3\text{NH}_3\text{I}$  (MAI) was purchased from Tokyo Chemical Industry (TCI Deutschland GmbH, Eschborn, Germany), and all other chemicals were purchased from Sigma-Aldrich and used as received.

#### 3.1. Perovskite Film Fabrication for PL Experiment

Glass substrates were washed and cleaned with acetone and isopropanol for 10 min each in ultrasonic baths. Then, these glass substrates were treated within an ozone chamber for approximately 10 min. Following that, in a nitrogen glovebox (both water and oxygen less than 10 ppm), the perovskite precursor, i.e., MAI and  $\text{PbCl}_2$  (3:1) in anhydrous *N,N*-dimethylformamide (DMF), was spin-coated



on glass substrates at 3000 rpm for 60 s. Then, these as-spun films were annealed at 100 °C in the nitrogen atmosphere for 60 min. Subsequently, 20 mg/mL phenyl-C61-butyric acid methyl ester (PCBM) dissolved in chlorobenzene were coated on the film at 2000 rpm for 30 s as a quencher layer. In the end, 40 mg/mL poly(methyl methacrylate) (PMMA) dissolved in butyl acetate (anhydrous, 99%) was spin-coated on the perovskite film at 2000 rpm for 60 s acting as a protection layer.

### 3.2. Conventional PL Characterization

#### 3.2.1. PLQE Measurements

Photoluminescence quantum yield (PLQE) was taken using an integrating sphere and a laser diode at a 485-nm wavelength (PicoQuant GmbH, Berlin, Germany). The spectra are spectrally corrected for grating, charge-coupled device (CCD) and fiber efficiencies.

#### 3.2.2. Time-Correlated Single Photon Counting

PL transients are measured with a time-correlated single photon counting (TCSPC) setup (FluoTime 200, PicoQuant GmbH). The excitation source was a pulsed laser diode with a 485-nm wavelength with 2- to 10-MHz repetition rate and a pulse duration of about 140 ps.

### 3.3. PL Imaging Setup

The setup used for PL imaging of perovskite films is based on a home-built confocal microscope. The excitation source was a pulsed diode laser (LDH-P-FA-530L, 20-MHz repetition rate, 70-ps pulse duration, PicoQuant GmbH). This laser beam was spatially filtered and directed to the microscope equipped with an infinity-corrected high-numerical-aperture oil-immersion objective (Plan Apo, 60×, numerical aperture 1.45; Olympus, Japan). The perovskite film was placed in the focal plane of the objective, and the sample position was controlled by a piezo-stage (Tritor 102 SG, piezosystem Jena GmbH, Jena, Germany). In order to homogeneously illuminate a large area (diameter ~60 μm) of the films, we additionally inserted a wide-field lens in the excitation beam path that focuses the laser light into the back-focal plane of the objective.

The PL signal was collected by the same objective, passed a long-pass filter (LP545, AHF analysentechnik AG, Tübingen, Germany) to suppress residual laser light and was imaged onto a CCD camera (Orca-ER, Hamamatsu, Japan) by an objective lens. We have done an estimation on the noise level of the PL intensity measurement as follows. The laser power stability is better than 3% (r.m.s.); to be conservative, we use 3% in the following, i.e.,  $s_{\text{Laser}} = 0.03$ . The CCD's dark current amounts to 0.03 electrons per pixel per second, i.e., with the used exposure times of <100 ms, this dark current is <0.003 electron per pixel per exposure. As will be clear from the numbers calculated below, this dark current is negligible and will not be considered further. The readout noise of the CCD-camera is 8 electrons (r.m.s.). The measured and displayed signals are given in AD counts (i.e., after signal amplification and AD conversion). The resulting conversion factor is 4.6 electrons per AD count according to the manufacturer. Finally, the created electrons have to be converted into detected photons to estimate the photon shot noise contributing to the signal. In the emission range of the samples around 800 nm, the quantum efficiency of the CCD amounts to 30%. For the data shown in Figure 3b,d, we estimate the noise level in the high signal regime starting at around 100 s. Here, the average signal is 2200 AD counts, corresponding to 10,120 electrons or 33,700 photons. For the readout noise, we then obtain  $s_{\text{CCD}} = 0.0008$ . From the number of detected photons, the shot noise is  $s_{\text{Shot}} = 0.005$ . Hence, in total, the noise level is  $s = \sqrt{s_{\text{Laser}}^2 + s_{\text{CCD}}^2 + s_{\text{Shot}}^2} = 0.03$ , which translates into 67 AD counts. Comparing this noise level to the observed signal fluctuations of about ±150 AD counts in Figure 3d, it is clear that these fluctuations cannot arise from noise. For the data shown in Figure 4, the situation is slightly different: using the displayed AD counts of around 500 in the high signal regime starting around 80 s, we obtain a noise level of 16 AD counts following the same

procedure as above. Hence, in the presence of the PCBM quencher layer, the observed fluctuations are largely determined by the noise level in these experiments.

#### 4. Conclusions

In summary, by employing the conventional PL and wide-field PL image characterization, we have observed the enhancement and fluorescence intermittency (PL blinking) in a mixed halide perovskite film. We attribute the PL enhancement to the trap-filling process. In the meantime, we suggest the PL blinking behavior to the enhanced Auger non-radiative recombination due to the additional charges within the grain. These charges possibly originate from the photogenerated charge carriers trapped by defects or the mobile ionized defects (e.g., iodide ions or iodide vacancies). This photoionized process results in the PL blinking, hindering the approach towards the Shockley–Queisser limit. Therefore, this finding provides unique insight to a guideline on how to further improve the PCE of perovskite solar cells.

**Supplementary Materials:** Supplementary materials can be accessed at: <http://www.mdpi.com/1420-3049/21/8/1081/s1>.

**Acknowledgments:** Financial support by the Bavarian State Ministry of Science, Research and the Arts for the Collaborative Research Network “Solar Technologies go Hybrid” and Federal Ministry of Education and Research BMBF (03SF0484C) are gratefully acknowledged. Richard Hildner, Jürgen Köhler, Anna Köhler, Thomas Unger and Carlos Andres Melo Luna acknowledge additional funding from the German Research Foundation DFG (GRK1640 and HI1508/2). Carlos Andres Melo Luna acknowledges funding from the Colombian Department of Science, Technology and Innovation (Colciencias, Project 71003).

**Author Contributions:** Cheng Li, Yu Zhong, Richard Hildner and Sven Huettner initiated and designed the study. Cheng Li, Yu Zhong, Carlos Andres Melo Luna, Thomas Unger, Konstantin Deichsel and Anna Gräser carried out the experiments and analyzed the data. Cheng Li, Yu Zhong, Carlos Andres Melo Luna, Konstantin Deichsel and Anna Gräser carried out the PL imaging measurements under supervision of Jürgen Köhler and Richard Hildner; Thomas Unger carried out the PL related experiments under supervision of Anna Köhler; Cheng Li, Yu Zhong and Anna Gräser prepared and fabricated devices. Cheng Li, Thomas Unger, Richard Hildner and Sven Huettner prepared the manuscript. All authors discussed, revised and approved the manuscript.

**Conflicts of Interest:** The authors declare no conflict of interest.

#### References

1. Kojima, A.; Teshima, K.; Shirai, Y.; Miyasaka, T. Organometal Halide Perovskites as Visible-Light Sensitizers for Photovoltaic Cells. *J. Am. Chem. Soc.* **2009**, *131*, 6050–6051. [[CrossRef](#)] [[PubMed](#)]
2. Yang, W.S.; Noh, J.H.; Jeon, N.J.; Kim, Y.C.; Ryu, S.; Seo, J.; Seok, S.I. High-performance photovoltaic perovskite layers fabricated through intramolecular exchange. *Science* **2015**, *348*, 1234–1237. [[CrossRef](#)] [[PubMed](#)]
3. Stranks, S.D.; Snaith, H.J. Metal-halide perovskites for photovoltaic and light-emitting devices. *Nat. Nanotechnol.* **2015**, *10*, 391–402. [[CrossRef](#)] [[PubMed](#)]
4. Song, T.-B.; Chen, Q.; Zhou, H.; Luo, S.; Yang, Y.; You, J.; Yang, Y. Unraveling film transformations and device performance of planar perovskite solar cells. *Nano Energy* **2015**, *12*, 494–500. [[CrossRef](#)]
5. Chen, Q.; Zhou, H.; Hong, Z.; Luo, S.; Duan, H.-S.; Wang, H.-H.; Liu, Y.; Li, G.; Yang, Y. Planar Heterojunction Perovskite Solar Cells via Vapor-Assisted Solution Process. *J. Am. Chem. Soc.* **2014**, *136*, 622–625. [[CrossRef](#)] [[PubMed](#)]
6. Stranks, S.D.; Eperon, G.E.; Grancini, G.; Menelaou, C.; Alcocer, M.J.P.; Leijtens, T.; Herz, L.M.; Petrozza, A.; Snaith, H.J. Electron-hole diffusion lengths exceeding 1 micrometer in an organometal Trihalide Perovskite absorber. *Science* **2013**, *342*, 341–344. [[CrossRef](#)] [[PubMed](#)]
7. Grancini, G.; Srimath Kandada, A.R.; Frost, J.M.; Barker, A.J.; de Bastiani, M.; Gandini, M.; Marras, S.; Lanzani, G.; Walsh, A.; Petrozza, A. Role of microstructure in the electron–hole interaction of hybrid lead halide perovskites. *Nat. Photonics* **2015**, *9*, 695–701. [[CrossRef](#)] [[PubMed](#)]
8. Fang, H.-H.; Raissa, R.; Abdu-Aguye, M.; Adjokatse, S.; Blake, G.R.; Even, J.; Loi, M.A. Photophysics of Organic–Inorganic Hybrid Lead Iodide Perovskite Single Crystals. *Adv. Funct. Mater.* **2015**, *25*, 2378–2385. [[CrossRef](#)]

9. Almora, O.; Zarazua, I.; Mas-Marza, E.; Mora-Sero, I.; Bisquert, J.; Garcia-Belmonte, G. Capacitive Dark Currents, Hysteresis, and Electrode Polarization in Lead Halide Perovskite Solar Cells. *J. Phys. Chem. Lett.* **2015**, *6*, 1645–1652. [[CrossRef](#)] [[PubMed](#)]
10. Sanchez, R.S.; Gonzalez-Pedro, V.; Lee, J.-W.; Park, N.-G.; Kang, Y.S.; Mora-Sero, I.; Bisquert, J. Slow Dynamic Processes in Lead Halide Perovskite Solar Cells. Characteristic Times and Hysteresis. *J. Phys. Chem. Lett.* **2014**, *5*, 2357–2363. [[CrossRef](#)] [[PubMed](#)]
11. Xing, G.; Mathews, N.; Sun, S.; Lim, S.S.; Lam, Y.M.; Grätzel, M.; Mhaisalkar, S.; Sum, T.C. Long-range balanced electron- and hole-transport lengths in organic-inorganic  $\text{CH}_3\text{NH}_3\text{PbI}_3$ . *Science* **2013**, *342*, 344–347. [[CrossRef](#)] [[PubMed](#)]
12. Hameiri, Z.; Mahboubi Soufiani, A.; Juhl, M.K.; Jiang, L.; Huang, F.; Cheng, Y.-B.; Kampwerth, H.; Weber, J.W.; Green, M.A.; Trupke, T. Photoluminescence and electroluminescence imaging of perovskite solar cells. *Prog. Photovolt. Res. Appl.* **2015**, *23*, 1697–1705. [[CrossRef](#)]
13. Swarnkar, A.; Chulliyil, R.; Ravi, V.K.; Irfanullah, M.; Chowdhury, A.; Nag, A. Colloidal  $\text{CsPbBr}_3$  perovskite nanocrystals: Luminescence beyond traditional quantum dots. *Angew. Chem. Int. Ed.* **2015**, *54*, 15424–15428. [[CrossRef](#)] [[PubMed](#)]
14. Dane, W.D.; Vorpahl, S.M.; Stranks, S.D.; Nagaoka, H.; Eperon, G.E.; Ziffer, M.E.; Snaith, H.J.; Ginger, D.S. Impact of microstructure on local carrier lifetime in perovskite solar cells. *Science* **2015**, *348*, 683–686.
15. Wen, X.; Ho-Baillie, A.; Huang, S.; Sheng, R.; Chen, S.; Ko, H.-C.; Green, M.A. Mobile Charge-Induced Fluorescence Intermittency in Methylammonium Lead Bromide Perovskite. *Nano Lett.* **2015**, *15*, 4644–4649. [[CrossRef](#)] [[PubMed](#)]
16. Herz, L.M. Charge-Carrier Dynamics in Organic-Inorganic Metal Halide Perovskites. *Annu. Rev. Phys. Chem.* **2015**, *67*. [[CrossRef](#)] [[PubMed](#)]
17. Stranks, S.D.; Burlakov, V.M.; Leijtens, T.; Ball, J.M.; Goriely, A.; Snaith, H.J. Recombination Kinetics in Organic-Inorganic Perovskites: Excitons, Free Charge, and Subgap States. *Phys. Rev. Appl.* **2014**, *2*. [[CrossRef](#)]
18. Yamada, Y.; Nakamura, T.; Endo, M.; Wakamiya, A.; Kanemitsu, Y. Photocarrier Recombination Dynamics in Perovskite  $\text{CH}_3\text{NH}_3\text{PbI}_3$  for Solar Cell Applications. *J. Am. Chem. Soc.* **2014**, *136*, 11610–11613. [[CrossRef](#)] [[PubMed](#)]
19. Miller, O.D.; Yablonovitch, E.; Kurtz, S.R. Intense internal and external fluorescence as solar cell approach the SQ efficiency limit. *IEEE J. Photovolt.* **2012**, *2*, 303–311. [[CrossRef](#)]
20. Tachikawa, T.; Karimata, I.; Kobori, Y. Surface charge trapping in organolead halide perovskites explored by single-particle photoluminescence imaging. *J. Phys. Chem. Lett.* **2015**, *6*, 3195–3201. [[CrossRef](#)]
21. Tian, Y.; Merdasa, A.; Peter, M.; Abdellah, M.; Zheng, K.; Ponseca, C.S.; Pullerits, T.; Yartsev, A.; Sundström, V.; Scheblykin, I.G. Giant photoluminescence blinking of perovskite nanocrystals reveals single-trap control of luminescence. *Nano Lett.* **2015**, *15*, 1603–1608. [[CrossRef](#)] [[PubMed](#)]
22. Li, C.; Tscheuschner, S.; Paulus, F.; Hopkinson, P.E.; Kießling, J.; Köhler, A.; Vaynzof, Y.; Huettnner, S. Iodine Migration and its Effect on Hysteresis in Perovskite Solar Cells. *Adv. Mater.* **2016**, *28*, 2446–2454. [[CrossRef](#)] [[PubMed](#)]
23. Yu, H.; Wang, F.; Xie, F.; Li, W.; Chen, J.; Zhao, N. The Role of Chlorine in the Formation Process of “ $\text{CH}_3\text{NH}_3\text{PbI}_{3-x}\text{Cl}_x$ ” Perovskite. *Adv. Funct. Mater.* **2014**, *24*, 7102–7108. [[CrossRef](#)]
24. Tan, Z.-K.; Moghaddam, R.S.; Lai, M.L.; Docampo, P.; Higler, R.; Deschler, F.; Price, M.; Sadhanala, A.; Pazos, L.M.; Credgington, D.; et al. Bright light-emitting diodes based on organometal halide perovskite. *Nat. Nanotechnol.* **2014**, *9*, 687–692. [[CrossRef](#)] [[PubMed](#)]
25. De Mello, J.C.; Wittmann, H.F.; Friend, R.H. An improved experimental determination of external photoluminescence quantum efficiency. *Adv. Mater.* **1997**, *9*, 230–232. [[CrossRef](#)]
26. Deschler, F.; Price, M.; Pathak, S.; Klintberg, L.E.; Jarausch, D.-D.; Higler, R.; Hüttner, S.; Leijtens, T.; Stranks, S.D.; Snaith, H.J.; et al. High Photoluminescence Efficiency and Optically Pumped Lasing in Solution-Processed Mixed Halide Perovskite Semiconductors. *J. Phys. Chem. Lett.* **2014**, *5*, 1421–1426. [[CrossRef](#)] [[PubMed](#)]
27. Yin, W.-J.; Shi, T.; Yan, Y. Unusual defect physics in  $\text{CH}_3\text{NH}_3\text{PbI}_3$  perovskite solar cell absorber. *Appl. Phys. Lett.* **2014**, *104*. [[CrossRef](#)]
28. Baumann, A.; Vöth, S.; Rieder, P.; Heiber, M.C.; Tvingstedt, K.; Dyakonov, V. Identification of Trap States in Perovskite Solar Cells. *J. Phys. Chem. Lett.* **2015**, *6*, 2350–2354. [[CrossRef](#)] [[PubMed](#)]

29. Wu, X.; Trinh, M.T.; Niesner, D.; Zhu, H.; Norman, Z.; Owen, J.S.; Yaffe, O.; Kudisch, B.J.; Zhu, X.-Y. Trap states in lead iodide perovskites. *J. Am. Chem. Soc.* **2015**, *137*, 2089–2096. [[CrossRef](#)] [[PubMed](#)]
30. Wetzelaer, G.-J.A.H.; Scheepers, M.; Sempere, A.M.; Momblona, C.; Ávila, J.; Bolink, H.J. Trap-Assisted Non-Radiative Recombination in Organic–Inorganic Perovskite Solar Cells. *Adv. Mater.* **2015**, *27*, 1837–1841. [[CrossRef](#)] [[PubMed](#)]
31. Zhao, C.; Chen, B.; Qiao, X.; Luan, L.; Lu, K.; Hu, B. Revealing Underlying Processes Involved in Light Soaking Effects and Hysteresis Phenomena in Perovskite Solar Cells. *Adv. Energy Mater.* **2015**, *5*. [[CrossRef](#)]
32. Deng, Y.; Xiao, Z.; Huang, J. Light-Induced Self-Poling Effect on Organometal Trihalide Perovskite Solar Cells for Increased Device Efficiency and Stability. *Adv. Energy Mater.* **2015**, *5*, 1500721. [[CrossRef](#)]
33. Noel, N.K.; Abate, A.; Stranks, S.D.; Parrott, E.S.; Burlakov, V.M.; Goriely, A.; Snaith, H.J. Enhanced Photoluminescence and Solar Cell Performance via Lewis Base Passivation of Organic–Inorganic Lead Halide Perovskites. *ACS Nano* **2014**, *8*, 9815–9821. [[CrossRef](#)] [[PubMed](#)]
34. Shockley, W.; Queisser, H.J. Detailed Balance Limit of Efficiency of p-n Junction Solar Cells. *J. Appl. Phys.* **1961**, *32*, 510–519. [[CrossRef](#)]
35. Haedler, A.T.; Kreger, K.; Issac, A.; Wittmann, B.; Kivala, M.; Hammer, N.; Kohler, J.; Schmidt, H.-W.; Hildner, R. Long-range energy transport in single supramolecular nanofibres at room temperature. *Nature* **2015**, *523*, 196–199. [[CrossRef](#)] [[PubMed](#)]
36. Tian, Y.; Peter, M.; Unger, E.; Abdellah, M.; Zheng, K.; Pullerits, T.; Yartsev, A.; Sundstrom, V.; Scheblykin, I.G. Mechanistic insights into perovskite photoluminescence enhancement: light curing with oxygen can boost yield thousandfold. *Phys. Chem. Chem. Phys.* **2015**, *17*, 24978–24987. [[CrossRef](#)] [[PubMed](#)]
37. Galisteo-López, J.F.; Anaya, M.; Calvo, M.E.; Míguez, H. Environmental Effects on the Photophysics of Organic–Inorganic Halide Perovskites. *J. Phys. Chem. Lett.* **2015**, *6*, 2200–2205. [[CrossRef](#)] [[PubMed](#)]
38. Tian, Y.; Merdasa, A.; Unger, E.; Abdellah, M.; Zheng, K.; McKibbin, S.; Mikkelsen, A.; Pullerits, T.; Yartsev, A.; Sundström, V.; et al. Enhanced Organo-Metal Halide Perovskite Photoluminescence from Nanosized Defect-Free Crystallites and Emitting Sites. *J. Phys. Chem. Lett.* **2015**, *6*, 4171–4177. [[CrossRef](#)] [[PubMed](#)]
39. Azpiroz, J.M.; Mosconi, E.; Bisquert, J.; de Angelis, F. Defect migration in methylammonium lead iodide and its role in perovskite solar cell operation. *Energy Environ. Sci.* **2015**, *8*, 2118–2127. [[CrossRef](#)]
40. Zhang, Y.; Liu, M.; Eperon, G.E.; Leijtens, T.C.; McMeekin, D.; Saliba, M.; Zhang, W.; de Bastiani, M.; Petrozza, A.; Herz, L.M.; et al. Charge selective contacts, mobile ions and anomalous hysteresis in organic-inorganic perovskite solar cells. *Mater. Horiz.* **2015**, *2*, 315–322. [[CrossRef](#)]
41. Yuan, Y.; Huang, J. Ion migration in organometal trihalide perovskite and its impact on photovoltaic efficiency and stability. *Acc. Chem. Res.* **2016**, *49*, 286–293. [[CrossRef](#)] [[PubMed](#)]
42. Hoke, E.T.; Slotcavage, D.J.; Dohner, E.R.; Bowring, A.R.; Karunadasa, H.I.; McGehee, M.D. Reversible photo-induced trap formation in mixed-halide hybrid perovskites for photovoltaics. *Chem. Sci.* **2015**, *6*, 613–617. [[CrossRef](#)]
43. Chen, S.; Wen, X.; Sheng, R.; Huang, S.; Deng, X.; Green, M.A.; Ho-Baillie, A. Mobile ion induced slow carrier dynamics in organic–inorganic perovskite CH<sub>3</sub>NH<sub>3</sub>PbBr<sub>3</sub>. *ACS Appl. Mater. Interfaces* **2016**, *8*, 5351–5357. [[CrossRef](#)] [[PubMed](#)]
44. Yuan, H.; Debroye, E.; Janssen, K.; Naiki, H.; Steuwe, C.; Lu, G.; Moris, M.; Orgiu, E.; Uji-i, H.; de Schryver, F.; et al. Degradation of methylammonium lead iodide perovskite structures through light and electron beam driven ion migration. *J. Phys. Chem. Lett.* **2016**, *7*, 561–566. [[CrossRef](#)] [[PubMed](#)]
45. Hentz, O.; Zhao, Z.; Gradečak, S. Impacts of Ion Segregation on Local Optical Properties in Mixed Halide Perovskite Films. *Nano Lett.* **2016**, *16*, 1485–1490. [[CrossRef](#)] [[PubMed](#)]
46. Frantsuzov, P.; Kuno, M.; Janko, B.; Marcus, R.A. Universal emission intermittency in quantum dots, nanorods and nanowires. *Nat. Phys.* **2008**, *4*, 519–522. [[CrossRef](#)]
47. Park, Y.-S.; Guo, S.; Makarov, N.S.; Klimov, V.I. Room temperature single-photon emission from individual perovskite quantum dots. *ACS Nano* **2015**, *9*, 10386–10393. [[CrossRef](#)] [[PubMed](#)]
48. D’Innocenzo, V.; Grancini, G.; Alcocer, M.J.P.; Kandada, A.R.S.; Stranks, S.D.; Lee, M.M.; Lanzani, G.; Snaith, H.J.; Petrozza, A. Excitons versus free charges in organo-lead tri-halide perovskites. *Nat. Commun.* **2014**, *5*. [[CrossRef](#)] [[PubMed](#)]
49. Galland, C.; Ghosh, Y.; Steinbruck, A.; Sykora, M.; Hollingsworth, J.A.; Klimov, V.I.; Htoon, H. Two types of luminescence blinking revealed by spectroelectrochemistry of single quantum dots. *Nature* **2011**, *479*, 203–207. [[CrossRef](#)] [[PubMed](#)]

50. Anger, P.; Bharadwaj, P.; Novotny, L. Enhancement and Quenching of Single-Molecule Fluorescence. *Phys. Rev. Lett.* **2006**, *96*. [[CrossRef](#)] [[PubMed](#)]
51. Efros, A.L.; Rosen, M. Random telegraph signal in the photoluminescence intensity of a single quantum dot. *Phys. Rev. Lett.* **1997**, *78*, 1110–1113. [[CrossRef](#)]
52. Tvingstedt, K.; Malinkiewicz, O.; Baumann, A.; Deibel, C.; Snaith, H.J.; Dyakonov, V.; Bolink, H.J. Radiative efficiency of lead iodide based perovskite solar cells. *Sci. Rep.* **2014**, *4*. [[CrossRef](#)] [[PubMed](#)]
53. Tress, W.; Marinova, N.; Inganäs, O.; Nazeeruddin, M.K.; Zakeeruddin, S.M.; Graetzel, M. Predicting the open-circuit voltage of  $\text{CH}_3\text{NH}_3\text{PbI}_3$  perovskite solar cells using electroluminescence and photovoltaic quantum efficiency spectra: the role of radiative and non-radiative recombination. *Adv. Energy Mater.* **2015**, *5*. [[CrossRef](#)]
54. Shao, Y.; Xiao, Z.; Bi, C.; Yuan, Y.; Huang, J. Origin and elimination of photocurrent hysteresis by fullerene passivation in  $\text{CH}_3\text{NH}_3\text{PbI}_3$  planar heterojunction solar cells. *Nat. Commun.* **2014**, *5*. [[CrossRef](#)] [[PubMed](#)]
55. Xu, J.; Buin, A.; Ip, A.H.; Li, W.; Voznyy, O.; Comin, R.; Yuan, M.; Jeon, S.; Ning, Z.; McDowell, J.J.; et al. Perovskite-fullerene hybrid materials suppress hysteresis in planar diodes. *Nat. Commun.* **2015**, *6*. [[CrossRef](#)] [[PubMed](#)]

**Sample Availability:** Samples of the perovskite films are available from the authors on request.



© 2016 by the authors; licensee MDPI, Basel, Switzerland. This article is an open access article distributed under the terms and conditions of the Creative Commons Attribution (CC-BY) license (<http://creativecommons.org/licenses/by/4.0/>).

## **Supplementary Materials**

# **Emission Enhancement and Intermittency in Polycrystalline Organolead Halide Perovskite Films**

Cheng Li, Yu Zhong, Carlos Andres Melo Luna, Thomas Unger, Konstantin  
Deichsel, Anna Gräser, Jürgen Köhler, Anna Köhler, Richard Hildner and  
Sven Huettnner



## 1. Device Structure

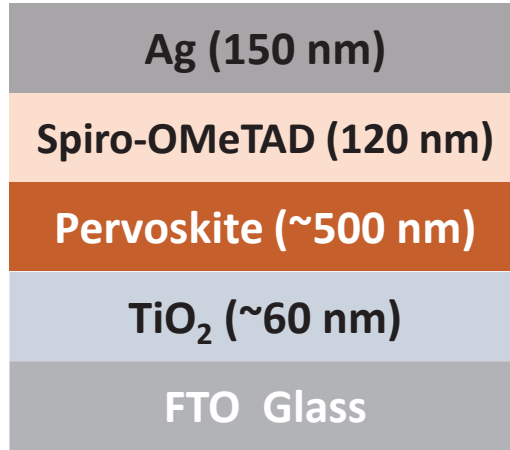


**Figure S1:** The schematic diagram of a typical perovskite solar cell.

## 2. Evolution of Photoluminescence at Different Excitation Intensities

A pure perovskite film on glass (like in Figure 3) was measured under low ( $44 \text{ mW/cm}^2$ , Figure S2a,c) and higher excitation intensity ( $280 \text{ mW/cm}^2$ ; Figure S2b,d). Both curves were fitted by a bi-exponential function, showing a much faster increase process with time constants of 4 s and 120 s at the higher excitation intensity.

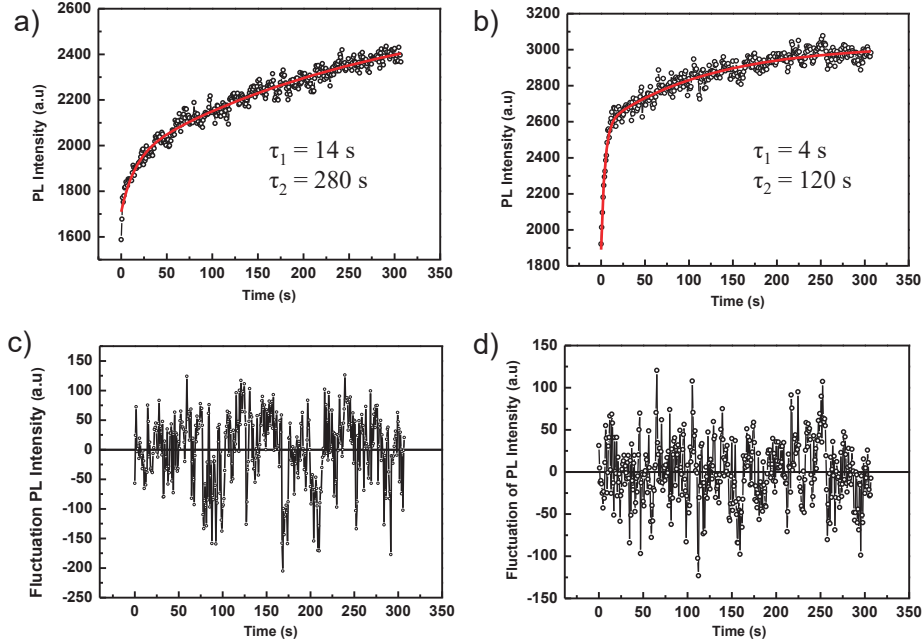


**Figure S2:** Comparison of PL intensity trajectory extracted from the same device in the sequence of images with excitation intensities of (a)  $44 \text{ mW/cm}^2$  and (b)  $280 \text{ mW/cm}^2$ , respectively. The red lines are the corresponding bi-exponential fits; (c,d) are the fluctuation of the PL intensity under excitation intensities of  $44 \text{ mW/cm}^2$  and  $280 \text{ mW/cm}^2$ , respectively.

### 3. Blinking in Detail

A video file is available for download, showing the PL intermittency in the pristine  $\text{CH}_3\text{NH}_3\text{PbI}_{3-x}\text{Cl}_x$  perovskite film (excitation intensity  $44 \text{ mW/cm}^2$ ). The sequence is played 1.4x faster than real time. The diameter of the illumination spot is  $\sim 60 \mu\text{m}$ .

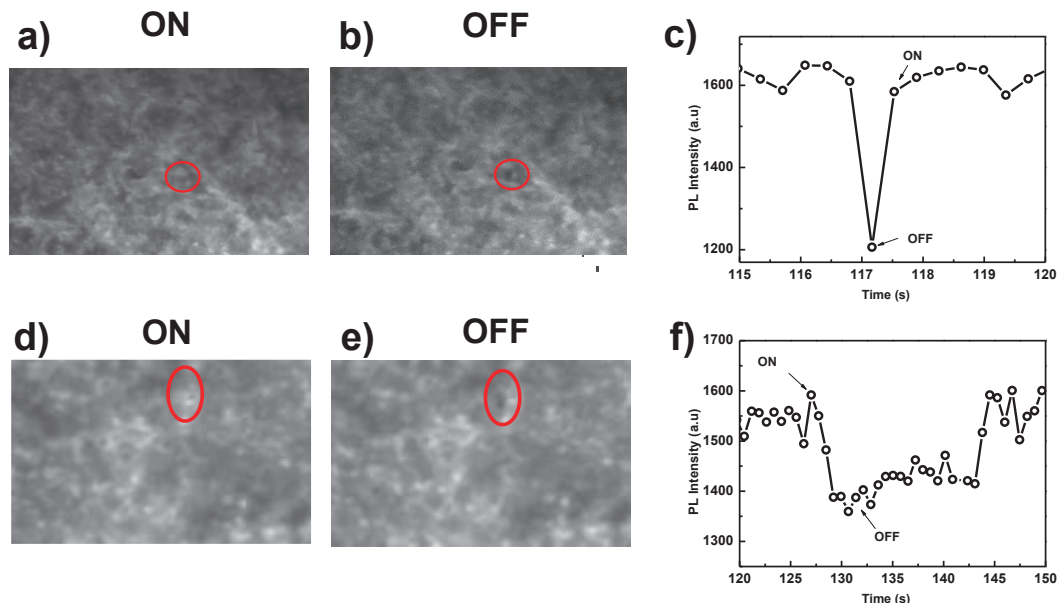


**Figure S3:** Different grains with PL blinking behaviors. (a) to (c) are one single grain with short OFF states; (d) to (f) are one single grain with longer OFF states.

### 4. Photoluminescence Quantum Efficiency

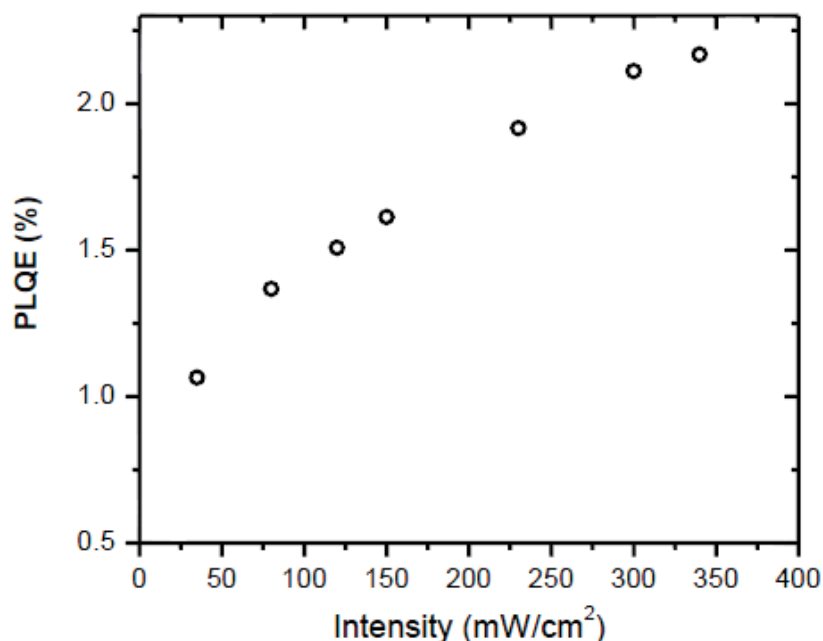


**Figure S4:** PLQE measurement of the perovskite/PCBM device, which exhibits PL quenching compared to the one without the PCBM quencher layer.

# **5** *In situ* Investigation of Light Soaking in Organolead Halide Perovskite Films

Yu Zhong, Carlos Andres Melo Luna, Richard Hildner, Cheng Li and Sven

Huettner

Published in

*APL Materials*, **2019**, 7, 041114

(DOI: 10.1063/1.5086125)

# In situ investigation of light soaking in organolead halide perovskite films

Cite as: APL Mater. 7, 041114 (2019); doi: 10.1063/1.5086125

Submitted: 18 December 2018 • Accepted: 13 March 2019 •

Published Online: 16 April 2019



Yu Zhong,<sup>1</sup> Carlos Andres Melo Luna,<sup>2,3</sup> Richard Hildner,<sup>2,a)</sup> Cheng Li,<sup>1,b),c)</sup> and Sven Huettner<sup>1,b)</sup>

## AFFILIATIONS

<sup>1</sup>Department of Chemistry, University of Bayreuth, Bayreuth 95447, Germany

<sup>2</sup>Spectroscopy of Soft Matter and Bayreuth Institute of Macromolecular Research, University of Bayreuth, Bayreuth 95447, Germany

<sup>3</sup>Centre for Bioinformatics and Photonics—CIBioFi, Universidad del Valle, 760032 Cali, Colombia

**Note:** This paper is part of the special topic on Perovskite Semiconductors for Next Generation Optoelectronic Applications.

**a)Current address:** Zernike Institute for Advanced Materials, University of Groningen, 9747 AG Groningen, The Netherlands.

**b)Authors to whom correspondence should be addressed:** [cheng.li@uni-bayreuth.de](mailto:cheng.li@uni-bayreuth.de) and [sven.huettner@uni-bayreuth.de](mailto:sven.huettner@uni-bayreuth.de)

**c)Current address:** School of Electronic Science and Engineering, Xiamen University, Xiamen, 361005, China.

## ABSTRACT

Organolead halide perovskite solar cells (PSCs) have generated extensive attention recently with power conversion efficiency (PCE) exceeding 23%. However, these PSCs exhibit photoinduced instability in the course of their current-voltage measurements. In this work, we study the light-induced behavior in  $\text{CH}_3\text{NH}_3\text{PbI}_{3-x}\text{Cl}_x$  films *in situ*, by employing wide-field photoluminescence (PL) microscopy to obtain both the spatially and temporally resolved PL images simultaneously. Along with the increase in the PL intensity under continuous illumination, some areas render PL inactive. By characterizing the excitation energy dependent long-time PL decay behavior, we suggest that the PL quenching can be ascribed to a localized accumulation of iodide ions driven by the optical field. This ion localization leads to an enhancement of non-radiative recombination. The appearance of the PL inactive areas in the perovskite film impedes its photovoltaic device performance approaching the theoretical maximum PCE. Therefore, the herein presented real-time investigation of the light soaking of perovskite films is a versatile and adaptable method providing more details to improve the performance of PSCs.

© 2019 Author(s). All article content, except where otherwise noted, is licensed under a Creative Commons Attribution (CC BY) license (<http://creativecommons.org/licenses/by/4.0/>). <https://doi.org/10.1063/1.5086125>

Organolead halide perovskites [e.g.,  $\text{CH}_3\text{NH}_3\text{PbX}_3$  ( $X = \text{I}, \text{Cl}, \text{Br}$ )] have received intensive attention since 2012,<sup>1,2</sup> as they offer a new class of photovoltaic materials for low-cost and high-efficiency solar cells. Experiments toward a better understanding of their properties and fabrication processes have extensively been carried out, ranging from fundamental studies to device applications and long-term stability tests.<sup>3–5</sup> To minimize the degradation of the perovskite materials, scientists have made improvements on film quality and device stability, by controlling crystalline grain growth,<sup>6,7</sup> developing quasi-2D structures,<sup>8,9</sup> or incorporating different cations.<sup>10,11</sup> However, the detailed mechanism on optical/electrical induced degradation is still not fully elucidated.

Photoluminescence (PL), i.e., the radiative recombination process after optical excitation, has been demonstrated to give a strong correlation with film quality and device performance. The PL decay can demonstrate the charge carrier life time,<sup>12,13</sup> the spatial

distribution of defect density, and the charge carrier recombination.<sup>14,15</sup> For instance, in the vicinity of perovskite grain boundaries, more defects are prevalent, resulting in non-radiative decay and a lower PL intensity.<sup>16</sup> Any non-radiative recombination would impair the carrier density buildup, preventing the photovoltaic device from approaching the theoretical Shockley-Queisser efficiency limit, i.e., the maximum theoretically achievable power conversion efficiency (PCE).<sup>17</sup>

The light soaking behavior of perovskite films is crucial for long-term stability of devices. It is reported that within light-soaking, the performance of perovskite solar cells (PSCs) improves.<sup>18,19</sup> However, under long-time illumination, perovskite films may also undergo at first reversible transformation<sup>20,21</sup> and then irreversible degradation.<sup>22,23</sup> These reversible transformations can be attributed to the formation of light-activated trap states<sup>20</sup> or photo-induced halide ion segregation.<sup>21</sup> In this work, we focus on the reversible

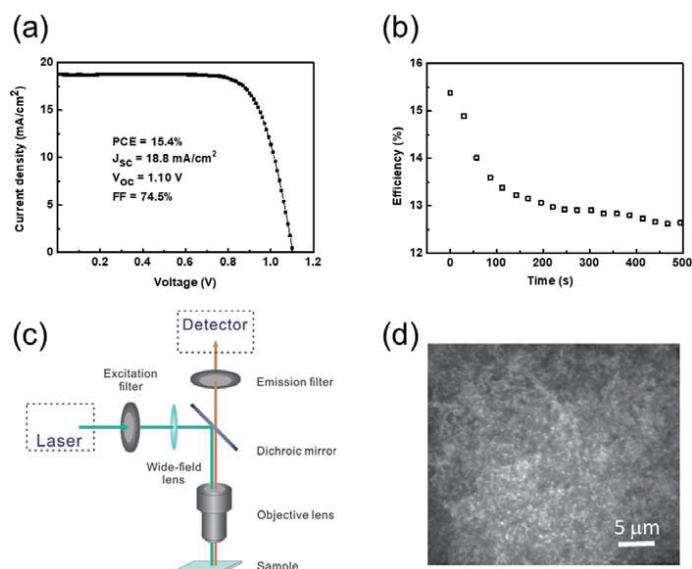


**FIG. 1.** (a)  $J$ - $V$  curve of a PSC with the structure FTO/compact  $\text{TiO}_2/\text{CH}_3\text{NH}_3\text{PbI}_{3-x}\text{Cl}_x/\text{Spiro-OMeTAD}/\text{Au}$ . (b) The PCE decay of a planar PSC under continuous illumination (AM 1.5G) in nitrogen atmosphere with the scan rate of 0.8 V/s. (c) Schematic diagram of a wide-field PL microscope. (d) Wide-field PL image of a perovskite film using an exposure time of 50 ms and an excitation intensity of 40  $\text{mW}/\text{cm}^2$  at 532 nm wavelength.

changes in perovskite films. With a temporally and spatially resolved PL imaging method,<sup>24</sup> the presence of PL inactive areas on a micrometer scale was detected during light soaking, which should result from halide ion accumulation. By varying the laser intensity, the PL decay dynamics were studied.

Planar PSCs based on  $\text{CH}_3\text{NH}_3\text{PbI}_{3-x}\text{Cl}_x$  were fabricated, with the highest PCE of 15.4% [current density-voltage ( $J$ - $V$ ) curve shown in Fig. 1(a)]. The device structure of these PSCs is shown in Fig. S3 of the supplementary material. We characterized the time dependent PCE of a solar cell device under continuous illumination (standard AM 1.5G illumination of 100  $\text{mW}/\text{cm}^2$ ) in nitrogen atmosphere. It was scanned from positive voltage to negative, noted as reverse scan. The PCE decreases to 12.6% within 500 s, as shown in Fig. 1(b). For comparison, we measured the PCE of a PSC without continuous illumination and the PCE showed a slight decrease. Already after 30 s of continuous light soaking, the PCE yielded a clear reduction for the herein used material system [illustrated in Fig. S5(a) of the supplementary material]. This suggests that this PCE decay is ascribed to the constant illumination rather than the electrical scanning. On the other hand, this light-induced PCE decay can be recovered in dark, as demonstrated in Fig. S5(b) of the supplementary material.

A thorough  $J$ - $V$  characterization is presented in Fig. S4 of the supplementary material. With different scan rates and scan directions, the performance of a PSC varies. This is the hysteresis behavior discussed in many papers.<sup>25–28</sup> The relationship between the hysteresis and ion migration has been comprehensively reported.<sup>26,28</sup> Our PSC yields a distinct hysteresis behavior, which reveals that ion migration exists in this perovskite material. With continuous illumination, the hysteresis behavior of the PSC decreases (shown in Fig. S4-2 of the supplementary material). The PCE in forward scan increases (from negative voltage to positive) and in reverse scan decreases. It indicates the halide ion redistribution in perovskite.

The changes in short circuit current density ( $J_{sc}$ ), open circuit voltage ( $V_{oc}$ ), and fill factor (FF) under illumination are shown in Fig. S3 of the supplementary material. There is an obvious reduction of  $V_{oc}$ , while  $J_{sc}$  keeps nearly constant. For comparison, as shown in Fig. S5(a) of the supplementary material, a distinct  $V_{oc}$  decays with 30 s of illumination. In most cases, one dominant reason of the deterioration of a solar cell  $V_{oc}$  is the poor external luminescence efficiency.<sup>15</sup> The lower external luminescence reveals that some photons are wasted in nonradiative recombination or parasitic optical absorption.<sup>17,29</sup> For a working PSC, the decrease in external luminescence can result from the accumulation of ions on the interface.<sup>30</sup> Our measurements indicate that besides the bias-driven ion effect, the illumination is another factor of luminescence decay. Tracking the long-time PL behavior with a wide-field PL microscope is a good way to locally study the carrier recombination in perovskite films. Thus, we employed this method to investigate the light-induced long-term decay effect. The detailed description of this technique has been reported elsewhere.<sup>31,32</sup> Briefly, a wide field PL microscope equipped with an oil-immersion objective with a 100 $\times$  magnification, a 532 nm laser for excitation, and a fast charge-coupled device (CCD) camera was employed to track the time dependent fluorescence as shown in Fig. 1(c). Note that the perovskite films were covered with polymethyl methacrylate (PMMA) to be protected from ambient air.<sup>33</sup> To illuminate a large area (diameter  $\sim 60\ \mu\text{m}$ ) of the film homogeneously, we additionally inserted a wide-field lens in the excitation beam path. Rather than small areas characterized by classical confocal microscopy,<sup>34</sup> this allows us to characterize the temporal and spatial evolutions of the PL intensity in a larger area with time-resolution as short as 50 ms and a spatial resolution of about 300 nm. Figure 1(d) shows a PL image of a  $\text{CH}_3\text{NH}_3\text{PbI}_{3-x}\text{Cl}_x$  perovskite film. It displays densely packed grains with a few pinholes, which is consistent with the image taken by a scanning electron

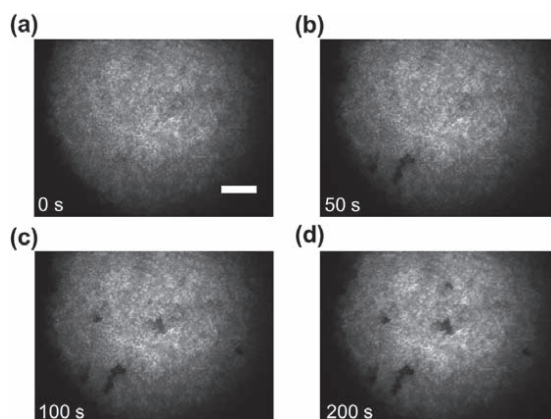


**FIG. 2.** [(a)–(d)] Temporal evolution of a PL image on the surface of perovskite under light illumination of 40 mW/cm<sup>2</sup> at 532 nm wavelength. The scale bar is 10 μm, and the integration time is 50 ms. The corresponding video is shown in S10 of the [supplementary material](#).

microscope (SEM) (Fig. S6-1 of the [supplementary material](#)). Due to the limited resolution of optical microscopy, grains with size smaller than 300 nm cannot be distinguished anymore. Correlated SEM and PL images at one spot are presented in Fig. S6-2 of the [supplementary material](#) and we can observe the PL emission from each crystal grain. Additionally, the morphology of this perovskite film is similar to the perovskite film spin coated on the TiO<sub>2</sub> layer (Fig. S6-3 of the [supplementary material](#)). Thus,

it is acceptable to use this perovskite film in order to study the light-soaking behavior.

Figure 2 shows a series of PL images of the perovskite surface under continuous light illumination (532 nm, 40 mW/cm<sup>2</sup>). Beside a PL intensity increase of the whole film, certain dark regions are observed. The first PL dark region, which is in the left bottom part of the image [see Fig. 2(b)], appeared within 10 s. This indicates that charge carrier recombination in these areas transforms from radiative to non-radiative. With longer illumination time, the number of dark areas increases. The overall PL evolution is shown in the [supplementary material](#), S10 Video. This phenomenon is described as the appearance of PL inactive areas or PL quenching in this work. We analyze the temporal PL intensity of one PL inactive area and find that the PL intensity yields an enhancement within the first 45 s and then it decreases, as illustrated in Fig. 3(a). Except for the PL inactive areas, the PL intensity of the other part increases, as shown in Fig. 3(b). This PL increase of the perovskite film under illumination has been reported,<sup>35,36,32</sup> arising from traps filled,<sup>37</sup> or defect annihilation during light illumination.<sup>38,39</sup>

The phenomenon that the PL intensity of the perovskite film decreases after a PL enhancement has been discussed recently. Gottesman *et al.* observed that the PL of a CH<sub>3</sub>NH<sub>3</sub>PbI<sub>3</sub> film gradually decreased by ~40% under 1 h illumination.<sup>40</sup> Juan *et al.* found a PL decrease following a PL enhancement of the bulk perovskite film both in air and in nitrogen.<sup>41</sup> The  $V_{oc}$  of PSCs is related to the PL intensity because the PL lowering indicates that the generation of trap states reduces the quasi-Fermi-level for the electrons<sup>42</sup> and consequently leads to a decrease in the  $V_{oc}$ .<sup>18,19</sup> In Fig. S3(c) of the [supplementary material](#), the  $V_{oc}$  of a PSC shows an obvious decrease within the first 100 s and resembles the time when the PL dark areas show up.

In order to elucidate the origin of this PL quenching phenomenon, first, we need to assess whether it is caused by chemical

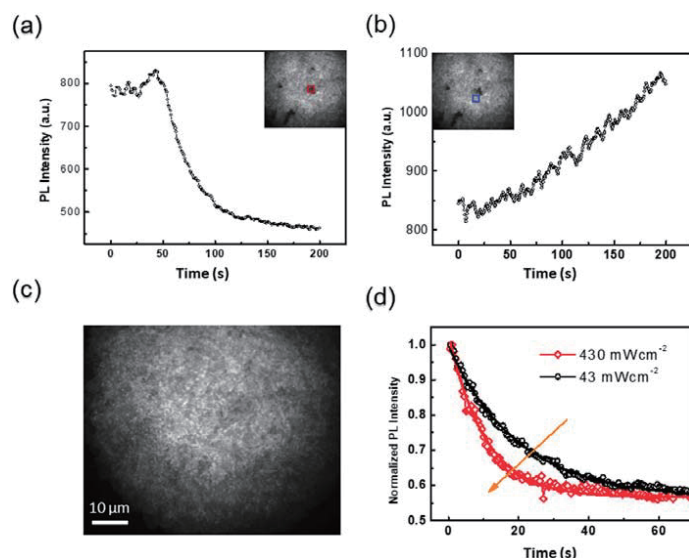


**FIG. 3.** [(a) and (b)] The average PL intensity of two local regions in the series of PL images in Fig. 2 as a function of time. The two insets in (a) and (b) demonstrate the location of these two regions. The time dependent PL intensity of the two rectangle areas was displayed. (c) The PL image of the perovskite film, which was observed in Fig. 2, was kept in dark after continuous illumination and was measured again here after its recovery. (d) Normalized temporal evolution of a PL intensity quenching area under continuous illumination of different intensities. The red and black solid lines are the fitting lines based on single exponential functions. The decay time is estimated 15.1 s and 29.4 s for illumination intensity 430 mW/cm<sup>2</sup> and 43 mW/cm<sup>2</sup>, respectively.



degradation of perovskite. After laser illumination, the perovskite film was kept in dark for several minutes and its PL image was obtained in Fig. 3(c). We found that the PL inactive or PL quenching areas in the film reverted to their PL active state, i.e., showing radiative recombination again. This indicates that this process is reversible, originating from ionic movement,<sup>32,20</sup> reversible structural transformation,<sup>40,43</sup> or surface charge trapping/detrapping<sup>44,45</sup> rather than an irreversible chemical degradation, e.g., long-term decomposition of perovskite<sup>46,22</sup> or gas release of  $\text{CH}_3\text{NH}_3\text{I}$  after long-term electrical biasing.<sup>47,48</sup> Furthermore, it seems not to originate from the reversible perovskite hydration process. When perovskite hydrates form, the PL intensity at boundaries tends to increase as shown in Fig. S9 of the [supplementary material](#). The reason is that perovskite hydrates first form at the grain interfaces and these hydrates will impede carrier transport along different grains.<sup>49,50</sup> As a result, the recombination at the grain interfaces is enhanced.<sup>49</sup> This is different from the results observed in Fig. 2.

To investigate the mechanism of the PL quenching, the temporal evolution of the PL signal on individual grains under different illumination intensities is studied. As shown in Fig. 3(a), the PL intensity in the dark areas decays under continuous light soaking. Taking into account three individual domains observed under different excitation intensities, we obtain that the long-term decay time is  $25 \pm 9$  s for  $43 \text{ mW/cm}^2$  and  $13 \pm 6$  s for  $430 \text{ mW/cm}^2$ , following single exponential functions. The PL intensity of these grains decays faster under high illumination ( $430 \text{ mW/cm}^2$ ) intensity than under low intensity ( $43 \text{ mW/cm}^2$ ), consistent with the observation by Chen *et al.*<sup>34</sup> The time scale of the PL decay is  $\sim 10$  s, which is in the same time scale of halide ion migration in the perovskite film.<sup>26,34,51</sup> Meanwhile, our J-V measurements on PSCs yield hysteric behavior, suggesting the possible halide ion (i.e., vacancy) migration. We can therefore associate this PL quenching behavior with the migration and accumulation of ions.

Several studies have proved the halide ion migration in the organolead perovskite film. By combination of time-of-flight secondary-ion-mass spectrometry (ToF-SIMS) and PL microscopy, deQuilettes *et al.* detected the iodide element signal through a depth profile at the illuminated region and showed the iodide redistribution with the optical field.<sup>38</sup> In addition, the results of scanning Kelvin probe microscopy (SKPM) demonstrated a surface potential shift of the perovskite layer under illumination,<sup>52–54</sup> which can drive the mobile ions. The activation energy of the iodide migration in the perovskite polycrystalline thin film has been estimated between  $\sim 0.1$  eV and  $\sim 0.6$  eV.<sup>51,55,56</sup> Xing *et al.*<sup>57</sup> found the reduction of the activation energy of mobile ions under illumination. Very recently, Li *et al.* pointed out the role of iodide vacancies as the main

migrating species respective to iodide ions.<sup>58</sup> Therefore, we reiterate that the light-induced electrical field in the film can promote the iodide ions/vacancies to migrate.

We propose that the origin of the PL inactive areas in Fig. 2 is the redistribution and localization of halide ions. Both Hoke *et al.*<sup>59</sup> and Yoon *et al.*<sup>21</sup> also successfully tracked the formation of I-rich and Br-rich domains in  $\text{MAPb}(\text{Br}_x\text{I}_{1-x})_3$  films, which is induced from the halide ion movement under illumination. As reported, halide ions in perovskites possess a relatively low activation energy, compared to other ions.<sup>56</sup> Therefore, with light-soaking, halide ions tend to migrate more readily in the perovskite film and localize at grain boundaries or some defective grains. That may happen, when halide ions are immobilized at grains with a high defect density potentially allowing the formation of further interstitial defects that render non-radiative recombination centers.<sup>60,61</sup> Another possibility is the segregation of halide ions at grain boundaries.<sup>62</sup> In these segregated domains, the recombination changes from radiative to non-radiative.

As briefly mentioned above, interstitial defects indeed may play a significant role in quenched photoluminescence, creating deep trap states and acting as non-radiative recombination centers.<sup>20,63</sup> It is worth mentioning that calculations attribute, among native point defects, only iodine interstitials to form deep carrier traps and non-radiative recombination centers, whereas all vacancies, cation interstitials, and some antisite defects create only shallow levels.<sup>60,61</sup> The origin of point defects shall be found in Frenkel defects, forming a vacancy and an interstitial, which have been reported to be abundant in MAPi films.<sup>64</sup> The much higher diffusion constant of vacancies compared to interstitials leaves behind interstitials as non-radiative recombination centers.<sup>65,60,66</sup> In a similar context, it has been reported that a bias voltage is applied on a perovskite film with laterally configured electrodes, facilitating an increasingly PL quenched region starting from the positive electrode. This is a consequence of iodide vacancies migrating towards the negative electrode,<sup>32,34</sup> changing the effective electron-hole concentration<sup>58</sup> and leaving a larger number of interstitials behind acting as non-radiative quenching sites.

We found that two main factors for the appearance of these PL inactive areas are the optical intensity gradient of the light source and the film quality. Another PL microscope with a white light-emitting diode (LED) was used to observe this light-soaking effect. In the center of the illuminated area, few PL dark areas were detected. Most PL dark areas are present at the edge of the exposed area (shown in Fig. 4). This is exactly correlated with the light source beam profile as shown in Fig. S8(b) of the [supplementary material](#) with a strong intensity gradient right at the edge of the illuminated

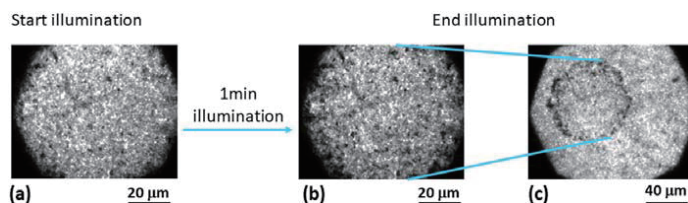


**FIG. 4.** Perovskite film was observed at the beginning (a) and the end [(b) and (c)] of illumination. The light source is a white LED with a short pass filter of 440 nm. Its beam profile is displayed in Fig. S8(b) of the [supplementary material](#). The difference between (b) and (c) is that a different object lens was used. Only the region in (b) was under illumination and the other regions were in dark. The guideline means that the region between the guidelines in (c) is the same region in (b).

area. It reveals that the horizontal optical intensity gradient is crucial for driving mobile ions and ion-aggregated PL quenching behavior. We also notice that an old film shows more PL inactive areas than a fresh film. It is ascribed to the degradation of perovskite and more defects or mobile ions in the old film. Thus, the film quality and the presence of surface defects is an important factor. To check this, we employed this experiment on a perovskite film with PCBM molecules, which have been shown to passivate surface/grain boundary defects.<sup>67,68</sup> This passivated perovskite film exhibits little difference in PL images before and after illumination, even at high excitation intensities and gradients [as displayed in Figs. S7(e)–S7(j) of the [supplementary material](#)]. It needs to be noted that not only the passivated defects in perovskite films but also the weakened light-induced field by PCBM contributes to this phenomenon.

By combining the above analysis, the proposed mechanism of PL quenching phenomenon is illustrated in Fig. 5. Before illumination, the iodide ions are uniformly distributed in the perovskite film, as shown in Fig. 5(a). Under illumination, the optical field decreases with penetration depth and is laterally limited by

its spot size, giving rise to gradients in the diffusion constants of ion field both vertically and horizontally, which redistributes iodide ions. During the migration process, regions with higher density of defects can result in the localization of ions.<sup>61,69,70</sup> Different effects can lead to non-radiative recombination: Charge accumulation at surface and grain boundaries enhance Auger-type non-radiative recombination, which is predominantly seen in nanoparticles.<sup>69</sup> Iodide interstitials, in particular, have been pointed out to create deep level defects, resulting in non-radiative recombination centers.<sup>61</sup> Also, the change in the effective hole concentration towards more intrinsic may reduce the PL quantum yield.<sup>58</sup> Given the fact that the herein observed effects are rather inhomogeneously distributed and become stronger with lower quality of films, the assumption is that the creation of defect sites (i.e., interstitials) is caused by the local sample inhomogeneities and the accumulation of iodide ions at defective grains as illustrated in Fig. 5(c). The migration pathway can be through the iodine interstitial sites.<sup>71</sup> When the illumination intensity increases, the activation energy of halide ions decreases,<sup>57,72</sup> leading to a faster migration and hence an enhanced possible trapping and accumulation of ions at defect sites resulting in a faster PL decay of these regions. This explains the observation in Fig. 4(c) that more PL inactive areas appear at the edge beyond the illuminated area, where the iodide ions are driven out. Once they reach the non-illuminated area, their mobility will decrease and they will be almost immobile there, thus leading to a certain localization of redistributed iodide ions. We speculate that this additionally increases the chance for the formation of interstitial defects taking into account their low formation energy,<sup>39,73</sup> rendering non-radiative recombination centers.

The appearance of dark PL-inactive areas in perovskite films under illumination reveals that the migration and accumulation of halide ions has a negative effect on the stable output of perovskite photovoltaics. Thus, suppressing the halide ion migration in the perovskite films is one of the key issues to further improve the performance and stability of photovoltaic devices. Controlling the crystal quality and size can be an effective way,<sup>74</sup> as most of the mobile ions originate from defects at the grain boundaries/surface.<sup>36,70,75</sup> Another choice is passivating the defects with external particles, such as PCBM<sup>68</sup> or K<sup>+</sup>.<sup>11</sup> Meanwhile, the intensity distribution of the light source should be an issue for the stable output of PSCs.

In summary, wide-field PL microscopy is demonstrated as a simple and versatile method in characterizing the quality and stability of perovskite films. We employed wide-field PL microscopy to *in situ* investigate the PL changes of a perovskite film with light soaking on time scales of seconds. Besides the PL enhancement, some areas in the film yield a PL quenching. This PL quenching behavior plays an important role in PSCs because non-radiative recombination prevents PCEs from approaching the Shockley-Queisser efficiency limit. By characterizing the intensity dependent PL long-time decay process, we observe that the migration and localization of iodide ions in the perovskite film within an optical field gradient contribute to this non-radiative recombination. It is the first time to visually observe the accumulation of iodide ions during light soaking inducing non-radiative recombination. This either occurs at defective sites that are prone to accumulate and trap ions or at the gradient between the illuminated and non-illuminated areas.

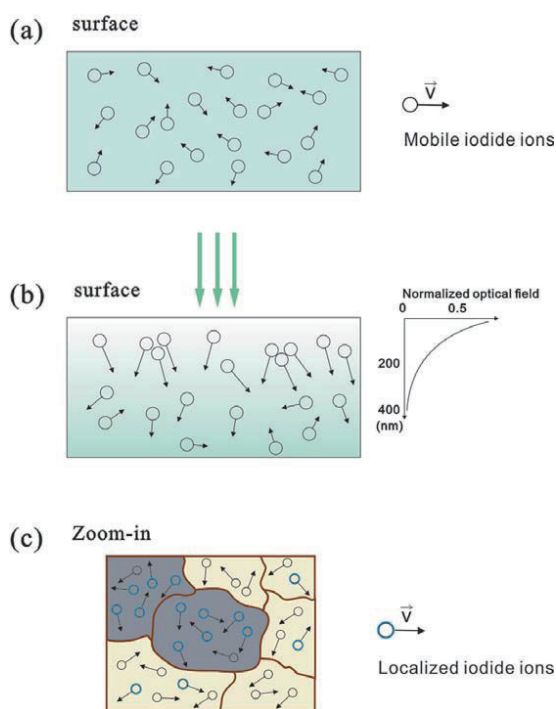


**FIG. 5.** The schematic of light-induced PL inactive areas: (a) The perovskite film without illumination. The iodide ions uniformly distribute through the film and have limited mobility. (b) Under illumination, the iodide ions get more energy and higher mobility. They can drift with the local optical field. (c) The mobile iodide ions can drift within a certain distance. When the local region has more defects, the ions will move there. The accumulation of iodide ions leads to non-radiative recombination. The arrow in the figure is for the possible moving direction of iodide ions and the magnitude of the arrow is for the mobility.

See [supplementary material](#) for the sample preparation method, characterization details, the change in  $V_{oc}$ ,  $J_{sc}$ , and FF with light soaking, the observation of  $\text{CH}_3\text{NH}_3\text{PbI}_{3-x}\text{Cl}_x$  film with AFM, SEM, and PL microscopy, and the beam profile of light source.

Financial support by the Bavarian State Ministry of Science, Research and the Arts for the Collaborative Research Network “Solar Technologies go Hybrid” and Federal Ministry of Education as well as the German Research Foundation (DFG) is gratefully acknowledged. Richard Hildner and Carlos Andres Melo Luna acknowledge additional funding from the German Research Foundation DFG (No. GRK1640). Yu Zhong acknowledges funding from the China Scholarship Council. Carlos Andres Melo Luna acknowledges funding from the Colombian Science, Technology and Innovation Fund-General Royalties System (Fondo CTeI-Sistema General de Regalías, Contract No. BPIN 2013000100007) and CIBioFi. We thank Jürgen Köhler and Kevin Wilma for experimental support.

## REFERENCES

- W. S. Yang, J. H. Noh, N. J. Jeon, Y. C. Kim, S. Ryu, J. Seo, and S. I. Seok, *Science* **348**, 1234 (2015).
- H.-S. Kim, C.-R. Lee, J.-H. Im, K.-B. Lee, T. Moehl, A. Marchioro, S.-J. Moon, R. Humphry-Baker, J.-H. Yum, J. E. Moser, M. Grätzel, and N.-G. Park, *Sci. Rep.* **2**, 591 (2012).
- S. D. Stranks, G. E. Eperon, G. Grancini, C. Menelaou, M. J. P. Alcocer, T. Leijtens, L. M. Herz, A. Petrozza, and H. J. Snaith, *Science* **342**, 341 (2013).
- G. Xing, N. Mathews, S. Sun, S. S. Lim, Y. M. Lam, M. Gratzel, S. Mhaisalkar, and T. C. Sum, *Science* **342**, 344 (2013).
- F. Panzer, C. Li, T. Meier, A. Köhler, and S. Huettnner, *Adv. Energy Mater.* **7**, 1700286 (2017).
- X. Li, D. Bi, C. Yi, J.-D. Décoppet, J. Luo, S. M. Zakeeruddin, A. Hagfeldt, and M. Grätzel, *Science* **353**, 58 (2016).
- N.-G. Park, M. Grätzel, T. Miyasaka, K. Zhu, and K. Emery, *Nat. Energy* **1**, 16152 (2016).
- Z. Wang, Q. Lin, F. P. Chmiel, N. Sakai, L. M. Herz, and H. J. Snaith, *Nat. Energy* **2**, 17135 (2017).
- G. Grancini, C. Roldán-Carmona, I. Zimmermann, E. Mosconi, X. Lee, D. Martineau, S. Narbey, F. Oswald, F. De Angelis, M. Graetzel, and M. K. Nazeeruddin, *Nat. Commun.* **8**, 15684 (2017).
- M. Saliba, T. Matsui, K. Domanski, J.-Y. Seo, A. Ummadisingu, S. M. Zakeeruddin, J.-P. Correa-Baena, W. R. Tress, A. Abate, A. Hagfeldt, and M. Gratzel, *Science* **354**, 206 (2016).
- D.-Y. Son, S.-G. Kim, J.-Y. Seo, S.-H. Lee, H. Shin, D. Lee, and N.-G. Park, *J. Am. Chem. Soc.* **140**, 1358 (2018).
- J. A. Giesecke, M. C. Schubert, B. Michl, F. Schindler, and W. Warta, *Sol. Energy Mater. Sol. Cells* **95**, 1011 (2011).
- Z. Hameiri, A. Mahboubi Soufiani, M. K. Juhl, L. Jiang, F. Huang, Y.-B. Cheng, H. Kampwerth, J. W. Weber, M. A. Green, and T. Trupke, *Prog. Photovoltaics: Res. Appl.* **23**, 1697 (2015).
- K. Zheng, K. Zidek, M. Abdellah, M. E. Messing, M. J. Al-Marri, and T. Pullerits, *J. Phys. Chem. C* **120**, 3077 (2016).
- W. Tress, *Adv. Energy Mater.* **7**, 1602358 (2017).
- D. W. de Quilletes, S. M. Vorpahl, S. D. Stranks, H. Nagaoka, G. E. Eperon, M. E. Ziffer, H. J. Snaith, and D. S. Ginger, *Science* **348**, 683 (2015).
- O. D. Miller, E. Yablonovitch, and S. R. Kurtz, *IEEE J. Photovoltaics* **2**, 303 (2012).
- Y. Deng, Z. Xiao, and J. Huang, *Adv. Energy Mater.* **5**, 1500721 (2015).
- C. Zhao, B. Chen, X. Qiao, L. Luan, K. Lu, and B. Hu, *Adv. Energy Mater.* **5**, 1500279 (2015).
- W. Nie, J.-C. Blancon, A. J. Neukirch, K. Appavoo, H. Tsai, M. Chhowalla, M. A. Alam, M. Y. Sfeir, C. Katan, J. Even, S. Tretiak, J. J. Crochet, G. Gupta, and A. D. Mohite, *Nat. Commun.* **7**, 11574 (2016).
- S. J. Yoon, S. Draguta, J. S. Manser, O. Sharia, W. F. Schneider, M. Kuno, and P. V. Kamat, *ACS Energy Lett.* **1**, 290 (2016).
- W. Huang, S. J. Yoon, and P. Sapkota, *ACS Appl. Energy Mater.* **1**, 2859 (2018).
- R. P. Xu, Y. Q. Li, T. Y. Jin, Y. Q. Liu, Q. Y. Bao, C. O’Carroll, and J. X. Tang, *ACS Appl. Mater. Interfaces* **10**, 6737 (2018).
- C. A. Combs, *Curr. Protoc. Neurosci.* **50**, 2.1.1 (2010).
- S. N. Habisreutinger, N. K. Noel, and H. J. Snaith, *ACS Energy Lett.* **3**, 2472 (2018).
- C. Li, S. Tscheuschner, F. Paulus, P. E. Hopkinson, J. Kiefling, A. Köhler, Y. Vaynzof, and S. Huettnner, *Adv. Mater.* **28**, 2446 (2016).
- B. Chen, M. Yang, X. Zheng, C. Wu, W. Li, Y. Yan, J. Bisquert, G. Garcia-Belmonte, K. Zhu, and S. Priya, *J. Phys. Chem. Lett.* **6**, 4693 (2015).
- D. A. Jacobs, Y. Wu, H. Shen, C. Barugkin, F. J. Beck, T. P. White, K. Weber, and K. R. Catchpole, *Phys. Chem. Chem. Phys.* **19**, 3094 (2017).
- R. T. Ross, *J. Chem. Phys.* **46**, 4590 (1967).
- A. M. Soufiani, Z. Hameiri, S. Meyer, S. Lim, M. J. Y. Tayebjee, J. S. Yun, A. Ho-Baillie, G. J. Conibeer, L. Spiccia, and M. A. Green, *Adv. Energy Mater.* **7**, 1602111 (2017).
- A. T. Haedler, K. Kreger, A. Issac, B. Wittmann, M. Kivala, N. Hammer, J. Köhler, H.-W. Schmidt, and R. Hildner, *Nature* **523**, 196 (2015).
- C. Li, A. Guerrero, Y. Zhong, A. Gräser, C. A. M. Luna, J. Köhler, J. Bisquert, R. Hildner, and S. Huettnner, *Small* **13**, 1701711 (2017).
- H. Yu, F. Wang, F. Xie, W. Li, J. Chen, and N. Zhao, *Adv. Funct. Mater.* **24**, 7102 (2014).
- S. Chen, X. Wen, R. Sheng, S. Huang, X. Deng, M. A. Green, and A. Ho-Baillie, *ACS Appl. Mater. Interfaces* **8**, 5351 (2016).
- C. Li, Y. Zhong, C. Luna, T. Unger, K. Deichsel, A. Gräser, J. Köhler, A. Köhler, R. Hildner, and S. Huettnner, *Molecules* **21**, 1081 (2016).
- Y. Tian, A. Merdasa, E. Unger, M. Abdellah, K. Zheng, S. McKibbin, A. Mikkelsen, T. Pullerits, A. Yartsev, V. Sundström, and I. G. Scheblykin, *J. Phys. Chem. Lett.* **6**, 4171 (2015).
- S. Chen, X. Wen, S. Huang, F. Huang, Y.-B. Cheng, M. Green, and A. Ho-Baillie, *Sol. RRL* **1**, 1600001 (2017).
- D. W. deQuilletes, W. Zhang, V. M. Burlakov, D. J. Graham, T. Leijtens, A. Oshero, V. Bulović, H. J. Snaith, D. S. Ginger, and S. D. Stranks, *Nat. Commun.* **7**, 11683 (2016).
- E. Mosconi, D. Meggiolaro, H. J. Snaith, S. D. Stranks, and F. De Angelis, *Energy Environ. Sci.* **9**, 3180 (2016).
- R. Gottesman, L. Gouda, B. S. Kalanoor, E. Haltzi, S. Tirosh, E. Rosh-Hodesh, Y. Tischler, A. Zaban, C. Quarti, E. Mosconi, and F. De Angelis, *J. Phys. Chem. Lett.* **6**, 2332 (2015).
- J. F. Galisteo-López, M. Anaya, M. E. Calvo, and H. Míguez, *J. Phys. Chem. Lett.* **6**, 2200 (2015).
- S. D. Stranks, V. M. Burlakov, T. Leijtens, J. M. Ball, A. Goriely, and H. J. Snaith, *Phys. Rev. Appl.* **2**, 034007 (2014).
- R. Gottesman and A. Zaban, *Acc. Chem. Res.* **49**, 320 (2016).
- T. Tachikawa, I. Karimata, and Y. Kobori, *J. Phys. Chem. Lett.* **6**, 3195 (2015).
- H. Yuan, E. Debroye, G. Caliendo, K. P. F. Janssen, J. van Loon, C. E. A. Kirschhock, J. A. Martens, J. Hofkens, and M. B. J. Roeflaers, *ACS Omega* **1**, 148 (2016).
- G. Niu, W. Li, F. Meng, L. Wang, H. Dong, and Y. Qiu, *J. Mater. Chem. A* **2**, 705 (2014).
- X. Deng, X. Wen, J. Lau, T. Young, J. Yun, M. Green, S. Huang, and A. W. Y. Ho-Baillie, *J. Mater. Chem. C* **4**, 9060 (2016).
- H. Yuan, E. Debroye, K. Janssen, H. Naiki, C. Steuwe, G. Lu, M. Moris, E. Orgiu, H. Uji-i, F. De Schryver, P. Samori, J. Hofkens, and M. Roeflaers, *J. Phys. Chem. Lett.* **7**, 561 (2016).

- <sup>49</sup>A. M. A. Leguy, Y. Hu, M. Campoy-Quiles, M. I. Alonso, O. J. Weber, P. Azarhoosh, M. Van Schilfgaarde, M. T. Weller, T. Bein, J. Nelson, P. Docampo, and P. R. F. Barnes, *Chem. Mater.* **27**, 3397 (2015).
- <sup>50</sup>Z. Song, A. Abate, S. C. Watthage, G. K. Liyanage, A. B. Phillips, U. Steiner, M. Graetzel, and M. J. Heben, *Adv. Energy Mater.* **6**, 1600846 (2016).
- <sup>51</sup>C. Eames, J. M. Frost, P. R. F. Barnes, B. C. O'Regan, A. Walsh, and M. S. Islam, *Nat. Commun.* **6**, 7497 (2015).
- <sup>52</sup>J. R. Harwell, T. K. Baikie, I. D. Baikie, J. L. Payne, C. Ni, J. T. S. Irvine, G. A. Turnbull, and I. D. W. Samuel, *Phys. Chem. Chem. Phys.* **18**, 19738 (2016).
- <sup>53</sup>V. W. Bergmann, S. A. L. Weber, F. Javier Ramos, M. K. Nazeeruddin, M. Grätzel, D. Li, A. L. Domanski, I. Lieberwirth, S. Ahmad, and R. Berger, *Nat. Commun.* **5**, 5001 (2014).
- <sup>54</sup>V. W. Bergmann, Y. Guo, H. Tanaka, I. M. Hermes, D. Li, A. Klasen, S. A. Bretschneider, E. Nakamura, R. Berger, and S. A. L. Weber, *ACS Appl. Mater. Interfaces* **8**, 19402 (2016).
- <sup>55</sup>J. M. Azpiroz, E. Mosconi, J. Bisquert, and F. De Angelis, *Energy Environ. Sci.* **8**, 2118 (2015).
- <sup>56</sup>C. Li, A. Guerrero, Y. Zhong, and S. Huettnner, *J. Phys.: Condens. Matter* **29**, 193001 (2017).
- <sup>57</sup>J. Xing, Q. Wang, Q. Dong, Y. Yuan, Y. Fang, and J. Huang, *Phys. Chem. Chem. Phys.* **18**, 30484 (2016).
- <sup>58</sup>C. Li, A. Guerrero, S. Huettnner, and J. Bisquert, *Nat. Commun.* **9**, 5113 (2018).
- <sup>59</sup>E. T. Hoke, D. J. Slotcavage, E. R. Dohner, A. R. Bowring, H. I. Karunadasa, and M. D. McGehee, *Chem. Sci.* **6**, 613 (2015).
- <sup>60</sup>M. H. Du, *J. Phys. Chem. Lett.* **6**, 1461 (2015).
- <sup>61</sup>M. H. Du, *J. Mater. Chem. A* **2**, 9091 (2014).
- <sup>62</sup>D. J. Slotcavage, H. I. Karunadasa, and M. D. McGehee, *ACS Energy Lett.* **1**, 1199 (2016).
- <sup>63</sup>D. Meggiolaro, S. G. Motti, E. Mosconi, A. J. Barker, J. Ball, C. Andrea Riccardo Perini, F. Deschler, A. Petrozza, and F. De Angelis, *Energy Environ. Sci.* **11**, 702 (2018).
- <sup>64</sup>S. T. Birkhold, J. T. Precht, R. Giridharagopal, G. E. Eperon, L. Schmidt-Mende, and D. S. Ginger, *J. Phys. Chem. C* **122**, 12633 (2018).
- <sup>65</sup>D. Meggiolaro, E. Mosconi, and F. De Angelis, *ACS Energy Lett.* **3**, 447 (2018).
- <sup>66</sup>H. Shi and M. H. Du, *Phys. Rev. B* **90**, 174103 (2014).
- <sup>67</sup>Y. Shao, Z. Xiao, C. Bi, Y. Yuan, and J. Huang, *Nat. Commun.* **5**, 5784 (2014).
- <sup>68</sup>J. Xu, A. Buin, A. H. Ip, W. Li, O. Voznyy, R. Comin, M. Yuan, S. Jeon, Z. Ning, J. J. McDowell, P. Kanjanaboos, J.-P. Sun, X. Lan, L. N. Quan, D. H. Kim, I. G. Hill, P. Maksymovych, and E. H. Sargent, *Nat. Commun.* **6**, 7081 (2015).
- <sup>69</sup>X. Wen, A. Ho-Baillie, S. Huang, R. Sheng, S. Chen, H. Ko, and M. A. Green, *Nano Lett.* **15**, 4644 (2015).
- <sup>70</sup>Y. Yuan and J. Huang, *Acc. Chem. Res.* **49**(2), 286 (2016).
- <sup>71</sup>J. L. Minns, P. Zajdel, D. Chernyshov, W. Van Beek, and M. A. Green, *Nat. Commun.* **8**, 15152 (2017).
- <sup>72</sup>Y. C. Zhao, W. K. Zhou, X. Zhou, K. H. Liu, D. P. Yu, and Q. Zhao, *Light: Sci. Appl.* **6**, e16243 (2017).
- <sup>73</sup>W. J. Yin, T. Shi, and Y. Yan, *Appl. Phys. Lett.* **104**, 063903 (2014).
- <sup>74</sup>W. Nie, H. Tsai, R. Asadpour, A. J. Neukirch, G. Gupta, J. J. Crochet, M. Chhowalla, S. Tretiak, M. A. Alam, and H. Wang, *Science* **347**, 522 (2015).
- <sup>75</sup>J. S. Yun, J. Seidel, J. Kim, A. M. Soufiani, S. Huang, J. Lau, N. J. Jeon, S. Il Seok, M. A. Green, and A. Ho-Baillie, *Adv. Energy Mater.* **6**, 1600330 (2016).

## Supplementary Materials

# *In-Situ* Investigation of Light Soaking in Organolead Halide Perovskite Films

Yu Zhong,<sup>1</sup> Carlos Andres Melo Luna,<sup>2,3</sup> Richard Hildner,<sup>2,a</sup> Cheng Li,<sup>1,b</sup> and  
Sven Huettnner<sup>1,b</sup>

*1 Department of Chemistry, University of Bayreuth, Bayreuth 95447, Germany*

*2 Experimental Physics IV and Bayreuth Institute of Macromolecular Research, University of Bayreuth,  
Bayreuth 95447, Germany*

*3 Centre for Bioinformatics and Photonics—CIBioFi, Universidad del Valle, 760032 Cali, Colombia*

<sup>a</sup> Current address: Zernike Institute for Advanced Materials, University of Groningen, 9747AG Groningen, The Netherlands

<sup>b</sup> Author to whom correspondence should be addressed: [cheng.li@uni-bayreuth.de](mailto:cheng.li@uni-bayreuth.de) and [sven.huettnner@uni-bayreuth.de](mailto:sven.huettnner@uni-bayreuth.de)

## S1: Sample Preparation

The solar cell with the structure shown in Figure S3, was fabricated as follows. A compact  $\text{TiO}_2$  layer was deposited on fluorine-doped tin oxide ( $\text{F:SnO}_2$ ) coated glass by spraying a solution of titanium diisopropoxide bis(acetylacetonate) (0.6 mL) in ethanol (21.4 mL) at 450 °C for 90 min in ambient atmosphere. Then the perovskite precursor solution ( $\text{CH}_3\text{NH}_3\text{I}:\text{PbCl}_2=3:1$  in DMF) was spin coated at 3000 rpm for 60s, followed by annealing at 100 °C for 70 min in a nitrogen glovebox. Subsequently, Spiro-OMeTAD (2,2',7,7'-Tetrakis-(N,N-di-4-methoxyphenylamine)-9,9'-spirobifluorene) solution was deposited by spin-coating at 4000 rpm for 30s, working as the hole transport layer. The devices were kept in a dry box overnight for the oxidation of Spiro-OMeTAD layer. Finally, an 80 nm gold electrode was deposited in a thermal evaporator chamber (Edwards Auto 306) at a pressure of  $1 \times 10^{-6}$  mbar. The effective electrode area was 9 mm<sup>2</sup> or 16 mm<sup>2</sup>.  $\text{CH}_3\text{NH}_3\text{I}$  was purchased from Dyesol Company, and all the other chemicals were purchased from Sigma-Aldrich and used as received.

## S2: Characterization Setup

*J-V* measurements were performed in inert environment with a Keithley 2400 source measure unit under 100 mW/cm<sup>2</sup> illumination from a solar simulator. The light intensity was calibrated by a Silicon detector. There was no biasing process prior to the scanning. We scanned the PSC from 1.2 V to -0.1 V (reverse scan) or from -0.1V to 1.2V (forward scan) with different speed. The step was 0.01 V.

For the PL imaging measurements, perovskite films were fabricated by spin coating the precursor solution on a clean glass substrate followed by annealing at 100 °C in nitrogen glovebox for 70 min, then 40 mg/mL PMMA dissolved in butyl acetate (anhydrous, 99%) was spin-coated on the perovskite film at 2000 rpm for 60 s acting as a protect layer. To obtain a uniform film, the glass substrate was under ozone plasma for 10 min before spin coating.

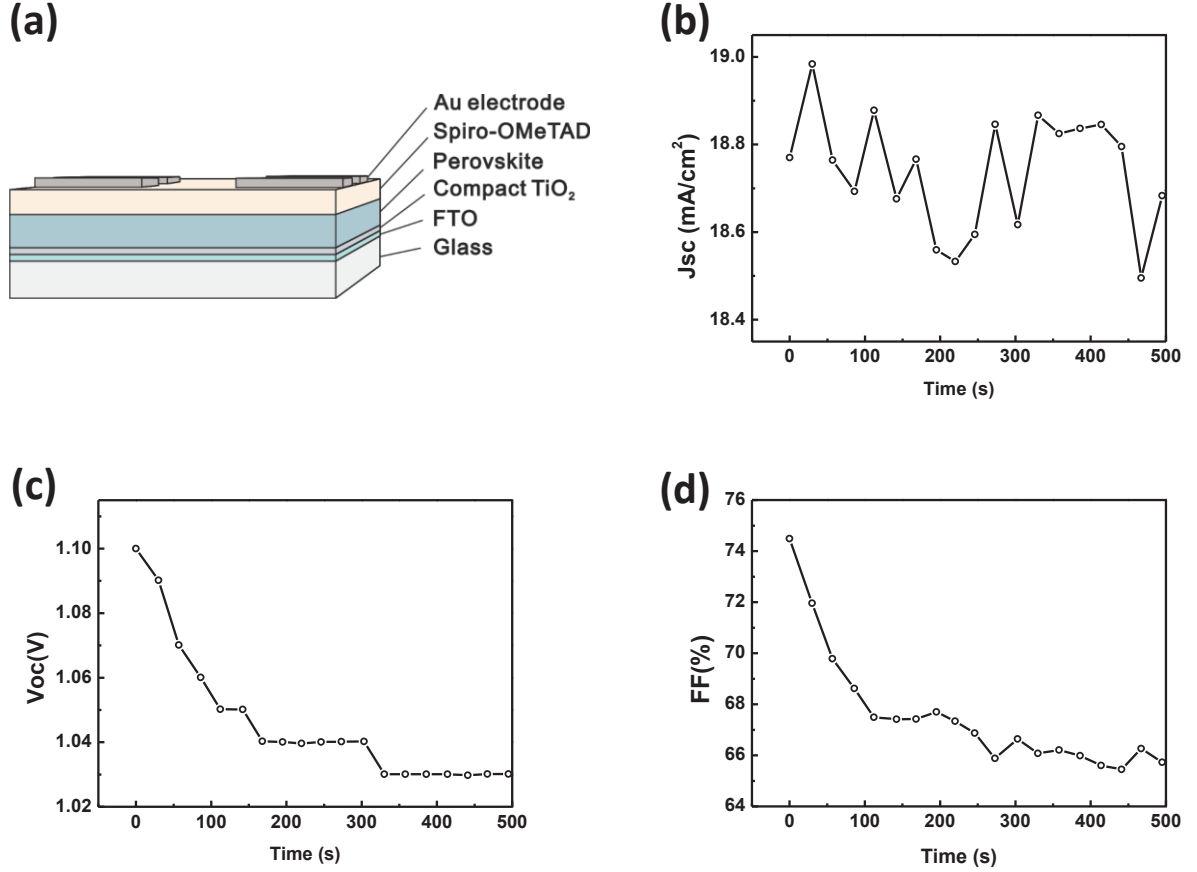
The schematic diagram of PL microscope configuration is shown in Figure 1(c). The excitation source was a pulsed diode laser (LDH-P-C-4508-B, Picoquant; 20MHz repetition rate, 70 ps pulse duration). The excitation power can be modulated by Neutral Density Filters. The dichroic mirror was tilted at 45° to the incoming excitation light (wavelength: 532 nm) and reflected the excitation light at a 90° angle directly through objective lens and onto the sample. A wide-field lens was inserted between the filter for the excitation light and the dichroic mirror. The beam profile is displayed in Figure S7(a). In order to adjust the sample in the focal plane of the objective lens, the sample position was placed by a piezo-stage (Triton 102 SG, piezosystem Jena GmbH, Jena, Germany). The PL emission of the perovskite film was collected by the same objective lens, and then it passed a long-pass filter (LP545, AHF analysentechnik AG, Tübingen, Germany), and finally was captured by a CCD camera (Orca-ER, Hamamatsu, Japan).

The PL images in Figure 4 and S6 were taken by a PL microscope (Microscope Axio Imager.A2m, Zeiss) employing a white light LED in combination with a dichroic mirror and a PL filter (HC 440 SP, AHF analysentechnik AG) in the excitation beam path and another filter

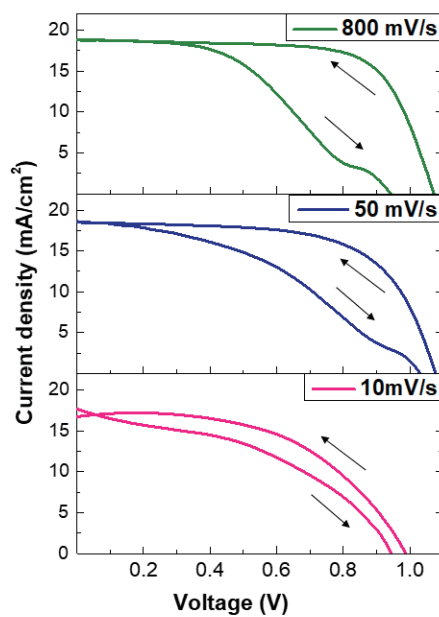


(HC-BS 484, AHF analysentechnik AG) for the emitted PL signal from the sample. This allowed an exciton with blue light up to 440nm and a detection from 490nm and above. The beam profile is displayed in Figure S7b. A CCD camera (Pco. Pixel fly, PCO AG) was employed to record PL images with the exposure time of 200 ms.

### S3: PSC architecture and its $J_{sc}$ , $V_{oc}$ and FF change with light soaking



**Figure S3:** (a) The schematic diagram for the architecture of a planar perovskite solar cell. The time-dependent performance of a perovskite solar cell under continuous illumination ( $100 \text{ mW} \cdot \text{cm}^{-2}$ ): (b)  $J_{sc}$ ; (c)  $V_{oc}$ ; (d) FF.

**S4: J-V measurements under different condition**

**Figure S4-1:**  $J$ - $V$  curve measurements of one PSC with different scan rates and scan directions.

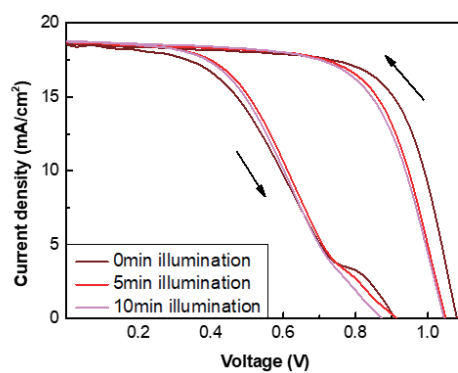


**Figure S4-2:**  $J$ - $V$  curve measurements of one PSC under illumination. The difference of the reverse- and forward- scan decreases within illumination. Scan speed: 800 mV/s.

### S5: The PCE Change under Different Conditions

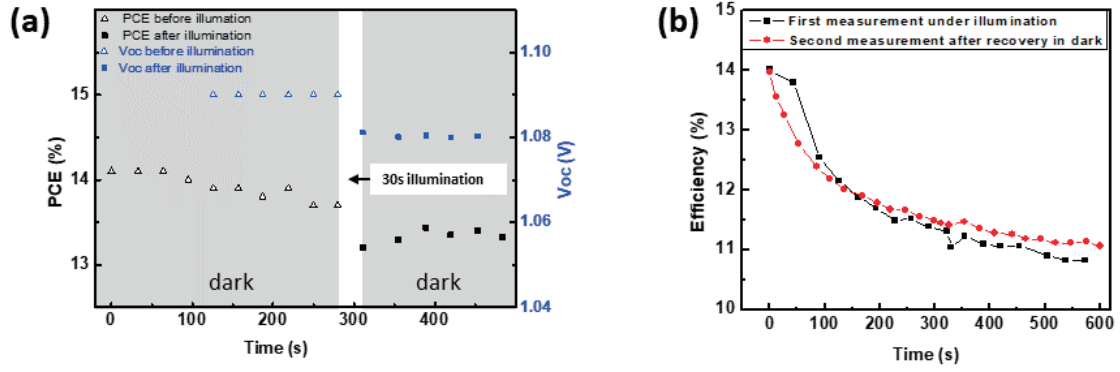


**Figure S5:** (a) The efficiency change and  $V_{oc}$  change of a device, which was kept sequentially in dark for 280s, under illumination ( $100 \text{ mW} \cdot \text{cm}^{-2}$ ) for 30s and in dark for 300s. The experiment condition of dark means that light is only on during the J-V curve measurement and light is off after each J-V curve measurement. (b) The efficiency decay of a perovskite solar cell under continuous illumination. The second measurement was conducted after the recovery of the device in dark. Between two measurements the device was kept in  $\text{N}_2$  glove box.

### S6: The Morphology of Perovskite Film

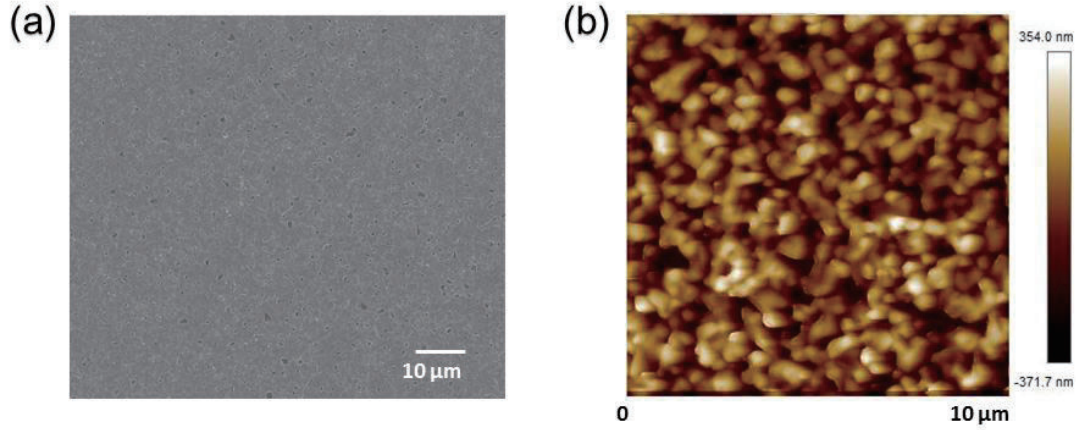


**Figure S6-1:** Morphology of MAPbI<sub>3-x</sub>Cl<sub>x</sub> perovskite film on glass (a) SEM image and (b) AFM image.

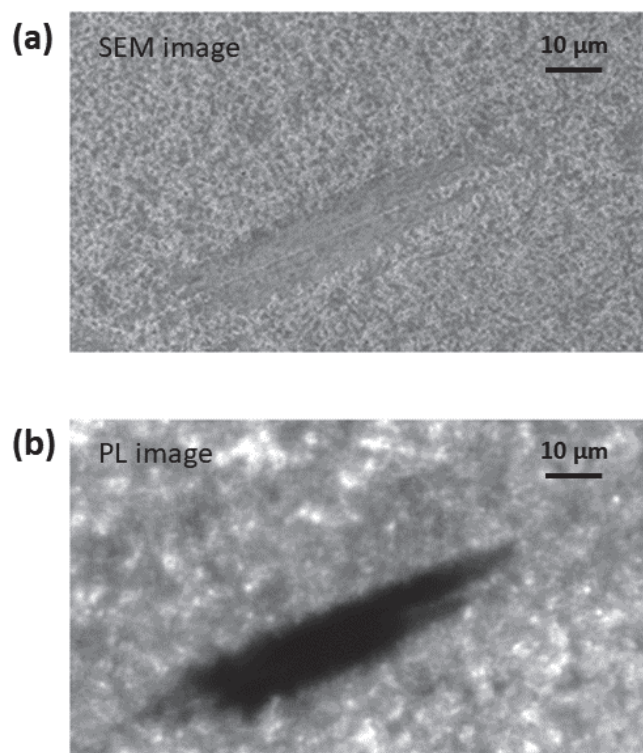
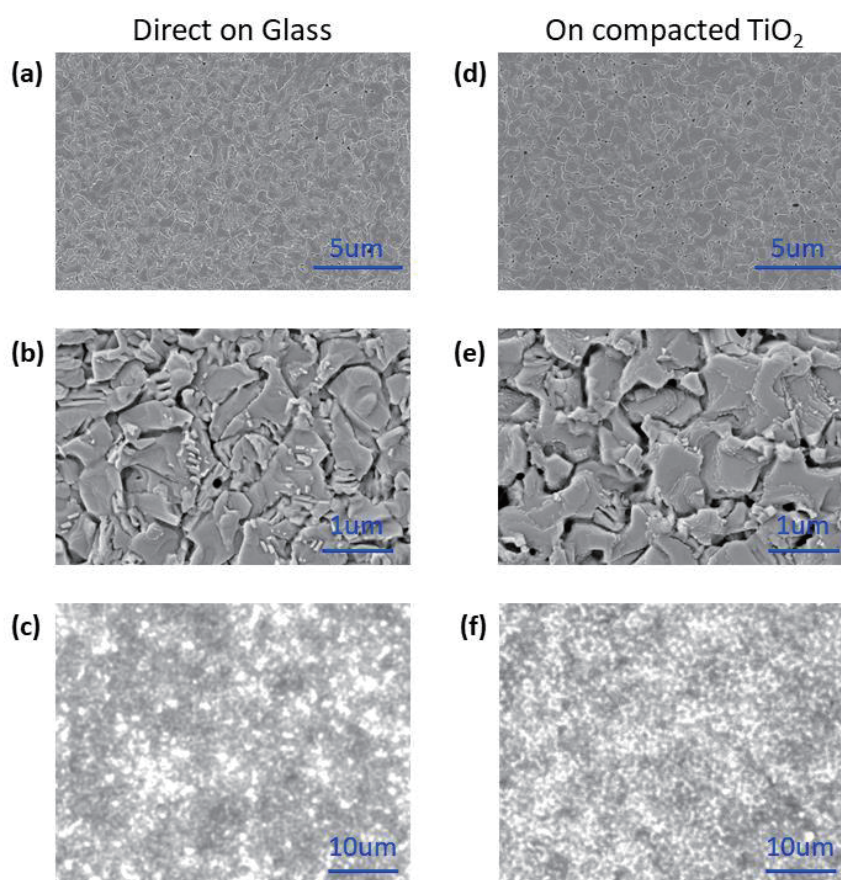
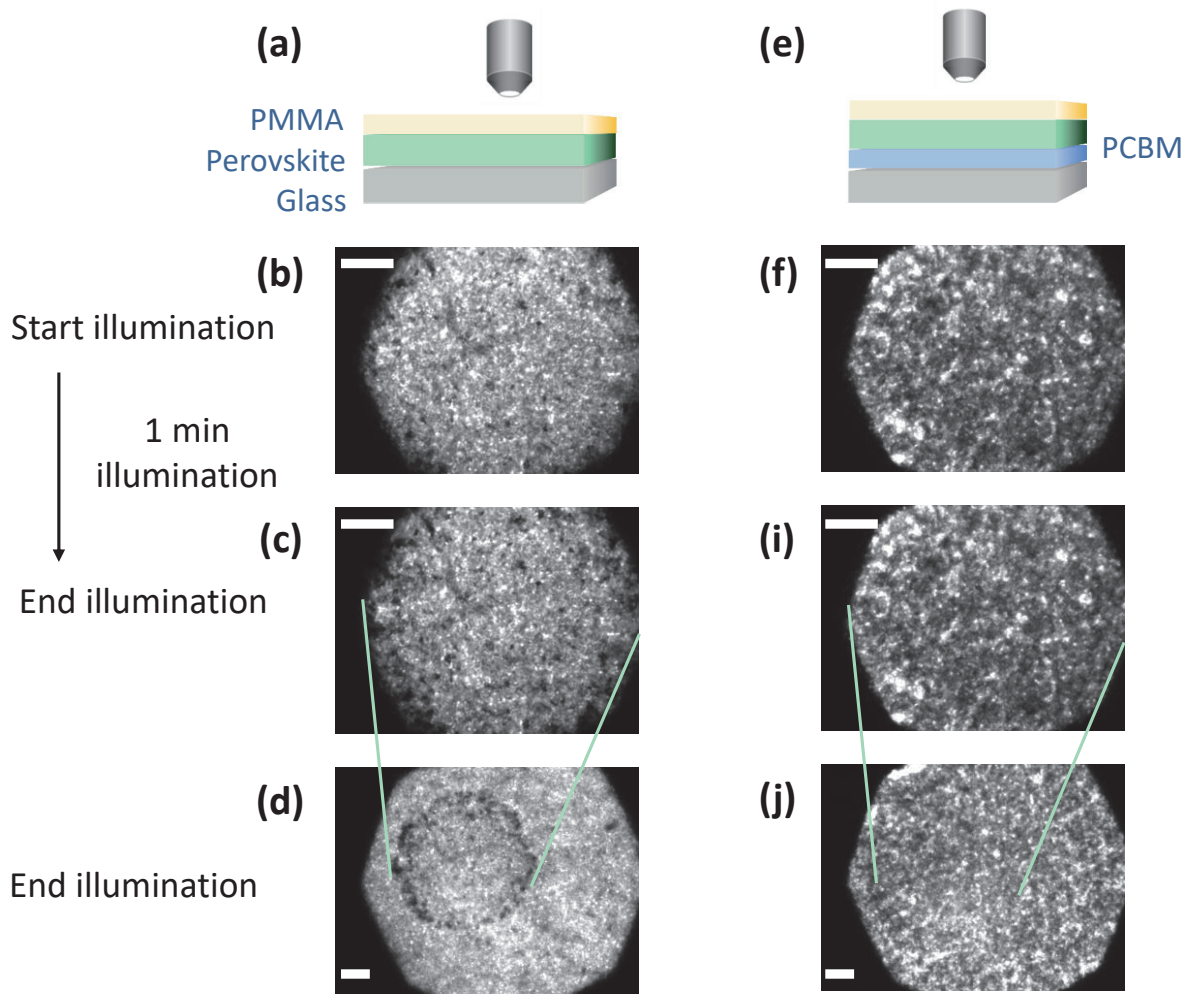


Figure S6-2: (a) SEM image and (b) PL image of the perovskite film at the same spot. The stripe is intentionally made in order to correlate these two images.

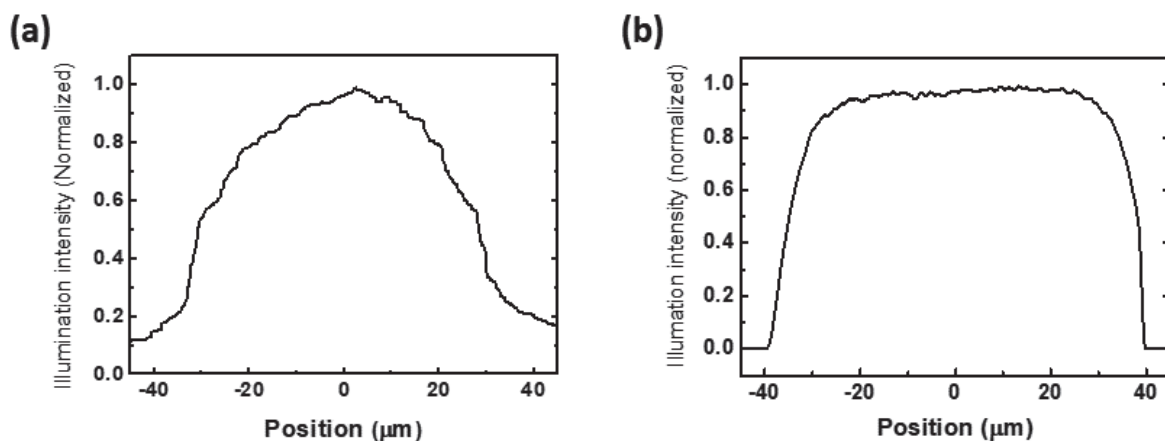


**Figure S6-3:** SEM images of perovskite film direct on glass (a), (b) and on compacted TiO<sub>2</sub> layer (d),(e). PL images of perovskite film direct on glass (c) and on compacted TiO<sub>2</sub> layer (f). The grain size and the emission do not show a significant difference. It needs to be mentioned that there tend to be more pin holes in the perovskite film processed on a compacted TiO<sub>2</sub> layer.

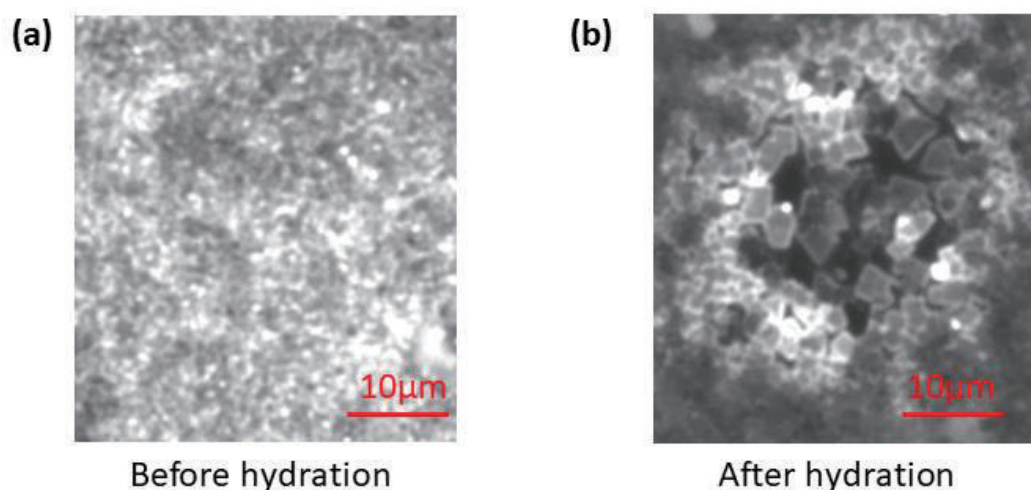
**S7: PL Images of Perovskite Film with/without PCBM Passivation**

**Figure S7:** (a-d) Perovskite films without and (e-j) with a PCBM layer under a PL microscope with different times of illumination and different magnification. (b) and (f) show the PL at the beginning of illumination; (c) and (i) after 1min of illumination. (d) and (j) are PL images of perovskite film after 1min illumination ( $450 \text{ mW/cm}^2$ ) but with a lower magnification exposing the illuminated spot as marked. It is apparent that the edge of the illuminated area, shows a strong PL decay in (d), while in (j) there is no distinct boundary between the exposed area and the unexposed area. The scale bar in every figure is  $20 \mu\text{m}$ . Figure (b) to (d) have already been shown in the main manuscript. We display these here again to make a clear comparison with PCBM passivated system.



**S8: Light Source Beam Profile**

**Figure S8:** The beam profile of the two light sources used in this study: (a) Green laser source, yielding a Gaussian distribution; within the center of 20  $\mu\text{m}$ -radius circle, the intensity decays by around 40%. (b) White LED with a variance of <10% within a radius of 20  $\mu\text{m}$ . “0” in x-axis stands for the center of the beam.

**S9: PL Images of Perovskite Film with/without hydration**

**Figure S9:** Perovskite films (a) before and (b) after 20min hydration. It is visible that some area becomes dark and the boundary of large domains ( $\sim 2 \mu\text{m}$ ) becomes brighter. This phenomenon is different from the light soaking behavior observed in Figure 2 and Figure 4.

**S10: Video of Long-Time PL Quenching of Perovskite Film**

The video displays PL changes of a perovskite film under continuous illumination (532 nm  $40\text{mW}/\text{cm}^2$ ) that some areas yield PL quenching besides the overall PL intensity enhancement. The local PL images were recorded every 500 ms.



# 6    **Role of PCBM in the Suppression of Hysteresis in Perovskite Solar Cells**

Yu Zhong, Martin Hufnagel, Mukundan Thelakkat, Cheng Li and Sven Huettnner

Published in

*Advanced Functional Materials*, **2020**, 1908920

(DOI: 10.1002/adfm.201908920)

## FULL PAPER

## Role of PCBM in the Suppression of Hysteresis in Perovskite Solar Cells

Yu Zhong, Martin Hufnagel, Mukundan Thelakkat, Cheng Li,\* and Sven Huettnner\*

The power conversion efficiency of inorganic–organic hybrid lead halide perovskite solar cells (PSCs) is approaching that of those made from single crystalline silicon; however, they still experience problems such as hysteresis and photo/electrical-field-induced degradation. Evidences consistently show that ionic migration is critical for these detrimental behaviors, but direct in-situ studies are still lacking to elucidate the respective kinetics. Three different PSCs incorporating phenyl-C61-butyric acid methyl ester (PCBM) and a polymerized form (PPCBM) is fabricated to clarify the function of fullerenes towards ionic migration in perovskites: 1) single perovskite layer, 2) perovskite/PCBM bilayer, 3) perovskite/PPCBM bilayer, where the fullerene molecules are covalently linked to a polymer backbone impeding fullerene inter-diffusion. By employing wide-field photoluminescence imaging microscopy, the migration of iodine ions/vacancies under an external electrical field is studied. The polymerized PPCBM layer barely suppresses ionic migration, whereas PCBM readily does. Temperature-dependent chronoamperometric measurements demonstrate the reduction of activation energy with the aid of PCBM and X-ray photoemission spectroscopy (XPS) measurements show that PCBM molecules are viable to diffuse into the perovskite layer and passivate iodine related defects. This passivation significantly reduces iodine ions/vacancies, leading to a reduction of built-in field modulation and interfacial barriers.

at 2009,<sup>[1]</sup> has attracted an unprecedented attention. Since then, extensive research has been carried out, ranging from crystalline structure characterization,<sup>[2]</sup> device performance optimization<sup>[3,4]</sup> to stability investigations,<sup>[5]</sup> etc. Though the surprising and remarkable progress has been achieved, perovskite solar cells (PSCs) are still suffering from several problems impeding a quick commercialization. Among those are the current density–voltage (*J*–*V*) hysteresis,<sup>[6,7]</sup> (the discrepancy of *J*–*V* curve between two sweeping directions)<sup>[8]</sup> or photo/electrical-induced degradation and stability,<sup>[9]</sup> for example. Recent evidences consistently demonstrate that ionic migration is responsible for these unsolicited behaviors.<sup>[10–14]</sup> The complexity of the investigation arises from the strong coupling between ionic migration and free charge carrier transport under external photo/electrical fields. Therefore, direct in situ characterization of the ionic movement via electrical and optical methods is becoming an emergent subject and will be used in this work.

## 1. Introduction

Driven by the demand for low cost and high-efficiency renewable energy sources, organometal trihalide perovskite (e.g.,  $\text{CH}_3\text{NH}_3\text{PbI}_3$  and  $\text{CH}_3\text{NH}_3\text{SnI}_3$ ), first emerged as solar cells


It is widely observed that the involvement of phenyl-C61-butyric acid methyl ester (PCBM) molecules, either by mixing within the bulk,<sup>[15,16]</sup> or inserting a single layer into devices,<sup>[17,18]</sup> is able to significantly alleviate or eliminate hysteresis. Wojciechowski et al.<sup>[19]</sup> ascribed the reduced hysteresis to the enhanced electron transfer at the  $\text{TiO}_2$ /perovskite interface by a self-assembled monolayer of fullerenes. Xing et al.<sup>[20]</sup> observed the reduction of perovskite/ $\text{TiO}_2$  interfacial barrier by inserting a PCBM layer. Shao et al.<sup>[17]</sup> attribute the elimination of hysteresis to the passivation of charge trap states in the bulk of perovskite film during the thermal annealing process. Xu et al.<sup>[15]</sup> found that the ion migration is significantly suppressed when PCBM are absorbed on Pb-I antisite defects. In this paper we will investigate the role of PCBM in detail. We utilize PCBM molecules as well as a polymerized form of PCBM molecules to corroborate their function, that is, investigate the influence of incorporation or interdiffusion, their function as an interlayer or a passivating agent. We intentionally used the typical organo-lead halide perovskite material ( $\text{CH}_3\text{NH}_3\text{PbI}_{3-x}\text{Cl}_x$ ) with significant hysteresis. Very recent developments in perovskite solar cells often involve materials such as  $\text{FAI}^{[21]}$  or 2D-perovskite<sup>[22]</sup> materials, where the hysteresis phenomena is not so obvious, which makes it more difficult to study the crucial role of PCBM on hysteresis suppression.

Wide-field photoluminescence (PL) imaging microscopy is employed to in situ study the motion of ions under an external

Y. Zhong, Dr. C. Li, Dr. S. Huettnner  
Department of Chemistry  
University of Bayreuth  
Universitätsstr. 30, Bayreuth 95440, Germany  
E-mail: sven.huettnner@uni-bayreuth.de

Dr. M. Hufnagel, Prof. M. Thelakkat  
Applied Functional Polymers  
University of Bayreuth  
Universitätsstr. 30, Bayreuth 95440, Germany

Prof. C. Li  
School of Electronic Science and Engineering  
Xiamen University  
Xiamen 361005, China  
E-mail: chengli@xmu.edu.cn

 The ORCID identification number(s) for the author(s) of this article can be found under <https://doi.org/10.1002/adfm.201908920>.

© 2020 The Authors. Published by WILEY-VCH Verlag GmbH & Co. KGaA, Weinheim. This is an open access article under the terms of the Creative Commons Attribution License, which permits use, distribution and reproduction in any medium, provided the original work is properly cited.

DOI: 10.1002/adfm.201908920

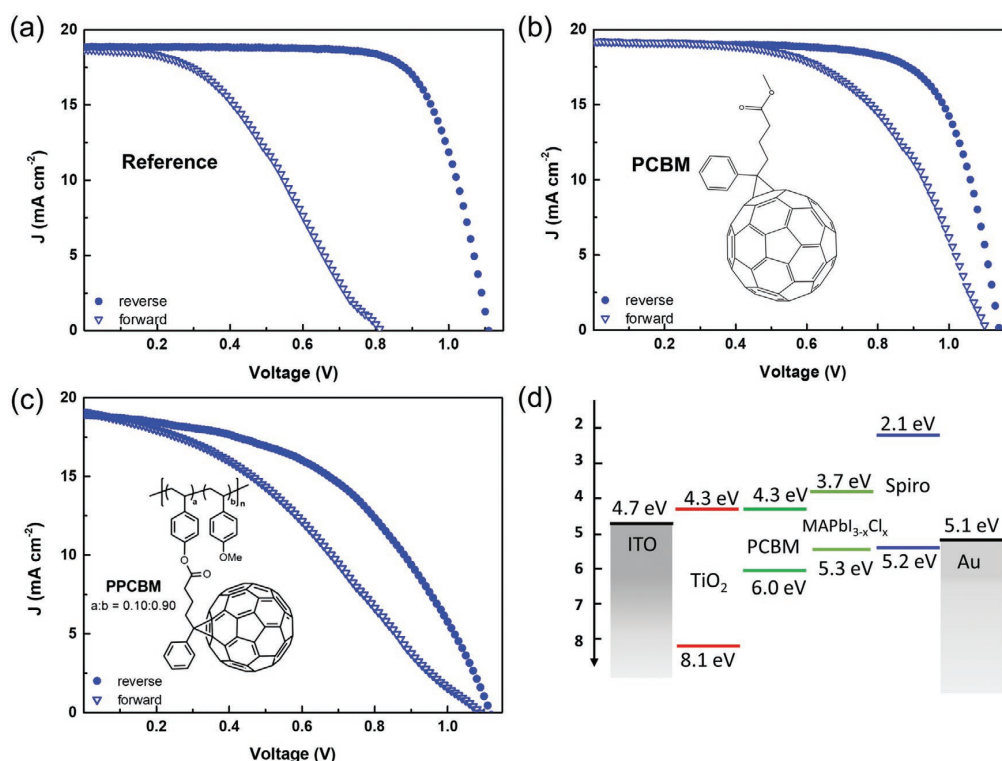


**Figure 1.** a–c)  $J$ – $V$  curve characterization of different PSCs. a) Reference device, that is, FTO/compact  $\text{TiO}_2$ /perovskite/Spiro-OMeTAD/Au. b) Solar cells with a PCBM molecule layer, that is, FTO/compact  $\text{TiO}_2$ /PCBM/perovskite/Spiro-OMeTAD/Au. c) Solar cells with a PPCBM layer, that is, FTO/compact  $\text{TiO}_2$ /PPCBM/perovskite/Spiro-OMeTAD/Au. d) Energy diagram of the perovskite device. Insets in (b) and (c) are the chemical structure of PCBM molecule and PPCBM, respectively. The scanning speed is  $0.8 \text{ V s}^{-1}$ .

electrical field in three individual systems: 1) single perovskite film 2) perovskite film deposited on top of a PCBM layer, called perovskite/PCBM bilayer 3) perovskite/PCBM-grafted polymer (PPCBM) bilayer. With this set of device structures we are able to identify the function of the PCBM layer and especially address its incorporation or interdiffusion and grain boundary passivation. Furthermore, we carry out the stepwise temperature dependent chronoamperometric measurements to obtain the activation energy of ion migration in PSCs, with and without PCBM layer respectively. X-ray photoemission spectroscopy (XPS) depth profiling indicates the incorporation or diffusion of PCBM molecules into the perovskite film, resulting in reduced ionic migration within perovskite layer. Therefore, PCBM can play an important role in the suppression of hysteresis by reducing ionic migration.

## 2. Results and Discussion

**Figure 1a** displays the  $J$ – $V$  curve of a reference PSC using a mixed halide perovskite precursor ( $\text{CH}_3\text{NH}_3\text{I}:\text{PbCl}_2 = 3:1$ ). Note that in the reverse sweeping, from positive to negative voltage, as shown in **Table 1**, the efficiency is  $\approx 15.5\%$ , however, in the forward sweeping, from negative to positive voltage, the efficiency drops to  $6.2\%$ . When a PCBM layer is inserted between the perovskite and the  $\text{TiO}_2$  electron transport layer (ETL), as

shown in **Figure 1b**, the power conversion efficiency ( $\eta$ ) of solar cells is comparable with the reference device in reverse scan direction. In forward scan direction, the PCBM-inserted devices yield a better performance, that is, fill factor (FF) and open-circuit voltage ( $V_{oc}$ ), in comparison with that of the reference device. The photovoltaic parameters from a series of solar cells with and without PCBM are shown in **Figure S1**, Supporting Information. To quantitatively compare the hysteresis between the different solar cell structures, we utilize the so-called hysteresis index (HI). The HI is defined as<sup>[23,24]</sup>

$$HI = \frac{J_{\text{reverse}}\left(\frac{V_{oc}}{2}\right) - J_{\text{forward}}\left(\frac{V_{oc}}{2}\right)}{J_{\text{reverse}}\left(\frac{V_{oc}}{2}\right)} \quad (1)$$

A solar cell without hysteresis yields an HI of 0, while a HI of 1 corresponds to a hysteresis as high as the magnitude of the photocurrent. The HIs are derived from the results in **Figure 1** and listed in **Table 1**. The data imply that the hysteresis of PCBM-incorporated devices significantly decreases compared with reference one.

To further study the role of the PCBM layer, we replace the PCBM layer with a polymerized PPCBM layer. The synthesis of this PPCBM is describe elsewhere.<sup>[25]</sup> This PPCBM has a

**Table 1.** Summary of device performance in Figure 1.

Device type	Scan direction	$V_{oc}$ [V]	$J_{sc}$ [mA cm <sup>-2</sup> ]	FF [%]	$\eta$ [%]	Hysteresis Index
Reference	Forward	0.82	18.8	40.3	6.2	0.20
	Reverse	1.10	19.0	73.4	15.5	
PCBM layer	Forward	1.11	19.4	55.1	11.8	0.03
	Reverse	1.14	19.3	71.4	15.7	
PPCBM	Forward	1.10	19.1	35.1	7.4	0.19
	Reverse	1.11	19.0	48.7	10.4	

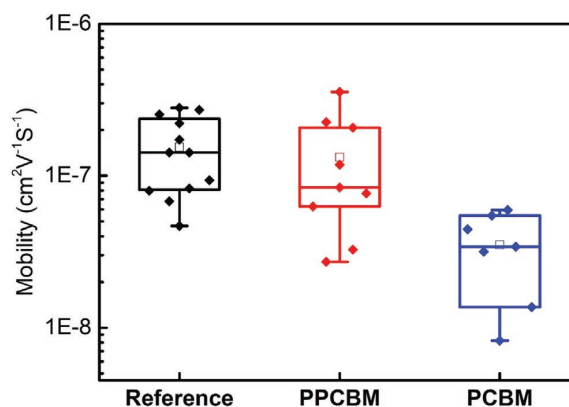
molecular weight of  $M_n = 17.2 \text{ kg mol}^{-1}$  and poly-dispersity of  $\bar{D} = 1.27$  (measured with size-exclusion chromatography with chlorobenzene as eluent and polystyrene calibration). Interestingly, the HI becomes large again with the utilization of this PPCBM. The HI approaches the value of the reference solar cell. In this PPCBM shown in inset of Figure 1c, PCBM molecules are bound to a polymer backbone and therefore immobilized within the polymer layer. This result implies that the diffusion of PCBM molecules into the perovskite layer is crucial to the elimination of hysteresis in PSCs, consistent with the requirement of thermal annealing to passivate the defects and decrease the trap density in the perovskite layer.<sup>[20]</sup> Here, we note that, the relatively poorer performance of the device with PPCBM is probably caused by its relatively lower electron mobility,<sup>[26]</sup> hindering the effective electron extraction by TiO<sub>2</sub>/FTO layer.

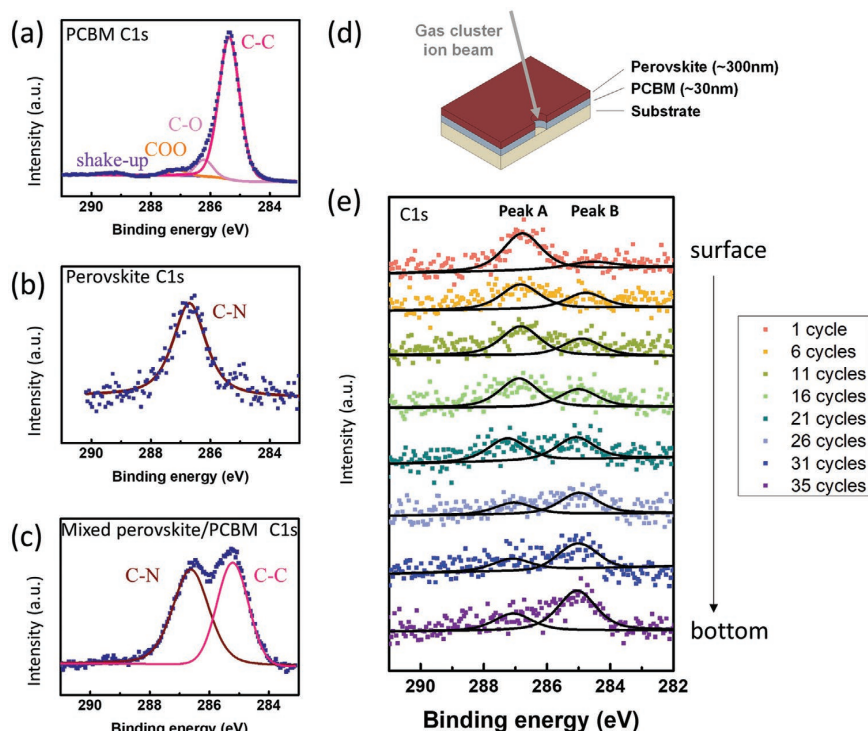
Though various models for the  $J$ - $V$  curve hysteresis have been proposed, including ferroelectricity,<sup>[27]</sup> charge trapping/detrapping,<sup>[28]</sup> modulated Schottky barriers<sup>[29]</sup> etc., it is supported by many evidences that a combination of ion migration<sup>[30,31]</sup> and polarization at interfaces<sup>[32,33]</sup> serves as an essential factor in the hysteretic behavior in PSCs. To study the ionic migration process, perovskite films with laterally-configured electrodes have demonstrated to be an excellent platform.<sup>[34,35]</sup> In addition, PL is an indication of the charge carrier recombination pathway<sup>[36]</sup> which has been employed to study the detailed charge carrier dynamic processes within the perovskite film.<sup>[37,38]</sup> Here, we investigate the dynamics of ion/vacancy migration with lateral interdigitating electrodes (Figure S3, Supporting Information) under an electrical field characterized by temporal-resolved PL imaging microscopy (Figure S4, Supporting Information), while the corresponding current is measured. The films were excited with blue light and their PL response  $> 700 \text{ nm}$  was imaged. A detailed description of the setup has been reported previously.<sup>[39,40]</sup> In brief, we modified a commercial PL microscope and used a blue light excitation filter, dichroic mirror, and a fast charge-coupled device (CCD) camera to capture the PL response in wide field with high time resolution. PL images of the perovskite films were recorded while a fixed external electric field was applied laterally and its time-dependent current was measured.

Figure S5, Supporting Information depicts the temporal PL evolution of a perovskite film under a constant electrical field. It is observed that the overall PL intensity decreases after the injection of electrons. The reason is the formation of the quenching defect when electrons are injected.<sup>[41]</sup> It has been observed that the defects, for example, Frenkel defects with iodine vacancies and interstitials,<sup>[42]</sup> formed during the low-temperature fabrication method,<sup>[43]</sup> can be driven by the external electrical field.<sup>[12,42]</sup>

Our previous study showed that migrating iodine vacancies play a major role and migrate within the applied electric field. On their way towards the cathode, they partially compensate for interstitial defects but also leave behind a significant number of non-radiative recombination centers as their counterpart in Frenkel defects.<sup>[39]</sup> The migration of vacancies goes ahead with a decrease of the electron-hole concentration corresponding to an effective reduction p-doping density. This phenomenon is shown in Figure S5a–d, Supporting Information. A PL dark area expands from the positive side to negative side. As evidence of the reduction of electron-hole density (less p-type doping), the measured current decays, as displayed in Figure S5e, Supporting Information. Applying a dynamic model for the current within the device leads to the ionic mobility in perovskite reference samples  $(2 \pm 1) \times 10^{-7} \text{ cm}^2 \text{ V}^{-1} \text{ s}^{-1}$ .<sup>[39]</sup> The model used to determine the mobility is demonstrated in Section S6, Supporting Information.

Results were obtained for all three device structures, as illustrated in Figure 2. The ionic mobility of perovskite/PPCBM is  $(1 \pm 1) \times 10^{-7} \text{ cm}^2 \text{ V}^{-1} \text{ s}^{-1}$ , which is in similar range as the perovskite reference sample. The mobility of perovskite/PCBM system, however, is only  $(4 \pm 2) \times 10^{-8} \text{ cm}^2 \text{ V}^{-1} \text{ s}^{-1}$  almost one order of magnitude lower than that of the two other structures as illustrated in Figure 2. This shows that the ionic migration in perovskite films deposited on a PCBM layer is significantly reduced compared to the pure perovskite film and the perovskite film on PPCBM. As we have mentioned above, the hysteresis is

**Figure 2.** The ionic mobility in perovskite film. The results are derived from time-dependent current, as illustrated in Figure S5, Supporting Information.



**Figure 3.** XPS spectra of C1s peak on a) PCBM, b) perovskite, and c) perovskite/PCBM mixed sample. d) perovskite/PCBM bilayer sample for depth profile and e) its depth profile results after sputtering of gas cluster ion beam, where peaks A and B correspond to C1s from perovskite and PCBM respectively.

strongly related to the ionic migration in PSCs. Ions accumulate at the contacts on either side, with the ETL or hole transport layer (HTL), which will influence the built-in potential. Furthermore, a properly aligned built-in potential is favorable for charge injection and is also related to the maximum achievable  $V_{oc}$ .<sup>[30]</sup>

We find that PCBM which can freely interact or interdiffuse within a perovskite film decreases the ionic migration, and hence reduces the hysteresis in PCBM. In comparison, the glass transition temperature  $T_g = 144^\circ\text{C}$  of this PPCBM is above the processing temperature of the perovskite, the PPCBM layer does not allow any strong interdiffusion within the perovskite film.<sup>[25]</sup> Thus, the PCBM groups solely locate at the interface. The PSCs using a PPCBM layer between  $\text{TiO}_2$  and perovskite still suffer severe hysteresis. This gives rise to the assumption that PCBM molecules indeed diffuse into perovskite films facilitating a passivating effect towards ionic migration. In order to corroborate our results, we analyzed the depth profile of a perovskite/PCBM bilayer sample with XPS in detail.

**Figure 3a** and **b** show the C1s spectra of a pure PCBM film and a pure perovskite film. PCBM shows a main peak at 285.3 eV, which originates from the C–C bond of the fullerene moiety.<sup>[44,45]</sup> The typical C1s signal of a perovskite film is the C–N feature of  $\text{CH}_3\text{NH}_3^+$  (286.7 eV).<sup>[46,47]</sup> Furthermore, a third sample was processed, which was prepared by directly mixing the perovskite precursor solution with PCBM in a molar ratio of  $\text{Pb}:\text{PCBM} = 500:1$  and annealing. It is noted that the morphology of this intermixed film is sufficiently good to carry out

our XPS analysis, but it does not allow the fabrication of proper solar cell devices. The C1s spectrum of this mixed perovskite/PCBM film (displayed in Figure 3c) is composed of two distinct peaks, which are ascribed to the C–N bond from perovskite and the C–C bond from PCBM. It indicates that the contribution of  $\text{CH}_3\text{NH}_3\text{PbI}_{3-x}\text{Cl}_x$  and PCBM can be easily separated by analyzing the C1s peak. With this information we performed a depth profile of a perovskite/PCBM bilayer sample. A gas cluster ion beam (GCIB) was used to sputter into the organic film and to obtain a depth profile of the perovskite/PCBM bilayer sample, displayed in Figure 3d. The C1s spectrum obtained after every cycle (0.5 min per cycle) of GCIB sputtering is shown in Figure 3e. The sputter rate is  $\approx 17\text{ nm min}^{-1}$  and after 18 min GCIB sputtering, the substrate surface was reached. It is obvious that through the perovskite layer two C1s peaks were detected. Peak A, at higher binding energy, which is ascribed to  $\text{CH}_3\text{NH}_3^+$  from the perovskite, locates between 286.7 and 287.0 eV. This peak shifts to a lower position when it reaches the interface. This thickness-dependent shift has been reported.<sup>[46]</sup> The appearance of additional peaks formed by sputtering and beam damage have been excluded as shown in Figure S7, Supporting Information. Peak B, at around 285.3 eV, was also detected during the beginning cycles. Based on the results above, Peak B is attributed to the C–C bond stemming from PCBM, and shows their prevalence within the perovskite layer. The detected PCBM may partially come from the dissolved PCBM in dimethylformamide during spin



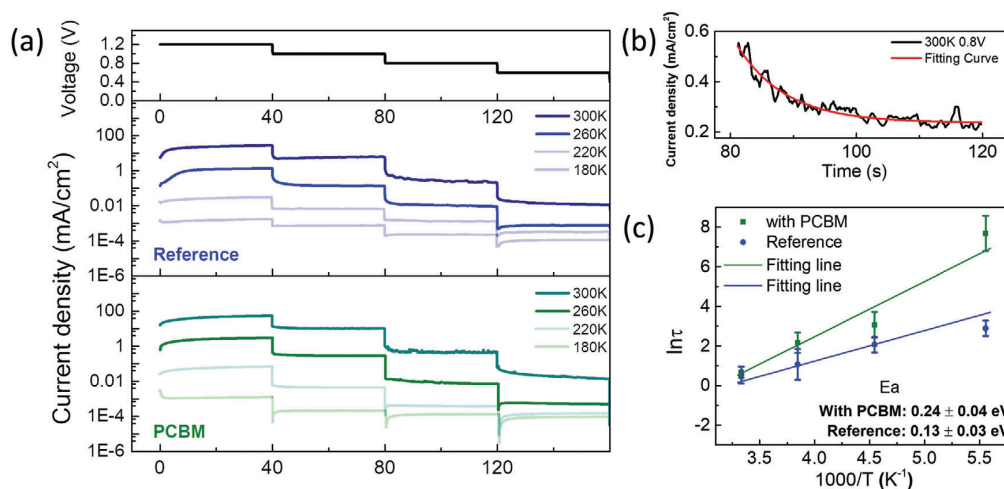


**Figure 4.** a) Temperature dependent chronoamperometric curve of reference device (blue) and PCBM (green) device, from 1.2 to 0.6 V with step of 0.2 V, each voltage lasts 40 s. The top part shows the applied voltage. b) Time dependent current density and fitting single exponential line at 0.8 V, 300 K. c) Activation energy of iodide ions in pure perovskite (reference) and perovskite on PCBM layer devices (PCBM device), respectively.

coating, as we make a detailed discussion in Figure S12, Supporting Information. Furthermore, PCBM molecules can also diffuse into perovskite film during film annealing. The evidence of fullerene diffusion through (amorphous/crosslinked<sup>[48]</sup> and crystalline<sup>[49]</sup>) polymer films has been demonstrated and was also suggested for perovskite films.<sup>[17]</sup> Our XPS results corroborate that PCBM molecules can readily diffuse into a  $\approx 300$  nm perovskite film at 105 °C within 75 min. This incorporation or interdiffusion into grain boundaries of the PCBM molecules seems to significantly reduce and hinder ionic migration.<sup>[50]</sup>

A further parameter which directly describes the viability for ion migration is the related activation energy. In a working perovskite solar cell, ions can migrate under an applied bias due to the prevalence of defects and may involve MA ions/vacancies<sup>[51,52]</sup> or iodine ions/vacancies.<sup>[53,54]</sup> Among them, the dominant moving species are iodine ions/vacancies.<sup>[55]</sup> The movement of these defects is in the form of hopping, also described as “jumping” in early days, between neighboring sites within the bulk with a rate  $\Gamma$  that can be expressed in an Arrhenius relation:<sup>[56]</sup>

$$\Gamma \propto \exp\left(\frac{-E_A}{k_B T}\right) \quad (2)$$

in which  $E_A$  is the activation energy, the energy required to move the defects from the equilibrium states to the neighbor sites in the bulk of perovskite.  $k_B$  and  $T$  are Boltzmann constant and absolute temperature, respectively.

Furthermore, we analyzed the activation barrier of ion migration of a pure perovskite film and another processed on a PCBM layer. This was done by applying voltage steps (0.2 V) to the device from 1.2 to 0.6 V and measuring the current evolution versus time, as shown in Figure 4a. The using voltage steps last 40s. The electrical current exhibits a decay-function at each voltage step. A single exponential function  $e^{-t/\tau}$  was used to evaluate the time constants as shown in Figure 4b. An

Arrhenius plot shows a linear relationship between  $\ln(\tau)$  and  $1/T$  and suggests that the movement of ions is facilitated by a single hopping mechanism.<sup>[56]</sup> The constant of  $\tau$  related with the “jumping rate” of ions  $\Gamma$  is used to describe the ionic migration within the bulk of the perovskite film.<sup>[57]</sup>

As shown in Figure 4c, it indicates that ions are moving faster in the perovskite film than the one on PCBM layer in all temperatures, consistent with the pervious PL microscopy observation. In the meantime, we note that the activation energy  $E_A$  of the pure perovskite is  $0.13 \pm 0.03$  eV. This value agrees with a previous experiment and theoretical papers,  $\approx 0.2$  eV.<sup>[29,51,58]</sup> In direct comparison the measured activation energy with a PCBM layer is  $0.24 \pm 0.04$  eV, implying a higher energy required to drive these ions from equilibrium sites to the nearby sites in perovskite with the presence of PCBM molecules.

Taking account of the above experiments, the mechanism of suppression of hysteresis in PSCs incorporating with PCBM molecules becomes clearer. As proposed previously that the origin of the hysteresis in PSCs is due to the migration of iodine ions/vacancies. These ions are driven by the external field and accumulate at the interface between perovskite/ETL and HTL. This accumulation effectively enhances or decreases the built-in potential.<sup>[59]</sup> While, in PSCs incorporating with PCBM layer, PCBM molecules distribute within the bulk of perovskite film. Absorbed at perovskite defective sites along the grain boundaries, these PCBM molecules passivate these defect states, for example, iodine interstitials or iodide vacancies as we propose, decreasing or even halting ion migration within the perovskite film. It is possible that iodide ions from defects form strong bonding with PCBM molecules, by direct electron transfer from anions (iodide ions here).<sup>[15]</sup> In this respect, the iodide ions/defects are immobilized by tying up with the PCBM molecules in the bulk of perovskite. Alternatively, PCBM molecules only form a physical hindrance for the ion migration or occupy some vacancy space, as displayed in Figure 5c. As a consequence, the moving defect density in perovskite



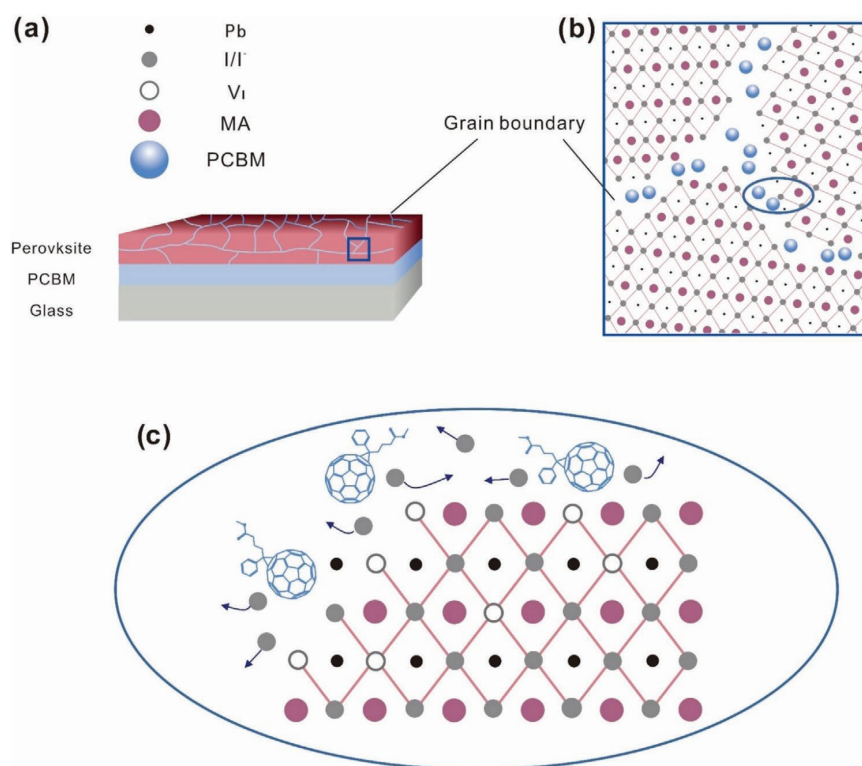


**Figure 5.** Schematic diagram for the PCBM passivating iodide ion related defects in perovskite materials, particularly in the vicinity of grain boundary. a) Schematic of a perovskite film deposited on PCBM layer. b) Zoom in image of the rectangle area in (a), showing PCBM molecules penetrate into the grain boundary of perovskite layer. c) Zoomed-in image of circle area in (b), showing that PCBM molecules form hindrance of the iodide ions movement.

reduces and the hysteresis is significantly suppressed due to the reduction of ionic migration.

For the PPCBM inserted device, the joint fullerene molecules are difficult to diffuse through the perovskite bulk material. Thus, the suppression of hysteresis is not distinct in these devices. However,  $V_{oc}$  of these devices in forward scan and reverse scan yields no pronounced difference. The reason is that the mismatch of  $\text{TiO}_2$ /perovskite interface is weakened by the PPCBM layer.<sup>[60]</sup> The interfacial barrier is hard to form at this contact and thus the change of the built-in potential is tiny. The ionic migration still exists in this perovskite/PPCBM bilayer system and so we observed a clear S-shape curve in forward scan direction.

It is necessary to note that apart from iodide ions, methylammonium ( $\text{MA}^+$ ) ions may play a role in the hysteresis and degradation of perovskites.<sup>[52,61]</sup> The interaction between PCBM and  $\text{MA}^+$  as well as characterization of  $\text{MA}^+$  migration, however, are still not clearly elucidated. In addition, more and more evidences offer to present the critical role of grain boundary in the ion migration. However, due to resolution limitation of PL imaging microscopy, which is in  $\approx \mu\text{m}$  scale, it is difficult to directly explore the ion motion in the vicinity of grain boundary in our perovskite films (with grain size  $\approx 100$  nm). In the following experiment, by investigating perovskite films with various sizes, it is possible to reveal the influence of grain boundary or even directly visualize the migration of ions in the grain boundary.

Our study also provides prospects for addressing the hysteresis problem in perovskite light-emitting diodes (LEDs), which is also much of concern.<sup>[62]</sup> Reducing defect/ion accumulation at perovskite/external contacts can increase the device stability as it has been demonstrated with the help of 2D or low-dimensional layered perovskites.<sup>[63]</sup> PCBM, however, may have to be used with care in LED devices as PCBM can greatly quench the emission of LEDs. Immobile (i.e., polymerized) derivatives, instead may become of great interest as PSC/ETL interlayers.

### 3. Conclusion

In summary, the comparison of PSCs using PCBM and PPCBM layer reveals that diffusion of PCBM molecules into grain boundaries of a polycrystalline perovskite film takes place and plays a significant role in the suppression of hysteresis in  $J$ - $V$  curve. By employing PL imaging microscopy, we directly in situ visualize and parameterize the ionic migration under external electrical fields. The ionic mobility is reduced by one order of magnitude, and temperature dependent chronoamperometric measurements show that the activation energy increases with the presence of PCBM molecules. Accounting for these results, we close with a proposed mechanism in the suppression of hysteresis in PSCs with PCBM layer. PCBM molecules immobilize

the iodine ions or vacancies in the bulk of the perovskite layer, reducing the impact of modulation of internal field/interfacial barriers under the external electrical field. This finding will pave paths to the improvement on the device stability and better performance. We reiterate that especially grain boundaries are responsible for an effective ion/vacancy migration which can be impeded through efficient passivation.

#### 4. Experimental Section

**Sample Preparation:**  $\text{CH}_3\text{NH}_3\text{I}$  (MAI) was purchased from Dyesol company, Spiro-OMeTAD was purchased from Merck company, all the other chemicals were purchased from Sigma-Aldrich and were used as received without further purification. For  $\text{CH}_3\text{NH}_3\text{PbI}_{3-x}\text{Cl}_x$  precursor solution,  $\text{CH}_3\text{NH}_3\text{I}$ , and  $\text{PbCl}_2$  were dissolved in anhydrous Dimethylformamide at 3:1 molar ratio. Preparation of Spiro-OMeTAD solution: 72.3 mg Spiro-OMeTAD was dissolved in 1 mL chlorobenzene with an additive of 43.2  $\mu\text{L}$  4-tert-butylpyridine. After that, 26.3  $\mu\text{L}$  lithium bis(trifluoromethane)sulfonimide solution (520 mg  $\text{mL}^{-1}$  in acetonitrile) was added.

Fluorine-doped tin oxide ( $\text{F:SnO}_2$ ) coated glass was patterned by Zn power and HCl solution. FTO glasses were washed successively with acetone, 2% hellmanex diluted in deionized water, deionized water, and isopropanol for 10 min each. A compact  $\text{TiO}_2$  layer was deposited by spraying a solution of titanium diisopropoxide bis(acetylacetonate) (0.6 mL) in ethanol (21.4 mL) at 450 °C for 90 min in ambient atmosphere. The PCBM and PPCBM layer thicknesses were optimized for best electronic performance. For PCBM a 10 mg  $\text{mL}^{-1}$  solution in chlorobenzene was spin-coated at 3000 rpm for 30 s. After 10 min annealing at 100 °C,  $\text{CH}_3\text{NH}_3\text{PbI}_{3-x}\text{Cl}_x$  perovskite solution was spin-coated on the PCBM layer at 3000 rpm for 60 s. For the devices using PPCBM, 5 mg  $\text{mL}^{-1}$  PPCBM in 1,2-dichlorobenzene was spin-coated at 2000 rpm for 30 s. Following that, the  $\text{CH}_3\text{NH}_3\text{PbI}_{3-x}\text{Cl}_x$  perovskite solution was spin-coated on this PCBM layer at 3000 rpm for 60 s. After drying in a nitrogen glovebox for 30 min, the as-spun films were annealed at 105 °C for 1 h 15 min on a hotplate. Subsequently, the hole transport layer (Spiro-OMeTAD solution) was deposited by spin-coating at 4000 rpm for 30 s. The device fabrication steps above were carried out in a nitrogen filled glovebox. After this, devices were transported to a dry box and stored there overnight enabling Spiro-OMeTAD oxidation. Finally, a 70 nm Au electrode was deposited by thermal evaporation in a chamber with a pressure of  $1 \times 10^{-6}$  mbar. The structure of the fabricated solar cell is FTO/ $\text{TiO}_2$ /perovskite/Spiro-OMeTAD/Au or FTO/ $\text{TiO}_2$ /PCBM or PPCBM/perovskite/Spiro-OMeTAD/Au.

Perovskite films for PL imaging microscopy and XPS are prepared as follows: The glass substrates were cleaned using an ultrasound bath with acetone for 5 min and another 5 min in isopropanol. After treatment with  $\text{O}_3$  plasma, the perovskite precursor solution was spin coated on the substrates in a  $\text{N}_2$  glove box. For perovskite PCBM bulk heterojunction devices, the perovskite precursor solution was mixed together with the PCBM solution with molar ratio Pb/PCBM = 500:1. For the perovskite/PCBM bilayer and perovskite/PPCBM devices, the perovskite film was directly deposited on the PCBM layer or PPCBM layer. All the films were annealed at 105 °C for 1 h 15 min. For PL imaging microscopy, in order to apply electrical field, lateral configured gold electrodes were evaporated on top of these films using a shadow mask. The distance between parallel electrodes was 200  $\mu\text{m}$  and the interdigitating electrode geometry provided a ratio between channel width  $W$  and length  $L$ ,  $W/L$  of 500. In the end, to protect the film from the oxygen and water, a 40 mg  $\text{mL}^{-1}$  poly(methyl methacrylate) (PMMA) solution dissolved in butyl acetate (anhydrous, 99%) was spin-coated at speed of 2000 rpm for 60 s.

**J–V Measurement of Device:** J–V measurements were carried out within inert environment using a Keithley 2400 source measure unit under 100  $\text{mW cm}^{-2}$  illumination from an AM 1.5 solar simulator (Oriel company). The active area of 4 and 9  $\text{mm}^2$  were defined by the overlap of

a black mask aperture area, the FTO and the evaporated top electrode. The light intensity was calibrated by a Si detector. No biasing process was applied prior to the scanning, we scanned from 1.2 to  $-0.1$  V and then measured the reverse scanning continuously. The scanning speed is 0.8  $\text{V s}^{-1}$  and each step was 0.01 V. Number of power line cycles (NPLC) was 0.1.

**PL Imaging Microscopy:** The setup of PL microscope is shown in detail in Figure S4, Supporting Information. The excitation source was a white light LED and it was combined with a dichroic mirror and a PL filter (HC 440 SP, AHF analysentechnik AG) in the excitation beam path. There was another filter (HC-BS 484, AHF analysentechnik AG) for the emitted PL signal from the sample. As a result, the wavelength of excitation beam was up to 440 nm and the emission signal comes to detector was above 490 nm. All the PL images were recorded by a CCD camera (Pco. Pixel fly, PCO AG) with an exposure time of 200 ms. For in situ electric measurement, samples were fixed on the microscope table and regions between Au electrodes were focused. An electric field was applied between the Au electrodes, simultaneously PL images were captured. The applied electric field varied from 5 to 40 V.

**XPS Characterization:** All the XPS measurements were carried with a PHI 5000 VersaProbe III system. An Al K $\alpha$  excitation source was used ( $h\nu = 1486.6$  eV) at a pass energy of 55 eV. A gas cluster ion beam (GCIB) forming clusters of  $\approx 2500$  Argon atoms was used to sputter the film step by step with a sputtering energy of 10 kV 30 nA and a duration of 0.5 min of each cycle.

**Temperature Dependent Chronoamperometric Measurements:** For temperature dependent J–V curves measurement, the samples were put into a continuous flow cryostat (Oxford Instruments, Optistat CF). PSCs (with and without PCBM layer) with effective area 4  $\text{mm}^2$  were measured in different temperatures (180, 220, 260, and 300°K) without light illumination. Step-wise voltage was applied to the cell from 1.2 to 0.6 V with the step of  $-0.2$  V. The corresponding current density was recorded per microsecond.

#### Supporting Information

Supporting Information is available from the Wiley Online Library or from the author.

#### Acknowledgements

The authors gratefully acknowledge the financial support by the Bavarian State Ministry of Science, Research, and the Arts for the Collaborative Research Network “Solar Technologies go Hybrid,” and the German Research Foundation (DFG). Y.Z. acknowledges funding from China Scholarship Council. C.L. acknowledges funding from the National Natural Science Foundation of China (61974126, 51902273). The authors thank Prof. Richard Hildner for experimental support. They thank the Bavarian Polymer Institute enabling the SEM characterization.

#### Conflict of Interest

The authors declare no conflict of interest.

#### Keywords

ion migration, J–V curve hysteresis, PCBM, perovskites

Received: October 28, 2019

Revised: January 27, 2020

Published online:

- [1] A. Kojima, K. Teshima, Y. Shirai, T. Miyasaka, *J. Am. Chem. Soc.* **2009**, *131*, 6050.
- [2] D. P. Nenon, J. A. Christians, L. M. Wheeler, J. L. Blackburn, E. M. Sanehira, B. Dou, M. L. Olsen, K. Zhu, J. J. Berry, J. M. Luther, *Energy Environ. Sci.* **2016**, *9*, 2072.
- [3] D. Luo, W. Yang, Z. Wang, A. Sadhanala, Q. Hu, R. Su, R. Shivanna, G. F. Trindade, J. F. Watts, Z. Xu, T. Liu, K. Chen, F. Ye, P. Wu, L. Zhao, J. Wu, Y. Tu, Y. Zhang, X. Yang, W. Zhang, R. H. Friend, Q. Gong, H. J. Snaith, R. Zhu, *Science* **2018**, *360*, 1442.
- [4] F. Zhang, D. Bi, N. Pellet, C. Xiao, Z. Li, J. J. Berry, S. M. Zakeeruddin, K. Zhu, M. Grätzel, *Energy Environ. Sci.* **2018**, *11*, 3480.
- [5] Z. Wang, Q. Lin, F. P. Chmiel, N. Sakai, L. M. Herz, H. J. Snaith, *Nat. Energy* **2017**, *2*, 17135.
- [6] S. Ravishanker, S. Gharibzadeh, C. Roldán-Carmona, G. Grancini, Y. Lee, M. Ralaivisoa, A. M. Asiri, N. Koch, J. Bisquert, M. K. Nazeeruddin, *Joule* **2018**, *2*, 788.
- [7] W. Tress, N. Marinova, T. Moehl, S. M. Zakeeruddin, M. K. Nazeeruddin, M. Grätzel, *Energy Environ. Sci.* **2015**, *8*, 995.
- [8] H. J. Snaith, A. Abate, J. M. Ball, G. E. Eperon, T. Leijtens, N. K. Noel, S. D. Stranks, J. T.-W. Wang, K. Wojciechowski, W. Zhang, *J. Phys. Chem. Lett.* **2014**, *5*, 1511.
- [9] R. Gottesman, L. Gouda, B. S. Kalanoor, E. Haltzi, S. Tirosh, E. Rosh-Hodesh, Y. Tischler, A. Zaban, C. Quarti, E. Mosconi, F. De Angelis, *J. Phys. Chem. Lett.* **2015**, *6*, 2332.
- [10] S. Meloni, T. Moehl, W. Tress, M. Frankevičius, M. Saliba, Y. H. Lee, P. Gao, M. K. Nazeeruddin, S. M. Zakeeruddin, U. Rothlisberger, M. Grätzel, *Nat. Commun.* **2016**, *7*, 10334.
- [11] C. Li, S. Tscheuschner, F. Paulus, P. E. Hopkinson, J. Kießling, A. Köhler, Y. Vaynzof, S. Huettnner, *Adv. Mater.* **2016**, *28*, 2446.
- [12] C. Li, A. Guerrero, Y. Zhong, A. Gräser, C. A. M. Luna, J. Köhler, J. Bisquert, R. Hildner, S. Huettnner, *Small* **2017**, *13*, 1701711.
- [13] L. Bertoluzzi, R. A. Belisle, K. A. Bush, R. Cheacharoen, M. D. McGehee, B. C. O'Regan, *J. Am. Chem. Soc.* **2018**, *140*, 12775.
- [14] A. Oranskaia, J. Yin, O. M. Bakr, J.-L. Brédas, O. F. Mohammed, *J. Phys. Chem. Lett.* **2018**, *9*, 5474.
- [15] J. Xu, A. Buin, A. H. Ip, W. Li, O. Voznyy, R. Comin, M. Yuan, S. Jeon, Z. Ning, J. J. McDowell, P. Kanjanaboos, J.-P. Sun, X. Lan, L. N. Quan, D. H. Kim, I. G. Hill, P. Maksymovych, E. H. Sargent, *Nat. Commun.* **2015**, *6*, 7081.
- [16] F. Zhang, W. Shi, J. Luo, N. Pellet, C. Yi, X. Li, X. Zhao, T. J. S. Dennis, X. Li, S. Wang, Y. Xiao, S. M. Zakeeruddin, D. Bi, M. Grätzel, *Adv. Mater.* **2017**, *29*, 1606806.
- [17] Y. Shao, Z. Xiao, C. Bi, Y. Yuan, J. Huang, *Nat. Commun.* **2014**, *5*, 5784.
- [18] E. Bi, H. Chen, F. Xie, Y. Wu, W. Chen, Y. Su, A. Islam, M. Grätzel, X. Yang, L. Han, *Nat. Commun.* **2017**, *8*, 15330.
- [19] K. Wojciechowski, S. D. Stranks, A. Abate, G. Sadoughi, A. Sadhanala, N. Kopidakis, G. Rumbles, C.-Z. Li, R. H. Friend, A. K.-Y. Jen, H. J. Snaith, *ACS Nano* **2014**, *8*, 12701.
- [20] G. Xing, B. Wu, S. Chen, J. Chua, N. Yantara, S. Mhaisalkar, N. Mathews, T. C. Sum, *Small* **2015**, *11*, 3606.
- [21] N. J. Jeon, J. H. Noh, W. S. Yang, Y. C. Kim, S. Ryu, J. Seo, S. I. Seok, *Nature* **2015**, *517*, 476.
- [22] H. Tsai, W. Nie, J. C. Blancon, C. C. Stoumpos, R. Asadpour, B. Harutyunyan, A. J. Neukirch, R. Verduzco, J. J. Crochet, S. Tretiak, L. Pedesseau, J. Even, M. A. Alam, G. Gupta, J. Lou, P. M. Ajayan, M. J. Bedzyk, M. G. Kanatzidis, A. D. Mohite, *Nature* **2016**, *536*, 312.
- [23] R. S. Sanchez, V. Gonzalez-Pedro, J. W. Lee, N. G. Park, Y. S. Kang, I. Mora-Sero, J. Bisquert, *J. Phys. Chem. Lett.* **2014**, *5*, 2357.
- [24] X. Cao, Y. Li, C. Li, F. Fang, Y. Yao, X. Cui, J. Wei, *J. Phys. Chem. C* **2016**, *120*, 22784.
- [25] M. Hufnagel, M.-A. Muth, J. C. Brendel, M. Thelakktat, *Macromolecules* **2014**, *47*, 2324.
- [26] M. Hufnagel, M. Thelakktat, *J. Polym. Sci., Part B: Polym. Phys.* **2016**, *54*, 1125.
- [27] J. M. Frost, K. T. Butler, F. Brivio, C. H. Hendon, M. van Schilfarga, A. Walsh, *Nano Lett.* **2014**, *14*, 2584.
- [28] X. Wu, M. T. Trinh, D. Niesner, H. Zhu, Z. Norman, J. S. Owen, O. Yaffe, B. J. Kudsich, X.-Y. Zhu, *J. Am. Chem. Soc.* **2015**, *137*, 2089.
- [29] C. Li, S. Tscheuschner, F. Paulus, P. E. Hopkinson, J. Kießling, A. Köhler, Y. Vaynzof, S. Huettnner, *Adv. Mater.* **2016**, *28*, 2446.
- [30] D. A. Jacobs, Y. Wu, H. Shen, C. Barugkin, F. J. Beck, T. P. White, K. Weber, K. R. Catchpole, *Phys. Chem. Chem. Phys.* **2017**, *19*, 3094.
- [31] C. Li, A. Guerrero, Y. Zhong, S. Huettnner, *J. Phys.: Condens. Matter* **2017**, *29*, 193001.
- [32] W. Tress, *J. Phys. Chem. Lett.* **2017**, *8*, 3106.
- [33] P. Lopez-Varo, J. A. Jiménez-Tejada, M. García-Rosell, S. Ravishanker, G. Garcia-Belmonte, J. Bisquert, O. Almora, *Adv. Energy Mater.* **2018**, *8*, 1702772.
- [34] Y. Deng, Z. Xiao, J. Huang, *Adv. Energy Mater.* **2015**, *5*, 1500721.
- [35] S. T. Birkhold, J. T. Precht, H. Liu, R. Giridharagopal, G. E. Eperon, L. Schmidt-Mende, X. Li, D. S. Ginger, *ACS Energy Lett.* **2018**, *3*, 1279.
- [36] Y. Yamada, T. Nakamura, M. Endo, A. Wakamiya, Y. Kanemitsu, *J. Am. Chem. Soc.* **2014**, *136*, 11610.
- [37] S. Chen, X. Wen, R. Sheng, S. Huang, X. Deng, M. A. Green, A. Ho-Baillie, *ACS Appl. Mater. Interfaces* **2016**, *8*, 5351.
- [38] D. W. de Quilettes, S. M. Vorpahl, S. D. Stranks, H. Nagaoka, G. E. Eperon, M. E. Ziffer, H. J. Snaith, D. S. Ginger, *Science* **2015**, *348*, 683.
- [39] C. Li, A. Guerrero, S. Huettnner, J. Bisquert, *Nat. Commun.* **2018**, *9*, 5113.
- [40] Y. Zhong, C. A. M. Luna, R. Hildner, C. Li, S. Huettnner, *APL Mater.* **2019**, *7*, 041114.
- [41] E. Bandiello, J. Ávila, L. Gil-Escrig, E. Tekelenburg, M. Sessolo, H. J. Bolink, *J. Mater. Chem. A* **2016**, *4*, 18614.
- [42] E. Mosconi, F. De Angelis, *ACS Energy Lett.* **2016**, *1*, 182.
- [43] X. Wu, M. T. Trinh, D. Niesner, H. Zhu, Z. Norman, J. S. Owen, O. Yaffe, B. J. Kudsich, X.-Y. Zhu, *J. Am. Chem. Soc.* **2015**, *137*, 2089.
- [44] J. M. Lownsbury, J. C. Sharp, E. J. Mann, C. T. Campbell, *J. Phys. Chem. C* **2015**, *119*, 18444.
- [45] R. P. Vasquez, R. A. Brain, D. Ross, N. Yeh, *Surf. Sci. Spectra* **1992**, *1*, 242.
- [46] S. Olthof, K. Meerholz, *Sci. Rep.* **2017**, *7*, 40267.
- [47] Q. Sun, P. Fassl, D. Becker-Koch, A. Bausch, B. Rivkin, S. Bai, P. E. Hopkinson, H. J. Snaith, Y. Vaynzof, *Adv. Energy Mater.* **2017**, *7*, 1700977.
- [48] F. Fischer, T. Hahn, H. Bässler, I. Bauer, P. Strohmriegel, A. Köhler, *Adv. Funct. Mater.* **2014**, *24*, 6172.
- [49] B. Watts, W. J. Belcher, L. Thomsen, H. Ade, P. C. Dastoor, *Macromolecules* **2009**, *42*, 8392.
- [50] Y. Yuan, J. Huang, *Acc. Chem. Res.* **2016**, *49*, 286.
- [51] J. M. Azpiroz, E. Mosconi, J. Bisquert, F. De Angelis, *Energy Environ. Sci.* **2015**, *8*, 2118.
- [52] Y. Yuan, J. Chae, Y. Shao, Q. Wang, Z. Xiao, A. Centrone, J. Huang, *Adv. Energy Mater.* **2015**, *5*, 1500615.
- [53] T. Y. Yang, G. Gregori, N. Pellet, M. Grätzel, J. Maier, *Angew. Chem., Int. Ed.* **2015**, *54*, 7905.
- [54] Y. Yuan, Q. Wang, Y. Shao, H. Lu, T. Li, A. Gruverman, J. Huang, *Adv. Energy Mater.* **2016**, *6*, 1501803.
- [55] C. Eames, J. M. Frost, P. R. F. Barnes, B. C. O'Regan, A. Walsh, M. S. Islam, *Nat. Commun.* **2015**, *6*, 7497.
- [56] G. H. Vineyard, *J. Phys. Chem. Solids* **1957**, *3*, 121.
- [57] C. Wert, C. Zener, *Phys. Rev.* **1949**, *76*, 1169.

- [58] H. Yu, H. Lu, F. Xie, S. Zhou, N. Zhao, *Adv. Funct. Mater.* **2016**, 26, 1411.
- [59] Y. Zhang, M. Liu, G. E. Eperon, T. C. Leijtens, D. McMeekin, M. Saliba, W. Zhang, M. De Bastiani, A. Petrozza, L. M. Herz, M. B. Johnston, H. Lin, H. J. Snaith, *Mater. Horiz.* **2015**, 2, 315.
- [60] G. Garcia-Belmonte, J. Bisquert, *ACS Energy Lett.* **2016**, 1, 683.
- [61] T. Leijtens, E. T. Hoke, G. Grancini, D. J. Slotcavage, G. E. Eperon, J. M. Ball, M. De Bastiani, A. R. Bowring, N. Martino, K. Wojciechowski, M. D. McGehee, H. J. Snaith, A. Petrozza, *Adv. Energy Mater.* **2015**, 5, 1500962.
- [62] Z.-K. Tan, R. S. Moghaddam, M. L. Lai, P. Docampo, R. Higler, F. Deschler, M. Price, A. Sadhanala, L. M. Pazos, D. Credgington, F. Hanusch, T. Bein, H. J. Snaith, R. H. Friend, *Nat. Nanotechnol.* **2014**, 9, 687.
- [63] C. Li, N. Wang, A. Guerrero, Y. Zhong, H. Long, Y. Miao, J. Bisquert, J. Wang, S. Huettner, *J. Phys. Chem. Lett.* **2019**, 10, 6857.

Copyright WILEY-VCH Verlag GmbH & Co. KGaA, 69469 Weinheim, Germany, 2020.

## Supporting Information

For *Adv. Funct. Mater.*, DOI: 10.1002/adfm.201908920

# Role of PCBM in the Suppression of Hysteresis in Perovskite Solar Cells

Yu Zhong, Martin Hufnagel, Mukundan Thelakkat, Cheng Li,\* Sven Huettnner\*

\* Author to whom correspondence should be addressed: [cheng.li@uni-bayreuth.de](mailto:cheng.li@uni-bayreuth.de) and [sven.huettnner@uni-bayreuth.de](mailto:sven.huettnner@uni-bayreuth.de)

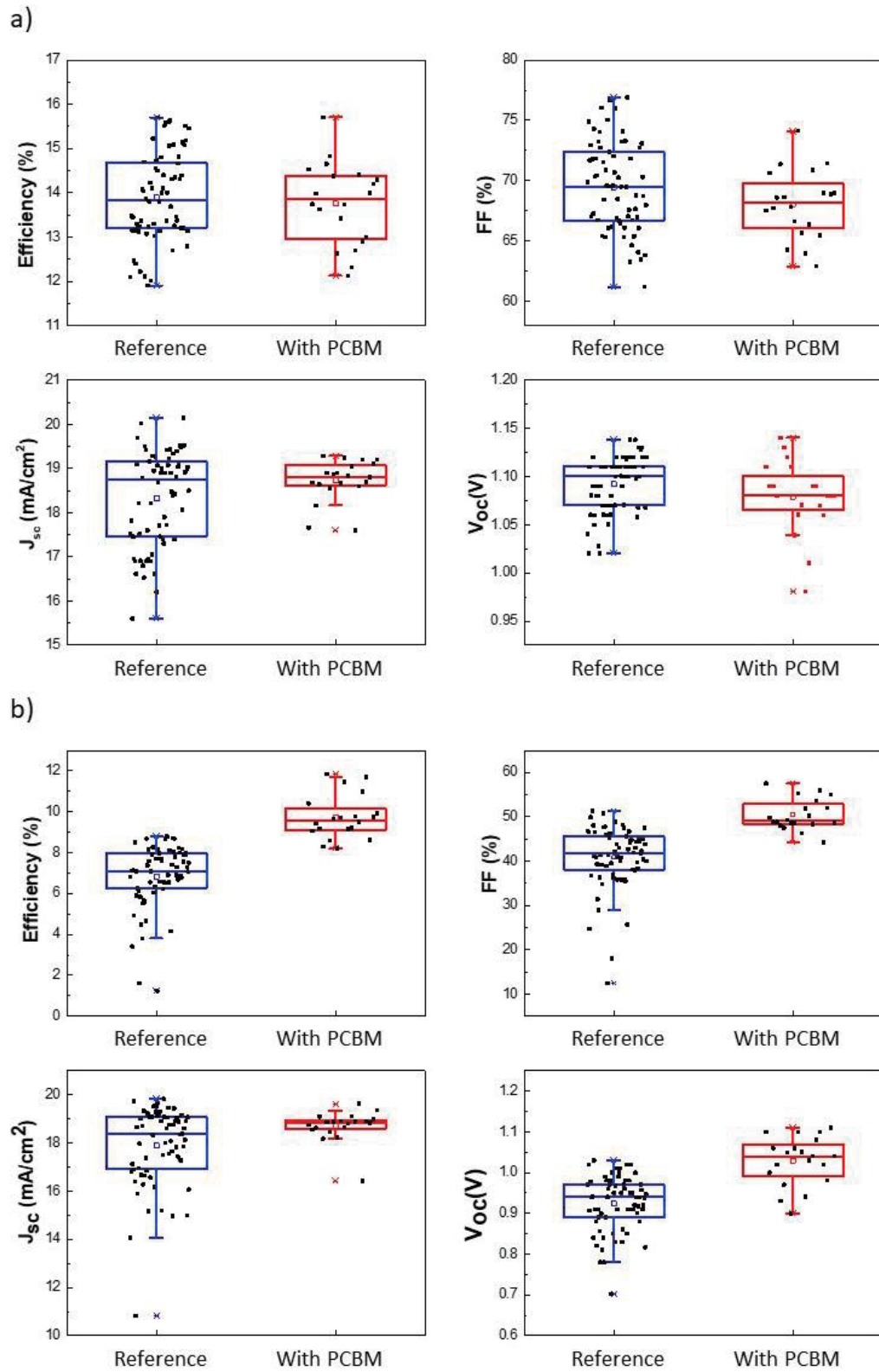


**Figure S1:** Photovoltaic parameters extracted from current–voltage measurements of a series of solar cells with two different structures. (a) and (b) show the parameters of reverse sweeping and forward sweep separately. Reference: FTO/compact TiO<sub>2</sub>/perovskite/Spiro-OMeTAD/Au; with PCBM: FTO/compact TiO<sub>2</sub>/PCBM/perovskite/Spiro-OMeTAD/Au.



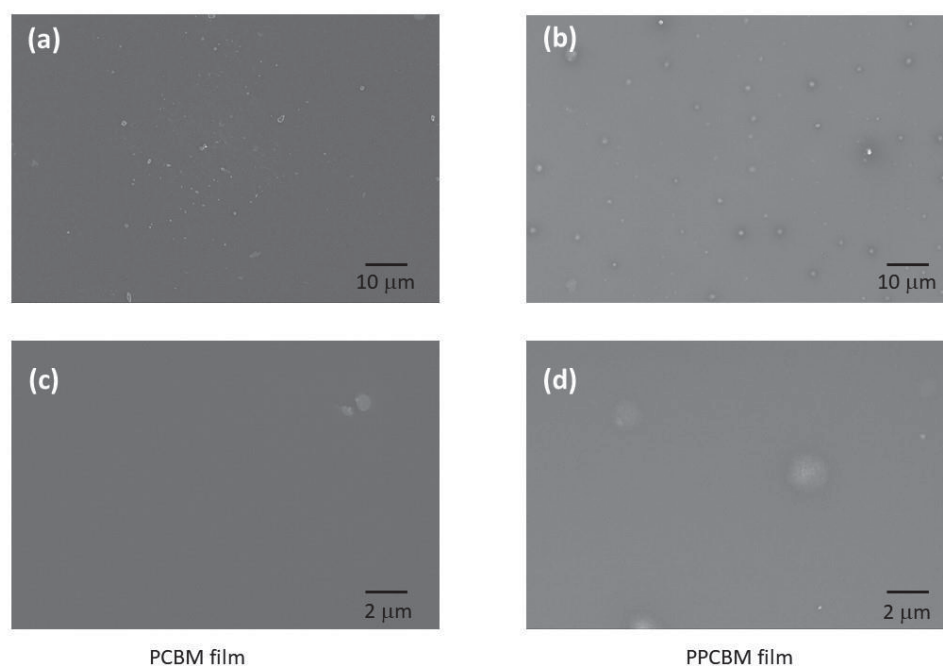


**Figure S2-1:** SEM images: (a) and (c) PCBM film (b) and (d) PPCBM film. The dots in the images are PCBM aggregations or phase segregation of PPCBM.

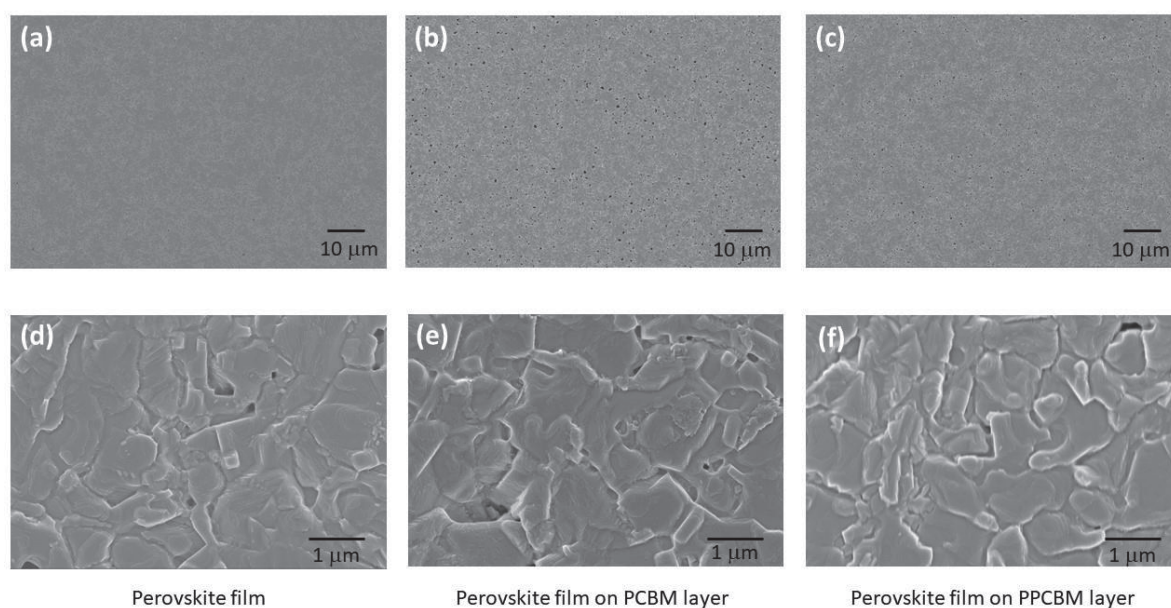


**Figure S2-2:** SEM images of perovskite film formed on different bottom layer: (a) and (d) on glass, (b) and (e) on PCBM layer, (c) and (f) on PPCBM layer. Despite of more pinholes in perovskite films on PCBM and PPCBM, they do not show an obvious difference.

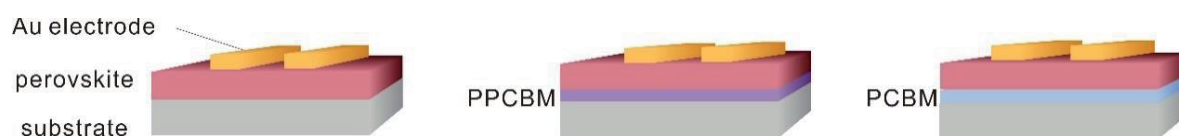


**Figure S3:** Device architecture with lateral electrodes. Through the electrodes, electric field can be applied on the perovskite material and its time-resolved PL images are recorded. (a) is perovskite reference. (b) is perovskite/PPCBM bilayer system. (c) is perovskite/PCBM bilayer system.

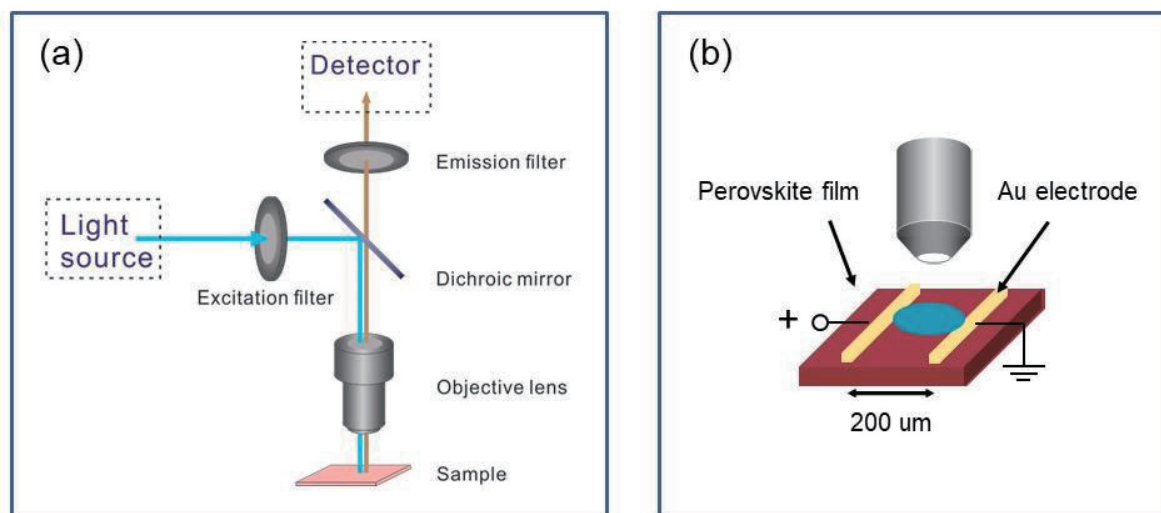


**Figure S4:** (a) Schematic diagram of photoluminescence imaging microscopy. The specimen is illuminated with a green laser (wavelength: 432nm). The blue line is the incident beam. The orange line is the emission signal. (b) Schematic diagram for the ion migration observation setup using the PL imaging microscopy. An electric field is applied between the two lateral Au electrodes.

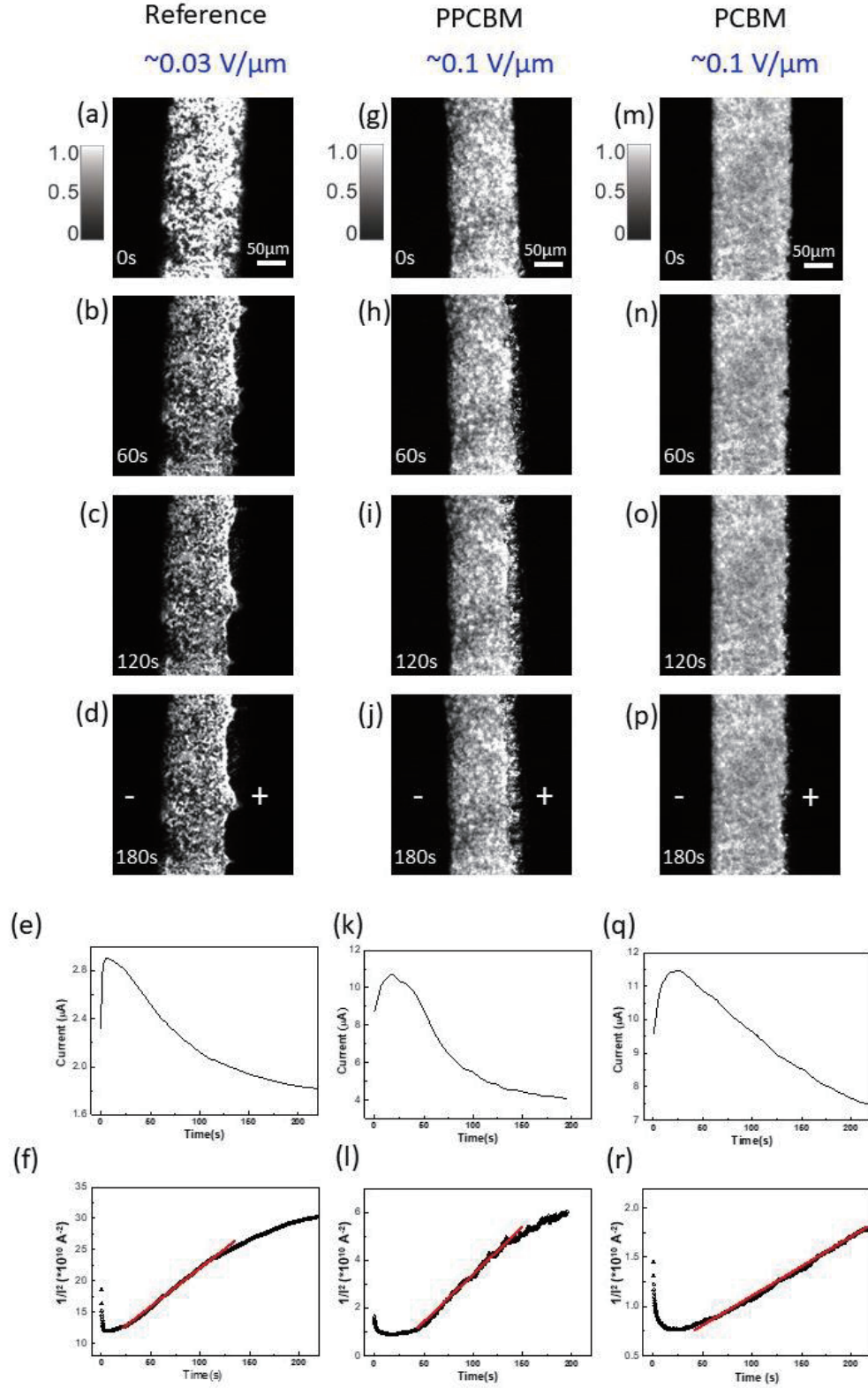


**Figure S5:** (a)~(d) Temporal-resolved PL images of  $\text{MAPbI}_x\text{Cl}_{3-x}$  reference sample under an external electrical field, (e) is its time-dependent current and (f) depicts  $1/I^2$  over time. (g)~(j) PL images of a perovskite/PPCBM bilayer sample under external electrical field, (k) is its time-dependent current and (l) depicts  $1/I^2$  with time. (m)~(p) PL images of a perovskite/PCBM bilayer sample under external electrical field, (q) is its time-dependent current and (r) depicts  $1/I^2$  over time.

The intensity scale bar and size scale bar (50 $\mu\text{m}$ ) for the PL images is the same in each row. The device structures are shown in Figure S3. The emissive part is the perovskite, which is between two Au electrodes. The applied bias is noted above each image row in blue. When a bias is applied between the two electrodes, the current and the PL changes are *in situ* recorded. The plus and minus sign stand for its positive and negative electrodes. The exposure time per image is 200 ms. The illumination intensity is  $\sim 35 \text{ mW/cm}^2$ . The red line in (f), (i) and (r) is the fitting line, showing the linear relationship between  $1/I^2$  and  $t$  in a certain region.

### S6: The dynamic model to determine iodine vacancy mobility <sup>[1]</sup>

The electrical field can induce the iodine vacancies  $\text{V}_\text{I}^+$  drift. The iodine vacancies fill the anode area up to a density  $C_\text{m}$ , compensating its original p-doping and reduce majority carrier density:  $p_\text{I} = p_0 - C_\text{m}$ .  $p_0$  represents the doping of perovskite before electrical field and  $p_\text{I}$  is the doping level after the flow of iodine vacancy  $\text{V}_\text{I}^+$ . These iodine vacancies drift from the positive side to the negative side, leaving behind the reduction of radiative recombination rate. This is related to observation in Figure S5 that PL starts to quench from the anode area.

To better demonstrate the model, we introduce two variables:

$$\gamma = \frac{p_0}{p_1} - 1 \quad \text{and} \quad a = \frac{2\gamma v_0}{d I_0^2}.$$

( $d$ : the distance between anode and cathode;  $v_0$ : the initial velocity of PL quenching;  $I_0$ : initial electrical current)

The electrical current depends on time:

$$I(t) = (1 + \frac{2\gamma v_0 t}{d})^{-1/2} I_0 \quad \text{Equation 1}$$

By transforming Equation 1, it is obtained:

$$\frac{1}{I^2} = \frac{1}{I_0^2} + at \quad \text{Equation 2}$$

So in Figure S5 (f), (i) and (r), the red fitting lines follow Equation 2 and the slope is  $a$ .

The initial velocity is:

$$v_0 = \frac{p_0 \mu_c V}{p_1 d} \quad \text{Equation 3}$$

( $V$ : applied electrical field,  $\mu_c$ : the mobility of iodine vacancy)

Finally, we can obtain:

$$\mu_c = \frac{ad^2 I_0 I^2}{2V(I_0 - I)}$$

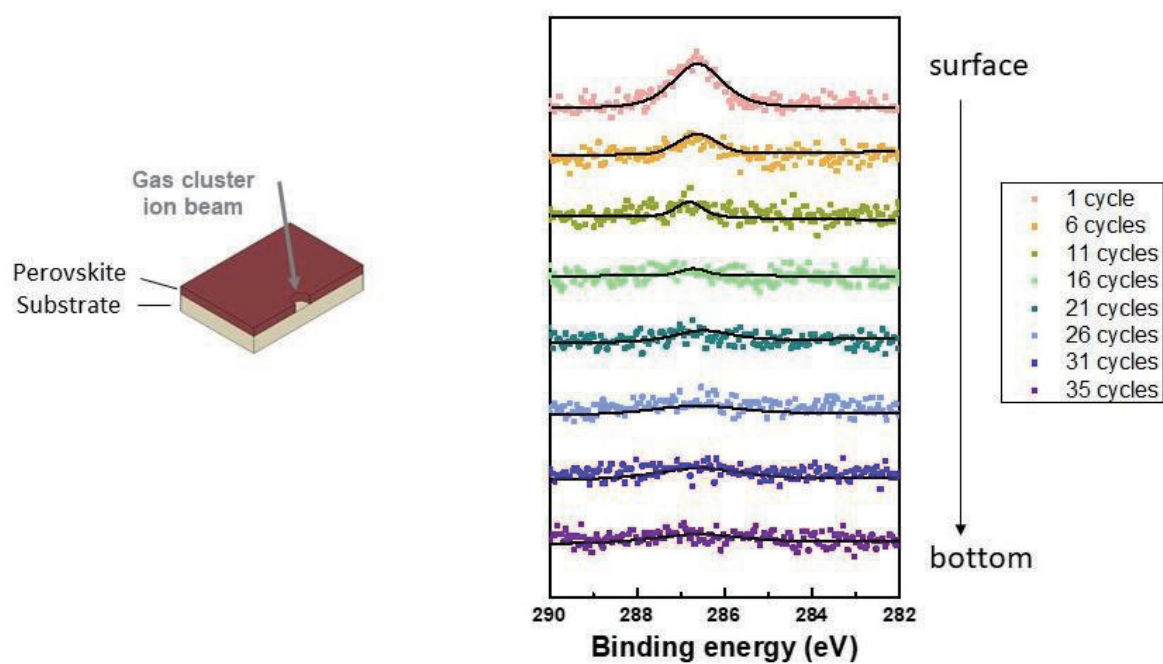


**Figure S7:** XPS spectra of C1s peak from perovskite reference sample with sputtering visualized on the left. Right: C1s peak of perovskite film after different sputtering cycles.

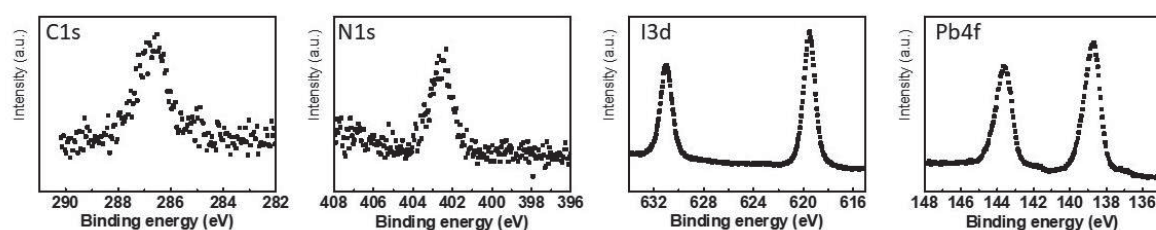


**Figure S8:** XPS spectra of a perovskite reference sample.

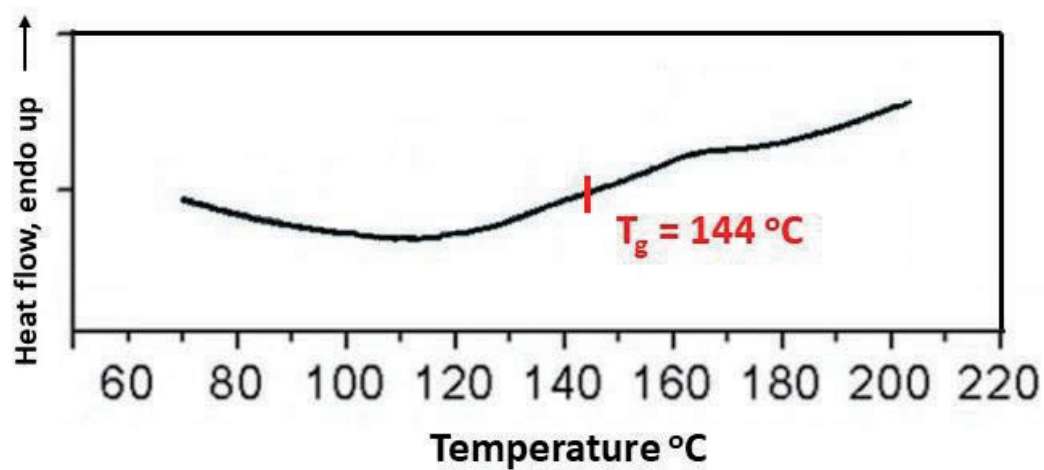


Figure S9: Differential scanning calorimetry of PPCBM as discussed in detail in by Hufnagel et al.<sup>[2]</sup>

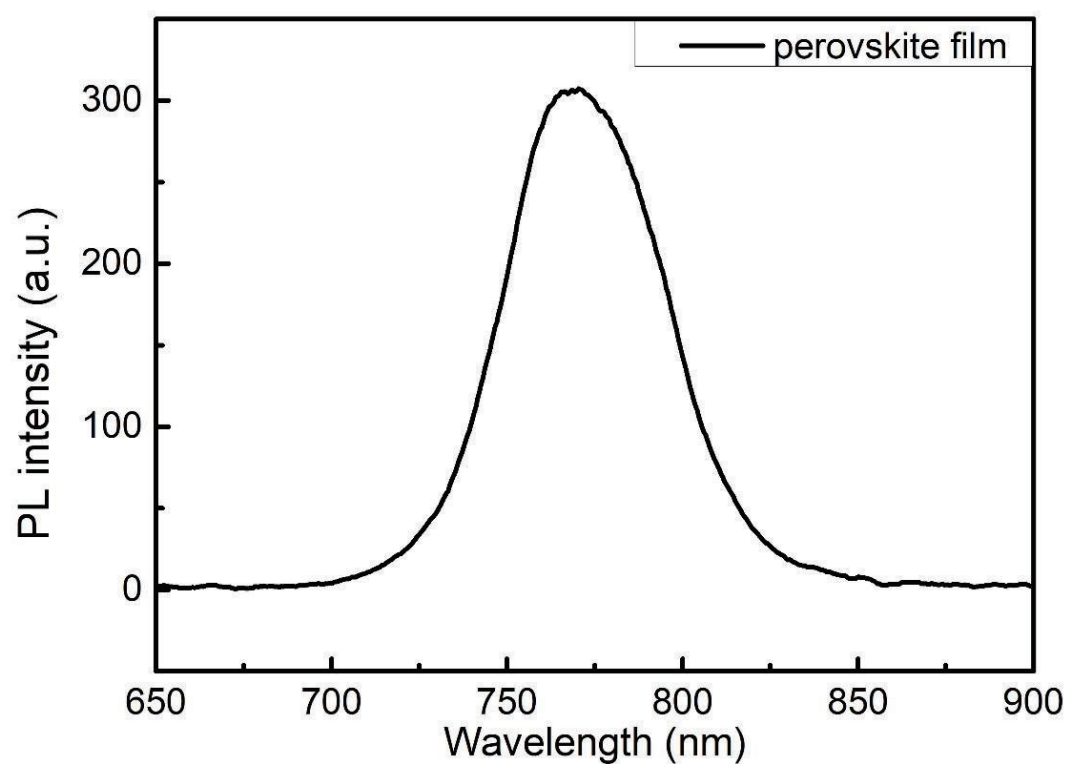
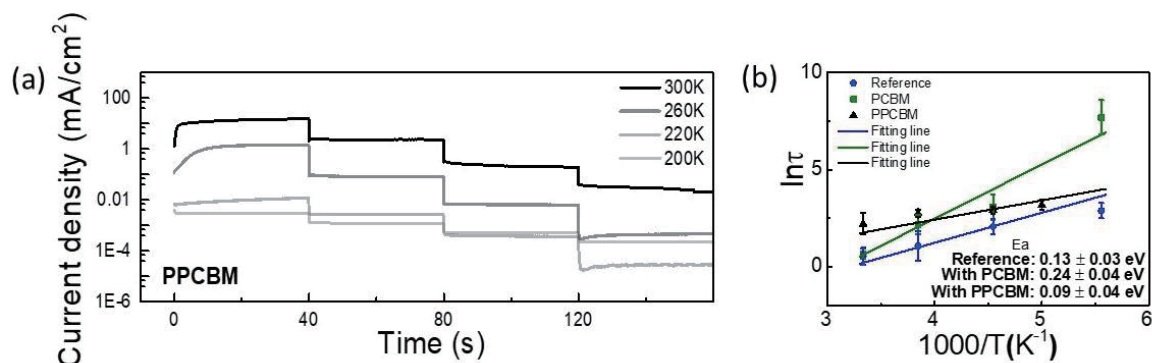
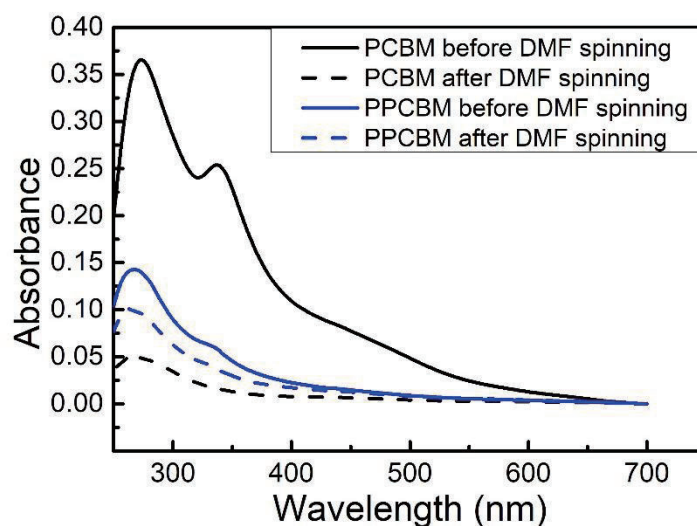


Figure S10: PL spectrum of a reference perovskite film.





**Figure S11:** (a) Temperature dependent chronoamperometric curve of PPCBM device, from 1.2 V to 0.6 V with step of 0.2 V, each voltage lasts 40 sec. (b) Activation energy of iodide ions in pure perovskite (reference), perovskite on PCBM layer and perovskite on PPCBM layer devices, respectively. The activation energy in perovskite on PCBM layer is higher than that in pure perovskite and perovskite on PPCBM layer, indicating the passivation effect of PCBM layer.



**Figure S12:** Absorption spectra of a PCBM film and a PPCBM film, when spin coating pure DMF solvent on top of the film (3000 rpm, 60s). Comparing with PCBM film, the absorbance reduction of PPCBM film is small. As PPCBM is hard to dissolve in DMF, the incorporated PPCBM in perovskite film during spin coating process is little. The solubility of PCBM in DMF is small, but the process is fast. It shows that there is a fraction of PCBM that can be partially dissolved in DMF during the perovskite spin coating process and already be incorporated within in perovskite film next to interdiffusion during the perovskite annealing step. The absorbance data shows, that the initial PPCBM layer is significantly thinner compared to the PCBM layer. Both layers have been optimized towards their best electronic properties in the devices.

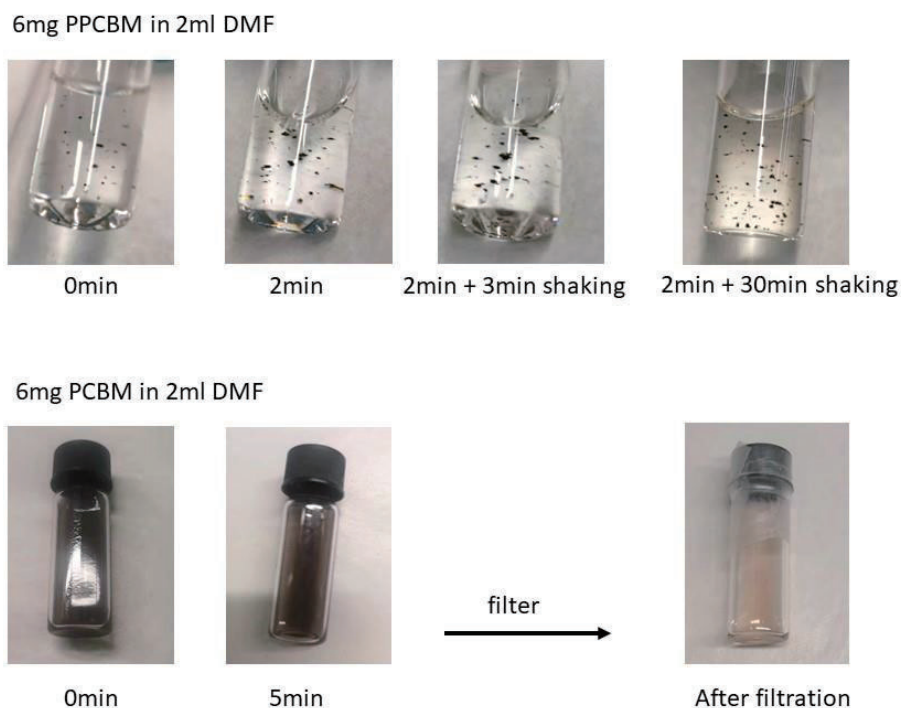


**Figure S13:** Images taken when we dissolved 6mg PPCBM or PCBM in 2 ml DMF. For PPCBM, no obvious change was observed after 2 minutes' standing and 3 minutes' shaking. After 30 minutes' shaking, PPCBM started slowly to dissolve partially in DMF. For PCBM, the powder was dispersed in DMF. The PCBM suspension became black immediately, however no complete dissolution could be reached, showing that the solubility limit already has been reached. After filtration, most of the PCBM was filtered showing the small amount of PCBM that could be dissolved in DMF. These quick solubility tests were conducted at room temperature. We note, that these tests only show qualitative trends of DMF as a bad solvent.

## References

- [1] C. Li, A. Guerrero, S. Huettnner, J. Bisquert, *Nat. Commun.* **2018**, 9, 5113.
- [2] M. Hufnagel, M.-A. Muth, J. C. Brendel, M. Thelakkat, *Macromolecules* **2014**, 47, 2324

# 7 Investigating Two-Step MAPbI<sub>3</sub> Thin Film Formation during Spin Coating by Simultaneous *in situ* Absorption and Photoluminescence Spectroscopy

Mihirsinh Chauhan,<sup>‡</sup> Yu Zhong,<sup>‡</sup> Konstantin Schötz, Brijesh Tripathi, Anna Köhler, Sven Huettnner and Fabian Panzer

(<sup>‡</sup> Both authors contributed equally.)

Published in

*Journal of Materials Chemistry A*, **2020**, 8, 5086

(DOI: 10.1039/c9ta12409h)



Cite this: *J. Mater. Chem. A*, 2020, **8**, 5086

# Investigating two-step MAPbI<sub>3</sub> thin film formation during spin coating by simultaneous *in situ* absorption and photoluminescence spectroscopy†

Mihirsinh Chauhan,<sup>†ab</sup> Yu Zhong,<sup>†ac</sup> Konstantin Schötz,<sup>a</sup> Brijesh Tripathi,<sup>†d</sup> Anna Köhler,<sup>†ad</sup> Sven Huettnert<sup>c</sup> and Fabian Panzer<sup>†\*a</sup>

To date, the two-step processing method represents an attractive route for the thin film formation of halide perovskites. However, a fundamental understanding of the film formation dynamics in the case of spin coating methylammonium iodide (MAI) on PbI<sub>2</sub> has not been established yet. Here we apply *in situ* optical spectroscopy during the two-step film formation of the model halide perovskite MAPbI<sub>3</sub> via spin coating. We identify and analyze in detail the optical features that occur in the photoluminescence and the corresponding absorption spectra during processing. We find that the film formation takes place in five consecutive steps, including the formation of a MAPbI<sub>3</sub> capping layer via an interface crystallization and the occurrence of an intense dissolution–recrystallization process. Consideration of confinement and self-absorption effects in the PL spectra, together with consideration of the corresponding absorption spectra allows quantification of the growth rate of the initial interface crystallization, which is found to be 11 nm s<sup>−1</sup> under our processing conditions. We find that the main dissolution–recrystallization process happens at a rate of 445 nm s<sup>−1</sup>, emphasizing its importance to the overall processing.

Received 11th November 2019  
Accepted 23rd January 2020

DOI: 10.1039/c9ta12409h

rsc.li/materials-a

## 1. Introduction

The ongoing increase in the efficiencies of perovskite-based optoelectronic devices, in particular solar cells, has been delighting the research community for several years now. Key aspects for this development were various breakthroughs in the thin film processing of the perovskite layer. One of the most important solution-based processing approaches to date is the so-called two-step method, which was first reported in 2013.<sup>1,2</sup> In this method, a PbI<sub>2</sub> layer is produced in a first processing step, *e.g.* via spin coating, and then brought into contact with methylammonium iodide (MAI) dissolved in an alcohol, *e.g.* isopropanol (IPA), in a second processing step, thus initiating the growth of the perovskite MAPbI<sub>3</sub>. It is possible to realize the second processing step either by exposing the PbI<sub>2</sub> layer to a MAI gas phase, by dipping the PbI<sub>2</sub> layer into a MAI solution, or by spin coating the latter onto the

PbI<sub>2</sub> substrate. The main advantage of the two-step method is seen in the supposedly higher process control compared to other processing methods.<sup>3</sup> However, it became clear in the last few years that, similar to other solution-based film processing methods, the final morphological and thus optoelectronic properties sensitively depend on the precise processing conditions of the two-step method.<sup>4–8</sup> Some studies have investigated the film formation dynamics during the two-step method<sup>9</sup> and found that the MAPbI<sub>3</sub> crystallization process depends *e.g.* on the MAI concentration,<sup>10,11</sup> temperature,<sup>11,12</sup> and the timing of the processing steps.<sup>2</sup> Depending on the specific processing conditions it is possible that different types of crystallizations occur, namely *in situ* interface transformation or solid–liquid recrystallization, or both.<sup>13,14</sup> So far, most of the knowledge about the crystallization behavior of the two-step method was obtained for the case of dipping the PbI<sub>2</sub> layer in MAI solution, where crystallization takes place on relatively long time scales.<sup>3</sup> In contrast, faster crystallization takes place when applying MAI/IPA via spin-coating, which leads to more homogeneous, compact and smoother films and thus to better solar cells, making it a more technology relevant processing strategy.<sup>4</sup> Recently we developed a measurement setup that allows the measurement of absorption spectra and, in parallel, photoluminescence (PL) *in situ* during solution-based processing of semiconductor materials, such as spin-coating.<sup>15</sup> By investigating the optical properties of halide perovskites, it is possible to extract detailed information about

<sup>a</sup>Soft Matter Optoelectronics, University of Bayreuth, 95440 Bayreuth, Germany. E-mail: fabian.panzer@uni-bayreuth.de

<sup>b</sup>School of Technology, Pandit Deendayal Petroleum University, 382007 Gandhinagar, India

<sup>c</sup>Department of Chemistry, University of Bayreuth, 95440 Bayreuth, Germany

<sup>d</sup>Bayreuth Institute of Macromolecular Research (BIMF), Bavarian Polymer Institute (BPI), University of Bayreuth, 95440 Bayreuth, Germany

† Electronic supplementary information (ESI) available. See DOI: 10.1039/c9ta12409h

‡ These authors contributed equally.

their electronic structure, and concomitantly about their composition.<sup>16–20</sup> Thus, in this work, we use *in situ* absorption and simultaneous PL spectroscopy to investigate the film formation dynamics of MAPbI<sub>3</sub> for a two-step processing approach using spin coating. We observe changes in both absorption and PL during the spin-coating process. This allows us to categorize the film formation process into five different time ranges. By carefully considering quantum confinement and self-absorption effects, we analyze in detail the spectroscopic changes in the different time ranges. This allows associating the changes in the optical properties with specific morphological states. We find that both interface crystallization and a dissolution–recrystallization process occur. Based on our results it is possible to understand the full sequence of perovskite formation dynamics that occur in the two-step processing *via* spin coating.

## 2. Results

In the first processing step we spin coat a solution of PbI<sub>2</sub> in dimethylformamide (DMF) (461 mg ml<sup>−1</sup>) onto a glass substrate (Fig. 1a) and anneal it at 100 °C for 5 minutes (Fig. 1b). This leads to a compact PbI<sub>2</sub> thin film. In the second processing step, we drop 200 µL of MAI dissolved in IPA (40 mg ml<sup>−1</sup>) onto the PbI<sub>2</sub> film to induce the MAPbI<sub>3</sub> crystallization and immediately start spin coating (corresponding to  $t = 0$  s), where the target spin speed of 1000 rpm min<sup>−1</sup> is reached after 2 seconds (Fig. 1c). The temperature of the sample and MAI solvent during the spin coating is kept at 26 °C. During this second processing step, we monitor the optical properties, *i.e.* absorption and PL, using a home-built spin coater and optical detection system, both described in detail in ref. 15. In brief, the rotating substrate with the solution is excited with a white-light-source pulsed at 11 Hz from underneath the chuck of the spin-coater, through a hole, and its transmission is recorded with a glass fiber cable connected to a spectrograph.

During the off-periods, a laser beam at 520 nm (2.38 eV) excites the sample and the resulting luminescence is recorded using the same glass fiber cable connected to the spectrograph. In this way, pairs of transmission and PL spectra are measured at a rate of 11 pairs per second. To correct the transmission of

MAPbI<sub>3</sub>  $I(t)$  for the transmission of the setup  $I_0$ , we also recorded the transmission signal obtained with a quartz substrate and subtracted it so as to obtain the time dependent optical density using the relation  $OD(t) = \log(I_0/I(t))$ . The resulting spectrum is shown in the ESI (Fig. S1†). It turns out that a reflection signal from the initially unreacted PbI<sub>2</sub> film obscures the clear identification of the MAPbI<sub>3</sub> absorption in particular in the early stages, when the MAPbI<sub>3</sub> signal is still weak. We therefore also recorded the transmission signal obtained from a quartz substrate covered with a PbI<sub>2</sub> film and used this as reference value  $I_{ref}$  to calculate the time dependent optical density as  $OD(t) = \log(I_{ref}/I(t))$ , shown in Fig. 2a. One may argue that, at later stages, this procedure implies subtracting a no longer existing reflection signal as the PbI<sub>2</sub> layer has been used up. However, once the PbI<sub>2</sub> has been used up, the absorption from the MAPbI<sub>3</sub> is sufficiently strong, so this small subtraction has essentially no effect. All spectra are also set to a common baseline to account for fluctuations in optical scattering. Fig. 2 shows the evolution of the absorption spectra (Fig. 2a) and of the corresponding PL spectra (Fig. 2b), where each PL spectrum is normalized to its maximum value. They are both plotted as 2D color maps, so the color indicates the intensity of PL or optical density (OD). For reference and visualization, the absorption and PL spectra at 14 s are indicated at the side of the maps.

From Fig. 2a it becomes clear that there is little change in the absorption within the first 12 seconds of processing, while the main increase in absorption intensity occurs between 12 and 14 s. From about 14 s onwards, the absorption remains largely unaltered. We point out that the absorption cannot be evaluated quantitatively within the first 4 s, since until then the pipette, used to distribute the MAI solution across the glass substrate at the beginning of spin coating, was in the beam path. In contrast to the absorption, a photoluminescence peak prevails over the entire time range investigated (Fig. 2b). Its energetic position and width changes in the first 14 seconds and remains constant thereafter. It is noteworthy that this PL has a finite intensity even when there is only very little absorption from the MAPbI<sub>3</sub>, implying a high quantum yield compared to that in later stages, when there is significant MAPbI<sub>3</sub> absorption. For reference, a plot of the PL spectra with absolute intensities is given in the ESI (Fig. S1†).

To analyze the different spectroscopic signatures and temporal changes in more detail, we display the temporal evolution of different spectral features in Fig. 2c. The optical density at 1.665 eV indicates how the MAPbI<sub>3</sub> absorption develops with time. We also show the evolution of the PL peak position and the two photon energies at which the PL has dropped to 25% of its maximum intensity (essentially following the turquoise line in Fig. 2b). This is referred to as the “high edge” and “low edge”. Furthermore, the temporal evolution of the integrated PL intensity, corrected for the concomitant changes of the absorption at the laser excitation wavelength (2.38 eV) normalized to the value after 10 seconds, is shown. This indicates the relative change of the PL quantum yield (PLQY).

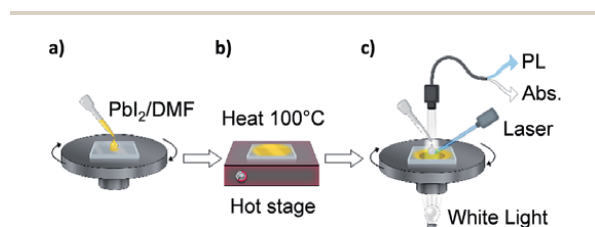


Fig. 1 The preparation of MAPbI<sub>3</sub> film and the *in situ* spectroscopy setup. (a) PbI<sub>2</sub> in DMF is spin coated on a glass substrate. (b) Heat annealing of the PbI<sub>2</sub> layer. (c) MAI in IPA is spin coated on the PbI<sub>2</sub> layer and, during spin coating, PL and absorption of the film are detected.

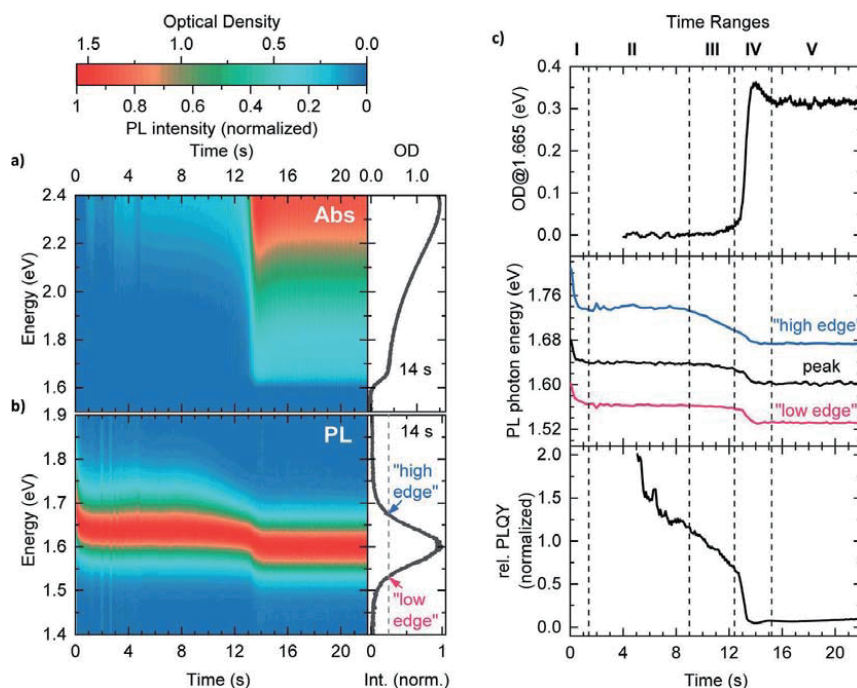


Fig. 2 (a) 2D absorption map. The colour indicates the optical density. (b) PL map, with every spectrum being normalized. (c) Evolution of (top panel) the optical density at 1.665 eV, (middle panel) the PL at the positions of the peak, "high edge" and "low edge", and (bottom panel) the PLQY relative to the value at 10 s.

If we take a closer look at the time evolution of the optical parameters described above (Fig. 2c), we can identify five consecutive time ranges between which specific spectral changes of PL or absorption occur. We briefly describe what characterizes these different regimes, before analyzing each regime in detail. In the first time range, *i.e.* the first 1.4 seconds, indicated as I in Fig. 2c, we observe photoluminescence, and its spectrum shows a fast initial shift towards lower energies. In the subsequent time range II, *i.e.* the next 8 seconds, the PL shape remains constant, while there is no noticeable change in absorption intensity from 4 s onwards. In time range III, the absorption increases slightly, and there are spectral changes in the PL. The high-energy edge of the PL shifts to lower energies, while the position of the low-energy edge remains constant. Range IV can be associated with a steep increase and subsequent decreases in absorption. Simultaneously a further shift of the whole PL spectrum to lower energies occurs, accompanied by a significant reduction of the relative PLQY. After that, in range V, no further change in the absorbance or PL occurs.

#### Range I

As mentioned above, absorption in range I cannot be evaluated. However, directly after applying the MAI solution to the PbI<sub>2</sub> layer, an initial PL spectrum with a maximum at 1.68 eV occurs, which shifts within the first 1.4 seconds by about 50 meV to lower energies (Fig. 3a top). Fig. 3b shows the temporal evolution of the energetic position of the PL peak, together with a fit

to an exponential decay that gives a time constant of  $0.23 \pm 0.05$  s. We note that the spectral shape of the PL peak is not symmetrical. Rather, it shows a high energy tail that becomes particularly obvious when fitting a hyperbolic secant *e.g.* to the spectrum at 1.4 s (Fig. S2†). Such a line shape was previously found to account well for thermal and inhomogeneous broadening of the PL peak shape of halide perovskites.<sup>21</sup>

To further investigate what may give rise to the high-energy PL tail and the initially blue-shifted position of the maximum, we recall that PL spectra that were blue shifted compared to their bulk PL have been repeatedly associated in the past with a confinement effect of the excited state by a finite crystallite size.<sup>22–25</sup> For MAPbI<sub>3</sub>, this effect occurs for crystallite or grain sizes below approximately 25–30 nm.<sup>26–28</sup> We follow the approach outlined by Parrott *et al.* to correlate the measured PL peak position with the crystal size<sup>27</sup> using the equation

$$E = E_g + b/d^2 \quad (1)$$

where  $E_g$  corresponds to the band gap energy, which we set to 1.63 eV. The parameter  $b$  represents a constant, which in the literature is found to be in the range between 1 and 5 eV nm<sup>2</sup> for MAPbI<sub>3</sub>,<sup>27,29</sup> so we assume a value of 3 eV nm<sup>2</sup> (see the ESI for more details†). With the help of eqn (1), the evolution of peak position with time translates into an evolution of film thickness with time (Fig. 3b and S3†). It appears that the film formation starts at a thickness of about 8 nm, increases to about 20 nm



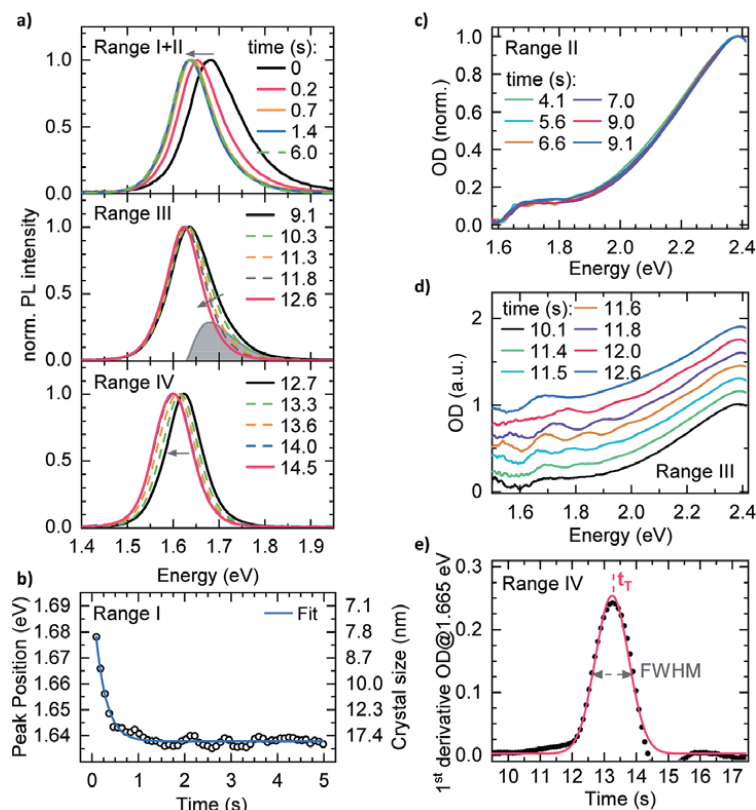


**Fig. 3** (a) Evolution of PL during processing. Top: normalized PL within the first 1.4 s (range I) and at 6.0 s (range II). Middle: normalized PL from 9.1 s (black line) to 12.6 s (red line) (range III). The difference between the spectra at 9.1 s and 12.6 s is shown in grey. Bottom: normalized PL from 12.7 s to 14.5 s (range IV). (b) Temporal evolution of the PL peak position together with an exponential decay fit. Also the crystal size that corresponds to a certain PL peak position, as described in the text, is given. (c) Normalized absorption spectra between 4.1 s (red) and 9.1 s of processing (range II). (d) Absorption spectra from 10.1 s to 12.6 s (range III). For clarity each spectrum is offset by 0.15. (e) The 1<sup>st</sup> derivative of OD at 1.665 eV together with a fit of a Gaussian. The peak position is defined as transition time  $t_T$ .

within the first 1.5 s, and then remains constant. A fit to the evolution of crystal size in the range up to 1.0 s gives an initial MAPbI<sub>3</sub> growth rate for the film thickness in the range of  $11 \pm 2$  nm s<sup>-1</sup> (Fig. S3†).

### Range II

The measured absorption spectra between 4.1 and 9.1 s in range II correspond to the known MAPbI<sub>3</sub> absorption spectrum and its shape remains constant over time (Fig. 3c). After the initial spectral changes in time range I, the shape of the PL spectrum stabilizes from about 1.5 s onwards. This defines the beginning of range II. The PL shape remains nearly constant until a processing time of 9.1 s.

### Range III

While the shape of the absorption spectrum does not change over time at the beginning of range III, we observe a modulation of the measured spectra in the time range between 11.4 s and 12.6 s (Fig. 3d). This may be associated with a thin film

interference effect, which is often used to optically determine the thickness of thin films.<sup>30</sup> The layer thickness  $d$  can be calculated from the spectral position of the extrema using the equation<sup>31,32</sup>

$$d = \frac{\lambda_1 \lambda_2}{2(\lambda_1 n_2 - \lambda_2 n_1)} \quad (2)$$

where  $\lambda_1$  and  $\lambda_2$  correspond to the wavelengths of two adjacent maxima or minima and  $n_1$  and  $n_2$  represent the refractive index of the layer material at  $\lambda_1$  and  $\lambda_2$ . While the determination of  $\lambda_1$  and  $\lambda_2$  is relatively easily accessible from the measured spectra (see Fig. S7 for details†), it is not so obvious which material causes the thin film interference in range III. If the thicknesses are calculated using the refractive indices for MAPbI<sub>3</sub> (~2.4–2.5) or PbI<sub>2</sub> (~3.1–3.2), the resulting values are clearly too high compared to the thicknesses determined based on the absorption and profilometer data (see the ESI for details†). If the refractive indices of isopropanol (~1.3–1.4) are used, we obtain a thickness of 3.6  $\mu$ m at 11.4 s, which rapidly decreases to 1.4  $\mu$ m at 12.6 s.

From 9.1 s onward, the spectral shape of the PL evolves. The high-energy edge shifts from 1.74 eV at 9.1 s to 1.70 eV at 12.6 s, *i.e.* by about 40 meV. In the same time range, the spectral position of the low edge shifts merely by 7 meV, starting from 1.56 eV (Fig. 2b and c and 3a middle panel). This spectral dynamic results in an asymmetric narrowing of the measured PL peak from the high-energy edge. At first sight, this might be interpreted as a self-absorption effect in which the PL intensity reduces in the spectral overlap region of PL and absorption.<sup>33</sup> To check the plausibility of the self-absorption scenario in time range III, we used the PL spectrum at the beginning of range III (*i.e.* at 9.1 s) as the reference spectrum to calculate the absorption edge using the subsequent PL spectra (see Fig. S4†). This is a well-known approach, especially for the optical investigation of inorganic semiconductors, where information about the absorption edge can be obtained based on PL data.<sup>34,35</sup> However, we find that the absorption edges determined by this approach do not match well with the absorption edges determined by the optical density measurements in terms of both shape and energetic position (Fig. S4†). To assess the influence of self-absorption on the PL more precisely, we analyzed the PL spectra in range III using a quantitative model we had already successfully used in the past for this purpose.<sup>36</sup> An important feature of this model is that it takes into account extended optical paths in the material due to internal reflections at the layer interfaces. We find that in realistic and exaggerated scenarios with regard to assumed layer thicknesses and/or boundary layer properties, it is virtually impossible to model the experimentally observed narrowing of only one PL edge (Fig. S5†). Rather, a spectral shift of the entire spectrum would result from an increasing amount of self-absorption, which also agrees with other literature reports.<sup>27,36</sup> From the absorption data in range III we further observe that the absorption is relatively low ( $OD < 0.01$  at 1.67 eV), which is further in agreement with the notion that a significant self-absorption effect in time range III is absent.<sup>27,37</sup>

However, it is noticeable that at the end of range III the PL peak appears more symmetrical, compared to its spectral shape at the beginning of range III. The difference spectrum calculated from the PL spectra at 9.1 s and 12.6 s (shaded area in Fig. 3a middle panel) peaks at 1.68 eV. This matches with the peak position of the first measured PL spectrum at 0 s. If we also calculate the difference spectra between the PL spectrum at 9.1 s and the other spectra in range III, they result in essentially the same spectral shape with the peak position at 1.68 eV (Fig. S6†). It is important to note that this difference spectrum does not shift to the red with increasing time. Rather, exactly the same spectrum prevails at all times, yet its intensity reduces. Thus, the spectral changes in range III can also be understood as decreasing intensity of an additional higher energetic PL feature, which finally disappears at the end of range III.

Given the spectral coincidence of the additional high-energy PL feature with the PL in the early stages, it is reasonable to attribute this feature to small crystallites where the exciton wavefunction is still confined and thus the transition is blue-shifted. Using eqn (1), the peak position of the difference PL at 1.68 eV would correspond to a crystal size of about 15 nm.

#### Range IV

The significant increase in absorption between 12.6 and 14.0 s is the most noticeable spectral change in range IV (Fig. 2a). To quantify this increase more precisely, it is advantageous to calculate the derivative of the time-dependent OD at 1.665 eV, which leads to a peak shape.<sup>38</sup> By fitting a Gaussian to this peak, we can quantify the transition time  $t_T$  from the maximum. The full width at half maximum (FWHM) gives information about the width of the transition (Fig. 3e). We find  $t_T = 13.3$  s and  $FWHM = 1.2$  s.

The increase in absorption can be associated with an increase in film thickness. To this end, we used the absorption coefficient of MAPbI<sub>3</sub> from the literature<sup>39</sup> to convert the time-dependent (offset-corrected) optical density from Fig. 2c in the energy range between 1.6 eV and 1.7 eV into a time-dependent layer thickness, shown as black circles in Fig. 4 (see also Fig. S8 for details†). The steep increase in the absorption spectrum then corresponds to an increase of layer thickness from about 50 nm at the beginning to about 500 nm at the end of range IV. If we approximate this evolution by a linear fit in the range between 13 and 14 s, this results in a growth rate of  $445 \pm 15$  nm s<sup>-1</sup> (Fig. S9†). Also indicated in Fig. 4 is the film thickness that results from fitting the interference pattern in range III using the refractive index of isopropanol (orange diamonds), and the film thickness that is obtained in the early stages from fitting the shift in the PL spectra using eqn (1) (red squares).

Simultaneously with the steep increase in absorption, the entire PL spectrum shifts from 1.63 eV to 1.60 eV (see Fig. 2c and 3a bottom). If we assume that this shift is due to self-absorption, we can derive the associated film thickness that causes such an absorption. We did this using a modelling approach that considers multiple reflections and that is detailed in ref. 36. As detailed in the ESI (Fig. S10†), we start by using the PL spectrum at 12.7 s, *i.e.* at the beginning of range IV, and consider the intensity of MAPbI<sub>3</sub> absorption present in that moment to

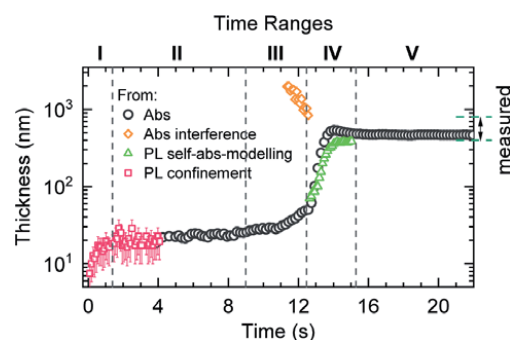


Fig. 4 The film thickness as a function of spin-coating time, derived with different approaches as detailed in the text. Black circles: derived by converting OD into thickness, orange diamonds: derived by fitting the interference pattern, red squares: derived by associating a PL shift with confinement effects, green triangles: derived by associating the PL shift with self-absorption of different thickness films.

calculate the PL spectrum that would result in the absence of self-absorption. The spectrum calculated in this way peaks at 1.63 eV, matching well with the measured PL spectrum after 1.4 s (end of range I), which confirms our approach. As the next step, we calculated the layer thickness necessary to modify this PL spectrum in such a way that it matches the measured PL spectra at each time in range IV (Fig. S11†). The thicknesses that we obtain by this approach are indicated as green triangles in Fig. 4. From the good agreement with the layer thicknesses obtained from considering the OD we conclude that our approach is correct, *i.e.* the shape of the PL spectra in range IV is indeed the result of self-absorption from the increasing amount of MAPbI<sub>3</sub>.

### Range V

The last time range, starting from 14.0 s, is characterized by the fact that there are no temporal changes in either absorption or PL, *i.e.* the film formation is complete. X-ray scattering results reveal that after time range V no PbI<sub>2</sub> exists in the film, suggesting a full conversion to MAPbI<sub>3</sub> (Fig. S12†). The layer thickness extracted using the absorption data is approximately 500 nm in range V, which matches well with the layer thickness range from 400 to 800 nm determined using a profilometer (Fig. 4). SEM images of a final film show a compact surface coverage and grain sizes in the range from 50 to 300 nm (Fig. S13†). While the relative PLQY has decreased significantly, the PL spectrum appears symmetric, suggesting that no additional PL signatures are present at the end of the processing.

## 3. Discussion

Having analyzed the spectral features in detail, we can now proceed to derive a possible model for the successive film formation. As before, we shall consider the different temporal regimes one after another. The overall picture we suggest is summarized in Fig. 5.

### Range I

The analysis of the PL spectra suggested the initial formation of small MAPbI<sub>3</sub> crystals with crystal sizes that confine the wavefunction below about 25 nm, immediately after applying the MAI solution on the PbI<sub>2</sub> layer. As suggested by the PL shift to

lower energies, these crystallites grow fast with a growth rate of 11 nm s<sup>-1</sup> to sizes above about 25 nm in the course of range I. The good match of the calculated crystal sizes from the confinement effect at the end of range I and the thickness extracted from the first reliable absorption spectra in range II of about 20 nm confirm our approach.

Fu *et al.* reported the initial formation of a MAPbI<sub>3</sub> capping layer when dipping PbI<sub>2</sub> layers into MAI/IPA solution, for concentrations above 10 mg ml<sup>-1</sup>.<sup>13</sup> The formation of this capping layer was also found to happen faster for higher concentrations, while the average grain size decreases.<sup>11,13</sup> The MAI concentration of 40 mg ml<sup>-1</sup> used in our study is well above 10 mg ml<sup>-1</sup>, so we associate the initial occurrence of PL and its rapid shift to lower energies with the spectroscopic signatures of the initial formation of MAPbI<sub>3</sub> crystallites that grow within range I so as to form a capping layer. This is also in agreement with the results from Schlipf *et al.* who investigated the MAPbI<sub>3</sub> two-step conversion process with time-resolved scattering methods and found a laterally confined crystal growth at the beginning of the crystallization.<sup>40</sup> Ko *et al.* reported that the growth rate of the MAPbI<sub>3</sub> nuclei is independent of the MAI concentration, investigating a range between 4 and 8 mg ml<sup>-1</sup>.<sup>11</sup> Their results on the evolution of grain size suggest a growth rate in the range between 10 and 20 nm s<sup>-1</sup>, which agrees very well with the value of 11 nm s<sup>-1</sup> that we find in range I using a concentration of 40 mg ml<sup>-1</sup>. This suggests that the growth rate of MAPbI<sub>3</sub> nuclei in the two-step process under ambient conditions remains mostly unchanged over at least an order of magnitude of MAI concentration.

The asymmetric shape of the PL spectrum at the end of range I indicates that after the initial MAPbI<sub>3</sub> crystallization, crystallites exist with grain sizes below the confinement limit, *i.e.* below about 25 nm. Ahn *et al.* derived a direct correlation between the MAI concentration and the resulting MAPbI<sub>3</sub> grain size in the case of the two-step method.<sup>12,41</sup> In this framework, a MAI concentration of 40 mg ml<sup>-1</sup> (0.25 M) as used in our study corresponds to an average grain size of approximately 50 nm (Fig. S14†), *i.e.* only slightly higher than the typical confinement limit of MAPbI<sub>3</sub>.<sup>26–28</sup> As the grains in polycrystalline perovskite thin films typically exhibit a size distribution, it appears reasonable that a certain fraction of the grains are below 50 nm, so a confinement effect follows.

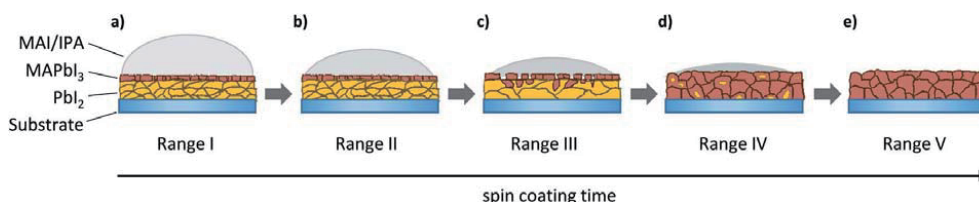


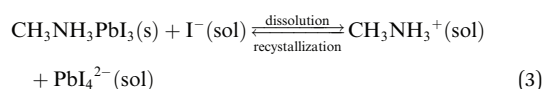
Fig. 5 (a) Range I: the formation of a MAPbI<sub>3</sub> capping layer. (b) Range II: further concentration of the MAI solution above the capping layer through evaporation in the course of several seconds, while the capping layer prevents further MAPbI<sub>3</sub> crystallization. (c) Range III: the iodine concentration increases because of the solvent evaporation and leads to the beginning of the dissolution of the MAPbI<sub>3</sub> capping layer. (d) Range IV: the fast dissolution–recrystallization process, when most of the MAPbI<sub>3</sub> forms. (e) Range V: all of the PbI<sub>2</sub> is transferred into MAPbI<sub>3</sub> and a stable state is reached.

**Range II**

After the formation of the initial capping layer, the lack of evolution in the spectra suggests that the morphology of the buried PbI<sub>2</sub> and of the MAPbI<sub>3</sub> capping layer formed in the initial period remains highly stable in time range II. This is consistent with reports where the capping layer was found to be very dense due to the higher density of PbI<sub>2</sub> compared to MAPbI<sub>3</sub>.<sup>42</sup> As a consequence, this has been shown to prevent MAI diffusion to the underlying PbI<sub>2</sub> and thus suppresses further MAPbI<sub>3</sub> crystallization.<sup>13</sup>

**Range III**

The formation of a dense MAPbI<sub>3</sub> capping layer in time range II obviously raises the question how the MAPbI<sub>3</sub> crystallization is to then proceed eventually. Here a key observation is that in time range III, the high-energy PL tail reduces with time. Importantly, this did not occur by a gradual red-shift of the blue tail, but by a gradual reduction of the PL spectrum that is associated with small crystallites of about 15 nm and below. The disappearance of these smaller crystallites suggests a dissolution process, similar to that observed when dipping PbI<sub>2</sub> layers in MAI solution.<sup>13,43</sup> Such a so-called “dissolution–recrystallization process” or “solid–liquid recrystallization” is described by the reaction



In this reaction, the balance is shifted to the right side and the formation of PbI<sub>4</sub><sup>2−</sup> complexes becomes more likely when the MAI concentration is sufficiently high. This explains why the process only sets in after a certain time – in our case after 9 s – when sufficient solvent has evaporated. The generated PbI<sub>4</sub><sup>2−</sup> complexes are known to dissolve existing MAPbI<sub>3</sub>, *e.g.* the capping layer, so that the underlying PbI<sub>2</sub> becomes accessible for the further MAPbI<sub>3</sub> crystallization.<sup>13</sup> The dissolution process is considered to start preferably at the grain boundaries and smallest grains,<sup>6,11,44</sup> and has also been suggested to take place in the case of two-step processing by spin coating.<sup>44</sup> Consequently, we associate our observed disappearance of the small crystallites with their dissolution in the framework of the dissolution–recrystallization process that sets in during time range III. Even though the smaller MAPbI<sub>3</sub> crystallites dissolve, we do not observe a reduction of absorption, but even a slight increase of the MAPbI<sub>3</sub> thickness from 25 to 50 nm within range III. This suggests that parallel to the dissolution of the smaller crystallites, the underlying PbI<sub>2</sub> reacts with MAI to form more MAPbI<sub>3</sub> which overcompensates for the loss from the dissolution process. Obviously, the newly formed MAPbI<sub>3</sub> does not occupy the space of the just-dissolved MAPbI<sub>3</sub>, but rather the deposits are added to the existing larger MAPbI<sub>3</sub> crystallites, similar to an Ostwald ripening process.

The occurrence of thin film interference in the absorption spectra in range III is consistent with the notion of a dissolution–recrystallization process. It is conceivable that the

interference stems from the MAI/IPA solution layer, possibly influenced by a deterioration of the layer coverage due to the dissolution process. However, it is not clear to what extent the PbI<sub>4</sub><sup>2−</sup> interacts with the MAI/IPA solution, from which a change in refractive index might occur. In such a case, we expect an increase in the refractive index of the solution layer, as lead halide systems typically exhibit a higher refractive index compared to IPA. Thus, the layer thickness obtained based on the refractive index values of IPA in Fig. 4 represents an upper limit. More detailed investigations are needed to fully address this aspect in the future.

**Ranges IV and V**

Further solvent evaporation rapidly increases the local MAI concentration and thus further accelerates the solid solution recrystallization process in time range IV. The steep increase of absorption suggests that the equilibrium in eqn (3) shifts significantly towards the recrystallization process. The time scale for the main dissolution–recrystallization process of 1.2 s that we obtained from Fig. 3e is significantly shorter than the typical time scales for this process in the case of dipping PbI<sub>2</sub> in MAI/IPA solution.<sup>6</sup> Similarly, the growth rate of 445 ± 15 nm s<sup>−1</sup> for the recrystallization process in range IV is much higher than the growth rate of the MAPbI<sub>3</sub> capping layer in range I. This could also explain the significant decrease of the PLQY within range IV, where the fast recrystallization leads to an increased defect density and thus to a more pronounced non-radiative PL decay. The grain sizes of a final film exceed 50 nm as determined by SEM (Fig. S13†). This agrees well with the symmetric shape of the PL spectrum and indicates that no more grains with sizes below 25 nm are present. The spectral position of the PL also matches with the expected bulk spectrum when accounting for self-absorption.

**4. Summary and conclusion**

Overall, we have monitored the complete two-step film formation process of MAPbI<sub>3</sub> by spin coating using optical spectroscopy. By analyzing the changes in the absorption and photoluminescence spectra, we could identify and quantify different steps in the film formation process. We found that film formation takes place in five consecutive steps, which are as follows: (I) the initial formation of a MAPbI<sub>3</sub> capping layer, (II) further concentration of the MAI solution above the capping layer through evaporation in the course of several seconds, while the capping layer prevents further MAPbI<sub>3</sub> crystallization, (III) the beginning of the dissolution of the MAPbI<sub>3</sub> capping layer due to the increased iodine concentration in the course of progressing solvent evaporation, (IV) a rapid main dissolution–recrystallization process, during which most of the MAPbI<sub>3</sub> crystallizes, and (V) the final, fully converted, temporally stable state. Consideration of confinement and self-absorption effects in the PL spectra, together with consideration of the corresponding absorption spectra made it possible to quantify the growth rate of the initial interface crystallization, which was found to be 11 nm s<sup>−1</sup>, and the main dissolution–



recrystallization process happens at a rate of 445 nm s<sup>-1</sup> under our experimental conditions. While the rate for the initial interface crystallization is comparable with results from the two-step method *via* dipping, the growth rate of the dissolution–recrystallization process is significantly higher. This is attributed to the high MAI concentration at the end of the solvent evaporation process. Since most of the MAPbI<sub>3</sub> forms in this short time span (range IV), our results demonstrate the importance of controlling the dissolution–recrystallization process during spin-coating, *e.g.* by controlling the solvent evaporation rate.

We note that the film formation dynamics, *i.e.* extent and timing of the interface crystallization and the dissolution–recrystallization process, depend on the morphology of the PbI<sub>2</sub> layer, which for example can differ significantly when processed on either a mesoscopic or a planar TiO<sub>2</sub> underlying layer.<sup>3</sup> Also, for other two-step processing approaches, solvated states can occur which also impact the reaction pathways and crystallization kinetics.<sup>45,46</sup>

Our work also demonstrates how the film formation process of halide perovskites can be investigated with the help of technically easily accessible *in situ* optical spectroscopy and its analysis. This approach can be easily applied to other, more complex perovskite material systems with mixed halide and/or A-site-cations and processing methods in the future. Our work will therefore help to better understand and optimize the film formation process of halide perovskites in general.

## 5. Experimental section

### Materials and thin film processing

Lead iodide (PbI<sub>2</sub>) beads, *N,N*-dimethylformamide (DMF), and isopropanol (IPA) were purchased from Sigma Aldrich company. Methylammonium iodide (MAI) was purchased from Dyesol company. 461 mg ml<sup>-1</sup> (1 M) PbI<sub>2</sub> was dissolved in dimethylformamide (DMF) and heated at 75 °C overnight. 40 µL PbI<sub>2</sub> solvent was spin coated on a glass substrate in a N<sub>2</sub> glovebox at 3000 rpm min<sup>-1</sup> for 50 s, followed by annealing at 100 °C for 5 min. After that, the PbI<sub>2</sub> film was moved to an ambient atmosphere with a humidity of ~50%. MAI solvent was prepared in IPA at a concentration of 40 mg ml<sup>-1</sup> (0.25 M). The PbI<sub>2</sub> film was placed in a homemade spin coater. 200 µL MAI solvent was dropped on the PbI<sub>2</sub> film and immediately spin coated at 1200 rpm min<sup>-1</sup>.

### *In situ* optical spectroscopy

For transmission measurements, a white LED is placed below the rotating chuck, with a bore along the rotation axis of the chuck allowing transmission of white light through the investigated layer and its collection *via* an optical fiber which guides the transmitted light into the detection system. For PL measurements, a diode laser (excitation wavelength: 520 nm) excites the sample area at a shallow angle with a laser power density of ~75 mW cm<sup>-2</sup>. Use of this laser power density allows estimation of the change in local temperature due to laser heating, which is found to be approximately 0.5 °C (see the ESI

for details†). The resulting PL is collected *via* the same optical fiber used for the transmission measurement.

## Conflicts of interest

There are no conflicts to declare.

## Acknowledgements

S. H., A. K. and Y. Z. acknowledge funding from the Bavarian State Ministry of Science, Research and the Arts for the Collaborative Research Network “Solar Technologies go Hybrid”. Y. Z. acknowledges funding from the China Scholarship Council. K. S. acknowledges financial support from the German National Science Foundation (Project KO 3973/2-1 and GRK 1640). M. C., A. K. and F. P. acknowledge support from the Marie Curie Innovative Training Network (ITN) INFORM. We thank the Bavarian Polymer Institute for SEM characterization.

## References

- 1 J. Burschka, N. Pellet, S.-J. Moon, R. Humphry-Baker, P. Gao, M. K. Nazeeruddin and M. Grätzel, *Nature*, 2013, **499**, 316.
- 2 J.-H. Im, I.-H. Jang, N. Pellet, M. Grätzel and N.-G. Park, *Nat. Nanotechnol.*, 2014, **9**, 927.
- 3 M. Becker and M. Wark, *Cryst. Growth Des.*, 2018, **18**, 4790–4806.
- 4 Z. Xiao, C. Bi, Y. Shao, Q. Dong, Q. Wang, Y. Yuan, C. Wang, Y. Gao and J. Huang, *Energy Environ. Sci.*, 2014, **7**, 2619–2623.
- 5 H. Chen, *Adv. Funct. Mater.*, 2017, **27**, 1605654.
- 6 T.-Y. Hsieh, C.-K. Huang, T.-S. Su, C.-Y. Hong and T.-C. Wei, *ACS Appl. Mater. Interfaces*, 2017, **9**, 8623–8633.
- 7 J. B. Patel, R. L. Milot, A. D. Wright, L. M. Herz and M. B. Johnston, *J. Phys. Chem. Lett.*, 2015, **7**, 96–102.
- 8 D. Barrit, P. Cheng, M.-C. Tang, K. Wang, H. Dang, D.-M. Smilgies, S. Liu, T. D. Anthopoulos, K. Zhao and A. Amassian, *Adv. Funct. Mater.*, 2019, **29**, 1807544.
- 9 H. Zhang, J. Mao, H. He, D. Zhang, H. L. Zhu, F. Xie, K. S. Wong, M. Grätzel and W. C. Choy, *Adv. Energy Mater.*, 2015, **5**, 1501354.
- 10 S. Mastroianni, F. Heinz, J.-H. Im, W. Veurman, M. Padilla, M. Schubert, U. Würfel, M. Grätzel, N.-G. Park and A. Hinsch, *Nanoscale*, 2015, **7**, 19653–19662.
- 11 H. Ko, D. H. Sin, M. Kim and K. Cho, *Chem. Mater.*, 2017, **29**, 1165–1174.
- 12 N. Ahn, S. M. Kang, J.-W. Lee, M. Choi and N.-G. Park, *J. Mater. Chem. A*, 2015, **3**, 19901–19906.
- 13 Y. Fu, F. Meng, M. B. Rowley, B. J. Thompson, M. J. Shearer, D. Ma, R. J. Hamers, J. C. Wright and S. Jin, *J. Am. Chem. Soc.*, 2015, **137**, 5810–5818.
- 14 S. Yang, Y. C. Zheng, Y. Hou, X. Chen, Y. Chen, Y. Wang, H. Zhao and H. G. Yang, *Chem. Mater.*, 2014, **26**, 6705–6710.
- 15 M. Buchhorn, S. Wedler and F. Panzer, *J. Phys. Chem. A*, 2018, **122**, 9115–9122.
- 16 S. Singh, C. Li, F. Panzer, K. Narasimhan, A. Graeser, T. P. Gujar, A. Köhler, M. Thelakkat, S. Huettnner and D. Kabra, *J. Phys. Chem. Lett.*, 2016, **7**, 3014–3021.

- 17 F. Panzer, S. Baderschneider, T. P. Gujar, T. Unger, S. Bagnich, M. Jakoby, H. Bässler, S. Hüttner, J. Köhler and R. Moos, *Adv. Opt. Mater.*, 2016, **4**, 917–928.
- 18 F. Panzer, C. Li, T. Meier, A. Köhler and S. Hüttner, *Adv. Energy Mater.*, 2017, **7**, 1700286.
- 19 A. Merdasa, A. Kiligaris, C. Rehmann, M. Abdi-Jalebi, J. Stöber, B. Louis, M. Gerhard, S. D. Stranks, E. L. Unger and I. G. Scheblykin, *ACS Energy Lett.*, 2019, **4**, 1370–1378.
- 20 J. Li, A. Dobrovolsky, A. Merdasa, E. L. Unger and I. G. Scheblykin, *ACS Omega*, 2018, **3**, 14494–14502.
- 21 M. Cadelano, M. Saba, N. Sestu, V. Sarritzu, D. Marongiu, F. Chen, R. Piras, F. Quochi, A. Mura and G. Bongiovanni, in *Perovskite Materials-Synthesis, Characterisation, Properties, and Applications*, IntechOpen, 2016.
- 22 F. Zhang, S. Huang, P. Wang, X. Chen, S. Zhao, Y. Dong and H. Zhong, *Chem. Mater.*, 2017, **29**, 3793–3799.
- 23 M. E. Kamminga, H.-H. Fang, M. R. Filip, F. Giustino, J. Baas, G. R. Blake, M. A. Loi and T. T. Palstra, *Chem. Mater.*, 2016, **28**, 4554–4562.
- 24 M. Anaya, A. Rubino, T. C. Rojas, J. F. Galisteo-López, M. E. Calvo and H. Míguez, *Adv. Opt. Mater.*, 2017, **5**, 1601087.
- 25 V. Malgras, S. Tominaka, J. W. Ryan, J. Henzie, T. Takei, K. Ohara and Y. Yamauchi, *J. Am. Chem. Soc.*, 2016, **138**, 13874–13881.
- 26 D. N. Dirin, L. Protesescu, D. Trummer, I. V. Kochetygov, S. Yakunin, F. Krumeich, N. P. Stadie and M. V. Kovalenko, *Nano Lett.*, 2016, **16**, 5866–5874.
- 27 E. S. Parrott, J. B. Patel, A.-A. Haghighirad, H. J. Snaith, M. B. Johnston and L. M. Herz, *Nanoscale*, 2019, **11**, 14276–14284.
- 28 L. Polavarapu, B. Nickel, J. Feldmann and A. S. Urban, *Adv. Energy Mater.*, 2017, **7**, 1700267.
- 29 A. Buin, R. Comin, A. H. Ip and E. H. Sargent, *J. Phys. Chem. C*, 2015, **119**, 13965–13971.
- 30 F. A. Jenkins and H. E. White, *Fundamentals of optics*, Tata McGraw-Hill Education, 1937.
- 31 J. Manificier, J. Gasiot and J. Fillard, *J. Phys. E: Sci. Instrum.*, 1976, **9**, 1002.
- 32 R. Munir, A. D. Sheikh, M. Abdelsamie, H. Hu, L. Yu, K. Zhao, T. Kim, O. E. Tall, R. Li and D. M. Smilgies, *Adv. Mater.*, 2017, **29**, 1604113.
- 33 A. Köhler and H. Bässler, *Electronic processes in organic semiconductors: An introduction*, John Wiley & Sons, 2015.
- 34 G. Rey, C. Spindler, F. Babbe, W. Rachad, S. Siebentritt, M. Nuys, R. Carius, S. Li and C. Platzer-Björkman, *Phys. Rev. Appl.*, 2018, **9**, 064008.
- 35 C. Prall, C. Kaspari, A. Knauer, K. Haberland, M. Weyers and D. Rueter, *TM, Tech. Mess.*, 2017, **84**, 747–752.
- 36 K. Schötz, M. A. Askar, W. Peng, D. Seeberger, P. T. Gujjar, M. Thelakkat, A. Köhler, S. Hüttner, M. O. Bakr, K. Shankar and F. Panzer, *J. Mater. Chem. C*, 2020, DOI: 10.1039/c9tc06251c.
- 37 T. Yamada, Y. Yamada, Y. Nakaike, A. Wakamiya and Y. Kanemitsu, *Phys. Rev. Appl.*, 2017, **7**, 014001.
- 38 T. Meier, T. P. Gujar, A. Schönleber, S. Olthof, K. Meerholz, S. van Smaalen, F. Panzer, M. Thelakkat and A. Köhler, *J. Mater. Chem. C*, 2018, **6**, 7512–7519.
- 39 T. W. Crothers, R. L. Milot, J. B. Patel, E. S. Parrott, J. Schlipf, P. Müller-Buschbaum, M. B. Johnston and L. M. Herz, *Nano Lett.*, 2017, **17**, 5782–5789.
- 40 J. Schlipf, P. Docampo, C. J. Schaffer, V. Körstgens, L. Bießmann, F. Hanusch, N. Giesbrecht, S. Bernstorff, T. Bein and P. Müller-Buschbaum, *J. Phys. Chem. Lett.*, 2015, **6**, 1265–1269.
- 41 A. E. Lewis, Y. Zhang, P. Gao and M. K. Nazeeruddin, *ACS Appl. Mater. Interfaces*, 2017, **9**, 25063–25066.
- 42 X. Cao, L. Zhi, Y. Jia, Y. Li, K. Zhao, X. Cui, L. Ci, D. Zhuang and J. Wei, *ACS Appl. Mater. Interfaces*, 2019, **11**, 7639–7654.
- 43 Q. Chen, H. Zhou, Z. Hong, S. Luo, H.-S. Duan, H.-H. Wang, Y. Liu, G. Li and Y. Yang, *J. Am. Chem. Soc.*, 2013, **136**, 622–625.
- 44 H. Ko, S. J. Yang, C. Park, D. H. Sin, H. Lee and K. Cho, *ACS Appl. Mater. Interfaces*, 2019, **11**, 7037–7045.
- 45 N. Ahn, D.-Y. Son, I.-H. Jang, S. M. Kang, M. Choi and N.-G. Park, *J. Am. Chem. Soc.*, 2015, **137**, 8696–8699.
- 46 Z.-w. Kwang, C.-W. Chang, T.-Y. Hsieh, T.-C. Wei and S.-Y. Lu, *Electrochim. Acta*, 2018, **266**, 118–129.



Electronic Supplementary Material (ESI) for Journal of Materials Chemistry A

This journal is © The Royal Society of Chemistry 2020

**Supporting Information for:**

**Investigating Two-Step MAPbI<sub>3</sub> Thin Film Formation  
during Spin Coating by Simultaneous in Situ Absorption  
and Photoluminescence Spectroscopy**

Mihirsinh Chauhan,<sup>1,2,#</sup> Yu Zhong,<sup>1,3,#</sup> Konstantin Schötz,<sup>1</sup> Brijesh Tripathi,<sup>2</sup> Anna  
Köhler,<sup>1,4</sup> Sven Huettner<sup>3</sup>, Fabian Panzer<sup>1\*</sup>

*1: Soft Matter Optoelectronics, University of Bayreuth, 95440 Bayreuth, Germany*

*2: School of Technology, Pandit Deendayal Petroleum University, 382007 Gandhinagar, India*

*3: Department of Chemistry, University of Bayreuth, 95440 Bayreuth, Germany*

*4: Bayreuth Institute of Macromolecular Research (BIMF) and Bavarian Polymer Institute (BPI),  
University of Bayreuth, 95440 Bayreuth, Germany.*

*#: Authors contributed equally*

Corresponding Author: [fabian.panzer@uni-bayreuth.de](mailto:fabian.panzer@uni-bayreuth.de)

### S1: Additional OD and PL spectra

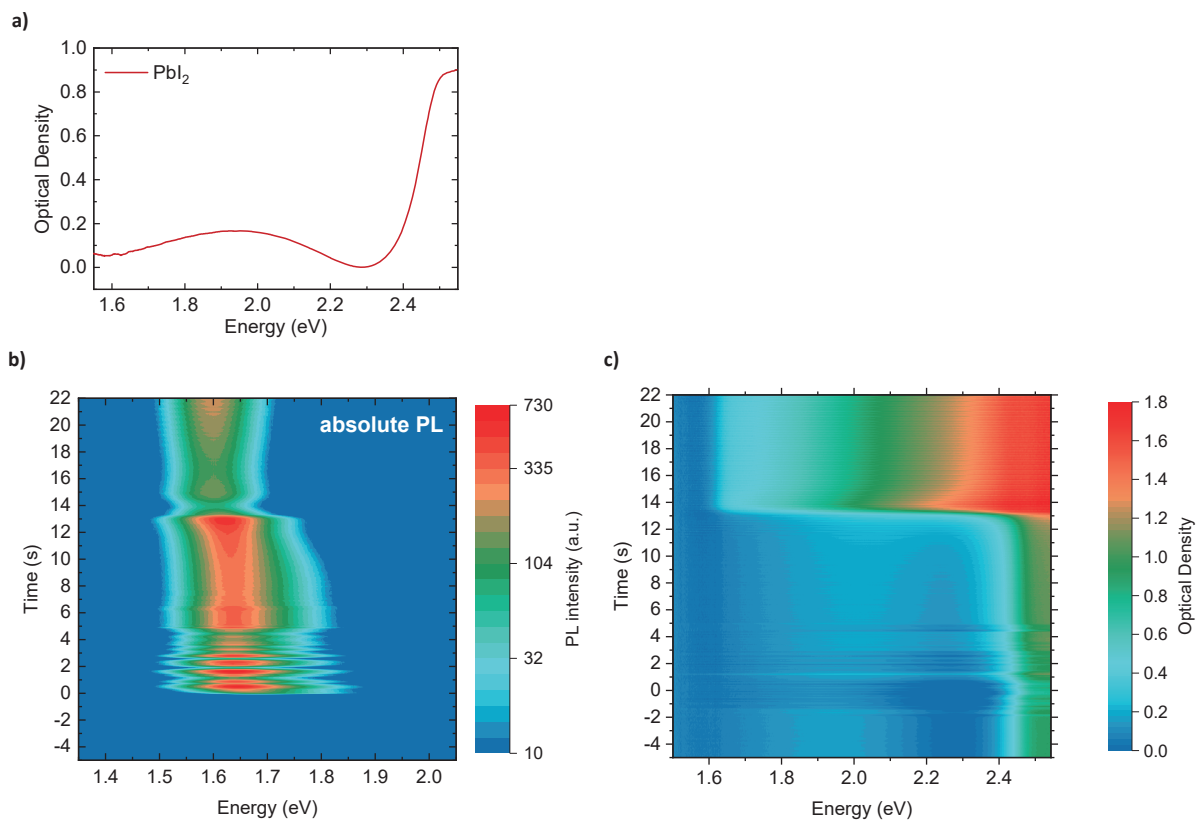


**Figure S1:** (a) Optical Density of the neat PbI<sub>2</sub> layer. (b) 2D map of the temporal evolution of the PL spectrum with absolute measured intensities as indicated with colors. (c) 2D map of the temporal evolution of the measured Optical Density with intensities as indicated with colors. As a reference spectrum  $I_0$ , the transmission through a blank quartz substrate was used.

### S2: Fitting of hyperbolic secant to measured PL in range I

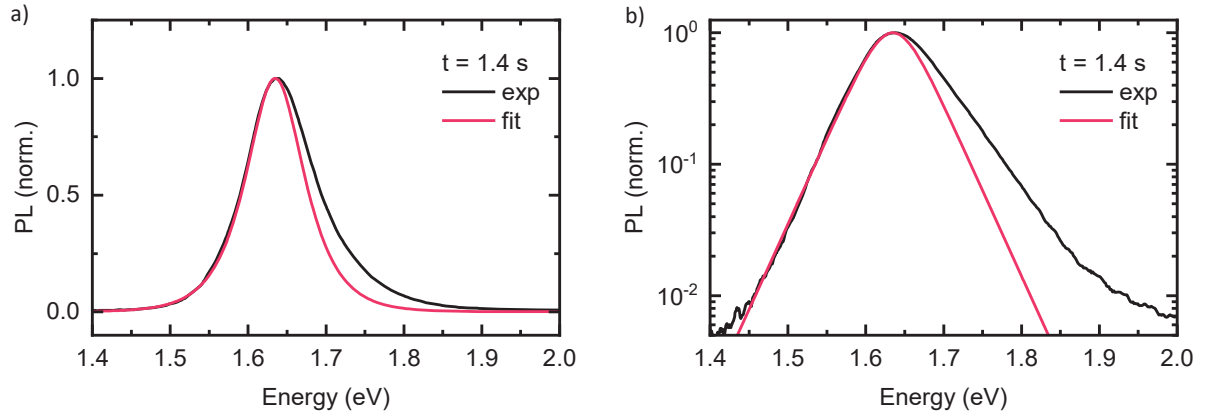


**Figure S2:** Normalized PL at  $t = 1.4$  s (black) and a fit using a hyperbolic secant, demonstrating the asymmetry of the measured PL line shape, plotted on a (a) linear intensity scale and (b) log intensity scale.

### S3: Calculation of MAPbI<sub>3</sub> crystal size from the PL spectra in range I using confinement approach:

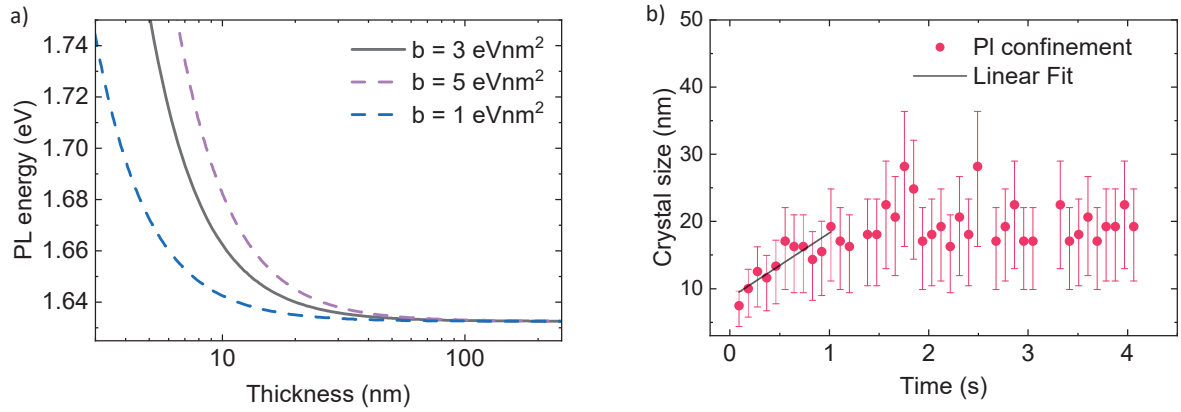


**Figure S3:** (a) Correlation between PL Peak energy  $E$  and crystal size  $d$  as proposed by Parrot et al.,<sup>1</sup>  $E = E_g + \frac{b}{d^2}$  with  $E_g = 1.63$  eV and different  $b$  values of  $1 \text{ eVnm}^2$  (dashed blue),  $3 \text{ eVnm}^2$  (solid black) and  $5 \text{ eVnm}^2$  (dashed purple). The curves for  $b = 1 \text{ eVnm}^2$  and  $b = 5 \text{ eVnm}^2$  were used to calculate the crystal size error. (b) Evolution of crystal size (red dots) within the first 4 seconds of processing, where the crystal size is calculated on the basis of the black line in (a). The initial growth rate was quantified using a linear fit in the time range up to 1.0 s (black line) where a slope of  $11 \pm 2 \text{ nm/s}$  is obtained.

#### S4: Extracted absorption edge of PL in range III

The optical density of the absorption edge was extracted by  $OD = -\log\left(\frac{PL_{\text{final}}}{PL_{\text{initial}}}\right)$ , where  $PL_{\text{initial}}$  is the PL at  $t = 9.1$  s and  $PL_{\text{final}}$  is the PL at  $t = 12.6$  s scaled to the red falling edge of  $PL_{\text{initial}}$ . Note that this scaling procedure does not alter the spectral shape of the obtained absorption, but only shifts it up in OD to avoid negative ODs.

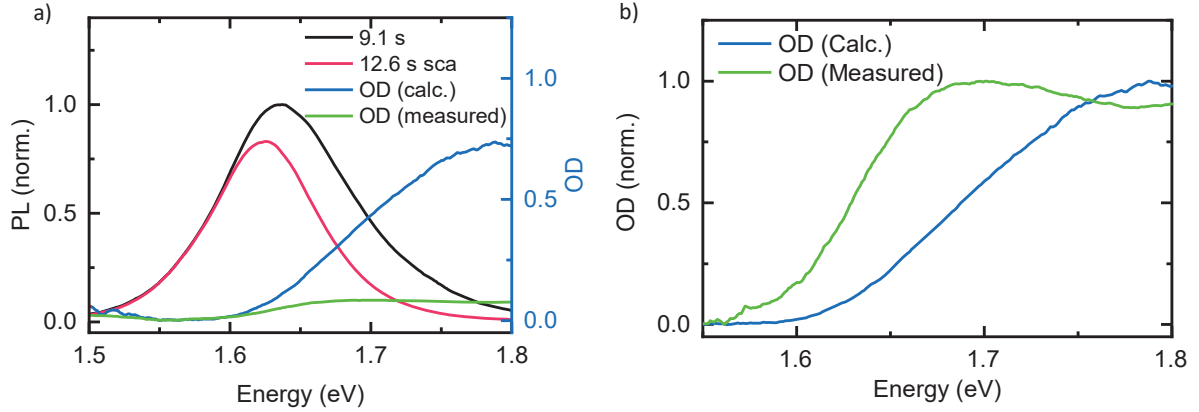


**Figure S4:** (a) PL at  $t = 12.6$  s (red) scaled to the lower energy edge of the PL at  $t = 9.1$  s (black) together with the calculated optical density if the spectral change was due to self-absorption (blue line) and the measured absorption edges determined by the measured optical density (green) at  $t = 12.6$  s, (b) Normalized calculated (blue) and measured (green) optical density at  $t = 12.6$  s, from which the deviations in both shape and energetic position become clear.

### S5: Effect of self-absorption in range III

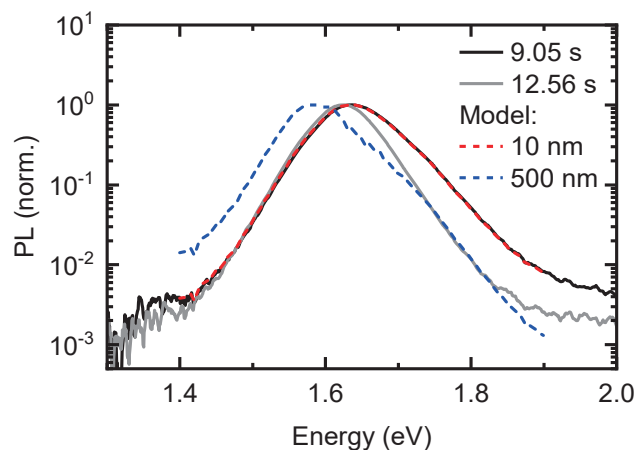


**Figure S5:** Normalized measured PL at  $t = 9.1$  s (black) and  $t = 12.6$  s (grey), together with modeled PL considering self-absorption and internal reflections, assuming the PL at  $t = 9.1$  s to correspond to the intrinsic PL spectrum. The significant mismatch between the modeled PL and the experimental one at 12.6 s demonstrates that the observed spectral change are not due to self-absorption effects.

### S6: Difference PL spectra in range III

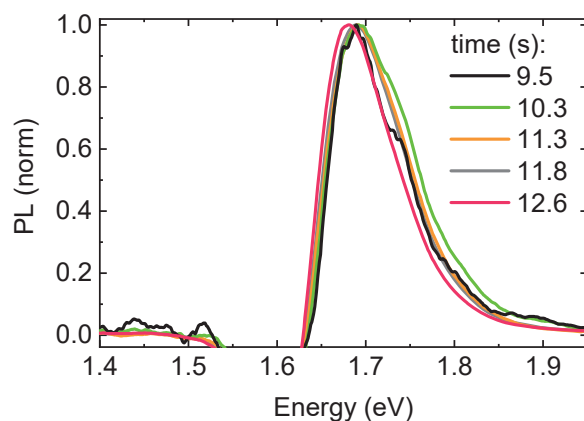


**Figure S6:** Normalized difference spectra between the PL spectrum at 9.1 s and the later spectra (times as indicated) in range III.

### S7: Thickness Calculation from Absorption Interference at range III

Interference fringes in the measured absorption spectra were observed at the end of range III, as shown in Figure S7a  $t_2 = 11.6$  s (red curve). Based on the appearance of this interference fringes, we can estimate the thickness of the sample, from the following equation:<sup>2,3</sup>

$$d = \frac{\lambda_1 \lambda_2}{2(\lambda_1 n_2 - \lambda_2 n_1)} \quad (S1)$$

$d$ : thickness of the sample;

$\lambda_1$  and  $\lambda_2$ : the wavelength at two adjacent maximum or minimum intensity;

$n_1$  and  $n_2$ : the sample refractive index at  $\lambda_1$  and  $\lambda_2$ .

To quantify the value of  $\lambda_1$  and  $\lambda_2$ , we use the normalized absorption e.g. at  $t_2 = 11.6$  s and subtract the absorption spectrum at  $t_1 = 9.1$  s (without interference) and obtain the blue curve in Figure S7a. The refractive index has been taken from Leguy et al., Sani et al. and Riccardo et al. for CH<sub>3</sub>NH<sub>3</sub>PbI<sub>3</sub>, isopropanol and PbI<sub>2</sub> respectively.<sup>4-6</sup> In the range between 550 – 750nm, the refractive indexes of these three materials are, 2.4~2.5 (CH<sub>3</sub>NH<sub>3</sub>PbI<sub>3</sub>), 1.3~1.4 (isopropanol) and 3.1~3.2 (PbI<sub>2</sub>). Depending on the chosen parameters the calculated thicknesses from Equation S1 differ (Figure S7b)

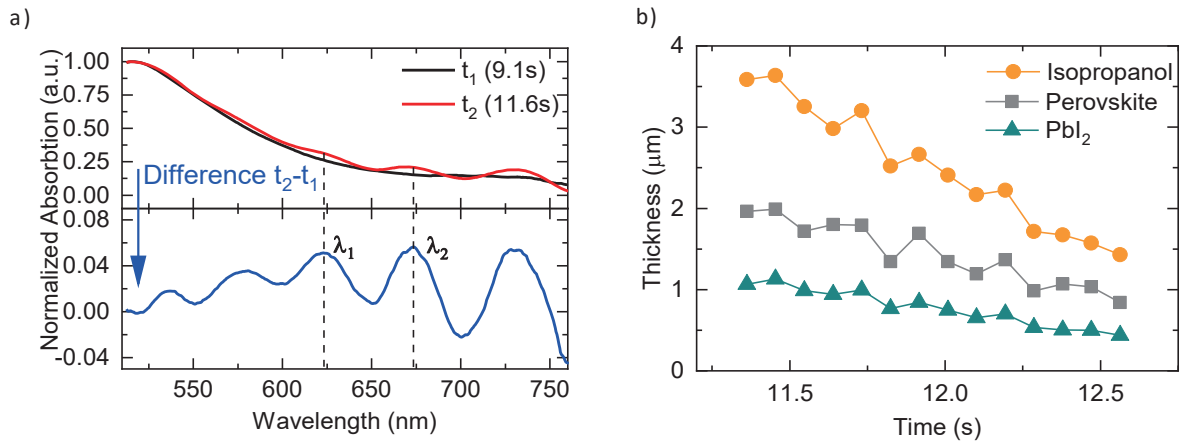


**Figure S7:** (a) Normalized absorption spectra at 9.1 s (black) and 11.6 s (red). The blue curve indicates the difference of absorption at  $t_2$  and its original absorption at  $t_1$  and was used to extract  $\lambda_1$  and  $\lambda_2$  (b) The calculated thickness from the interference fringes using the refractive index of isopropanol (yellow dots), MAPbI<sub>3</sub> (grey squares) and PbI<sub>2</sub> (green triangles).



### S8: Estimation of MAPbI<sub>3</sub> thickness from absorption data

From Lambert-Beer law,

$$I = I_0 e^{-a*d} \quad (S2)$$

$I_0$ : Incident intensity;

$I$ : Transmittance intensity;

$a$ : Absorption coefficient;

$d$ : Film thickness.

Then we can obtain the thickness from the following equation:

$$a = 2.303 \left( \frac{OD}{d} \right) \quad (S3)$$

OD: Optical density.

The absorption coefficient is extracted from literature,<sup>7</sup> as illustrated in Figure S8a. Figure S8b shows comparison of experimental absorption spectra and calculated absorption with thickness and absorption coefficient plotted in Figure 4 in the main text.

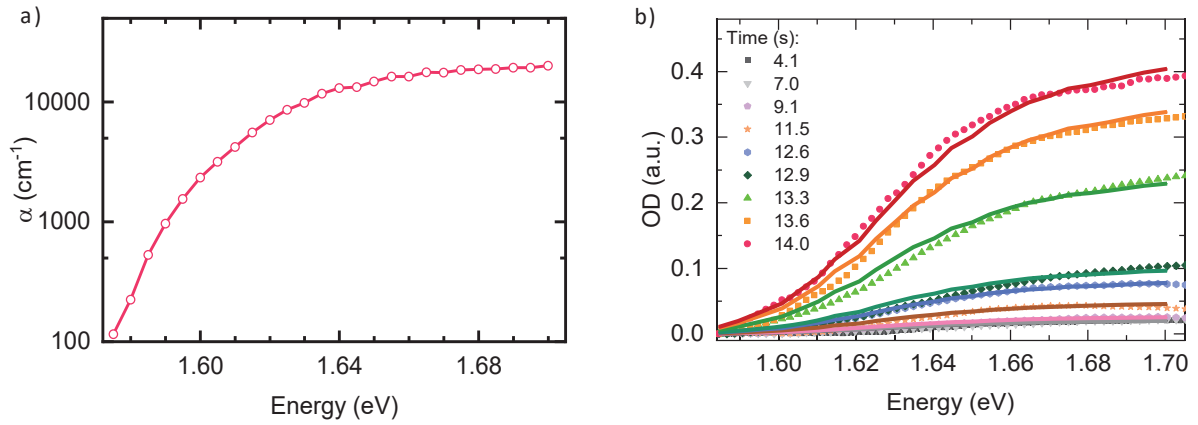


**Figure S8:** (a) Absorption coefficient of perovskite film used for thickness calculation,<sup>7</sup> (b) Experimental absorption spectra at different time (Symbol) and the corresponding calculated spectrum from absorption coefficient and thickness (lines).

### S9: Calculation of growth rate in range IV

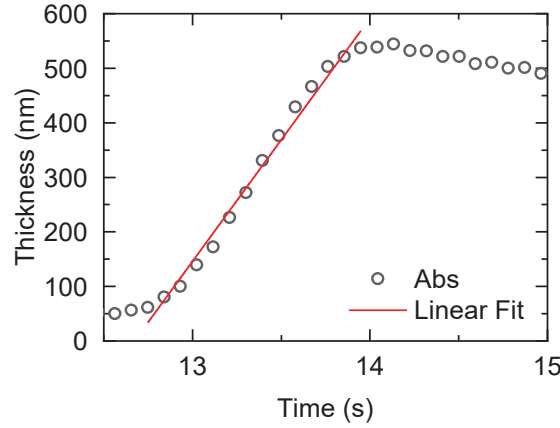


Figure S9: Linear fit to MAPbI<sub>3</sub> layer thickness in range IV to estimate the MAPbI<sub>3</sub> growth rate from resulting slope, where we find a value in the range of  $445 \pm 15$  nm/s.

### S10: Estimation of MAPbI<sub>3</sub> thickness from the PL spectra in range IV

As outlined in our previous work,<sup>8</sup> for a given intrinsic PL, the detectable PL after internal reflections and self-absorption can be expressed as

$$PL_{\text{detected}}(E) = C \cdot PL_{\text{direct}}(E) + PL_{\text{filtered}}(E) \quad (\text{S4})$$

$PL_{\text{direct}}(E)$  and  $PL_{\text{filtered}}(E)$  can be calculated according to the Beer-Lambert law,

$$PL_{\text{direct}}(E) = \int_0^L PL_{\text{int}}(E) \cdot n(x)^2 \cdot (1 - r_f) \cdot \exp[-\alpha(E) \cdot x] dx \quad (\text{S5})$$

$$PL_{\text{filtered}}(E) = \int_0^L \sum_{j=1} PL_{\text{int}}(E) \cdot n(x)^2 \cdot (1 - r_f) \cdot \{A_j + B_j\} dx \quad (\text{S6})$$

with  $A_j = r_f^j \cdot r_b^j \cdot \exp[-\alpha(E) \cdot (2jL + x)]$  considering the part of the PL that propagates from the site of generation,  $x_i$ , towards the front surface, and propagation towards the back surface is considered by  $B_j = r_f^{j-1} \cdot r_b^j \cdot \exp[-\alpha(E) \cdot ((2j - 1) \cdot L + (L - x))]$ . Here,  $\alpha(E)$  denotes the absorption coefficient of the material,  $r_f$  and  $r_b$  are the reflection probabilities at the front and back interface, respectively,  $n(x)$  is the charge carrier density and  $L$  denotes the layer thickness.  $C$  is a suppression constant, which accounts for a mismatch of excitation and detection spot, where  $C = 1$  means no suppression and  $C = 0$  full suppression of the direct PL. As the PL at the beginning of range IV is already affected by self-absorption, the intrinsic PL must be extracted by solving Equations S4-S6 for the intrinsic PL,  $PL_{\text{int}}(E)$ , which yields

$$\begin{aligned}
 PL_{\text{int}}(E) = PL_{\text{detected}}(E) & \cdot \left\{ C \right. \\
 & \cdot \int_0^L \left[ n(x)^2 \cdot (1 - r_f) \cdot \exp[-\alpha(E) \cdot x] \right. \\
 & \left. \left. + \sum_{j=1} n(x)^2 \cdot (1 - r_f) \cdot \{A_j + B_j\} dx \right] dx \right\}^{-1}
 \end{aligned} \tag{S7}$$

with  $L$  being the thickness of the MAPbI<sub>3</sub> layer at the beginning of region IV, as determined by the absorption data. The calculated intrinsic PL is shown in Figure S10. Using this intrinsic PL, the thickness of the MAPbI<sub>3</sub> layer at any time is obtained by a least-squares-fit of Equation S4, normalized, to the normalized experimental PL spectra, for a given parameter set with  $L$  being optimized.

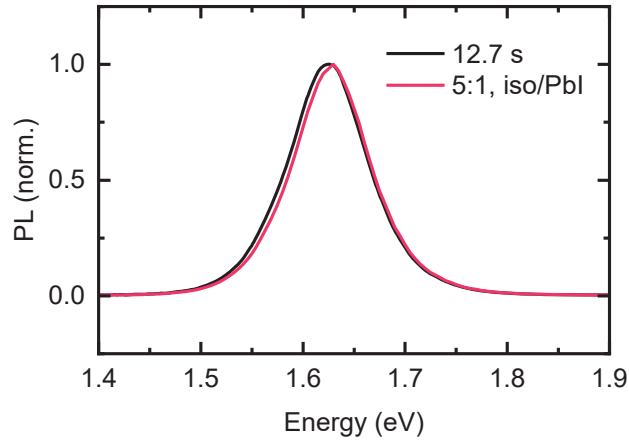


**Figure S10:** PL at 12.7 s and calculated intrinsic PL for an assumed layer thickness of 50 nm by inversely applying our model for calculating PL affected by self-absorption and internal reflections. The calculated intrinsic PL is then used for the estimation of the layer thickness for the following time steps.

$n(x)$  is approximated identical to the charge carrier density after laser excitation. By this, the model neglects charge carrier diffusion. In the case of thin layers, where the optical path length of the internally reflected light is on a similar length scale as the diffusion length of charge carriers, this is likely to affect the quantitative results of our model.

The reflection probabilities at the interfaces were estimated by calculating the angle-dependent reflection coefficients according to the Fresnel equations and then averaged over all possible incident angles. With refractive indices in the relevant energy range of 2.5 for MAPbI<sub>3</sub><sup>4,9</sup>, about 1.45 for glass<sup>10</sup>, 1.38 for isopropanol<sup>5</sup>, about 2.5 for PbI<sub>2</sub><sup>6</sup> and 1 for air, one obtains reflection probabilities of 0.85 for the interface MAPbI<sub>3</sub>-air, 0.7 for MAPbI<sub>3</sub>-glass, 0.71 for MAPbI<sub>3</sub>-isopropanol and about 0 for MAPbI<sub>3</sub>-PbI<sub>2</sub>. Except for the case of MAPbI<sub>3</sub>-PbI<sub>2</sub>, reflections at other interfaces are neglected for simplicity, but would lead to an increase of the overall “effective” reflection probability. Since MAPbI<sub>3</sub> and PbI<sub>2</sub> are nearly index-matched, we

consider instead the PbI<sub>2</sub>-glass interface with the same reflection probability as the MAPbI<sub>3</sub>-glass interface.

Figure S11a shows the obtained thicknesses for different interfaces (glass-perovskite-air (g-a) and glass-(PbI<sub>2</sub>-) perovskite-isopropanol (g-i)) and suppression constants  $C$ , together with the one obtained from the absorption measurements. All thicknesses obtained from the modelling agree well with the ones obtained from absorption. Best agreement is obtained for PbI<sub>2</sub> and isopropanol as surrounding media and a suppression constant of 0.3 (g-i, 0.3; blue triangles), while all other parameter sets yield slightly lower thicknesses. However, comparing the resulting modelled PL spectra (Figure S11c-f) with the experimental ones (Figure S11b) reveals that the PL from (g-i, 0.3) (Figure S11e) agrees worst with the experimental data, especially considering the temporal evolution of the high energy falling edge. Second best agreement considering the thicknesses is obtained with (g-i, 0.2), where also the modelled PL spectra (Figure S11f) match the experimental ones nicely. A very similar result is obtained with (g-a, 0.3), and (g-a, 0.2) yields again slightly smaller thicknesses.

To capture the temporal evolution of the thickness more accurately by our model, it would probably be necessary to consider a transition of the interfaces, starting from PbI<sub>2</sub> and isopropanol and ending with glass and air as surrounding media. Since we have no indication on when and how this transition happens, we can not examine this scenario closer.

However, we want to stress that even with the simple model discussed above, good agreement between the thickness from the PL modelling and the one from absorption measurements could be obtained. Further, this clearly demonstrates that the observed red-shift of the PL in range IV is due to self-absorption, and represents a good example of the magnitude of self-absorption, despite excitation and detection being on the same side of the thin film.

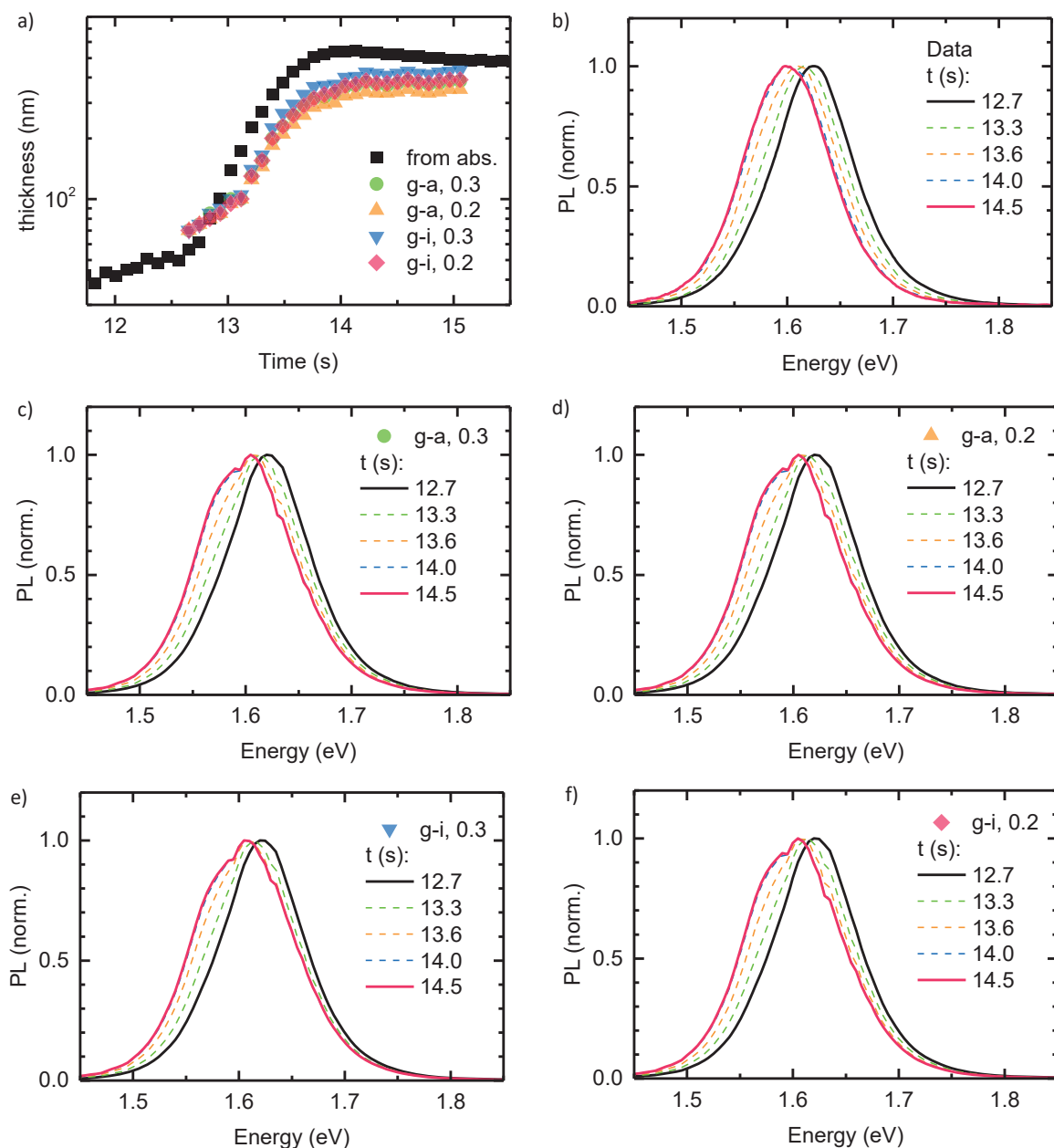


**Figure S11:** (a) MAPbI<sub>3</sub> layer thickness obtained from absorption measurements (black squares) together with the ones from optical modelling considering internal reflections and self-absorption. (b) Experimental PL spectra in range IV. (c-f) Modelled PL spectra considering internal reflections and self-absorption for different surrounding media (that is glass and air (g-a), or glass and isopropanol (g-i)) and different suppression constants of 0.3 and 0.2.

### S11: XRD measurements of the sample

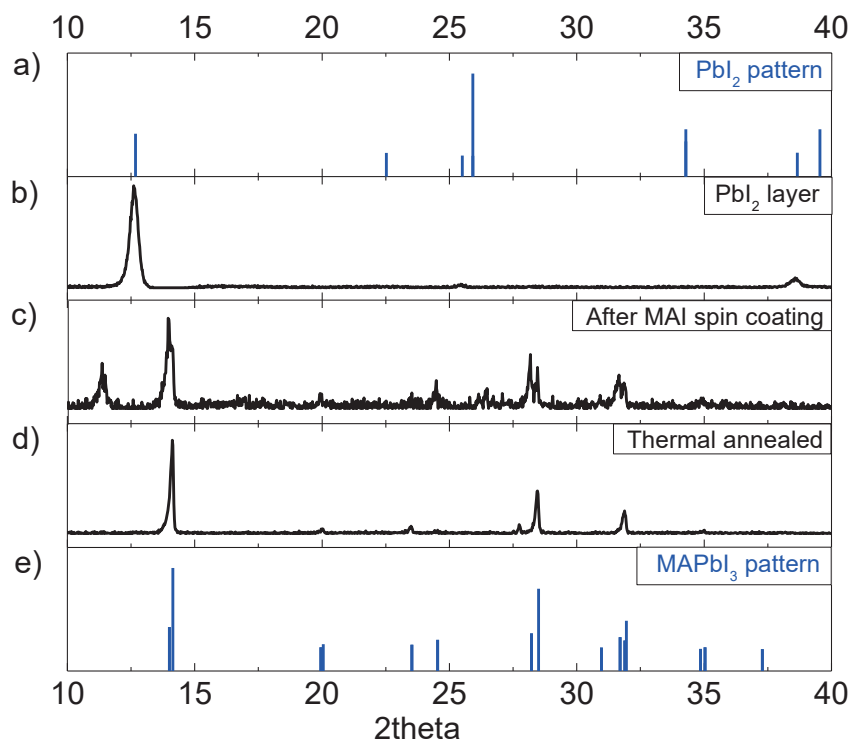


**Figure S12:** XRD pattern of (a) PbI<sub>2</sub> and (e) MAPbI<sub>3</sub> obtained from references.<sup>11, 12</sup> XRD spectra of (b) PbI<sub>2</sub> layer on glass substrate, (c) with MAI solvent spin coated on the PbI<sub>2</sub> layer and (d) the MAI + PbI<sub>2</sub> film after 45min thermal annealing.

Figure S12c shows that the formation of perovskite after the spin coating of MAI solvent. The peak  $2\theta = 11.4^\circ$  suggests the existence of dihydrate (MA)<sub>4</sub>PbI<sub>6</sub>·2H<sub>2</sub>O.<sup>4, 13</sup> while any sign of remaining educt phase e.g. PbI<sub>2</sub> is absent. After thermal annealing, the signal from the dihydrate completely vanishes (Figure S12d).



## S12: Estimation of average grain size of MAPbI<sub>3</sub> from SEM and theoretical model

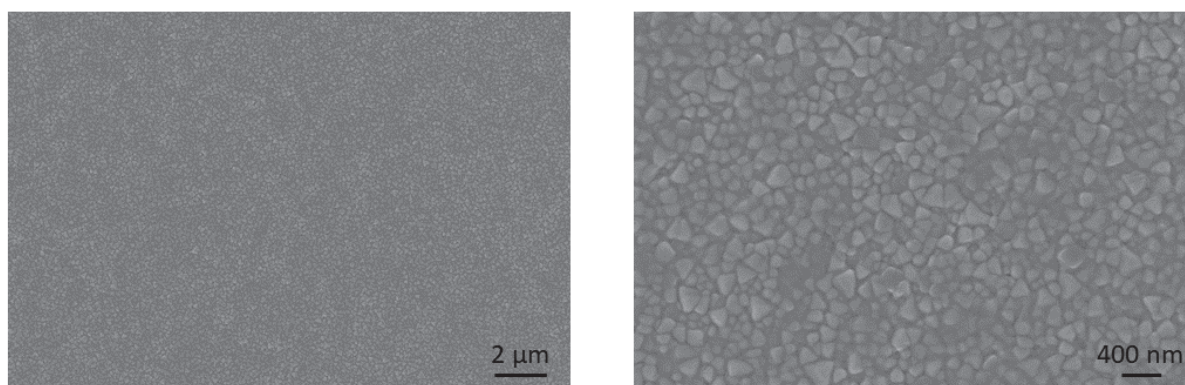


**Figure S13:** SEM images of the prepared film after spin coating. It yields compacted perovskite crystals. The size of the grains is between 50 nm-300 nm.

Theoretical model:

Ahn et al. derived the interaction formula to correlate grain size (Y) with MAI concentration (X) used in two step processing given as:<sup>14</sup>

$$\ln Y = \frac{1.22}{(\ln X - \ln C)^2} + 3.73 \quad (\text{S8})$$

Here, C = 0.02 M MAI solution has been taken as equilibrium concentration by assuming that 0.02 M MAI solution could not react with PbI<sub>2</sub> films at room temperature. Using these conditions, grain size expressed as:

$$Y = \exp(1.22/((\ln(X) - \ln(0.02))^2) + 3.73) \quad (\text{S9})$$

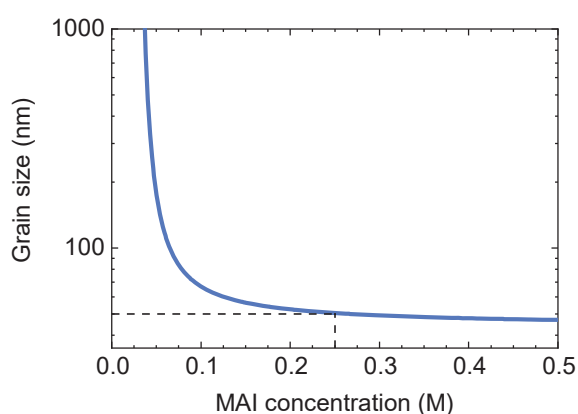


**Figure S14:** Average grain size of MAPbI<sub>3</sub> as a function of MAI concentration based on the model presented by Ahn et al.<sup>14</sup> The calculated grain size for 0.25 M (40 mg/ml) concentration (used for this study) is about 50 nm.

### S13: Estimation of local heating due to laser excitation

The temperature change of the excitation spot during laser light illumination is generally determined by the heat delivered  $Q$ , divided by the heat capacity  $C$  of the material, thus  $\Delta T = Q/C$ . The delivered heat by the laser per time  $\frac{\Delta Q_{\text{Laser}}}{\Delta t}$  is proportional to the laser fluence  $E_e$  multiplied by the area of the excitation spot  $A_{\text{spot}}$ . However, one has to consider that not all the laser light is absorbed. For the excitation wavelength of 520 nm, we observed a maximal optical density of 1 for the perovskite samples, thus 90 % of the laser light is absorbed, neglecting reflection, which would reduce the amount of absorbed light further. Additionally, not all of the absorbed energy is transformed into heat. One part of heat is provided by thermal relaxation of the carriers from their initial energy to the energy of the band gap, which gives a fraction of  $\frac{\Delta E}{E_{\text{photon}}} = \frac{2.38 \text{ eV} - 1.63 \text{ eV}}{2.38 \text{ eV}} = 0.315$ . The relaxed charge carriers can then either recombine radiatively or non-radiatively, producing heat. Assuming a PLQY of 0.1, corresponds to a fraction of non-radiative decay of 90%, so that we get another fraction of  $\frac{1.63 \text{ eV} \cdot 0.9}{2.38 \text{ eV}} = 0.616$ . Thus in sum, a fraction of  $f = 0.931$  of the irradiated energy is transformed to heat.

Since the sample is illuminated continuously during one frame (approx. 0.045 s) and the heat is not delivered instantly, one has to consider the cooling of the heated spot by thermal transport through the substrate to the spin coater. This is given by the heat equation:

$$\frac{\Delta Q}{\Delta t} = \frac{\lambda \Delta T}{l} A \quad (\text{S10})$$

where  $\lambda$  is the thermal conductivity,  $\Delta T$  is the temperature of the bath minus the temperature of the excitation spot,  $A$  is the area normal to the heat flow, and  $l$  is the length over which the dissipation takes place. Since the spot size is large compared to the thickness of the perovskite layer, lateral heat transport can be neglected and  $A = A_{\text{spot}}$ .

In thermal equilibrium, the decrease of heat by thermal transport is equal to the increase of heat by laser irradiation,

$$\frac{\Delta Q_{\text{ges}}}{\Delta t} = \frac{\lambda \Delta T}{l} A_{\text{spot}} + E_e \cdot f \cdot A_{\text{spot}} = 0 \quad (\text{S11})$$

Rearranging this equation for  $\Delta T$  gives

$$-\Delta T = \frac{E_e \cdot f \cdot l}{\lambda} \quad (\text{S12})$$

Considering the spin coater as a thermal bath with a constant temperature of 300 K, the heat transport takes place over the thickness of the substrate, that is  $l = 1 \text{ mm}$ . The thermal conductivity of fused silica, which transports the heat, is  $\lambda = 1.5 \frac{\text{W}}{\text{Km}}$ .<sup>15</sup> The fluence of the laser was determined to be  $E_e = 75 \text{ mW/cm}^2$ . Inserting this into equation S12, gives a heating of the sample of  $|\Delta T| \approx 0.5 \text{ K}$  upon laser exposure.

## References

1. E. S. Parrott, J. B. Patel, A.-A. Haghighirad, H. J. Snaith, M. B. Johnston and L. M. Herz, *Nanoscale*, 2019, **11**, 14276-14284.
2. J. Manifacier, J. Gasiot and J. Fillard, *J. Phys. E: Sci. Instrum.*, 1976, **9**, 1002.
3. R. Munir, A. D. Sheikh, M. Abdelsamie, H. Hu, L. Yu, K. Zhao, T. Kim, O. E. Tall, R. Li and D. M. Smilgies, *Adv. Mater.*, 2017, **29**, 1604113.
4. A. M. Leguy, Y. Hu, M. Campoy-Quiles, M. I. Alonso, O. J. Weber, P. Azarhoosh, M. Van Schilfgaarde, M. T. Weller, T. Bein and J. Nelson, *Chemistry of Materials*, 2015, **27**, 3397-3407.
5. E. Sani and A. Dell'Oro, *Optical Materials*, 2016, **60**, 137-141.
6. R. Frisenda, J. O. Island, J. L. Lado, E. Giovanelli, P. Gant, P. Nagler, S. Bange, J. M. Lupton, C. Schüller and A. J. Molina-Mendoza, *Nanotechnology*, 2017, **28**, 455703.
7. T. W. Crothers, R. L. Milot, J. B. Patel, E. S. Parrott, J. Schlipf, P. Müller-Buschbaum, M. B. Johnston and L. M. Herz, *Nano Lett.*, 2017, **17**, 5782-5789.
8. K. Schötz, M. A. Askar, W. Peng, D. Seeberger, P. T. Guijar, M. Thelakkat, A. Köhler, S. Huettnner, M. O. Bakr and K. Shankar, 2019, submitted.
9. L. J. Phillips, A. M. Rashed, R. E. Treharne, J. Kay, P. Yates, I. Z. Mitrovic, A. Weerakkody, S. Hall and K. Durose, *Data in brief*, 2015, **5**, 926-928.
10. I. Malitson, *Josa*, 1965, **55**, 1205-1209.
11. K. Persson, *Materials Data on Te<sub>2</sub>MoWSeS (SG: 156) by Materials Project*, LBNL Materials Project; Lawrence Berkeley National Lab.(LBNL), Berkeley, CA ..., 2017.
12. Y. Dang, Y. Liu, Y. Sun, D. Yuan, X. Liu, W. Lu, G. Liu, H. Xia and X. Tao, *CrystEngComm*, 2015, **17**, 665-670.
13. A. Halder, D. Choudhury, S. Ghosh, A. S. Subbiah and S. K. Sarkar, *The Journal of Physical Chemistry Letters*, 2015, **6**, 3180-3184.
14. N. Ahn, S. M. Kang, J.-W. Lee, M. Choi and N.-G. Park, *Journal of Materials Chemistry A*, 2015, **3**, 19901-19906.
15. B. H. De Jong, R. G. Beerkens, P. A. van Nijnatten and E. Le Bourhis, *Ullmann's Encyclopedia of Industrial Chemistry*, 2000.



# **8 Crystallization Kinetics of Controlled Solvent Vapor Assisted Annealing of Organolead Perovskite Film**

Yu Zhong, Dominik Seeberger, Anna Köhler, Fabian Panzer, Cheng Li, Sven  
Huettnner

Prepared for submission

# Crystallization Kinetics of Controlled Solvent Vapor Assisted Annealing of Organo Lead Perovskite Film

Yu Zhong,<sup>[a],[b]</sup> Dominik Seeberger,<sup>[a]</sup> Anna Köhler,<sup>[b]</sup> Fabian Panzer,<sup>[b]</sup> Cheng Li,<sup>\*,[c]</sup> Sven Huettner<sup>\*,[a]</sup>

[a] Y. Zhong, D. Seeberger, Dr. S. Huettner  
Department of Chemistry  
University of Bayreuth  
Universitätsstr.30, Bayreuth 95440, Germany  
E-mail: sven.huettner@uni-bayreuth.de

[b] Y. Zhong, Prof. A. Köhler, Dr. F. Panzer  
Optoelectronics of Soft Matter  
University of Bayreuth  
Universitätsstr.30, Bayreuth 95440, Germany

[c] Prof. C. Li.  
School of Electronic Science and Engineering  
Xiamen University  
Xiamen 361005, China  
E-mail: chengli@xmu.edu.cn

## Abstract

Organo metal halide perovskite solar cells continuously attract attention due to their progressive performance improvement in the last few years. One of the key factors contributing to this improvement is the significant enhancement of perovskite crystal quality, including its crystallinity and morphology. Among various methods, the solvent vapor assisted annealing (SVAA) method has been demonstrated as an effective way to achieve this enhancement. However, a comprehensive study of the detailed process during SVAA is still lacking. In this work, we constructed a setup to modulate SVAA conditions precisely in order to explore the crystallization kinetics. By controlling N,N-dimethylformamide (DMF) vapor concentration, the grain size of perovskite crystals can be tuned from 200 nm to several micrometers. By means of *in-situ* grazing incidence wide-angle X-ray scattering (GIWAXS), the formation of an intermediate, i.e. a MAI-PbI<sub>2</sub>-DMF complex, is elucidated. It is found that during SVAA the crystal growth process transfers into a more complicated Ostwald ripening process with the increasing DMF concentration. Moreover, this study points out the critical role of precisely controlling solvent vapor concentration during SVAA to obtain high-quality perovskite polycrystalline films.



## Introduction

Organo metal halide perovskites have shown an unprecedented development towards their application in solid-state solar cells since their first demonstration in 2012.<sup>1,2</sup> Regarding the steep increase in the efficiency of perovskite solar cells and the improvement of their stability, it is widely accepted that they are closely associated with the quality of the perovskite crystal. Researchers have devoted to develop methods in order to fabricate high-quality perovskite films, ranging from precursors modulation and solvents treatment to additives incorporation and further approaches.<sup>3–6</sup> Among them, a very effective method is to control the annealing condition during the perovskite formation, including the temperature and ambient conditions.<sup>7–9</sup> The implementation of solvent vapor during annealing, *e.g.* N,N-dimethylformamide (DMF),<sup>10</sup> dimethyl sulfoxide (DMSO),<sup>11</sup>  $\gamma$ -butyrolactone,<sup>12</sup> has been reported to be helpful. Zuo *et al.* have found an enhancement of the perovskite solar cell efficiency when MAPbI<sub>3</sub> film is exposed to DMF or DMSO vapor, reaching efficiencies of up to 19.2%.<sup>13</sup> The average grain size and quality of the perovskite films treated with solvent vapor can be significantly improved. With DMF vapor, grain sizes of more than 1.5  $\mu\text{m}$  have been demonstrated<sup>14,15</sup> and films with high crystallinity and reduced defects have been reported.<sup>16,17</sup>

Solvent vapor assisted annealing (SVAA) is a well-established method in altering polymer morphologies, block-copolymers or the fabrication of organic optoelectronic devices.<sup>18</sup> For example, the efficiency enhancement of poly(3-hexylthiophene)/[6,6]-phenyl-C61-butyric acid methyl ester (P3HT/PCBM) photovoltaic cells through SVAA method were found 10 years ago.<sup>19,20</sup> Further studies concentrated on the effect of SVAA on the structure of P3HT/PCBM layer, including phase separation and ordering of polymer blends.<sup>21–23</sup> Beside this, the SVAA method shows its promising prospects on a wide-range of semiconducting polymers.<sup>24,25</sup> Even though there are studies of perovskite SVAA method coming out, more fundamental investigations are still lacking. On this account, this paper is dedicated to the crystallization kinetics of SVAA of perovskite film.

Grazing incidence wide-angle X-ray scattering (GIWAXS) has emerged as a powerful tool to study *in-situ* perovskite crystallization kinetics of thin films.<sup>26–28</sup> GIWAXS results demonstrate that the heat-induced crystallization process of perovskite can be generally divided into three stages: solution stage, from solution to an intermediates stage, from the intermediates to the perovskite crystal.<sup>29,30</sup> D.T. Moore *et al.* have set a model to extract the activation energy for precursor-to-perovskite transition of thermal annealing.<sup>31</sup> For an SVAA process, K. Meng *et al.* compared the influence of different solvent vapors and found that DMF and DMSO molecules could serve as coordinating molecules to form an intermediate adduct during the annealing.<sup>32</sup> Based on these previous outcomes, we use GIWAXS to study the transformation of the intermediate phase and the crystallization kinetics. Especially, the influence of the DMF vapor concentration on the crystallization kinetics is in focus of this presented work.

In many studies, SVAA of perovskite films is carried out in a very simple way by putting an as-spun film and droplets of solvent in a petri dish and then heating the petri dish.<sup>10,17</sup> By means of this method, it is difficult to modulate the pressure and the duration of the solvent vapor during the annealing process. For any further industrial application SVAA needs to be performed in a much more controlled, up-scalable and reproducible way. Hence, we constructed a setup to precisely manipulate the solvent vapor pressure using digital flow controllers, which

has already been successfully utilized in semiconducting polymers studies.<sup>25,33,34</sup> This paper focuses on the investigation of perovskite film formation with SVAA by systematically changing the parameters, *e.g.* vapor concentration, vapor temperature and so on. This study can provide guidance for a further optimization of the annealing parameters to manufacture high-quality perovskite films. Moreover, it elucidates the formation pathway and mechanism.

## Results

We employed a two-step method to fabricate perovskite films. As shown in Figure 1(a), perovskite films were prepared by sequentially spin coating  $\text{PbI}_2$  solution (dissolved in DMF) and MAI solution (dissolved in isopropanol). Then, the films were annealed in a specially designed sample chamber, as shown in Figure 1(b) and Figure S1(a). The inlet of the chamber is connected to an inlet and an outlet gas line. For the outlet gas line, the  $\text{N}_2$  gas passing through the solvent bubbler will be saturated with the solvent vapor. We can change the saturation of the solvent vapor in the sample chamber, by adjusting the ratio between dry  $\text{N}_2$  gas with the fully saturated  $\text{N}_2$  gas from the bubbler. All of them are placed in an oven and the sample chamber can be additionally heated on by hotplate inside the oven. Through the oven, the temperature of the solvent bubbler and the pipelines can be controlled. According to Clausius-Clapeyron relation and ideal gas law,<sup>35</sup> the solvent concentration can be precisely regulated in a large range. An example of the DMF vapor concentration is illustrated in Figure 1(c) for several temperatures of solvent bubbler. The detailed estimation of the solvent vapor concentration in the sample chamber is expressed in S2. Moreover, the flow controller is digitally connected to a computer, allowing a precise control of time and flow rate.

In the subsequent experiment, the prepared films were transferred into the sample chamber after spin coating. The films were annealed for 45 min at 110 °C with different gas flow settings. For SVAA samples, they were annealed under DMF vapor within the first 30 min followed by 15 min of pure  $\text{N}_2$ . The reason to choose DMF is its good solubility of perovskite and  $\text{PbI}_2$ . To reduce the flow turbulence on the film surface, a low flow rate of 10  $\text{cm}^3/\text{min}$  was hold. After several trials, we set the solvent bubbler temperature to  $T_1 = 75\text{ }^\circ\text{C}$  and the vapor saturation to: 20%, 30%, 40%, 50%, 60% and 80%. This corresponds to DMF vapor concentration in the sample chamber of:  $0.54 \times 10^{-6}$ ,  $0.81 \times 10^{-6}$ ,  $1.1 \times 10^{-6}$ ,  $1.3 \times 10^{-6}$ ,  $1.6 \times 10^{-6}$ ,  $2.2 \times 10^{-6}$   $\text{mol}/\text{cm}^3$ . They are indicated by the triangle symbols in Figure 1(c).

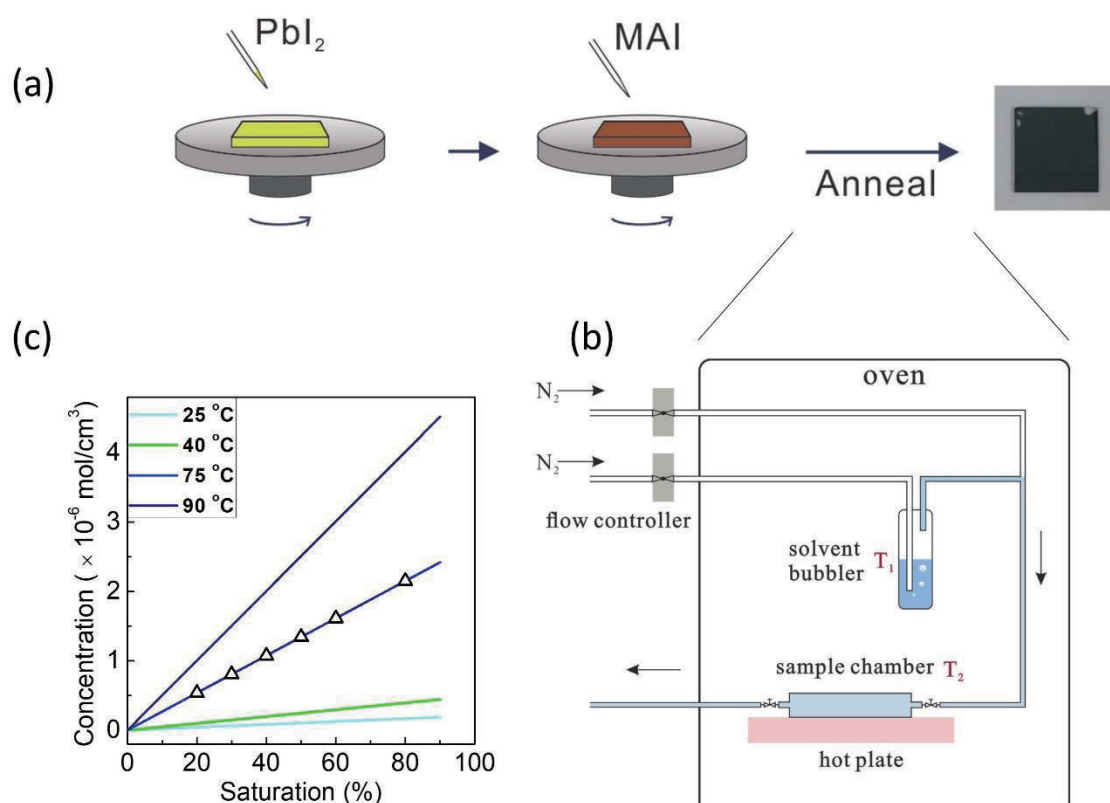


Figure 1: (a) The two-step method to prepare  $\text{MAPbI}_3$  perovskite film; (b) Schematic illustration of the solvent annealing setup.  $T_1$  and  $T_2$  are the temperatures of solvent bubbler and sample chamber, respectively. (c) The control of DMF vapor concentration by changing the solvent temperature and its saturation. The saturation can be adjusted by changing the two  $\text{N}_2$  inlet ducts ratio in (b). The temperature in the graph legend means the solvent bubbler temperature  $T_1$  in (b). The triangles represent the vapor conditions used in the following experiment.

Scanning electron microscope (SEM) images of perovskite films are shown in Figure 2(a). Moreover, XRD patterns of the films annealed with high DMF concentrations ( $1.3 \times 10^{-6}$ ,  $1.6 \times 10^{-6}$ ,  $2.2 \times 10^{-6} \text{ mol/cm}^3$ ) are shown in Figure S2, indicating full conversion from  $\text{PbI}_2$  and  $\text{MAI}$  to  $\text{MAPbI}_3$ .

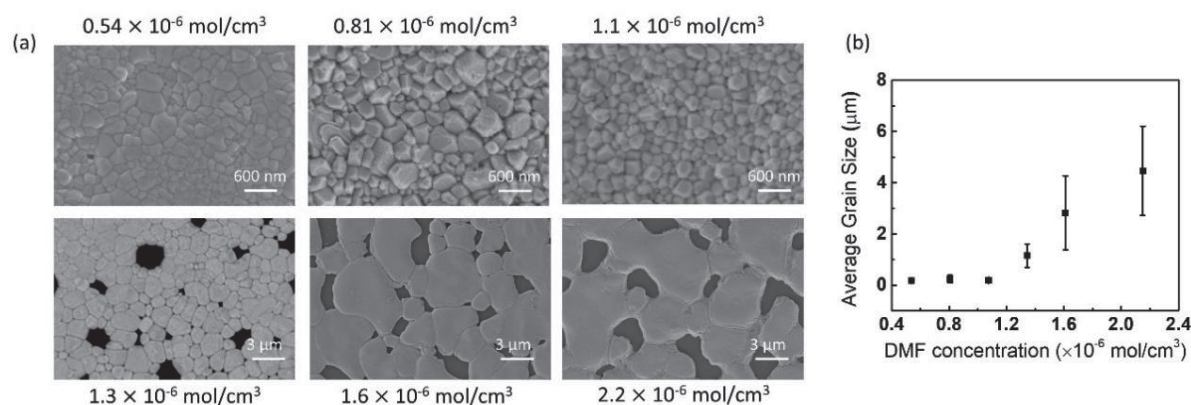


Figure 2: (a) The SEM images of perovskite films annealed with different DMF concentrations. The labels next to the SEM images are the corresponding DMF vapor concentrations. (b) The average crystal grain sizes of perovskite film annealed with different DMF concentration.

The SEM images in Figure 2(a) show that perovskite films yield larger grain sizes when they are annealed under higher DMF concentrations concomitant with a lower surface coverage. By analyzing the average grain size of perovskite crystals from the SEM images, we can obtain its

relationship to the DMF vapor concentration, as plotted in Figure 2(b). Below  $1.1 \times 10^{-6} \text{ mol/cm}^3$  the average grain size does not change significantly. When the DMF concentration increases to  $2.2 \times 10^{-6} \text{ mol/cm}^3$ , the average grain size reaches  $4.5 \text{ }\mu\text{m}$ . If we further increase the DMF concentration to  $3.8 \times 10^{-6} \text{ mol/cm}^3$ , as displayed in Figure S3 (a), the films become transparent after several minutes of SVAA. As observed by SEM, it shows a needle-like morphology on a millimeter scale instead of granule-like crystals, which is a sign of dissolution and recrystallization of the perovskite. These phenomena suggest that the SVAA method is a way to control the grain size and morphology of perovskite film, though the vapor saturation needs to be carefully controlled. To investigate the specific process in the SVAA method, we use grazing incidence wide-angle X-ray scattering (GIWAXS).

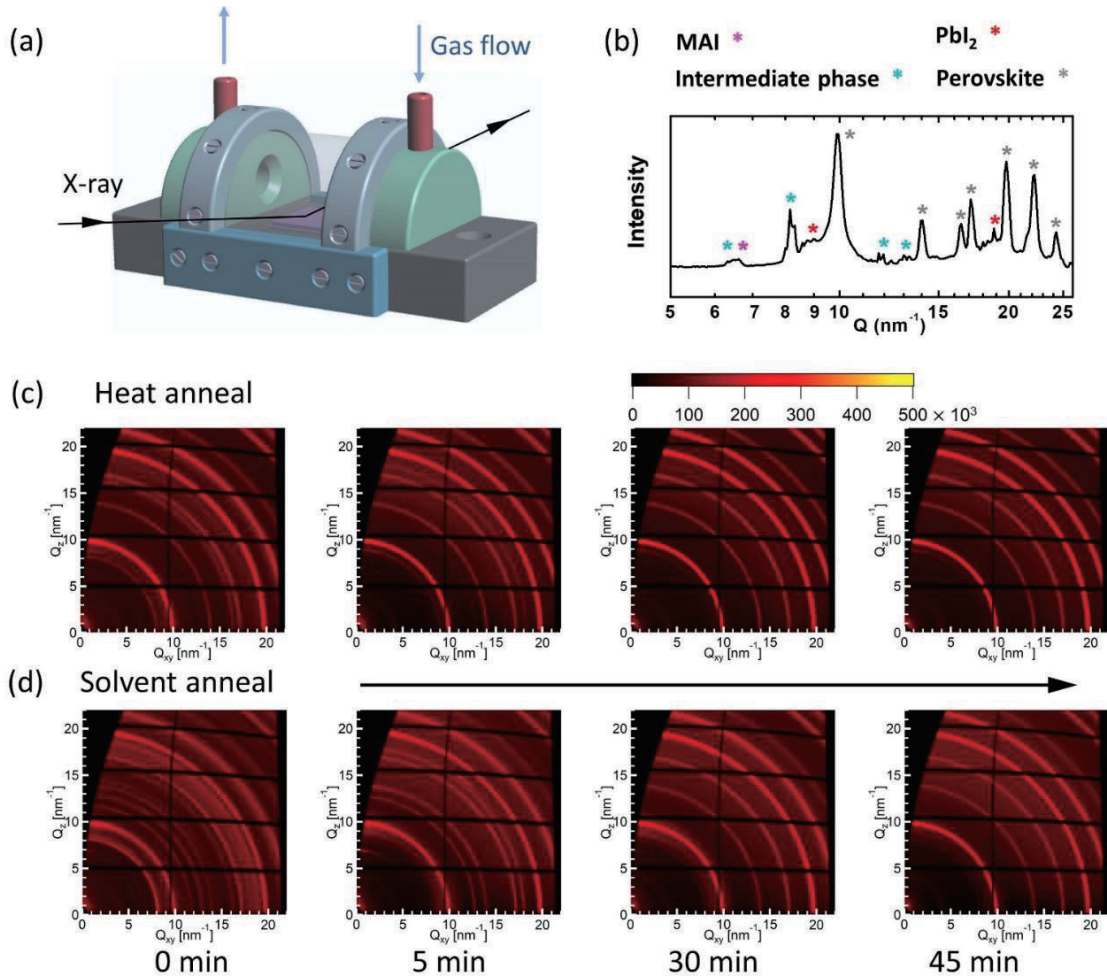


Figure 3: (a) Experimental setup for *in-situ* GIWAXS measurements of perovskite film annealing process. (b) Azimuthally integrated intensity plot of the GIWAXS patterns - after the deposition of MAI on  $\text{PbI}_2$  layer. The stars represent the characteristic peaks of MAI (pink),  $\text{PbI}_2$  (red), intermediate phase (blue) and perovskite (grey). X-ray scattering patterns of perovskite film during (c) heat annealing and (d) SVAA. Figures from left to right indicate the changes along with increasing annealing time.

GIWAXS measurements were carried out on as-spun samples during its annealing. The sample preparation is as illustrated in Figure 1(a). After spin coating MAI solvent on  $\text{PbI}_2$  layer, the sample was transferred into a self-designed chamber depicted in Figure 3(a) and it took approximately 5 min from the spin coater to the first GIWAXS measurement. A semi-cylinder covered by a kapton film allows X-rays to pass. The flow inlet of the chamber is connected to a solvent bubbler and two flow controllers, similar to the setup of Figure 1(b). The chamber and



the solvent temperatures are both controlled by cycling thermostats. The mounting of the chamber for GIWAXS measurement is displayed in Figure S1(b). With this setup, we are able to view the structure changes of perovskite film during heat annealing and SVAA *in situ*. A small limitation compared to the setup shown in Figure 1(b) is the more limited temperature range. Figure 3(b) shows a GIWAXS pattern of the film before annealing. This corresponds to our previous study, that the perovskite crystal structure forms when MAI diffuses into the  $\text{PbI}_2$  layer during spin coating.<sup>36</sup> Beside the strong perovskite signal at  $10.0 \text{ nm}^{-1}$ , there still exists some unreacted  $\text{PbI}_2$  and MAI within the film, indicated by peaks at  $9.0 \text{ nm}^{-1}$  and  $6.5 \text{ nm}^{-1}$ . The peak at  $8.2 \text{ nm}^{-1}$  is attributed to a MAI- $\text{PbI}_2$ -DMF complex<sup>37,38</sup>, which will be addressed in the following part. DMF is likely to be present as residual in the  $\text{PbI}_2$  layer.

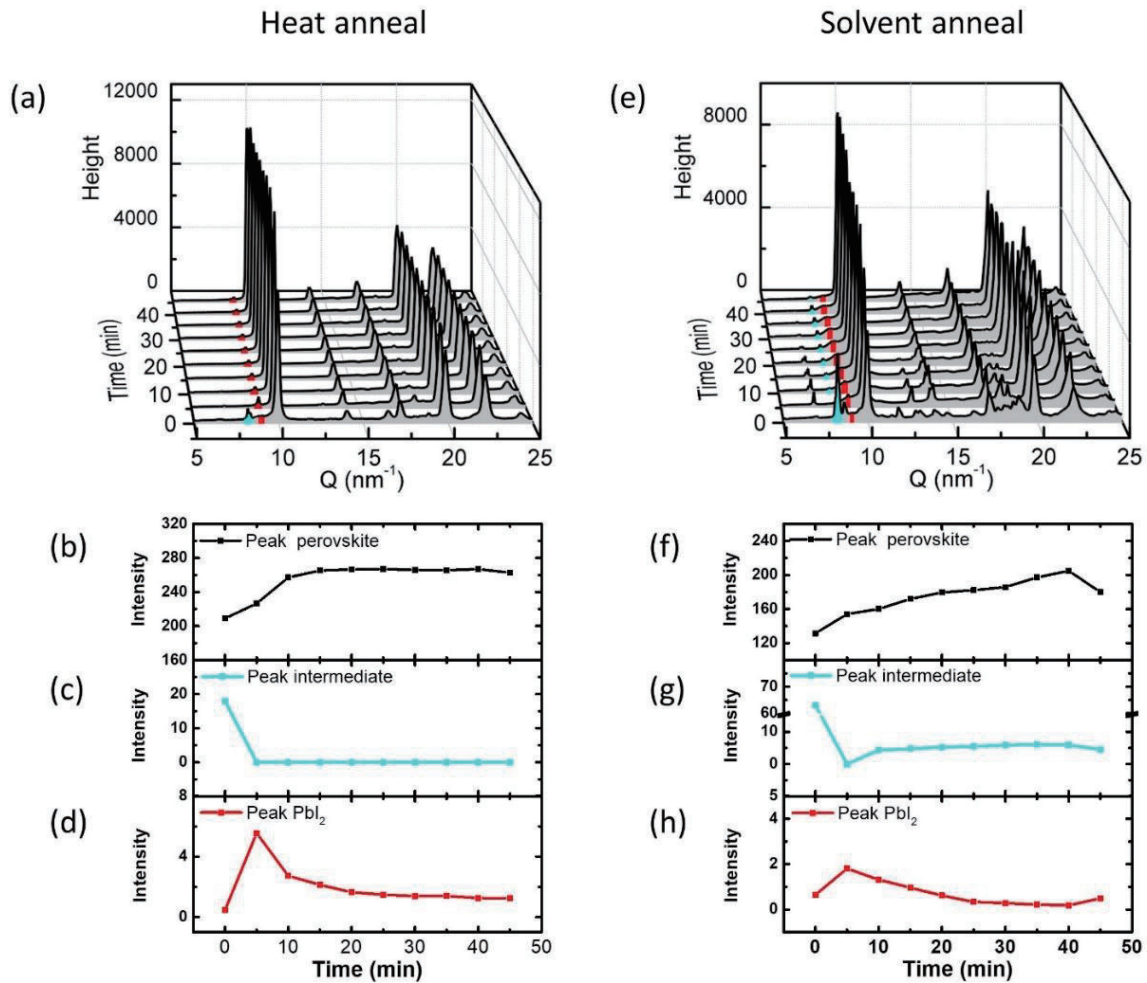


Figure 4: Azimuthally integrated intensity plot of the GIWAXS patterns of perovskite film during (a) heat annealing and (e) SVAA. Each intensity curve is integrated from radial rings over the entire GIWAX image. Intermediate phase peak at  $8.2 \text{ nm}^{-1}$  is marked by blue.  $\text{PbI}_2$  peak at  $9.0 \text{ nm}^{-1}$  is marked by red. (b), (c) and (d) are intensity of the peak at  $10.0 \text{ nm}^{-1}$  at  $8.2 \text{ nm}^{-1}$  and at  $9.0 \text{ nm}^{-1}$  in (a), respectively. (f), (g) and (h) are intensity of the peak at  $10.0 \text{ nm}^{-1}$  at  $8.2 \text{ nm}^{-1}$  and at  $9.0 \text{ nm}^{-1}$  in (e), respectively.

Figure 3 (c) and (d) display GIWAXS patterns of the sample with heat annealing and DMF SVAA in comparison. The heat annealing conditions were at  $120^\circ\text{C}$  for 45 min with a  $\text{N}_2$  flow of  $10 \text{ cm}^3/\text{min}$ . For solvent annealing, it was conducted at  $120^\circ\text{C}$  under DMF vapor for the first 30 min and under pure  $\text{N}_2$  for the last 15 min. The DMF vapor concentration in the first 30 min was  $1.0 \times 10^{-7} \text{ mol/cm}^3$ . Due to the setup restrictions during the X-ray scattering measurement,

it was difficult to achieve a very high saturation of DMF vapor. The first 2D GIWAXS pattern was recorded when the temperature of the chamber reached 120 °C. During the warming-up phase, the gas flow (either pure N<sub>2</sub> gas or N<sub>2</sub> gas saturated with DMF) was applied. The peak intensity of the heat annealed and solvent annealed sample at 0 min slightly differs, as the presence of DMF molecules can suppress the crystallization process before the temperature reaches 120 °C. Additionally, we need to mention that both heat annealed and solvent vapor assisted annealed samples exhibit a weak PbI<sub>2</sub> signal after 45 min for those samples that were *in-situ* X-ray characterized. When we measured the annealed perovskite film prepared with the similar method but without continuous X-ray scattering measurements, no PbI<sub>2</sub> peak was detected, as displayed in Figure S4(c). It indicates that the exposure to X-ray can lead to the degradation of MAPbI<sub>3</sub> at an elevated temperature. Two works from M. Alsari et al.<sup>39</sup> and R. L. Z. Hoyer et al.<sup>40</sup> also point out X-ray beam damage on perovskite sample. The decomposition product PbI<sub>2</sub> was unavoidable in our *in-situ* measurement even though we minimized any influence by shifting the sample after each X-ray exposure by 0.2 mm and by using short exposure times. As illustrated in Figure 4(b) and (c), the amount of PbI<sub>2</sub> is low after 45 min annealing, comparing to the peak intensity of perovskite. Hence, we assume there is no significant impact on the perovskite crystallization process.

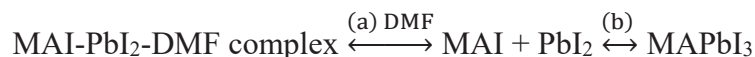
For a full study of GIWAXS results, we azimuthally integrated the 2D-patterns and showed them as one-dimensional scattering intensity curves, which allow a direct comparison of the crystallinity degree. As presented in Figure 4, the scattering patterns were plotted as a function of time and the peak areas of the perovskite (at 10.0 nm<sup>-1</sup>), the intermediate phase (at 8.2 nm<sup>-1</sup>) and the PbI<sub>2</sub> (at 9.0 nm<sup>-1</sup>) were analyzed. In general, we found that the intensity of the perovskite peak increased over time, reaching its maximum at 20 min for the heat annealed sample and 40 min for the solvent annealed sample. In the first 5 min, an increase of MAI intensity and PbI<sub>2</sub> intensity was observed in both samples (displayed in Figure 4(d), (h) and Figure S5), accompanied with the decrease of the intermediate phase. For the heat annealed sample, the PbI<sub>2</sub> intensity decreased after 5 min and no obvious changes were observed after 20 min. For the solvent annealed sample, the PbI<sub>2</sub> intensity also decreased after 5 min and increased slightly after 40 minutes. The main difference between these two samples was the intermediate phase. The heat annealed sample yielded no more intermediate phase after 5 min, while it appeared again after 10 min during SVAA. These results imply that for solvent annealed sample the transition into the perovskite is slowed down significantly and the intermediate phase play an important role in the crystal formation.

## Discussion

Based on the GIWAXS results, the sharp increase of MAI and PbI<sub>2</sub> noted in the first 5 min suggests that the intermediate phase transfers into PbI<sub>2</sub> and MAI. For the composition of the intermediate, one assumption is MAPbI<sub>3</sub>·DMF. However, MAPbI<sub>3</sub>·DMF will directly convert into MAPbI<sub>3</sub> after annealing and no MAI or PbI<sub>2</sub> will be formed,<sup>41</sup> which is not consistent with our observation. In this work, the observed intermediate phase is suggested to be MAI-PbI<sub>2</sub>-DMF complex. It has been reported that the scattering peak from MAI-PbI<sub>2</sub>-DMF complex (110) plane is ~8.19 nm<sup>-1</sup> and the MAI-PbI<sub>2</sub>-DMF complex was found in an as-spun film annealed in the temperature range between 40 °C and 80 °C.<sup>37</sup> Accordingly, the characteristic peak of this observed intermediate phase is at 8.2 nm<sup>-1</sup> and it matches the peak position of MAI-PbI<sub>2</sub>-DMF



complex. Based on this, we propose the following heat annealing crystallization mechanism:



Our proposition results from a number of considerations. First, when MAI was spin coated on  $\text{PbI}_2$ , the transformation into  $\text{MAPbI}_3$  immediately took place, as evident from the strong  $\text{MAPbI}_3$  related peaks right at the beginning of the SVAA process.<sup>36</sup> Simultaneously, some  $\text{PbI}_2$  and MAI would react with the residual DMF, thus forming MAI- $\text{PbI}_2$ -DMF complex. This is evidenced by the peak at  $8.2 \text{ nm}^{-1}$ . As shown in Figure 5(a), after spin coating, the film may contain following components:  $\text{MAPbI}_3$ ,  $\text{PbI}_2$ , MAI and MAI- $\text{PbI}_2$ -DMF complex. When the sample is annealed at  $120^\circ\text{C}$ , the complex converts within the first 5 minutes to MAI and  $\text{PbI}_2$ , as suggested by the initial fast growth of the  $\text{PbI}_2$  scattering signal and concomitant further growth of the perovskite scattering signal. The main transition during the heat annealing is the reaction (b), which occurs between MAI and  $\text{PbI}_2$  and leads to the formation of  $\text{MAPbI}_3$ . This transition is shown schematically in Figure (a) and (b).

For the sample annealed under a low DMF vapor concentration (DMF concentration  $< 1.3 \times 10^{-6} \text{ mol/cm}^3$ ), the decrease of the intermediate peak within the first 5 min is most likely a consequence of the concomitant heat treatment. Over time, the accumulating DMF molecules into the chamber can lead to the transition into MAI- $\text{PbI}_2$ -DMF complex. The appearance of this complex happens after approximately 10 min. From 10 min to 30 min, the perovskite scattering intensity continues to increase but with a lower increasing rate comparing to the heat annealed one, while the complex scattering intensity keeps almost unchanged. This observation suggests that the reaction (b) from MAI and  $\text{PbI}_2$  to  $\text{MAPbI}_3$  slows down and the amount of reacted DMF stays almost constant. Based on the relatively low MAI- $\text{PbI}_2$ -DMF complex intensity, we suggest that DMF in this case mostly reacts with the MAI and  $\text{PbI}_2$  on the surface or at the grain boundaries, where it is easier for DMF molecules to interact. The angle-dependent GIWAXS measurements in Figure S6 are consistent with this hypothesis, as the amount of MAI- $\text{PbI}_2$ -DMF complex on the top part of the film is higher than that in the bottom. After 30 min, the DMF vapor is removed and the sample is heat annealed from 30 min to 40 min in pure  $\text{N}_2$ . Within this period, the  $\text{MAPbI}_3$  intensity becomes higher which is originated from reaction (a) and (b). Based on the discussion above, we can explain the SVAA process with a low DMF concentration: DMF molecules interact with the surface of the film and diffuse into the film, forming an MAI- $\text{PbI}_2$ -DMF complex, through which enables the coalescence of two adjacent grains together and the formation of a larger grain. Its corresponding schematic is shown in Figure 5(c). The composition of the MAI- $\text{PbI}_2$ -DMF complex is proposed to be  $\text{PbI}_2 \cdot 3\text{MAI} \cdot \text{DMF}$  or  $\text{PbI}_2 \cdot \text{MAI}_2 \cdot \text{MA} \cdot \text{DMF}$  and from previous studies it appears at places where DMF and excess MAI exist.<sup>37,38</sup>

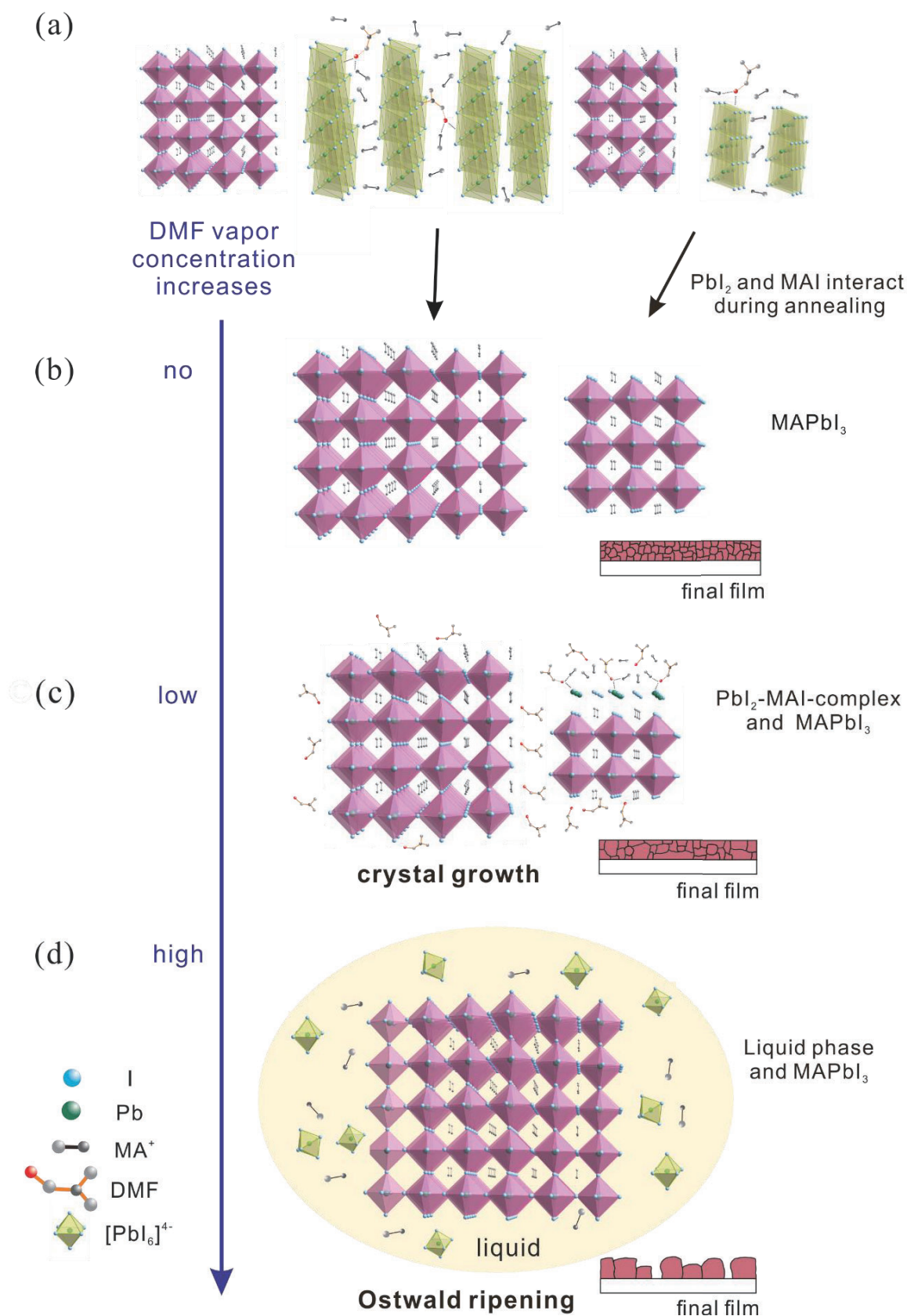


Figure 5: Schematic of MAPbI<sub>3</sub> perovskite thin film formation with different DMF concentrations and the corresponding final film morphology. (a) The film before annealing with prevalence of MAPbI<sub>3</sub>, PbI<sub>2</sub>, MAI and MAI-PbI<sub>2</sub>-DMF complex. The film is annealed (b) without DMF vapor, (c) with low DMF vapor concentration and (d) with high DMF vapor concentration. From a low to high DMF concentration, the perovskite formation process changes from crystal growth into Ostwald ripening and the final perovskite crystal sizes increase.

In the case of a high DMF vapor concentration (DMF concentration  $\geq 1.3 \times 10^{-6}$  mol/cm<sup>3</sup>), the observation of pinholes in the final perovskite film (shown in Figure 2(a)) implies the formation of a liquid phase when DMF vapor is continuously provided. This process may differ from the mechanism described above. Here, we propose a pathway under high DMF concentration:



When the DMF vapor concentration is high, the DMF molecules will not only react with MAI and PbI<sub>2</sub>, generating MAI-PbI<sub>2</sub>-DMF complex, but also DMF vapor can liquefy on the complex surface and dissolve the complexes and perovskite crystals, therefore forming a liquid phase. Due to the surface tension, this liquid can attach to MAPbI<sub>3</sub> crystals. Subsequently, the solute in the liquid phase grows on MAPbI<sub>3</sub> crystals, with the transition (d). After the removal of DMF vapor, the liquid phase can be desiccated and finally transfer into MAPbI<sub>3</sub>. The formation of liquid phase surrounding perovskite crystals is displayed in Figure 5(d) and this is considered to result in pinholes in the perovskite film. This pathway elaborates the possible reactions in SVAA process.

As mentioned above, most reported studies of SVAA method were conducted in a petri dish. In the case of a petri dish, the solvent vapor concentration can reach a relatively high concentration in a short time, e.g. the highest possible DMF concentration in a 10 cm-diameter petri dish with 10  $\mu\text{L}$  DMF solvent is  $1.6 \times 10^{-6}$  mol/cm<sup>3</sup>. However, the vapor concentration will decrease quickly after a maximum is reached with the increasing annealing time, because it is not a properly sealed system and solvent molecules are able to escape from the petri dish. In this way, the average vapor concentration during SVAA is relatively low and thus little or no liquid phase is formed. Though it is possible to prepare larger crystals with no pinholes, as shown in previous studies.<sup>10,17</sup>

In our controlled SVAA setup, there are still certain points concerning the condensation of DMF vapor into liquid and the influence of solvent vapor concentration on the crystal grain size, which will be addressed in the following part. The first question is how DMF vapor condenses when it becomes less saturated at a higher temperature in the sample chamber. According to the kinetics of phase transition-classical nucleation theory, the formation of a critical DMF liquid droplet homogeneously in the supersaturated gas phase is accompanied with the free energy change  $\Delta G_{\text{homogeneous}}$ . In our experiment, the DMF vapor condenses on perovskite crystals, which is understood as heterogeneous nucleation process. Comparing to the homogeneous nucleation in DMF vapor, the free energy barrier  $\Delta G_{\text{heterogeneous}}$  is lowered by the expression:  $\Delta G_{\text{heterogeneous}} = \frac{2-3\cos\theta+\cos^3\theta}{4} \times \Delta G_{\text{homogeneous}}$ , where  $\theta$  is the contact angle and  $0 \leq \frac{2-3\cos\theta+\cos^3\theta}{4} \leq 1$ .<sup>3542</sup> Thus, less energy is required for the heterogeneous nucleation, making the condensation of DMF vapor on the perovskite surface possible. Meanwhile, the supersaturation at the interface is the driving force for DMF condensation and the supersaturation is expressed by  $p/p_0$ , in which  $p$  is the actual vapor pressure at the surface and  $p_0$  is the equilibrium vapor pressure.<sup>43</sup> When we set a higher DMF concentration,  $p/p_0$  increases and the driving force as well. It indicates more DMF molecules merge into liquid phase.

As discussed above, the condensed DMF may dissolve both the MAI-PbI<sub>2</sub>-DMF complex and MAPbI<sub>3</sub> crystals. According to the final film morphology, the dissolved crystals are able to

redeposit onto large crystals. This phenomenon can be described by Ostwald ripening and explained by Ostwald-Freundlich equation:<sup>4445</sup>

$$\ln \frac{C_r}{C_p} = \frac{2\gamma V_m^s}{r_0 RT}$$

Here,  $C_p$  is the equilibrium solute concentration at a plane interface and  $C_r$  is the equilibrium solute concentration at liquid/crystal interface of the crystal particle with the radius  $r_0$  (under a given pressure  $p$  and a temperature  $T$ ).  $\gamma$  is the interfacial energy of the liquid/crystal interface.  $V_m^s$  is the molar volume of crystal and  $R$  is the ideal gas constant. This equation presents that equilibrium concentration  $C_r$  at the surface of smaller crystals is higher. Consequently, smaller crystals keep dissolving to raise the solute concentration for reaching the equilibrium concentration. As a result, part of perovskites dissolved in the liquefied DMF, forming the liquid phase displayed in Figure 5(d). Due to the surface tension, the liquid phase will adhere on the large crystals. The solute comes to the liquid/crystal interface of the large crystals and further grow on them, similar to the perovskite single crystal growth from a supersaturated solvent. Therefore, the SVAA process develops from a standard crystal growth process to an Ostwald ripening process, when the solvent vapor concentration reaches a high level. This difference in the perovskite formation mechanism is graphically clarified in Figure 5(c) and (d). Moreover, annealing with a higher DMF vapor concentration results in more liquefied DMF which can dissolve more perovskite crystals with small grain sizes. Thus, with increasing DMF vapor concentration, the average grain size increases and its coverage of the film decreases.

Many studies suggest that one effective way to enhance the performance of perovskite solar cells is to increase the perovskite crystal grain size, as perovskite grain boundaries yield a higher defect density than the crystal bulk.<sup>164647</sup> Poor surface coverage of perovskite film will cause internal charge carrier recombination, which has negative effects on the solar cell performance. The prepared perovskite films with DMF vapor assisted annealing currently are not able to maintain both large grain sizes and a full surface coverage at the same time. In order to obtain an optimal SVAA condition, studies will continue through different approaches. One is by choosing solvents with different perovskite solubility or boiling points. The second one is by adjusting the inlet flow vertically to the film surface to promote the crystal growth in horizontal direction which is beyond the scope of this work.

## Conclusion

In this work, we construct a SVAA setup for perovskite films manufacture, which enables the precise regulation of parameters during the SVAA process. Our study indicates that the grain size of perovskite films is closely associated with the DMF vapor concentration during the annealing. Based on *in-situ* GIWAXS measurements, we propose the pathways to form perovskite crystals: (1) in normal heat annealing method, direct from MAI + PbI<sub>2</sub>; (2) in SVAA method, first through MAI-PbI<sub>2</sub>-DMF complex and liquid phase, then to MAPbI<sub>3</sub> solid. In controlled SVAA, DMF plays two major roles. One serves as a reactant, forming MAI-PbI<sub>2</sub>-DMF complex; the second one is to dissolve the complex and perovskite crystals only under high DMF concentration, leading to Ostwald ripening phenomenon. Our work outlines in-depth crystallization kinetics of SVAA method and provides a guidance on perovskite crystal growth and further thin film processing optimization.



## Acknowledgements

The authors gratefully acknowledge the financial support by Bavarian State Ministry of Science, Research and the Arts for the Collaborative Research Network “Solar Technologies go Hybrid” and German Research Foundation (DFG). Y. Z. acknowledges the funding from China Scholarship Council. C. L. acknowledges funding from National Natural Science Foundation of China (61974126, 51902273). Y. Z., C. L. and S. H. thank German Academic Exchange Service (DAAD) within Bayreuth-Melbourne strategic partnership program for their support. A part of this research was undertaken on the SAXS/WAXS beamline at the Australian Synchrotron. We thank the Bavarian Polymer Institute for SEM characterization.

## References

- (1) Lee, M. M.; Teuscher, J.; Miyasaka, T.; Murakami, T. N.; Snaith, H. J. Efficient Hybrid Solar Cells Based on Meso-Superstructured Organometal Halide Perovskites. *Science*. **2012**, *338* (6107), 643–647.
- (2) Kim, H.-S.; Lee, C.-R.; Im, J.-H.; Lee, K.-B.; Moehl, T.; Marchioro, A.; Moon, S.-J.; Humphry-Baker, R.; Yum, J.-H.; Moser, J. E.; et al. Lead Iodide Perovskite Sensitized All-Solid-State Submicron Thin Film Mesoscopic Solar Cell with Efficiency Exceeding 9%. *Sci. Rep.* **2012**, *2*, 591.
- (3) Fassl, P.; Lami, V.; Bausch, A.; Wang, Z.; Klug, M. T.; Snaith, H. J.; Vaynzof, Y. Fractional Deviations in Precursor Stoichiometry Dictate the Properties, Performance and Stability of Perovskite Photovoltaic Devices. *Energy Environ. Sci.* **2018**, *11* (12), 3380–3391.
- (4) Pellet, N.; Gao, P.; Gregori, G.; Yang, T.-Y.; Nazeeruddin, M. K.; Maier, J.; Grätzel, M. Mixed-Organic-Cation Perovskite Photovoltaics for Enhanced Solar-Light Harvesting. *Angew. Chemie Int. Ed.* **2014**, *53* (12), 3151–3157.
- (5) Jeon, N. J.; Noh, J. H.; Kim, Y. C.; Yang, W. S.; Ryu, S.; Seok, S. Il. Solvent Engineering for High-Performance Inorganic–Organic Hybrid Perovskite Solar Cells. *Nat. Mater.* **2014**, *13* (9), 897–903.
- (6) Bai, S.; Da, P.; Li, C.; Wang, Z.; Yuan, Z.; Fu, F.; Kawecki, M.; Liu, X.; Sakai, N.; Wang, J. T.-W.; et al. Planar Perovskite Solar Cells with Long-Term Stability Using Ionic Liquid Additives. *Nature* **2019**, *571* (7764), 245–250.
- (7) Huang, L.; Hu, Z.; Xu, J.; Zhang, K.; Zhang, J.; Zhu, Y. Multi-Step Slow Annealing Perovskite Films for High Performance Planar Perovskite Solar Cells. *Sol. Energy Mater. Sol. Cells* **2015**, *141*, 377–382.
- (8) You, J.; Yang, Y. (Michael); Hong, Z.; Song, T.-B.; Meng, L.; Liu, Y.; Jiang, C.; Zhou, H.; Chang, W.-H.; Li, G.; et al. Moisture Assisted Perovskite Film Growth for High Performance Solar Cells. *Appl. Phys. Lett.* **2014**, *105* (18), 183902.
- (9) Sun, X.; Zhang, C.; Chang, J.; Yang, H.; Xi, H.; Lu, G.; Chen, D.; Lin, Z.; Lu, X.; Zhang, J.; et al. Mixed-Solvent-Vapor Annealing of Perovskite for Photovoltaic Device Efficiency Enhancement. *Nano Energy* **2016**, *28*, 417–425.
- (10) Yu, Y.; Wang, C.; Grice, C. R.; Shrestha, N.; Zhao, D.; Liao, W.; Guan, L.; Awni, R. A.; Meng, W.; Cimaroli, A. J.; et al. Synergistic Effects of Lead Thiocyanate Additive and Solvent Annealing on the Performance of Wide-Bandgap Perovskite Solar Cells. *ACS Energy Lett.* **2017**, *2* (5), 1177–1182.
- (11) Numata, Y.; Kogo, A.; Udagawa, Y.; Kunugita, H.; Ema, K.; Sanchira, Y.; Miyasaka, T. Controlled Crystal Grain Growth in Mixed Cation-Halide Perovskite by Evaporated Solvent Vapor Recycling Method for High Efficiency Solar Cells. *ACS Appl. Mater. Interfaces* **2017**, *9* (22), 18739–18747.
- (12) Luo, J.; Qiu, R. Z.; Yang, Z. S.; Wang, Y. X.; Zhang, Q. F. Mechanism and Effect of  $\gamma$ -Butyrolactone Solvent Vapor Post-Annealing on the Performance of a Mesoporous Perovskite Solar Cell. *RSC Adv.* **2018**, *8* (2), 724–731.
- (13) Zuo, L.; Dong, S.; De Marco, N.; Hsieh, Y. T.; Bae, S. H.; Sun, P.; Yang, Y. Morphology Evolution of High Efficiency Perovskite Solar Cells via Vapor Induced Intermediate Phases. *J. Am. Chem. Soc.* **2016**, *138* (48), 15710–15716.

- (14) Peng, H.; Lan, C.; Chen, S.; Fan, P.; Liang, G.; Lan, H. N,N-dimethylformamide Vapor Effect on Microstructural and Optical Properties of  $\text{CH}_3\text{NH}_3\text{PbI}_3$  Film during Solvent Annealing. *Surf. Coatings Technol.* **2019**, *359*, 162–168.
- (15) Zhang, F.; Song, J.; Zhang, L.; Niu, F.; Hao, Y.; Zeng, P.; Niu, H.; Huang, J.; Lian, J. Film-through Large Perovskite Grains Formation: Via a Combination of Sequential Thermal and Solvent Treatment. *J. Mater. Chem. A* **2016**, *4* (22), 8554–8561.
- (16) Tian, L.; Zhang, W.; Yu, H.; Peng, C.; Mao, H.; Li, Y.; Wang, Q.; Huang, Y. Post-Treatment of Perovskite Films toward Efficient Solar Cells via Mixed Solvent Annealing. *ACS Appl. Energy Mater.* **2019**, *2* (7), 4954–4963.
- (17) Liu, J.; Gao, C.; He, X.; Ye, Q.; Ouyang, L.; Zhuang, D.; Liao, C.; Mei, J.; Lau, W. Improved Crystallization of Perovskite Films by Optimized Solvent Annealing for High Efficiency Solar Cell. *ACS Appl. Mater. Interfaces* **2015**, *7* (43), 24008–24015.
- (18) Knoll, A.; Horvat, A.; Lyakhova, K. S.; Krausch, G.; Sevink, G. J. A.; Zvelindovsky, A. V.; Magerle, R. Phase Behavior in Thin Films of Cylinder-Forming Block Copolymers. *Phys. Rev. L* **2002**, *89* (3), 035501.
- (19) Li, G.; Shrotriya, V.; Huang, J.; Yao, Y.; Moriarty, T.; Emery, K.; Yang, Y. High-Efficiency Solution Processable Polymer Photovoltaic Cells by Self-Organization of Polymer Blends. *Nat. Mater.* **2005**, *4* (11), 864–868.
- (20) Zhao, Y.; Xie, Z.; Qu, Y.; Geng, Y.; Wang, L. Solvent-Vapor Treatment Induced Performance Enhancement of Poly(3-Hexylthiophene):Methanofullerene Bulk-Heterojunction Photovoltaic Cells. *Appl. Phys. Lett.* **2007**, *90* (4), 2005–2008.
- (21) Park, J. H.; Kim, J. S.; Lee, J. H.; Lee, W. H.; Cho, K. Effect of Annealing Solvent Solubility on the Performance of Poly(3-Hexylthiophene)/Methanofullerene Solar Cells. *J. Phys. Chem. C* **2009**, *113* (40), 17579–17584.
- (22) Crossland, E. J. W.; Rahimi, K.; Reiter, G.; Steiner, U.; Ludwigs, S. Systematic Control of Nucleation Density in Poly(3-Hexylthiophene) Thin Films. *Adv. Funct. Mater.* **2011**, *21* (3), 518–524.
- (23) Miller, S.; Fanchini, G.; Lin, Y. Y.; Li, C.; Chen, C. W.; Su, W. F.; Chhowalla, M. Investigation of Nanoscale Morphological Changes in Organic Photovoltaics during Solvent Vapor Annealing. *J. Mater. Chem.* **2008**, *18* (3), 306–312.
- (24) Hüttner, S.; Sommer, M.; Chiche, A.; Krausch, G.; Steiner, U.; Thelakkat, M. Controlled Solvent Vapour Annealing for Polymer Electronics. *Soft Matter* **2009**, *5* (21), 4206.
- (25) Sepe, A.; Rong, Z.; Sommer, M.; Vaynzof, Y.; Sheng, X.; Müller-Buschbaum, P.; Smilgies, D. M.; Tan, Z. K.; Yang, L.; Friend, R. H.; et al. Structure Formation in P3HT/F8TBT Blends. *Energy Environ. Sci.* **2014**, *7* (5), 1725–1736.
- (26) Schlipf, J.; Müller-Buschbaum, P. Structure of Organometal Halide Perovskite Films as Determined with Grazing-Incidence X-Ray Scattering Methods. *Adv. Energy Mater.* **2017**, *7* (16), 1700131.
- (27) Barrit, D.; Cheng, P.; Tang, M.; Wang, K.; Dang, H.; Smilgies, D.; Liu, S. (Frank); Anthopoulos, T. D.; Zhao, K.; Amassian, A. Impact of the Solvation State of Lead Iodide on Its Two-Step Conversion to MAPbI<sub>3</sub>: An In Situ Investigation. *Adv. Funct. Mater.* **2019**, *29* (47), 1807544.
- (28) Filonik, O.; Thordardottir, M. E.; Lebert, J.; Pröller, S.; Weiß, S.; Haur, L. J.; Priyadarshi, A.; Fontaine, P.; Müller-Buschbaum, P.; Mathews, N.; et al. Evolution of Perovskite Crystallization in Printed Mesoscopic Perovskite Solar Cells. *Energy Technol.* **2019**, *7* (10), 1900343.
- (29) Qin, M.; Tse, K.; Lau, T.; Li, Y.; Su, C.; Yang, G.; Chen, J.; Zhu, J.; Jeng, U.; Li, G.; et al. Manipulating the Mixed-Perovskite Crystallization Pathway Unveiled by In Situ GIWAXS. *Adv. Mater.* **2019**, *31* (25), 1901284.
- (30) Chang, C. Y.; Huang, Y. C.; Tsao, C. S.; Su, W. F. Formation Mechanism and Control of Perovskite Films from Solution to Crystalline Phase Studied by in Situ Synchrotron Scattering. *ACS Appl. Mater. Interfaces* **2016**, *8* (40), 26712–26721.



- (31) Moore, D. T.; Sai, H.; Tan, K. W.; Smilgies, D. M.; Zhang, W.; Snaith, H. J.; Wiesner, U.; Estroff, L. A. Crystallization Kinetics of Organic-Inorganic Trihalide Perovskites and the Role of the Lead Anion in Crystal Growth. *J. Am. Chem. Soc.* **2015**, *137* (6), 2350–2358.
- (32) Meng, K.; Wu, L.; Liu, Z.; Wang, X.; Xu, Q.; Hu, Y.; He, S.; Li, X.; Li, T.; Chen, G. In Situ Real-Time Study of the Dynamic Formation and Conversion Processes of Metal Halide Perovskite Films. *Adv. Mater.* **2018**, *30* (11), 1706401.
- (33) Anthamatten, M.; Letts, S. A.; Cook, R. C. Controlling Surface Roughness in Vapor-Deposited Poly (Amic Acid) Films by Solvent-Vapor Exposure. *Langmuir* **2004**, *20* (15), 6288–6296.
- (34) Zomerman, D.; Kong, J.; McAfee, S. M.; Welch, G. C.; Kelly, T. L. Control and Characterization of Organic Solar Cell Morphology Through Variable-Pressure Solvent Vapor Annealing. *ACS Appl. Energy Mater.* **2018**, *1* (10), 5663–5674.
- (35) Hentschke, R. *Thermodynamics*; Undergraduate Lecture Notes in Physics; Springer Berlin Heidelberg: Berlin, Heidelberg, 2014.
- (36) Chauhan, M.; Zhong, Y.; Schötz, K.; Tripathi, B.; Köhler, A.; Huettnner, S.; Panzer, F. Investigating Two-Step MAPbI<sub>3</sub> Thin Film Formation during Spin Coating by Simultaneous in Situ Absorption and Photoluminescence Spectroscopy. *J. Mater. Chem. A* **2020**, *8* (10), 5086–5094.
- (37) Guo, X.; McCleese, C.; Kolodziej, C.; Samia, A. C. S.; Zhao, Y.; Burda, C. Identification and Characterization of the Intermediate Phase in Hybrid Organic-Inorganic MAPbI<sub>3</sub> Perovskite. *Dalt. Trans.* **2016**, *45* (9), 3806–3813.
- (38) Chan Choi, Y.; Lee, S. W.; Jo, H. J.; Kim, D. H.; Sung, S. J. Controlled Growth of Organic-Inorganic Hybrid CH<sub>3</sub>NH<sub>3</sub>PbI<sub>3</sub> Perovskite Thin Films from Phase-Controlled Crystalline Powders. *RSC Adv.* **2016**, *6* (106), 104359–104365.
- (39) Alsari, M.; Bikondoa, O.; Bishop, J.; Abdi-Jalebi, M.; Ozer, L. Y.; Hampton, M.; Thompson, P.; Hörantner, M. T.; Mahesh, S.; Greenland, C.; et al. In Situ Simultaneous Photovoltaic and Structural Evolution of Perovskite Solar Cells during Film Formation. *Energy Environ. Sci.* **2018**, *11* (2), 383–393.
- (40) Hoyer, R. L. Z.; Schulz, P.; Schelhas, L. T.; Holder, A. M.; Stone, K. H.; Perkins, J. D.; Vigil-Fowler, D.; Siol, S.; Scanlon, D. O.; Zakutayev, A.; et al. Perovskite-Inspired Photovoltaic Materials: Toward Best Practices in Materials Characterization and Calculations. *Chem. Mater.* **2017**, *29* (5), 1964–1988.
- (41) Hao, F.; Stoumpos, C. C.; Liu, Z.; Chang, R. P. H.; Kanatzidis, M. G. Controllable Perovskite Crystallization at a Gas-Solid Interface for Hole Conductor-Free Solar Cells with Steady Power Conversion Efficiency over 10%. *J. Am. Chem. Soc.* **2014**, *136* (46), 16411–16419.
- (42) Xu, W.; Lan, Z.; Peng, B.; Wen, R.; Ma, X. Heterogeneous Nucleation Capability of Conical Microstructures for Water Droplets. *RSC Adv.* **2015**, *5* (2), 812–818.
- (43) Becker, R.; Döring, W. Kinetische Behandlung Der Keimbildung in Übersättigten Dämpfen. *Ann. Phys.* **1935**, *416* (8), 719–752.
- (44) Ostwald, W. Über Die Vermeintliche Isomerie Des Roten Und Gelben Quecksilbersoxyds Und Die Oberflächenspannung Fester Körper. *Zeitschrift für Phys. Chemie* **1900**, *34*, 495.
- (45) Freundlich, H. *Colloid and Capillary Chemistry*; New York, 1926.
- (46) DeQuilettes, D. W.; Vorpahl, S. M.; Stranks, S. D.; Nagaoka, H.; Eperon, G. E.; Ziffer, M. E.; Snaith, H. J.; Ginger, D. S. Impact of Microstructure on Local Carrier Lifetime in Perovskite Solar Cells. *Science*. **2015**, *348* (6235), 683–686.
- (47) Liu, T.; Su, P.; Liu, L.; Wang, J.; Feng, S.; Zhang, J.; Xu, R.; Yang, H.; Fu, W. An Ionic Compensation Strategy for High-Performance Mesoporous Perovskite Solar Cells: Healing Defects with Tri-Iodide Ions in a Solvent Vapor Annealing Process. *J. Mater. Chem. A* **2019**, *7* (1), 353–362.
- (48) Gann, E.; Caironi, M.; Noh, Y.-Y.; Kim, Y.-H.; McNeill, C. R. Diffractive X-Ray Waveguiding Reveals Orthogonal Crystalline Stratification in Conjugated Polymer Thin Films. *Macromolecules* **2018**, *51* (8), 2979–2987.

## Supporting Information

# Crystallization Kinetics of Controlled Solvent Vapor Assisted Annealing of Organo Lead Perovskite Film

Yu Zhong, Dominik Seeberger, Anna Köhler, Fabian Panzer, Cheng Li,\* Sven  
Huettner\*

\* Author to whom correspondence should be addressed: [cheng.li@uni-bayreuth.de](mailto:cheng.li@uni-bayreuth.de) and [sven.huettner@uni-bayreuth.de](mailto:sven.huettner@uni-bayreuth.de)

## S1: Experimental Procedures

PbI<sub>2</sub> beads, DMF (anhydrous 99.8%) and 2-propanol (anhydrous 99.5%) were from Sigma Aldrich Company. MAI was from Dyesol Company. PbI<sub>2</sub> beads were dissolved in DMF at 75 °C to get 1M solvent. MAI was dissolved in 2-Propanol to get 0.25M solvent. 80 µL PbI<sub>2</sub> solvent was spin coated on the substrate, which was treated with plasma before. Then the sample was annealed at 100°C for 5min and 400 µL MAI solvent was spin coated on the PbI<sub>2</sub> layer. After that, the sample was sealed in the sample chamber in the glovebox. The sample chamber was transferred into the oven and connected to the solvent chamber and N<sub>2</sub> gas. Next, the hotplate and gas flow were open. The sample was annealed at 110 °C for 45min with a constant gas flow of 10 cm<sup>3</sup>/min. For SVAA sample, it was annealed under DMF vapor with N<sub>2</sub> gas in the first 30min.

For GIWAXS measurement, samples were put in the chamber, which is shown in Figure 3(a). The chamber was placed on a holder, which could be heated. The annealed temperature for GIWAXS measurement is 120 °C. The reason is that the chamber for GIWAXS measurement is quite thick and the actual temperature in the chamber is below 120 °C, around 110 °C. *In-situ* GIWAXS measurements were performed at SAXS/WAXS beamline at Australian synchrotron. The X-ray energy is 11 keV with an incident angle of 0.22°. The scattered X-ray was detected by a 1M Pilatus detector positioned 36 cm behind the sample. Measurements started when the holder reached 120°C. A customized version of NIKA software based on Igor Pro from WaveMetrics was used to analysis the data.<sup>[1]</sup>

SEM images were taken by Zeiss Leo 1530 scanning electron microscope with field emission gun. The perovskite films were sputtered with a thin platinum layer before observation. The accelerating voltage for electrons is 3kV. The grain sizes of perovskite crystals were obtained from the SEM images with the help of Image J.

## S2: Estimation of Solvent Concentration in Chamber

The Clausius-Clapeyron relation shows the vapor pressure change along with temperature:<sup>[2]</sup>

$$\ln \frac{p_y}{p_x} = \frac{\Delta H_{\text{vap}}}{R} \left( \frac{1}{T_x} - \frac{1}{T_y} \right)$$

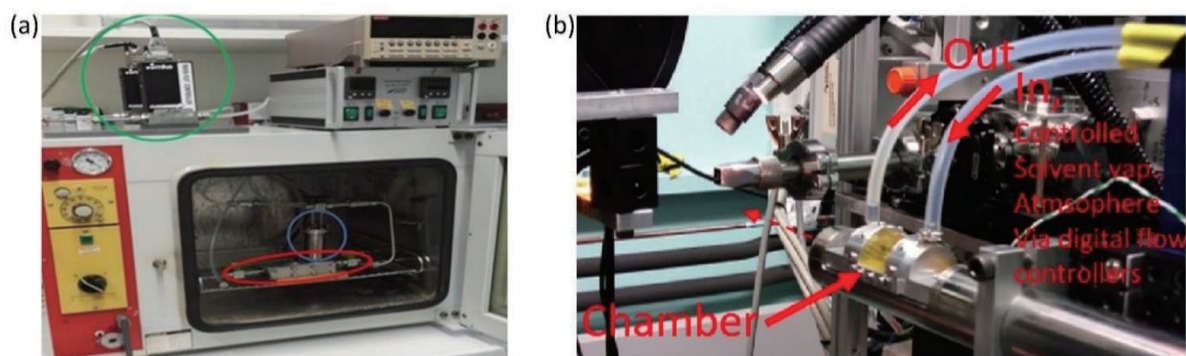
$p_y$  or  $p_x$  is the saturated vapor pressure at a given temperature  $T_x$  or  $T_y$ .  $T$  is the temperature.  $R$  is the gas constant (8.3145 J·mol<sup>-1</sup>·K<sup>-1</sup>).  $\Delta H_{\text{vap}}$  is the specific evaporation enthalpy. For DMF,  $\Delta H_{\text{vap}}$  = 46.7 kJ/mol. The vapor pressure at 293.15 K is 3.77 hPa.<sup>[3],[4]</sup> With these, the vapor pressure of DMF at a specific saturation can be calculated. The actual vapor pressure at temperature  $T_y$  with a specific saturation is:

$$p = \text{sat\%} * p_y$$

Then based on ideal gas concentration:  $n = \frac{pV}{RT}$ ,<sup>[2]</sup> we can get DMF concentration in the chamber:

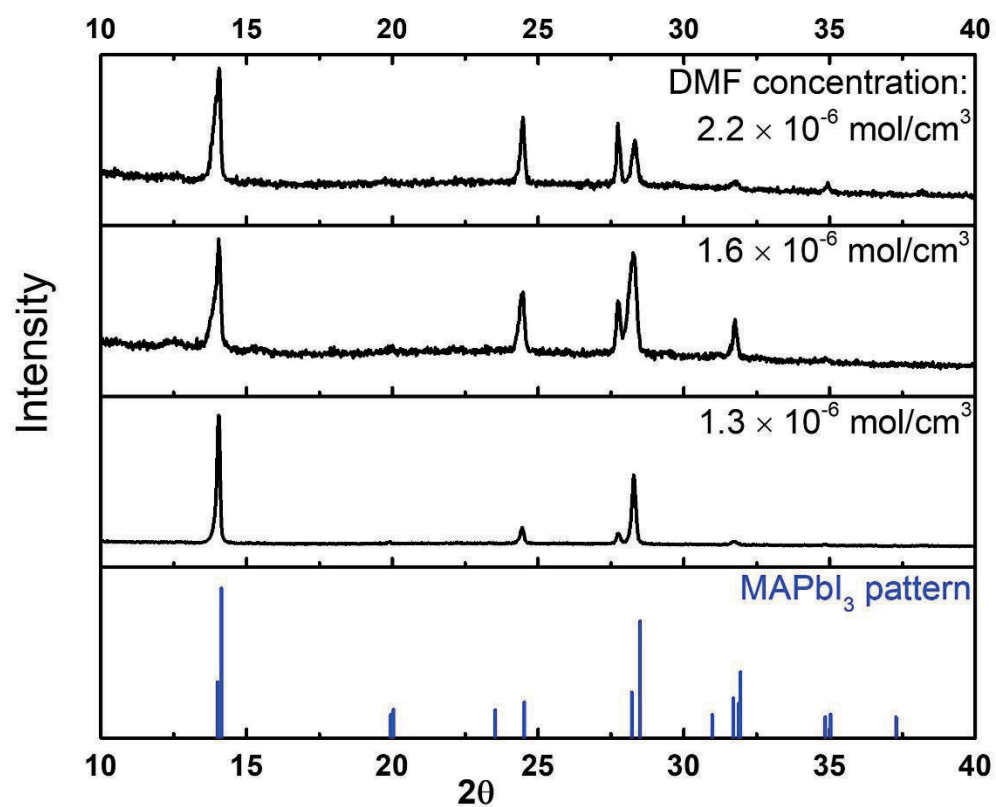
$$c = \frac{n}{V} = \frac{p}{RT}$$

### S3: SVAA Setup

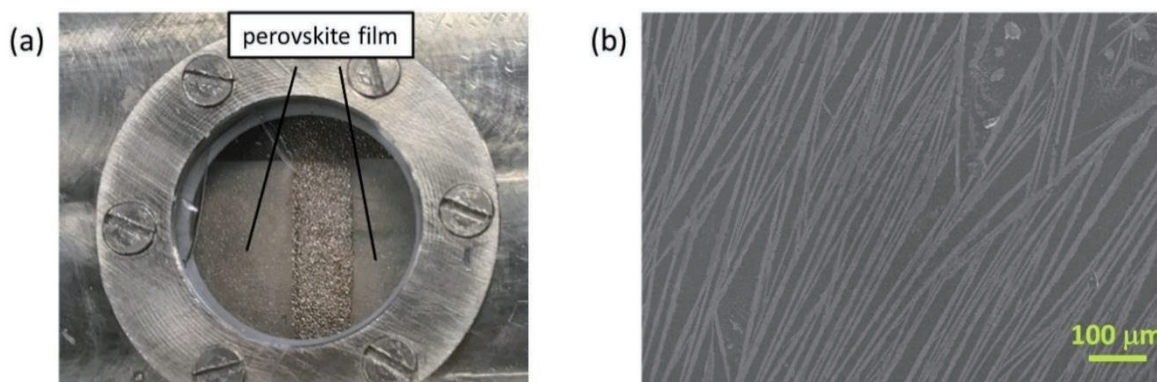


**Figure S1:** (a) The image of the solvent annealing setup shown in Figure 1(b). In the green circle, they are two flow controllers. In the blue circle, it is the solvent bubbler. In the red circle, it is the sample chamber. (b) The SVAA setup for GIWAXS measurement.

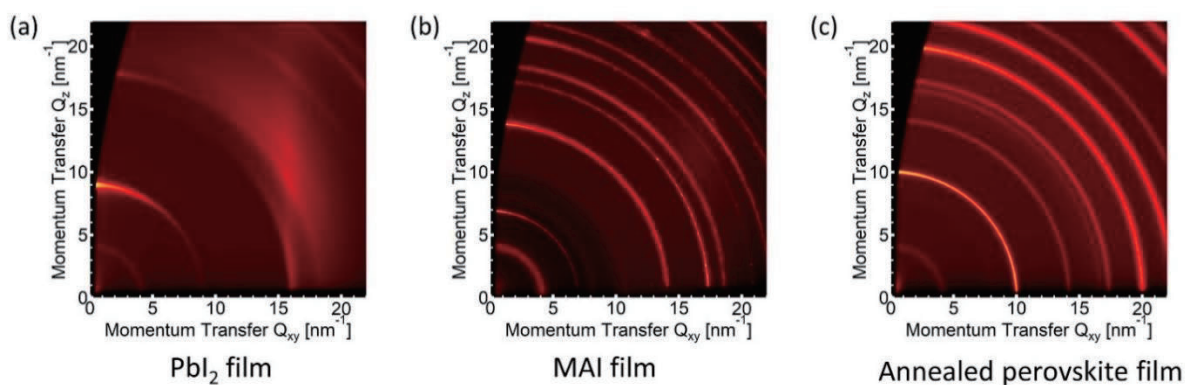
### S4: XRD Patterns of Perovskite Films



**Figure S2:** XRD patterns of the perovskite film annealed under DMF vapor. It shows full conversion into MAPbI<sub>3</sub> after SVAA.

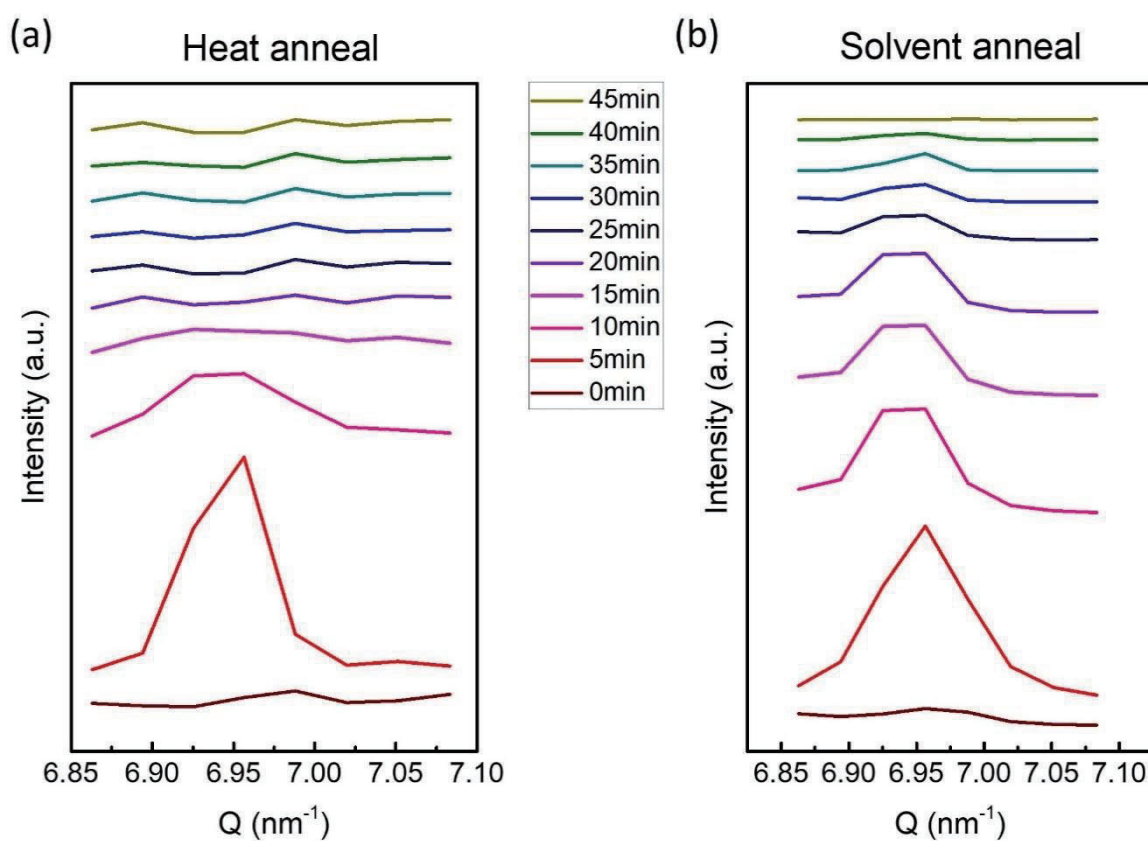
**S5: Morphology of Perovskite Films Annealed under High DMF Vapor**

**Figure S3:** Films annealed with the following condition: DMF concentration =  $3.8 \times 10^{-6}$  mol/cm<sup>3</sup> (Temperature of oven = 90 °C, DMF saturation = 75%) (a) Image taken during the solvent vapor annealing process (b) SEM image of the perovskite film after solvent vapor annealing.

**S6: GIWAXS Patterns of Reference Samples**

**Figure S4:** 2D-GIWAXS patterns of (a) PbI<sub>2</sub>, (b) MAI, (c) MAPbI<sub>3</sub>. The peak at 4.0 nm<sup>-1</sup> comes from the kapton film before the detector.



**S7: Time-Evolution of GIWAXS Pattern**

**Figure S5:** Azimuthally integrated intensity plot of the GIWAXS patterns in the range  $Q = 6.85 - 7.10 \text{ nm}^{-1}$ . The typical MAI peak locates in this region.



## S8: GIWAXS Patterns of Sample Annealed with DMF Vapor

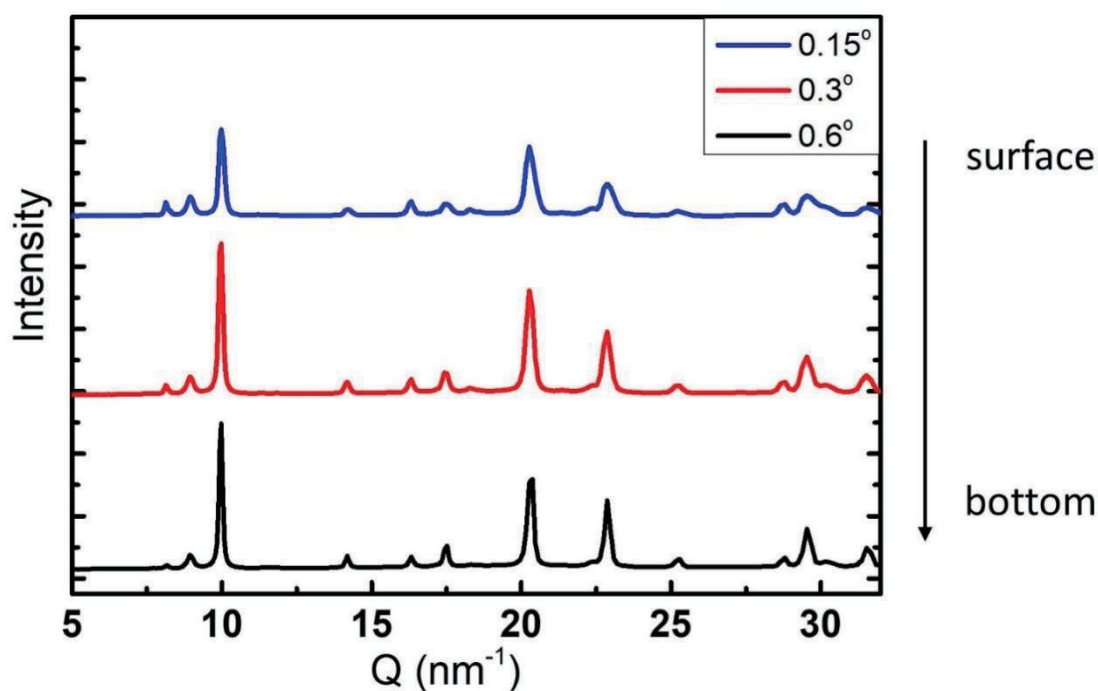


**Figure S6:** Azimuthally integrated intensity plot of the GIWAXS patterns with different incident angle: 0.15°, 0.3°, 0.6°. These data were taken at the 10min during SVAA with DMF concentration of  $1.8 \times 10^{-6}$  mol/cm<sup>3</sup>.

## References

- [1] E. Gann, M. Caironi, Y.-Y. Noh, Y.-H. Kim, C. R. McNeill, *Macromolecules* **2018**, *51*, 2979–2987.
- [2] R. Hentschke, *Thermodynamics*, Springer Berlin Heidelberg, Berlin, Heidelberg, **2014**.
- [3] K. Panneerselvam, M. P. Antony, T. G. Srinivasan, P. R. Vasudeva Rao, *Thermochim. Acta* **2009**, *495*, 1–4.
- [4] T. E. Daubert, *Physical and Thermodynamic Properties of Pure Chemicals : Data Compilation*, New York : Hemisphere Pub. Corp., **1989**.



## 9 Appendix

### 9.1 List of Publications

1. Y. Zhong, D. Seeberger, A. Köhler, F. Panzer, C. Li, S. Huettnner  
The Kinetics Study of Solvent Vapor Assisted Annealing Crystallization of Organo Lead Perovskite Film  
Prepared for submission
2. Y. Zhong, M. Hufnagel, M. Thelakkat, C. Li, S. Huettnner  
Role of PCBM in the Suppression of Hysteresis in Perovskite Solar Cells  
*Advanced Functional Materials*, **2020**, 1908920
3. M. Chauhan, <sup>‡</sup> Y. Zhong, <sup>‡</sup> K. Schötz, B. Tripathi, A. Köhler, S. Hüttner, F. Panzer (<sup>‡</sup> - equally contributed to the publication)  
Investigating Two-Step MAPbI<sub>3</sub> Thin Film Formation during Spin Coating by Simultaneous *in situ* Absorption and Photoluminescence Spectroscopy  
*Journal of Materials Chemistry A*, **2020**, 8, 5086-5094
4. C. Li, N. Wang, A. Guerrero, Y. Zhong, H. Long, Y. Miao, J. Bisquert, J. Wang, S. Huettnner  
Understanding the Improvement of Stability in Self-Assembled Multiple Quantum Wells Perovskite Light-Emitting Diode  
*The Journal of Physical Chemistry Letters*, **2019**, 10, 21, 6857-6864
5. Y. Zhong, C. A. M. Luna, R. Hildner, C. Li, S. Huettnner  
*In situ* Investigation of Light Soaking in Organolead Halide Perovskite Films  
*APL Materials*, **2019**, 7, 041114
6. K. P Goetz, K. Sekine, F. Paulus, Y. Zhong, D. Roth, D. B.-Koch, Y. J. Hofstetter, E. Michel, L. Reichert, M. Rudolph, S. Huettnner, Y. Vaynzof, E. M Herzig, S. Hashmi, J. Zaumseil  
The Effect of Side-Chain Length on the Microstructure and Processing Window of Zone-Cast Naphthalene-Based Bispentalenes  
*Journal of Materials Chemistry C*, **2019**, 7, 13493-13501
7. S.-G. Kim, C. Li, A. Guerrero, J.-M. Yang, Y. Zhong, J. Bisquert, S. Huettnner, N.-G. Park  
Potassium Ions as a Kinetic Controller in Ionic Double Layers for Hysteresis-Free Perovskite Solar Cells  
*Journal of Materials Chemistry A*, **2019**, 7, 18807-18815
8. M.-H. Wang, Z.-Y. Xue, Z.-W. Wang, W.-H. Ning, Y. Zhong, Y.-N. Liu, C.-F. Zhang, S. Huettnner, Y.-T. Tao  
Slight Structural Disorder in Bithiophene-based Random Terpolymers with Improved Power Conversion Efficiency for Polymer Solar Cells

*Chinese Journal of Polymer Science*, **2018**, 36, 1129-1138

9. Z. Xue, S. Wang, J. Yang, Y. Zhong, M. Qian, C. Li, Z. Zhang, G. Xing, S. Huettner, Y. Tao, Y. Li, W. Huang  
Enhanced Power Conversion Efficiency in Iridium Complex-based Terpolymers for Polymer Solar Cells  
*npj Flexible Electronics*, **2018**, 2, 1
  
10. X. Gao, M. Wang, X. Cao, J. Yang, Y. Zhong, Z. Zhang, C. Li, S. Huettner, Y. Tao, Y. Li, W. Huang  
Cyclometalated Pt Complex based Random Terpolymers as Electron Acceptors for all Polymer Solar Cells  
*Journal of Polymer Science Part A: Polymer Chemistry*, **2018**, 56, 105-115
  
11. C. Li, A. Guerrero, Y. Zhong, A. Gräser, C. A. M. Luna, J. Köhler, J. Bisquert, R. Hildner, S. Huettner  
Real-Time Observation of Iodide Ion Migration in Methylammonium Lead Halide Perovskites  
*Small*, **2017**, 13, 1701711
  
12. C. Li, A. Guerrero, Y. Zhong, S. Huettner  
Origins and Mechanisms of Hysteresis in Organometal Halide Perovskites  
*Journal of Physics: Condensed Matter*, **2017**, 29, 193001
  
13. Z. Wan, J. Yang, Y. Liu, S. Wang, Y. Zhong, C. Li, Z. Zhang, G. Xing, S. Huettner, Y. Tao, Y. Li, W. Huang  
Cyclometalated Pt Complex-based Random Terpolymers for Efficient Polymer Solar Cells  
*Polymer Chemistry*, **2017**, 8, 4729-4737
  
14. C. Li, Y. Zhong, C. Luna, T. Unger, K. Deichsel, A. Gräser, J. Köhler, A. Köhler, R. Hildner, S. Huettner  
Emission Enhancement and Intermittency in Polycrystalline Organolead Halide Perovskite Films  
*Molecules*, **2016**, 21, 8, 1081

## 9.2 Abbreviations

BCP: Bathocuproine

CPD: Chemical potential difference

DFT: Density function theory

DMF: Dimethylformamide

DMSO: dimethyl sulfoxide

EQE: External quantum efficiency

ETL: Electron transport layer

FA: Formamidinium

FF: Fill factor

FTO: Fluorine-doped tin oxide

GBL:  $\gamma$ -butyrolactone

GIWAXS: Grazing incidence wide-angle X-ray scattering

HTL: Hole transport layer

ICBA: Indene-C60 bisadduct

IPA: Isopropanol

IPCE: incident photon-to-electron conversion efficiency

ITO: Indium tin oxide

$J$ - $V$ : Current density-voltage

$J_{\text{mp}}$ : Current density at the maximum power point

$J_{\text{sc}}$ : Short-circuit current

KPM: Kelvin probe microscopy

MA: Methylammonium

MAI: Methylammonium iodide

OMHP: Organo metal halide perovskite

PCBM: Phenyl-C61-butyrac acid methyl ester

PCE: Power conversion efficiency

PL: Photoluminescence

PMMA: Polymethylmethacrylate

PPCBM: PCBM grafted polymer

PSC: Perovskite solar cell

PTAA: Poly(triaryl amine)

PTIR: Photothermal induced resonance

Spiro-OMeTAD: 2,2',7,7' - Tetrakis[N,N-di(4-methoxyphenyl)amino] - 9,9' – spirobifluorene

SVAA: Solvent vapor assisted annealing

ToF-SIMS: Time of flight secondary ion mass spectrometry

$V_{mp}$ : Voltage at the maximum power point

$V_{oc}$ : Open circuit voltage

XPS: X-ray photoelectron spectroscopy



## 9.3 Acknowledgements

Here, I would like to acknowledge all the people who supported me during my doctoral thesis. First of all, I acknowledge my mentors, Prof. Anna Köhler and Dr. Fabian Panzer, taking me as a PhD student in Experimental Physics II. Prof. Anna Köhler gives me trust and freedom on my research. Her seriousness on science and patience for students set the example for me how an outstanding scientist is. Dr. Fabian Panzer is always kind and support me a lot in the last one and half years of my PhD study. Every time I discussed with him, I was inspired by his brilliant ideas and rigorous thinking.

I express my gratitude to Prof. Sven Huettnner and Prof. Cheng Li, who were my mentors in the two and half years of my PhD study. They helped me to have systematical training on science, including experiment design, setup assembling, academic presentation, writing skills and so on, from which I will benefit in my future career. Even after they left University of Bayreuth, they still kept closed contact with me. If I meet some problems in research, they are always willing to give me a hand.

I would like to thank Prof. Mukundan Thelakkat for his support. He gave me the chance to have the access to their laboratory equipment and the material synthesized by his student Dr. Martin Hufnagel was shared to me. Besides these, his encouragement was so warm for me, who was a foreign student in Germany.

I show my thanks to Prof. Richard Hildner. He has provided me valuable suggestions on the application of PL microscopy. And his student Dr. Carlos Andres Melo Luna helped me to operate it. Without their assistance the first two projects couldn't go on so smoothly.

I want to acknowledge Prof. Eva. M. Herzig. Her advice for the scattering data analysis was helpful. She was so patient to explain all the questions I raised. I attended her lecture in one semester and I benefited a lot from the knowledge I learned in her lecture.

Many thanks to my colleague Philipp Ramming and especially for his assistance since 2019. The cooperation and discussion with him are always productive and joyful. I am grateful to my colleague Mihirsinh Chauhan and Konstantin Schötz. Their contribution to the analysis on the absorption and photoluminescence data made our cooperative work successful. I acknowledge Nico Leupold for his help in the impedance spectroscopy. I express my thanks to Seul-Gi Kim and Dr. Valerie Mitchell for their help when I was visiting their groups. Meanwhile, Seul-Gi Kim provided me useful advices on optimizing the solar cell efficiency.

I want to thank Irene Bauer for her solutions on chemical issues and Frank Schirmer for solving electronic and technical problems. The help from Michaela Fischer let me have no concerns for the administrative stuff. Meanwhile, I am glad to work with all the members in Experimental Physics II, because all of us work together to create a good academic atmosphere.

I acknowledge the support from Macromolecular Chemistry I, where I worked for more than 3 years. Dr John Mohanraj was nice to offer me assistance and I was always impressed by the discussion with him. No matter what kind of technical problems I met, Jonas Mayer could quickly find a solution for me. I am grateful to Dr. Reiner Giesa for organizing XRD machine and Martina Heider for the SEM measurements. I express my gratitude to the two secretaries, Petra Weiss and Christina Wunderlich. And thanks to Minde Jin for his kindly help.

I appreciate my former colleagues in Prof. Huettnner's group: Dr. Xudong Cao, Dr. Mengyu Chen, Benno Buchinger, Dominik Seeberger and Anna Gräser. In addition to the scientific parts,

the enjoyable office time really relaxed the stressful laboratory work. I also want to thank all of my friends who care for and support me.

Last but foremost, I owe my heartfelt thanks to my parents and my grandparents for their unconditional support. They have done so much for me since I was born. My special thanks also goes to my husband, Jian Zhang. Every time I was depressed, he accompanied me and encouraged me. Without him I would have not completed this dissertation.

## 9.4 Eidesstattliche Versicherung und Erklärungen

(§ 9 Satz 2 Nr. 3 PromO BayNAT)

Hiermit versichere ich eidesstattlich, dass ich die Arbeit selbstständig verfasst und keine anderen als die von mir angegebenen Quellen und Hilfsmittel benutzt habe (vgl. Art. 64 Abs. 1 Satz 6 BayHSchG).

(§ 9 Satz 2 Nr. 3 PromO BayNAT)

Hiermit erkläre ich, dass ich die Dissertation nicht bereits zur Erlangung eines akademischen Grades eingereicht habe und dass ich nicht bereits diese oder eine gleichartige Doktorprüfung endgültig nicht bestanden habe.

(§ 9 Satz 2 Nr. 4 PromO BayNAT)

Hiermit erkläre ich, dass ich Hilfe von gewerblichen Promotionsberatern bzw. -vermittlern oder ähnlichen Dienstleistern weder bisher in Anspruch genommen habe noch künftig in Anspruch nehmen werde.

(§ 9 Satz 2 Nr. 7 PromO BayNAT)

Hiermit erkläre ich mein Einverständnis, dass die elektronische Fassung meiner Dissertation unter Wahrung meiner Urheberrechte und des Datenschutzes einer gesonderten Überprüfung unterzogen werden kann.

(§ 9 Satz 2 Nr. 8 PromO BayNAT)

Hiermit erkläre ich mein Einverständnis, dass bei Verdacht wissenschaftlichen Fehlverhaltens Ermittlungen durch universitätsinterne Organe der wissenschaftlichen Selbstkontrolle stattfinden können.

.....

Ort, Datum, Unterschrift





